MICROSTRUCTUE AND MECHANICAL PROPERTY CONTROL DURING ADDITIVE MANUFACTURING

By

Abdullah F. Alhuzaim

A thesis submitted to University of Birmingham in partial fulfillment of the requirements for the degree of

DOCTOR OF PHILOSPHY

Metallurgy and Materials

School of Engineering

University of Birmingham

2021

Abstract

The microstructure of Inconel superalloy thin walls has been characterised. The thin walls were built using direct laser deposition (DLD) with variable parameters: a wide range of continuous laser powers with different pulsing types, frequencies, powder feed rates, scanning speeds and strategies. The walls were analysed to assess the role of the DLD parameters on the microstructure, elemental segregation, mechanical properties, discontinuities, cracks and build geometry, in order to identify the sensitivity of the grain and precipitate morphology to the various process parameters. The builds were examined using optical microscopy, scanning electron microscopy, energy dispersive X-ray analysis and electron backscattered diffraction. An analytical thermal camera and thermocouples were used to study the influence of deposit temperature on grain size and hardness. The power mode was used to control the heat input and cooling rates, which resulted in significant modifications in the microstructure and properties of the deposits. In this work, DLD was performed on IN718 and CM247LC Ni-superalloy using continuous wave laser power modes, and different pulsed wave modes to understand the impact on the product using advanced material characterisation techniques. The study showed that increasing the laser power gave rise to a columnar grain structure, and the grains became coarser as the laser power increased. Furthermore, the deposition path appeared to affect the orientation of the dendrites; this change can be attributed to the variation in the heat flux within the melt pool. Power pulsing increased the cooling rate and reduced the average heat input, and most importantly this broke the dendrites and disturbed the segregation process, thereby reducing the formation of Laves phase. The microstructure could be tailored to a specific size using pulsing, which could also reduce Nb segregation and so reduce the time needed for heat treatment after deposition. Furthermore, the pulse duration played a significant role in reducing segregation and eliminating cracking. A significant variation was observed in the grain size distribution and morphology while the porosity volume fraction was limited, and this varied marginally with the process parameters.

Keywords: Additive Manufacturing, Direct Manufacturing, Free form Fabrication, Metal Deposit, Plasma Arc Welding, Shot Form Feedstock Delivery

Dedication

This thesis is dedicated to my small family: Latifa, Fahad, Tadi, Ibrahim and Salman. Thank you for going through all of this with me. None of this would have been possible without the support I have received from all of you.

Acknowledgements

I would like to acknowledge and thank my mentor, thesis advisor and graduate school academic advisor, Professor Moataz Attallah, for his guidance and encouragement throughout my graduate career at the University of Birmingham and for leading me down the road of metallurgy and Materials Engineering. Because of Professor Moataz, I learned that there is much more to know about in the field of the third industrial revolution, 3D printing, than just designing and making parts.

Special thanks are reserved for my thesis committee members, Professor Robert Lancaster from Swansea University and Dr Yu Lung Chiu from the University of Birmingham, for reviewing this thesis and for offering their expert advice.

Many thanks are offered to Dr Stano Imbrogno for providing me with his professional knowledge of Materials Engineering and Dr Abdelmoez Hussein for help and support within the lab. Also, many thanks to Kathleen Waldron for the administrational support.

In addition, I would like to thank Eng. Mostafa Almahdi, CEO of the Royal Commission of Jubail, and Dr Ali Assiri, General Manager of the Education Sector in the Royal Commission of Jubail, for the scholarship opportunity to make this happen.

Lastly, I offer my regards and blessings to my family and friends who have supported me during my education and this research. The truth be told, I would far rather have spent some of the hours I spent on this research engaged in more leisurely activities. In the end, however, the effort was for a good cause, and the benefits will be reaped not only by us, but also by those closest to us.

Above all, utmost appreciation to the Almighty God for the divine intervention in this academic endeavour.

List of Publications

Parts of this dissertation have been published and presented in the publications and conferences mentioned below, as well as future articles to be submitted for publication and dissemination at internal conferences:

I. Abdullah Alhuzaim, Stano Imbrogno, Moataz M Attallah, "Controlling microstructural and mechanical properties of direct laser deposited Inconel 718 via laser power," Journal of Alloys and Compounds, vol. 872, 2021. 159588

CRediT authorship contribution statement
Abdullah Alhuzaim: designed the study and performed the experimental tests and the analysis of the results. Writing – review and editing under the supervision of Moataz Attallah. **Stano Imbrogno**: contribution to the experimental tests and analysis of the results under the supervision of Moataz Attallah. Reviewing the paper. **Moataz Attallah**: support on experimental feasibility and infrastructure.

II. Stano Imbrogno, Abdullah Alhuzaim, Moataz M. Attallah, "Influence of the laser source pulsing frequency on the direct laser deposited Inconel 718 thin walls," Journal of Alloys and Compounds, vol. 856, 2020. 158095

CRediT authorship contribution statement
Stano Imbrogno: designed the study and performed the experimental tests and the analysis of the results. Writing – review and editing under the supervision of Moataz Attallah. **Abdullah Alhuzaim**: contribution to the experimental tests and analysis of the results under the supervision of Moataz Attallah. Reviewing the paper. **Moataz Attallah**: support on experimental feasibility and infrastructure.

Papers in Preparation/Submission as a Primary Author

I. Chapter 4: Influence of Direct Laser Deposition Parameters on Geometrical and Microstructural Development – not publish yet still in preparation on the day submission.

II. Chapter 6: Influence of Power Mode on the Microstructural and Mechanical Properties Development - Not publish yet still in preparation on the day of dissertation submission

III. Chapter 7: Direct laser deposition of crack-free CM247LC thin walls: mechanical properties and microstructural effects of heat treatment – Under review by material design journal

Presentations in International Conferences

- Materials Science and Technology MS&T, symposium of Additive Manufactureing of Metals: Microstructure and Material properties presentation entitled: Microstructural and Mechanical Properties Control using Direct Laser Deposition in IN718 Ni-superalloy, October 2018, Columbus, Ohio, USA
- National Student Conference in Metallic Materials at University of Sheffield, 2018, the presentation entitled Microstructural and Mechanical Properties Control using Direct Laser Deposition in IN718 Ni-superalloy

Table of Contents

Glossary of Terms

Term	Definition
AM	Additive Manufacturing
ASTM	American Society for Testing and Materials
Ar	Argon
AWS	American welding society
A36	Plain carbon steel alloy
A286	Iron-based superalloy
BCC	Body-Centered Cubic
BCT	Body Centred Tetragonal
BD	Build Direction
BCT	Body Centred Tetragonal
BSE	Back Scattered Electron
C	Carbon
CAD	Computer Aided Design
Cb	Columbium
CC	Constant current
CET	Columnar to equiaxed transition
cfh	Cubic feet per hour
cm	Centimeter
CM247LC	Inconel superalloy type
CNC	Computer numerical control
c_p	Specific heat at constant pressure [J/(g·°C)]
Cr	Chromium
Cs	Cesium
Cu	Copper
CW	continuous wave
DED	Directed Energy Deposition
DAS	Dendrite Arm Spacing
DLD	Direct Laser Deposition
DLF	Direct Laser Fabrication
DoE	Design of Experiments
DSC	Differential Scanning Calorimetry
DP	depth of penetration
DM	Direct manufacturing
DPPW	Double Power Pulse Wave
d_{arc}	Arc diameter (mm)
DC	Direct current
DCEN	Direct current electrode negative
DDC	Ductility dip cracking
EBSD	Electron Back Scatter Diffraction
EDS	Energy-Dispersive X-ray Spectroscopy
EDM	electric discharge machine
EBSD	Electron Back Scatter Diffraction
EDS	Energy-Dispersive X-ray Spectroscopy
EBF_3	Electron beam free-form fabrication
EBW	Electron beam welding
etc.	Etcetera
FCC	Face Centre Cubic
Fe	Iron

FFF	Free-form fabrication
ft	Feet
ft·lb	Foot-pound
FZ	Fusion zone
G	Temperature/Thermal gradient
g	Gram
GPa	Gigapascal
GTAW	Gas tungsten arc welding
H	Hydrogen
HAZ	Heat-affected zone
HCP	Hexagonal close-packed
He	Helium
HLM	Hybrid layered manufacturing
HCC	High Cooling Cycle
h_t	Weld track height (mm.)
ICP	Inductively Coupled Plasma
In.	Inch
ipm	Inches per minute
IN718	Inconel 718
HSTA	Homogenisation, Solution and Aging Heat Treatment
J	Joule
K	Kelvin
kg	Kilogram
ksi	1,000 pounds per square inch
kW	Kilowatt
kV	Kilovolt
L	Liter
La	Lanthanum
LAM	Laser additive manufacturing
lb.	Pound
LBW	Laser beam welding
LCC	Low Cooling Cycle
L_p	laser power (watt)
L_d	laser spot size (mm)
LM	Layered manufacturing
m	Meter
mA	Milliampere
MD	Metal deposition
m_{dep}	Cumulative deposit mass (kg)
min	Minute
mm	Millimeter
Mn	Manganese
m_o	Original substrate mass (kg)
Mo	Molybdenum
MPa	Megapascal
MS	Martensitic start temperature
ms	Millisecond
Mt	Megatonnes
N	Nitrogen
Ni	Nickel

Nb	Niobium
Nd: YAG	neodymium-doped yttrium aluminium garnet
NNS	Near-net Shape Manufacturing
n_l	Layer "n" in the deposit
N_l	Number of layers per deposit
n_t	Track "n" in the deposit
N_t	Number of tracks per layer
nm	Nano meter (1 x 10^{-9} m)
O	Oxygen
Pa	Pascal
Pd	Palladium
PD	Power density (W/mm^2)
PFR	Powder Flow Rate
P/M	Powder metallurgy
ppm	Parts per million
P_{max}	maximum power value
P_{min}	minimum power value
psi	Pounds per square inch
PW	Pulsing Wave
PPW	Partial Pulse Wave
PDPPW	Partial Double Power Pulse Wave
PWHT	post weld heat treatment
R	growth velocity at the liquid-solid interface
RM	Rapid manufacturing
RP	Rapid prototyping
RT	Room Temperature
s	Second
SAE	Society of Automotive Engineers
SAC	strain-age cracking
SDAS	secondary dendrite arm spacing
SEM	Scanning Electron Microscopy
Si	Silicon
SLM	Selective Laser Melting
SMD	Shaped metal deposition
Sn	Tin
SS	Scanning Speed
SP	Standard Pulsing
S/L	solid/liquid
Ta	Tantalum
TCP	Topologically close-packed
TET	turbine entry temperature
Th	Thorium
Ti	Titanium
TiO_2	Rutile
t_{max}	maximum pulse duration
t_{min}	minimum pulse duration
T_{sur}	Surrounding/ambient temperature (°C)
t_t	Time to weld one track (s)
T_L	lengths of the pulse
TTT	Time-temperature- transformation

TV	Television
UNS	Unified Numbering System for Metals and Alloys
UoB	University of Birmingham
U.S.	United states
UTS	Ultimate tensile strength
V	Vanadium
V	Voltage
V_b	Filler ball volume ($mm.^3$)
V_l	scanning speed (mm/min)
W	Tungsten
W	Watt
WAP	Weighted Average Power
WPW	weld pool width
W_o	laser spot radius in millimetres
wt%	Weight percent
XRD	X-ray diffraction
Y	Yttrium
YS	Yield strength
Zr	Zirconium
Å	Ångström
γ	Gamma
γ'	Gamma prime
γ''	Gamma double prime
γ_p'	Cuboidal Gamma prime
γ_t'	ultra-fine cuboidal Gamma prime
δ	Delta Phase
ε	cooling rate in kelvins per second
μm	Micrometer (1×10^{-6} m)
π	Mathematical constant (≈ 3.14)
ρ	Density (g/cm^3)
σ	Sigma
μ	Mu
Σ	Summation
°	Degree (angle)
°C	Degree Celsius
°F	Degree Fahrenheit
θ	theta
%	Percent
±	Plus-minus
<	Less than
<<	Much less than
>	Greater than
>>	Much greater than
≥	Greater-than or equal to
≈	Almost equal to
=	Equal
#	Number
II	Roman numeral two
III	Roman numeral three
2D	Two-dimensional

304	Stainless steel alloy
3D	Three-dimensional
VIII	Roman numeral eight

Chapter 1. Introduction

This chapter provides a brief background of the importance of additive manufacturing (AM) and its rapid growth in industrial and research arenas, especially in relation to high-temperature materials, and their importance and applications. Additionally, this section covers the general concept of AM, the potential advantages and disadvantages of this technique, its uses within the petrochemical and aerospace sectors, and applications associated with Inconel-superalloys. Finally, gas turbine engines, which are one of the most significant applications of high-temperature materials, are discussed.

1.1 A brief background of high-temperature materials

One of the most important applications of high-temperature materials is in gas turbine engines, which are critical for the refining process and have become widely used in the petrochemical arena. Turbine engines are a complex piece of equipment comprising several components with many materials of varying mechanical properties. Such engines require high-temperature materials capable of withstanding intense heat (around 650 °C) and high stress, particularly at the turbine wheel blades, which are in direct contact with the emission gas at speeds as high as 100,000 rpm. A nickel-based superalloy is usually used to meet the requirements of turbine blades. There are few choices of nickel-based alloys that have been developed to meet these requirements, such as IN718 and CM247LC, which have good mechanical properties and microstructure stability at elevated temperatures. Nickel-based superalloys account for 40%–50% of the total weight of a turbine engine. A gas turbine is basically a tube with two open ends. Air enters through one end, is compressed, and mixed with fuel then burned in combustion chambers, and finally, the thrust exhaust through the other end continuously. The rotary and static sections of the compressor are primarily the components that come into contact with the gas stream in the cold section. This section is usually made from titanium alloy, as it

is light in weight and strong, and the temperature here is relatively low. In the hot section, on the other hand, a high-temperature material is needed that can maintain its mechanical properties close to the melting point, while also tolerating the severe environmental conditions, such as corrosion and oxidisation. Nickel-based superalloys are also, resistant to mechanical degradation caused by long-term loading, such as cyclic loading, and creep.

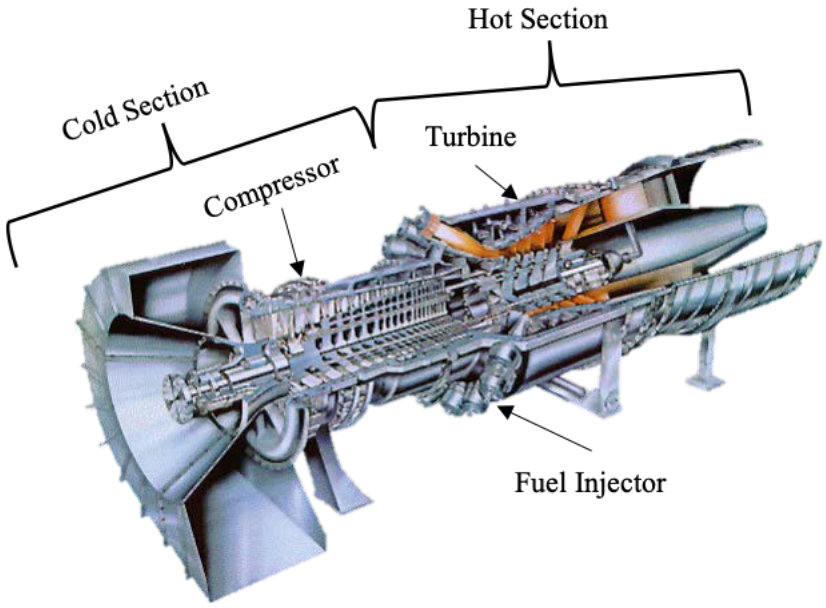

Figure 1.1: Illustration of a simple single spool gas turbine jet engine with the key stages. Note the Ni-based alloys are all in the fuel injector and turbine [1].

Thanks to their strength and excellent oxidisation resistance, superalloys based on nickel and iron are commonly used for various applications in the aerospace and nuclear fields. Among the nickel-iron superalloys, IN718 and CM248LC stand out for their superior mechanical properties and high corrosion resistance at temperatures up to 650 °C [2].

1.2 Additive manufacturing

The concept of directly manufacturing a component completely out of metal has been around for nearly 40 years [3]. AM is a technology that enables the manufacture of complex near-net-shape (NNS) components by the deposition of many consecutive 2D profiles, layer-

by-layer, by local melting using a heat source [4]. During the last decade, research into AM has attracted much attention, especially in the aerospace and petrochemical industries. This is due to AM technology's ability to produce complex designs quickly and with high levels of accuracy, as well as its ability to recycle materials. Many researchers and industrial organisations have been attracted to AM because of its advantages and benefits, and they understand the process's capabilities and limitations. The increased number of papers and patents on the use of AM/3D printing technology over the last 10 years demonstrates this. The number of published papers increased from under 500 per year in 2009 to over 8000 per year in 2019, as can be seen in Figure 1.2. Moreover, the number of patents filed grew from just above 2000 per year in 2009 to more than 10,000 per year in 2019.

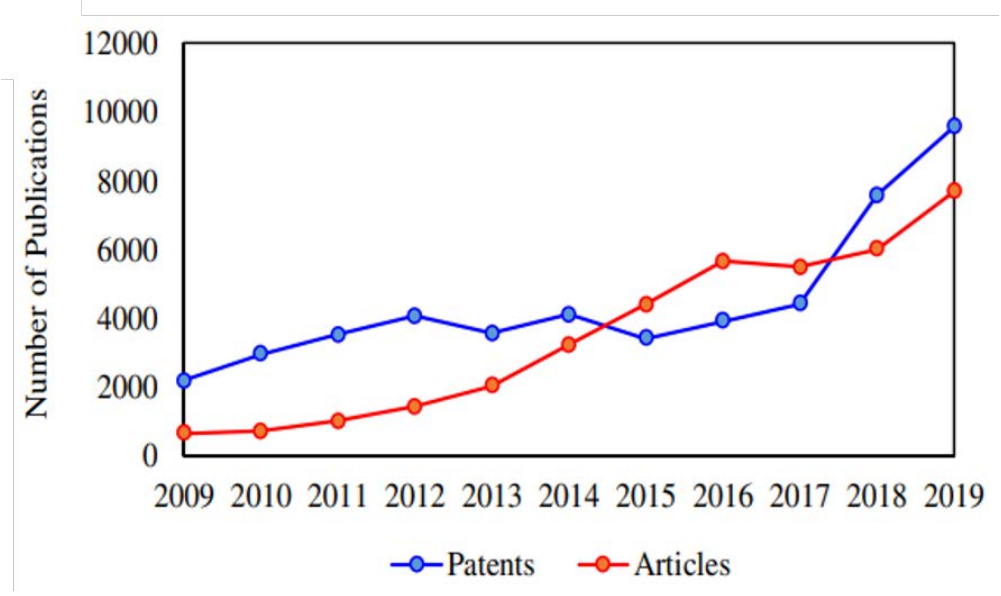

Figure 1.2: Number of published papers and patents on AM/3D printing technology [5]

According to the current Wohlers Report [6], in 2020, AM services and sales of equipment, software and materials accounted for 15.4 % of total AM industry revenues. As a result, the consumer in the electronics industry became the second most powerful consumer

industry by 14.7 %. The automotive industry consumer has the highest share of 16.4 percent. Figure 1.3 shows the revenues for AM products and services worldwide.

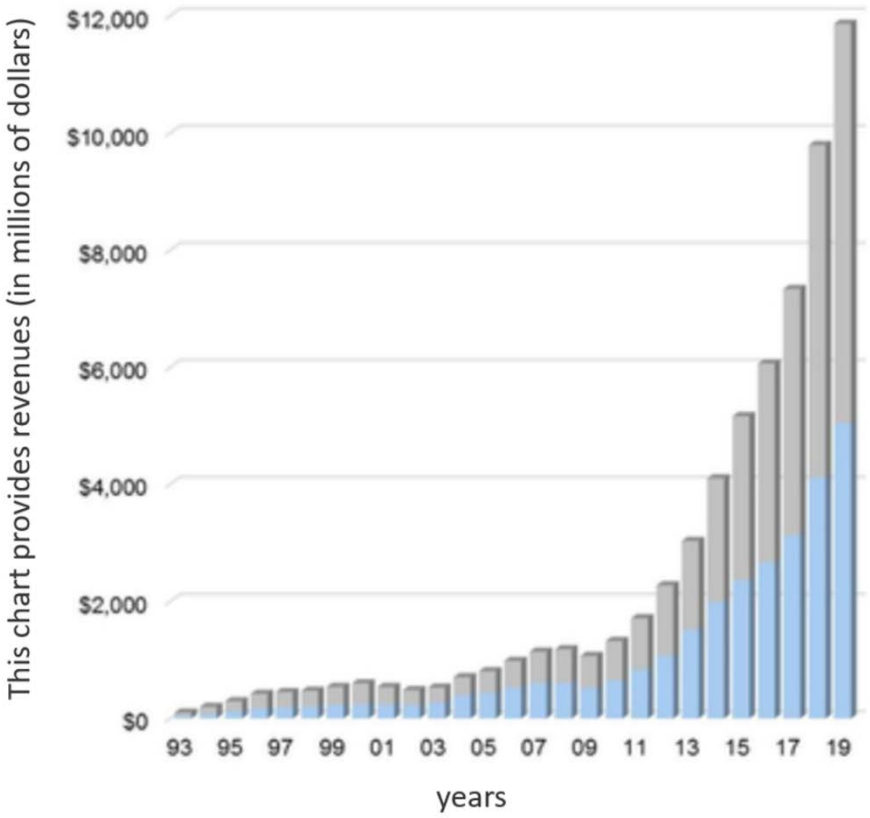

Figure 1.3: Revenues (in millions of dollars) for AM products and services worldwide. The lower (blue) segment of the bars represents products, while the upper (grey) segment represents services [6].

The ING, a multinational banking and financial services corporation [7], announced "3D Printing: a threat to global trade", and according to the report, U.S. imports will fall, reducing a trade deficit with countries like China, Mexico and Germany; local printed car parts will increase employment in U.S.-based automotive factories; and "50 percent of manufactured products will be printed in 2060", or even as early as 2040. According to the study by ING, 3D printing could account for more than half of all production within 40 years. The value of such products will be more than $6 trillion using current estimates, leading to headlines such as "3D

printing to wipe out 25 percent of world trade by 2060. These future scenarios for effect of 3D printing on world trade is illustrates in Figure 1.4.

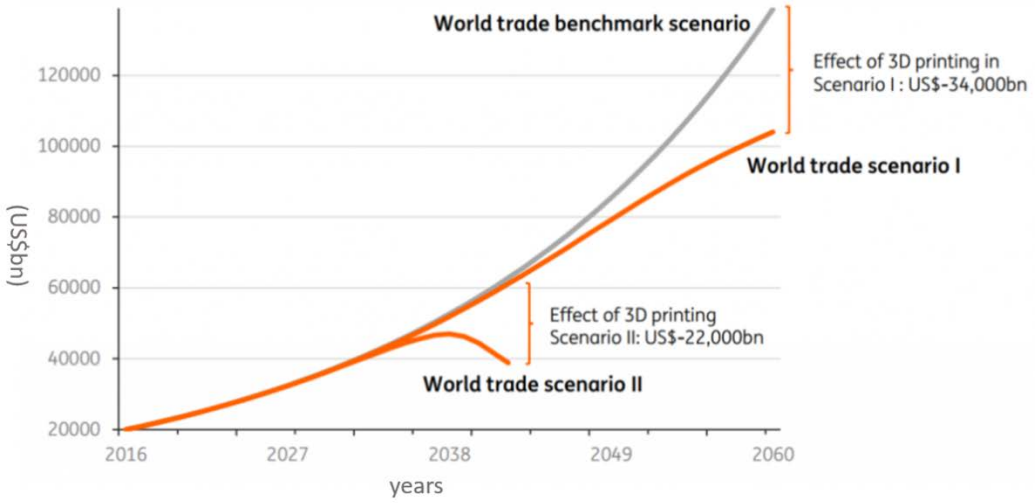

Figure 1.4: Scenarios for effect of 3D printing on world trade (goods and services) (US$bn). Graph via ING [8]

Figure 1.5 illustrates the number of individual items of material commercially available by type. The main AM materials are polymers and metals, with composites comprising a notable portion. Ceramics, sand and wax are specialised applications and systems, and are available from only a small number of suppliers [9].

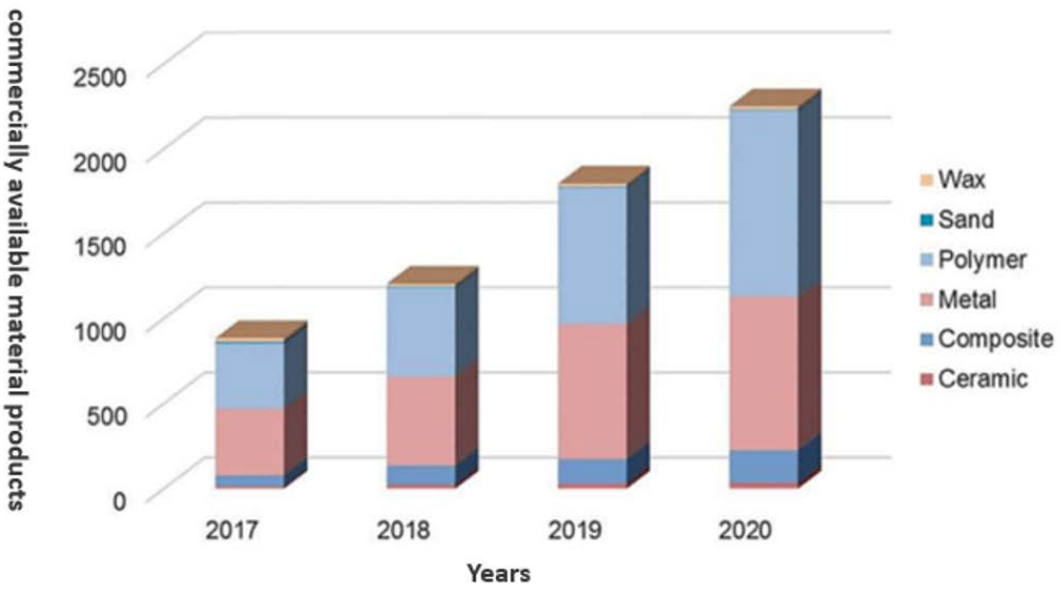

Figure 1.5: The number of commercially available material products by type [9] Source: 'Wohlers and Senvol database'

Figure 1.6 shows the AM metal products available over the last four years. Metal AM processes involve filaments, powders, sheets and wire stock [9].

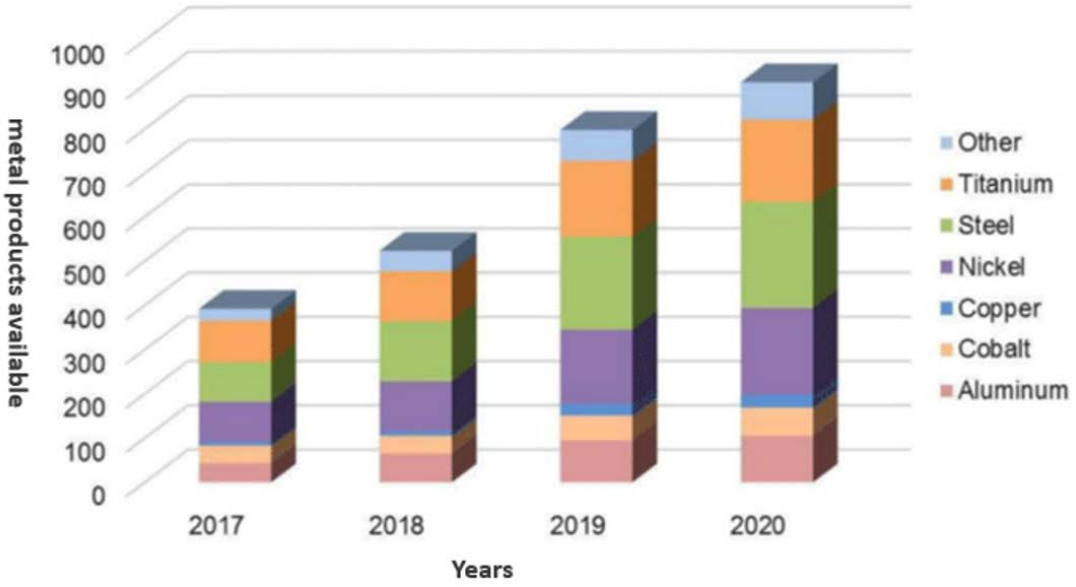

Figure 1.6: AM metal products available over the past four years [9] Source: Senvol Database

Nickel, steel, and titanium products have led the metals market by a large margin, while aluminium products are increasing. The 'Other' category includes iron, precious metals, and

refractory metals. Applications for these metals are growing, but a small number of suppliers are making the materials available.

1.2.1 Metal additive manufacturing

There are several AM techniques that can produce complex shapes, such as arc plus wire deposition, which can achieve high deposition rates, or blown powder, which is also called direct laser deposition (DLD). There are other AM techniques, including selective laser melting (SLM), which can produce complicated shapes with very fine details. AM has potential advantages for the manufacturing industry, such as reducing the machining and finishing needed for the final product to be manufactured, and thereby reducing the buy-to-fly ratio. Another benefit is the ability to manufacture complicated shapes in a short time without the need for the tools that would be required for casting or forging. Moreover, functionally graded material parts, or parts with different parameters and tailored microstructures, can be produced. Furthermore, AM uses approximately 90% less raw material than normal ingot cast-roll-forging and machining. DLD is also useful for repairing existing parts that would be impossible to repair using conventional methods. The DLD method has been used to repair turbine engine compressors and blisk air foils [10]. On the other hand, AM has limitations, such as the requirement for high capital investment for the machinery and highly skilled manpower to design and operate the machines. Moreover, deposition rates are relatively low, and it is difficult to detect defect formation during the process. In addition, there are no reliable standards for repeatability and reproducibility of the parts.

In metallic AM products, many parameters affect the build geometry and microstructure, including laser strength, scanning speed, powder feed rate, direction of deposition, spot size and layer overlap. Moreover, the raw materials, such as powder type, the feed stock deposition system and the geometric variables of the parts can complicate the development of appropriate

process control by introducing microstructural inhomogeneity within a single part. In addition, the substrate microstructure plays a role on the microstructure of the build [11-13]. Metallurgical phenomena, such as melting, solidification, solid-state phase transitions and solid-state deformation, are also directly related to AM characteristics, such as fluid flow, heat transfer and diffusion. Therefore, it is necessary to understand the relationship between process parameters and the creation of the microstructure properties in order to define the critical process parameters that influence the microstructure of the final component.

1.3.1 Direct energy deposition

Direct energy deposition (DED) a group of processes where the form of heat source is usually laser or electrons. DLD or direct laser fabrication (DLF), is a category of DED methods that concentrate thermal energy to melt and bind material in either powder or wire form. Also referred to as laser blown powder [14]. The heat source used in this technology is a laser, which melts the blown metal powder from the nozzle in a controlled manner. The three most commonly used lasers according to DLD literature are the diode laser (semiconductor or disc), CO_2 laser (molecular), and Nd:YAG laser (solid-state) [15]. The 3D parts are manufactured by depositing layers of 2D profiles stacked on top of each other. DLD is used for manufacturing net-shape components, repair, and overhaul.

1.3 Aims of project and research

The purpose of this work is to improve the understanding of the effect of DLD process parameters on Inconel superalloy deposition. The microstructure of DLD Ni-based superalloys is known to show a coarse columnar grain microstructure [16]. Furthermore, the orientation of the grains is influenced by the heat source's direction of motion [17]. In the as-built condition the components may also suffer from solute segregation, hot tearing and anisotropic mechanical properties [18]. Limited information on the microstructural and textural

development of each layer is available. In order to achieve the necessary microstructure (columnar or equiaxed), it is essential to obtain key process parameters. DLD tends to form segregation, which has a negative effect on mechanical properties.

Segregation can dissolve back into the matrix with exposure to heat [19], However, it would be useful to understand the effect of the process parameters on the grains' and precipitates' size, shape and morphology. Previous studies have shown that the microstructure can be affected by the cooling rate experienced during deposition [14]. In addition, it would be helpful to study the parameters to optimise the DLD process to reduce defects and produce fully dense material. In this study, single-walled parts will be built layer-by-layer using a variety of parameters, and the effect of each parameter on the microstructure will be studied.

The main objective of this research is:

- To investigate the DLD process parameters window (laser power, scanning speed and powder feed)
- To study the effect of different forms of laser power (continous, pulse, partial pulse and cooling cycles)
- To control the microstructural characteristics, i.e., how the microstructure, grain size and morphology, porosity and hardness, and the formation of the Laves phase are affected by the process parameters, and to produce fully dense components.

1.4 Thesis outline

This research project investigates and evaluates the DLD process in relation to nickel superalloys, and this is presented in the following: literature review (Chapter 2), experimental procedure (Chapter 3), influence of direct laser deposition parameters on geometrical and microstructural development (Chapter 4), controlling microstructural and mechanical properties of DLD Inconel 718 via laser power (Chapter 5), the influence of power mode on

the development of microstructural and mechanical properties (Chapter 6), direct laser deposition of crack-free CM247LC thin walls: mechanical properties and microstructural effects of heat treatment (Chapter 7) and conclusion and future work (Chapter 8).

In the literature review (Chapter 2), fundamental information about superalloys is presented, such as classification of superalloys, effects of alloy elements and phases, solidification theory and discontinuity. Additionally, basic information about different types of AM, specifically DLD, is explained and approaches to modifying the microstructure in AM are described.

The experimental procedure chapter (Chapter 3) describes the powder used, substrate preparation, and the building procedure and set-up. It also explains the laser power modes and types of pulses used, and the variation of frequency and cycle times. In addition, the polishing procedure and post-heat treatment and characterisation of samples used are also explained.

Chapter 4 focuses on the essential parameters, such as power, scanning speed, powder capture rate, powder feed, and nozzle z-increments. More specifically, it considers the effect of three power modes, continuous wave (CW), double power pulse wave (DPPW) and partial double power pulse wave (PDPPW), and three different scanning speeds (50, 250 and 500 mm/min) and the effect of scanning speed on capture rate. Moreover, the effect of powder feed and shielding gas pressure on build geometry and layer thickness are described.

In Chapter 5, the control of grain structure, texture, and micro-segregation of IN718 for a wide range of laser power using DLD is investigated along with the influence of laser power, thermal gradient and the cooling rate to the dendrite arm spacing (DAS), which influences the Nb segregation, on mechanical properties.

Chapter 6 investigates CW, pulse wave (PW) and partial power wave (PPW) power modes and the duration of the pulsing cycle. Moreover, the effects of the heat treatments

(solution annealed and aged) on microstructure morphology and Nb segregation reduction by modifying the pulse duration are investigated.

Chapter 7 studies the parameters for non-weldable CM247LC using CW and PW power modes to achieve a crack-free build during the deposition process and the post-thermal processing parameters required to achieve competitive mechanical properties.

Chapter 2. Literature Review

This chapter reviews the literature about the physical and chemical metallurgy of Ni-based superalloys. Specifically, this chapter considers IN718 and CM247LC, focusing on its grain size and morphology, its solidification behaviour, with emphasis on the γ' and γ″ strengthening phases, and the response to laser power and cooling rate. The role of laser power in AM is considered, particularly in DLD techniques, for the processing of Ni-based superalloys, and the tendency of different alloys to crack during processing is discussed.

2.1 Metallurgy of nickel superalloys

2.1.1 Overview

Inconel is a superalloy consisting of austenitic nickel chromium alloys. Inconel alloys are corrosion and oxidation resistant materials, and they are ideal for applications in harsh conditions, such as high heat and high pressure. On heating, a thick oxide layer forms, which prevents further attack on the surface. Inconel maintains its strength over a wide range of temperatures, so is suitable for applications at high temperatures at which aluminium and steel would yield to creep due to thermal induced vacancies in the crystal structure. Depending on the alloy, solid solution strengthening or precipitation hardening is used to produce Inconel's high temperature alloys [20].

The expression "superalloy" was first derived by an unknown source. In early research, they were referred to as "high temperature alloys". It was not until the late 40s, when the iconic fictitious character Superman became a TV hero and the word "super" became a popular adjective, that the term "super alloy" appeared. Therefore, it can be said that Superman has been instrumental in finding the extremely significant materials called superalloys [21].

Nickel-, nickel-iron- or cobalt-based heat-resistant alloys that combine mechanical strength with surface degradation resistance are referred to as superalloys. In practice, they are

primarily used for heat and/or corrosion resistance in gas turbines, coal conversion plants, chemical processes, and other advanced applications. The use of nickel-based alloys in load-bearing applications at temperatures higher than 80% of their first melting temperatures, a proportion greater than any other kind of engineering alloy, which is a distinguishing feature [22].

2.1.1.1 Classification of Superalloys:

Nickel-, iron- and cobalt-based superalloys are categorised by the predominant metal found in the alloy. Iron-based superalloys have a closed-packed FCC matrix with precipitate-forming and solid solution hardening elements [23]. These superalloys are the least expensive of the three types. Iron-based superalloys can be classified as austenitic and martensitic types. Austenitic alloys are more difficult to forge or machine than martensitic grades, because of their crack sensitivity. Most martensitic steels are difficult to weld using traditional methods [21].

The most complex and commonly used superalloys for high temperature applications are nickel-based superalloys [22]. They now account for more than half of the weight of advanced aircraft engines, especially in the hot section of the jet engine [24]. Spaceships, submarines, nuclear reactors, military electric motors, chemical processing vessels and heat exchanger tubing are examples of their applications [25].

Cobalt-based superalloys are less strong than nickel-based superalloys, but they can withstand higher temperatures. As they are not as hard as nickel-based superalloys, cobalt-based superalloys are less susceptible to thermal shock cracking than other superalloys. Cobalt-based superalloys are, therefore, better suited to components that must be worked or welded, such as those found in the combustion chamber's complex structures [25].

2.1.1.1.1 Oil and gas industry

These superalloys include chromium and molybdenum, which contribute to corrosion resistance. Alloy IN718 was originally developed for use in the aerospace industry and in gas turbines, but it has since become the preferred material for wellhead parts, auxiliary and down-hole equipment, and safety valves. Nickel-based superalloys are also used in other applications in the oil and gas industry. Oil and natural gas processing take place in corrosive and difficult conditions, with large amounts of chloride, carbon dioxide, hydrogen sulphide and free sulphur, at high pressure and intermediate temperatures of up to 232 °C. Therefore, the production of oil and natural gas under such conditions necessitates the use of advanced materials, such as nickel-based alloys IN718 and CM247LC [26].

IN718 alloy is a chemical compound with the formula 55Ni-21Cr-5Nb-3Mo wt%. Niobium is added to prevent cracking during welding. This alloy is used in turbine engines for aircraft, stationary gas turbines and in cryogenic tanks. Owing to its high strength, forgeability and weldability characteristics at 650 °C at a relatively low cost for its properties, Inconel 718 has been very useful in the aero-engine sector [24].

Increases in the combustion temperature of the product gases entering the turbine region of gas turbines, the turbine entry temperature (TET), have necessitated the production of Ni-based superalloys capable of withstanding higher temperatures and with improved thermodynamic performance [27]. As a result, newer alloys, such as CM247LC, have been produced to achieve excellent thermodynamic performance. CM247LC has outstanding high-temperature efficiency, but the presence of a high γ′-fraction in the microstructure limits weldability and makes the alloys more vulnerable to cracking during post-weld heat treatment, also known as strain-age cracking (SAC) [26]. Ductility dip cracking (DDC), which is defined as a decrease in ductility at intermediate temperatures (0.4%–0.7% of the melting point) and is typically associated with the formation of grain-boundary carbides in Ni superalloys, also

occurs in the superalloys. Other cracking processes, such as liquidation and solidification cracking, which may occur during alloy welding regardless of chemistry, may not be included in this correlation between alloy chemistry and weld susceptibility [28].

2.1.2 Effect of phase constituents in IN718 and CM247LC

Based on the strengthening phases, the superalloys can be divided into two groups:

- Gamma matrix (y)
- γ′ strengthened: hardened by the precipitation of the coherent phase (Ni_3Al) in a fine cuboidal form, usually produced by heat treatment; for example, CM247LC [29]
- γ″ strengthened: the body-centred tetragonal (BCT) phase γ″ (Ni_3Nb), which is precipitated as coherent disc shaped particles, is very hard; for example, Nb-containing alloys such as IN718 [29].
- The intermetallic precipitate, orthorhombic Ni Nb usually termed S or delta.
- Various carbides; most commonly cubic MC and M23C6.
- Various topological close packed (TCP) phases

2.1.2.1 The gamma phase (γ)

The γ FCC phase almost always contains high concentrations of cobalt, chromium, molybdenum, ruthenium, and rhenium, as these elements appear to remain in γ phase. These elements have 1 to 13% larger atomic diameters than nickel and the hardening effect is largely related to the atomic oversize. The FCC γ phase has the lowest diffusivity relative to its melting point and the highest normalised activation energy (Q/RT) for diffusion between the various crystal classes of transition metals. Owing to these two properties, the FCC γ phase exhibits greater creep than other crystal structures, such as HCP and BCC [30].

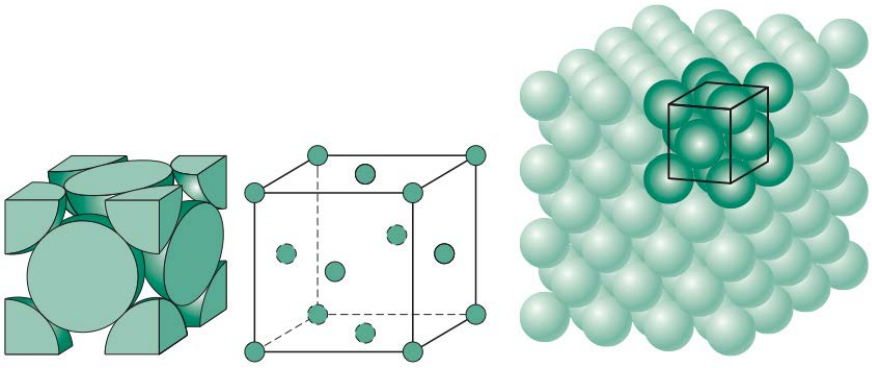

Figure 2.1: The unit cell of the face-centred cubic (FCC) crystal structure, which is displayed by nickel [31]

2.1.2.2 The gamma prime phase (γ')

In addition to the FCC phase, the Ni–Al system has a variety of other solid phases. Ni–Al bonding is favoured over Ni–Ni and Al–Al bonding. These phases, with chemical formulae Ni_3Al, NiAl, Ni_2Al_3, $NiAl_3$ and Ni_2Al_9, show a high degree of chemical ordering. The γ' phase (Ni_3Al) has a primitive cubic, L12, crystal structure, as shown in Figure 2.2, with Al atoms at the cube corners and Ni atoms at the γ' face centres. The formation of the phase is influenced by the numerous alloying additions. The ternary phase diagram for Ni-Al-X shows the effect of the alloying addition on the γ' phase, where X can be any element like Co, Cr, Ta and Ti, to facilitate this phase, and atoms like Ti and Ta replace Al. The γ' precipitates in a cube-cube orientation with the γ phase, and its cell edges are precisely parallel to the corresponding γ phase edges. Since the γ' is an atomically ordered structure, dislocations have a difficulty penetrating into it, such that the alloy is reinforced. The dislocation movement is based on the size of the precipitates, with ½<110> dislocation pairs cutting through small precipitates and Orowan looping bypassing large precipitates. γ′ has several favourable characteristics including the potential for high volume fractions (up to around 50 vol% depending on alloy composition), high solvus temperature, good ductility and a high yield stress which is maintained up to around 900°C. The result is that y'-strengthened alloys can exhibit yield strengths of around 1000 MPa sustainable up to around 900°C [23, 32].

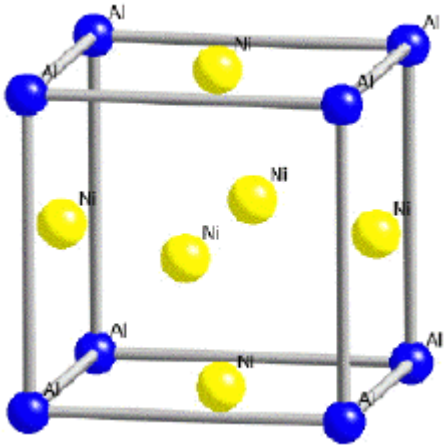

Figure 2.2: Crystal structure of the γ' Ni_3(Ti, Al) with Ni atoms at the face centres and Al atoms at the corners; Ti can take the place of Al in this phase [33]

2.1.2.3 The gamma double prime phase (γ'')

Superalloys that contain niobium, such as Inconel 718 and 706, have the crystal structure of the coherent BCT ordered compound Ni_3Nb with $D0_{22}$ formed as the primary strengthening step in Ni-Fe-based superalloys shown in Figure 2.4 (a). Figure 2.3 portrays the binary phase diagram of Ni and Nb. The γ″ phase (Ni_3Nb) is formed by a simple eutectic reaction involving γ and Ni_3Nb at a concentration of 22.5 wt% Nb. For Nb, the process has a maximum solubility of 18.2 wt%, which increases by 50% when Cr and Fe are added [34]. The γ″ has a disc-shaped morphology, with a diameter of about 50 nm and a thickness of about 10 nm shown in Figure 2.4 (b) [35]. Along the tetragonal c axis has three variants exist with their c-axis along different (100) directions shown on Figure 2.4 (c), it has a large lattice misfit, or mismatch between the γ′ and γ″ lattice parameters. Only a small amount of γ″ precipitate is needed to achieve the required strength due to the large coherency strain associated with its formation. The a/2<110> dislocation shears the γ″ plates, and the energy of the antiphase boundary created as a result is sufficient to couple the dislocations into pairs, if not quadruples [36].

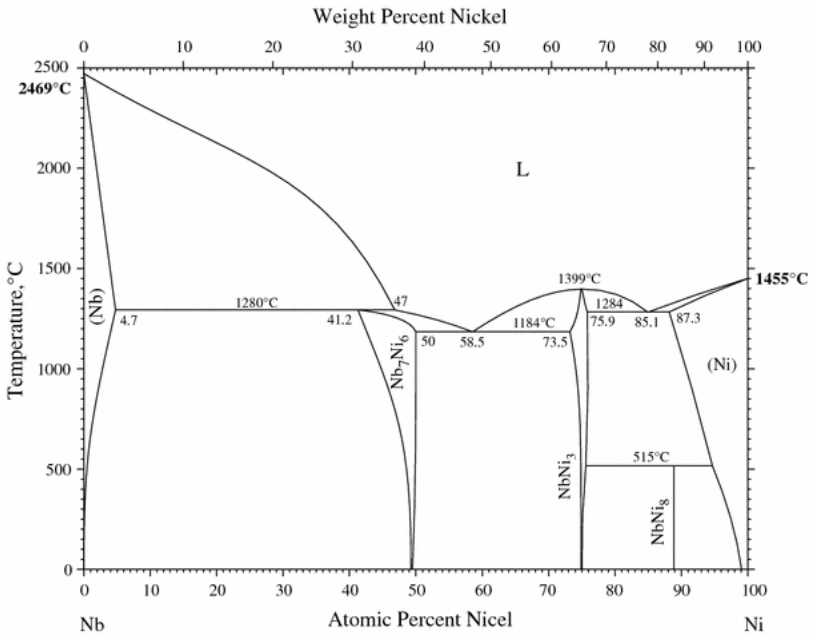

Figure 2.3: Crystal structure of the γ" (Ni_3Nb) phase with black circles denoting Nb atoms and blue circles denoting Ni atoms [37]

Furthermore, the precipitation kinetics of γ″ are slow due to its resistance to SAC during post-weld heat treatment, rendering the alloy weldable [38]. As γ″ is strengthened in the over-aged state, Ni-Fe-based superalloys are prone to the formation of an orthorhombic structure. Since this phase is incoherent with γ, it does not impart strength even when present in large amounts. Many Nb-bearing alloys (such as IN718) are susceptible to Laves phase formation rather than γ″. It is also, beneficial with respect to hardening of large components and to weldability [41].

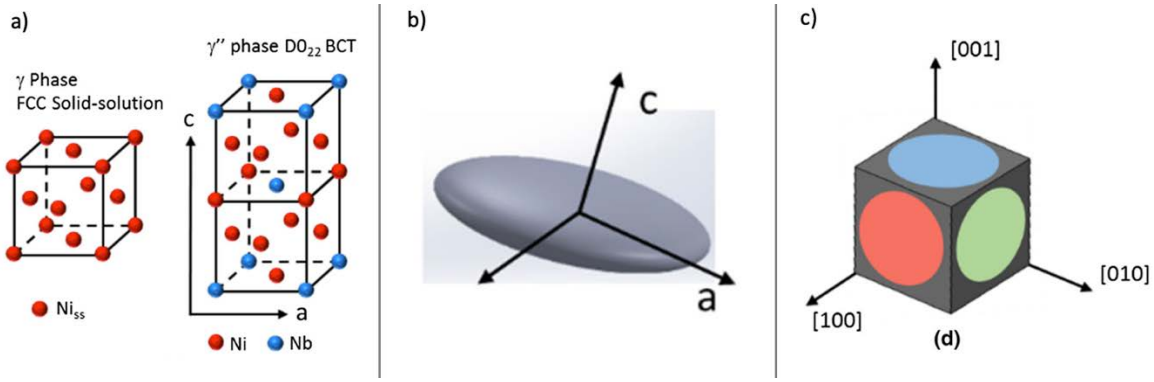

Figure 2.4: (a) The lattice structures of γ and γ" phases; (b) the γ" displays a disc-shaped particle with its c-axis normal to the disc plane; (c) three variants (illustrated in three different colours) exist with their c-axis along different (100) directions [39]

2.1.2.4 Delta phase (δ)

The δ phase is another Ni_3Nb phase with an orthorhombic crystal structure that is incoherent with the matrix, and it contains 6–8 wt% Nb. It precipitates at temperatures ranging from 700 to 1000 °C, with peak precipitation occurring at 900 °C. The nucleation may begin at the stacking faults of the γ″ phase, resulting in intergranular precipitation. The δ phase is more stable than the γ″ phase, but it takes longer to form because γ″ tends to form below 900 °C. Both phases are formed with Nb, but the δ phase is formed by the loss of the γ″ phase up to 900 °C, and the δ phase formation peaks after the γ″ precipitation stops [40]. The presence of the δ-phase is detrimental to the material properties due to its morphology where the creep properties of the material decrease with an increase in the amount of this phase. The δ-phase also improves the creep properties of the material provided that an appropriate morphology at the boundaries is achieved [41].

2.1.2.5 Topologically close-packed (TCP) phases

Excessive amounts of Cr, Mo, W and Re facilitate the formation of intermetallic phases with a complex crystal structure made up of distinct tessellated layers composed of arrays of hexagons, pentagons, and triangles, hence the name topologically close-packed (TCP) phases. Mechanical properties are typically harmed by these phases. They can take the form of thin linear plates that nucleate on a grain boundary or any of the phases that belong to this group (carbides, σ, μ and Laves) [42, 43].

The formation of σ and μ phases is more common in Ni-based superalloys, whereas Laves phases are more common in Ni-Fe-based superalloys. These phases will result in a reduction in rupture strength and ductility [44]. The formula for the σ phase is $(Fe, Mo)_x(Ni, Co)_y$, where x and y can be any number between 1 and 7. The refractory metals in the matrix are depleted during phase formation, resulting in a loss of matrix strength. The negative

consequences of the plate-like phases are poorly understood. $(Fe, Co)_7(Mo, W)_6$ is the general formula for the μ phase. The hexagonal crystal structure of the Laves phase has an AB_2-type composition. Fe_2Ti, Fe_2Nb, and Fe_2Mo are common examples, and $(Fe, Cr, Mn, Si)_2(Mo, Ti, Nb)$ is the general formula. Excessive quantities of this phase can reduce tensile ductility and creep properties at room temperature. Laves phases appear as thin plates, often nucleating on grain boundary carbides and generally have a detrimental effect on properties. For instance Laves phase are crack initiation sites and LCF life is impaired when Laves phases is present [43].

2.1.2.6 Carbides

Ni-based superalloys with appreciable carbon levels can form a variety of carbides depending on the alloy composition, processing path, and service history. MC, M_6C, $M_{23}C_6$, and M_7C_3 are some of the more common forms, where M stands for Cr, Mo, Ti, Ta or Hf. Since MC-type carbides, which are typically rich in Ti, Ta and Hf, form from the liquid phase at temperatures above 1038 °C, they are frequently found at interdendritic regions with no perceptible orientation relationship to the matrix. $M_{23}C_6$ forms due to the breakdown of the MC carbides between 750–810 °C during extended service exposure in the following sequence [44]:

$$MC + \gamma \rightarrow M_{23}C_6 + \gamma' \qquad \textit{Equation 2.1}$$

These carbides are most commonly found in Cr-rich alloys and form at grain boundaries. Carbides with favourable morphology at grain boundaries have been proved useful for grain size control and optimising of creep rupture life in a large number of superalloys [44].

2.1.3 Solidification theory

Solidification behaviour controls the size and morphology of the grains, the destruction of inclusions and segregation, the hot cracks and porosity for both AM and casting processes. It is important to comprehend the progression of the microstructure's solidification by looking at the nucleation and solid growth phases. Variations in solidification parameters such as

temperature gradient, growth rate, superheat and undercooling have occurred as a result of parameters improvements [45].

The solidification map in Figure 2.5 may be used to describe the microstructure's size and morphology variations. Temperature gradient and solidification rate are the two most critical variables in defining the solidification diagram. The temperature gradient, G, is the tangent of the melt pool's temperature profile with respect to distance. The solid/liquid (S/L) interface travel velocity, R, is the growth rate. While the product, GR, which is also known as the cooling rate, controls the size of the solidification structure, the ratio, G/R, is crucial in determining the solidification morphology preference [46].

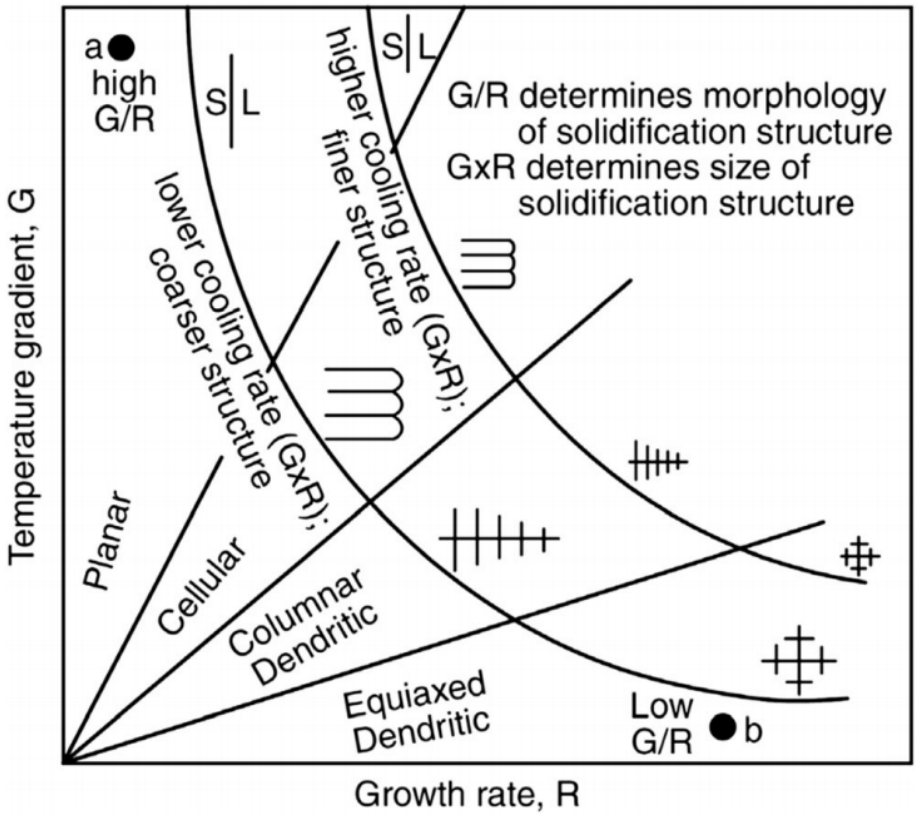

Figure 2.5: Solidification map showing the effect of temperature gradient, G, and growth rate, R, on the morphology and size of solidification microstructure[46]

2.1.3.1 Nucleation

There are two types of nucleation phenomena: heterogeneous nucleation, which occurs when solidification begins with a solid impurity within a liquid and only requires a 1 K undercooling; and homogeneous nucleation, which occurs when no nucleation site is present and requires a broad undercooling. With an undercooling of 1–2 K, nucleation in welding melt pools, which are similar to those in AM, is commonly observed [47, 48].

2.1.3.2 Growth

The solid phase grows by diffusion, or the addition of atoms from liquid to solid at the S/L interface. The melt pool's heat flow and related thermal gradients during solidification forms the relationship between the growth rate (R) and the thermal gradient (G) and defines the final microstructure of the primary phase. Solidification occurs in a planar, cellular, or dendritic manner based on the steady state microscopic shape of the S/L interface at the growth front. The different growth morphologies are dependent on the thermal gradient and rate of growth. Non-planar solidification structures in alloys come in a variety of shapes and sizes. Dendritic growth follows specific crystal directions, which are usually in the opposite direction to the heat flow. The maximum thermal gradient and the growth direction control the alignment of the dendrites [48-50].

2.1.3.3 Dendrites

AM typically results in a layered microstructure with a bead-like morphology. In general, directional solidification applies where the structure is mainly columnar dendrite. These dendrites have some characteristics, such as the dendrite tip radius, and primary and secondary dendrite spacing. The primary dendritic arm spacing (DAS, λ_1) indicates the maximum length of the separation between dendrites, and this can explain the thermal history through solution

time. In general, solution time is proportional to the square of the primary DAS. In other words if the primary dendrite spacing was decreased to half, the solution time would have been reduced to a quarter [47].

The secondary dendrite arm spacing (SDAS, λ_2) is a microstructural feature in materials with dendritic structures that is analogous to grain size in wrought structures. Increased strength and hardness, reduced interdendritic shrinkage porosity, and influences on electrical and thermal conductivity have all been found to be benefits of decreasing SDAS [51, 52]. Gaumann et al. [53] claimed that interdendritic spacing was found to be 30 times smaller in DLD than a typical as-cast microstructure, which could be due to the rapid cooling rate involved in DLD.

Columnar dendrites epitaxially grow towards the maximum temperature gradient nearly perpendicular to the solidification interface. Fine equiaxed dendritic arrangements with diameters of 3 to 5 μm dominate the "cell" structure. These equiaxed dendrites are aligned roughly perpendicular to the interface [54]. Chen et al. [55] found that the dendritic microstructure crystal orientation was increased by increasing the base cooling effect during the deposition. Moreover, highly ordered columnar dendrites were established, and a mono-crystalline texture was constructed. It is also well known that the cooling rate has a direct relationship with DAS, which can be mathematically defined by Equation 2.2 [56], where λ is the primary DAS in microns and ε is the cooling rate in kelvins per second.

$$\lambda = 80\varepsilon^{-0.33} \qquad \textit{Equation 2.2}$$

2.1.3.4 Segregation

Laser additive manufacturing (LAM) typically contributes to a refined microstructure and improved solute trapping through rapid solidification and cooling. Rapid Nb diffusion during solidification causes extreme Nb segregation at the S/L interface, resulting in a brittle

intermetallic and long-chained Laves phase in Inconel 718. Laves phase formation is extremely undesirable because it depletes the matrix of valuable alloy elements and helps to trigger and spread cracks quickly, especially by degrading mechanical properties, such as tensile ductility, ultimate tensile strength, fatigue-life, and fracture toughness. It is therefore crucial to evaluate Nb segregation and the formation of the Laves phase [57-59]. Xiao et al. [54] compared continuous wave (CW) and pulsed wave (PW) laser power modes and showed that the dendritic microstructure was refined and equiaxed, Nb segregation was reduced, and a fine and uncontrolled Laves phase occurred due to an enhanced cooling rate with one magnitude and a decreased solidifying duration of the molten pool. Furthermore, due to the decreased segregation of Nb, the PW sample responded well to ageing treatments, with increased hardness and more desirable tensile properties. Furthermore, because of the long chain-like Laves phase, the segregation of Nb and Mo in the CW sample was larger than that in the PW sample. In the CW study, the Nb concentration of the dendrite core regions was 2.38 wt%, which was 1.03 wt% lower than that of the PW sample (3.41 wt%). Furthermore, the distribution of the Mo concentration showed a similar pattern to the distribution of Nb.

2.1.4 Grain morphology

Processing parameters, such as laser power and scanning speed, have a big impact on the grain size and morphology, different grain morphology such as columnar grain or equiaxed grains Microstructures shown in Figure 2.6. The microstructural homogeneity and the degree of grain coarsening. that are heterogeneous in appearance are usually found in DLD products, with differences in the aspect ratio of the grain occurring over relatively small distances. Moat [16] and Wu et al. [60] showed laser AM forms large grain columnar structures which is adverse to mechanical characteristics. However, by selecting the appropriate process parameters, this grain structure shape may be modified.

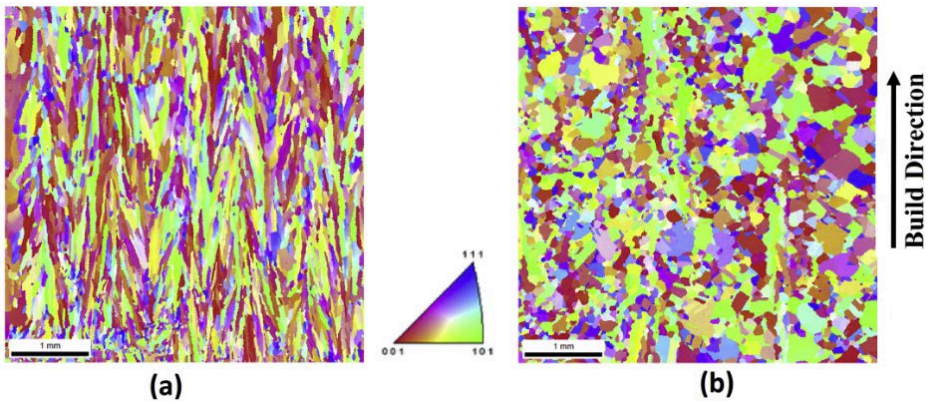

Figure 2.6: Inverse pole figure of samples with different grain morphology: (a) columnar grain, (b) equiaxed grains [61]

2.1.5 Grain size

The metallurgical final grain size is mainly determined by the overall cooling rate during the construction process (peak temperature). At lower temperatures, grain growth is decreased and a refined depositary microstructure is generated, leading to improved mechanical characteristics [62, 63]. Figure 2.7 shows a EBSD sample with small equiaxed grain in the sides and big columnar grain in middle.

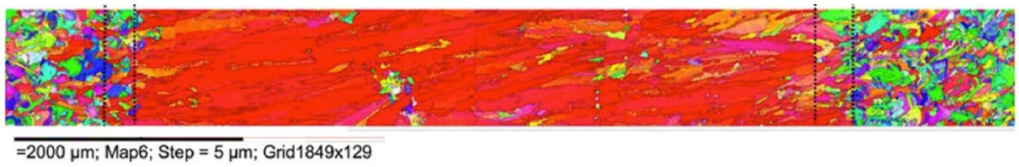

Figure 2.7: EBSD of sample shows small equiaxed grain vs. big columnar grain [64]

2.1.6 Columnar to equiaxed transition

The columnar to equiaxed transition (CET) occurs when equiaxed grain growth in the constitutionally undercooled liquid ahead of the columnar grains blocks the columnar growth front. The nucleation of randomly oriented crystals that expand in all directions to form a polycrystalline solid characterises an equiaxed grain structure. Equiaxed grains are desirable in processes such as casting and welding. The uniformity of material properties is improved with an equiaxed structure. The resulting grain morphology is columnar when the heat flux is

unidirectional. Changing AM process parameters may affect the melt pool's solidification rate and temperature gradients. Either an equiaxed or a columnar microstructure can be accomplished depending on the combination of solidification rate and temperature gradient [56].

In order to predict the microstructure of the final component, it is crucial to understand the factors that influence the transformation from columnar to equiaxed. Nastac et al. [65, 66] developed a solidification map of the columnar and equiaxed zones (see Figure 2.8), which shows that CET depends on the values of G and R, where R is the solidification rate or V as velocity of solidification (for superalloys, R $\approx 3 \times 10^{-4} \frac{\mathrm{m}}{\mathrm{s}}$) and G is the temperature gradient (for superalloys G $\approx 1.5 \times 10^{2}$C m)[50].

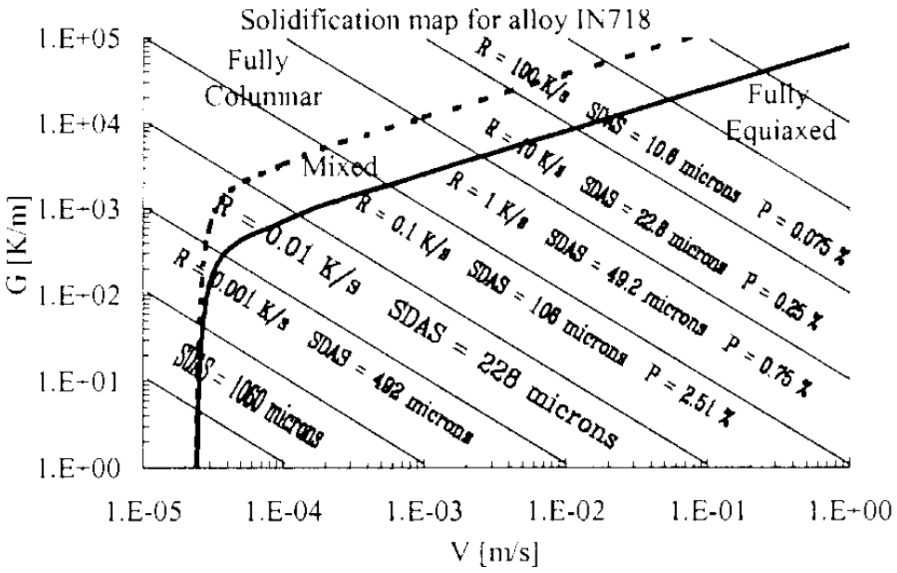

Figure 2.8: Solidification map for IN718 [66]

2.1.7 Thermal gradient and solidification rate

The thermal gradient at the S/L interface plays a significant role in determining the solidification substructure in the weld pool. The thermal gradient in the solid, G_L, determines the solidification and morphology of the microstructure of the build. G_L increases as the

thermal conductivity of the material decreases. Furthermore, GL increases in high energy density processes, such as EBW [49].

2.1.8 Post-heat treatments

Yu at el. [67] compared IN718 ingots in the as-received state, and with a solution heat treatment and a standard ageing treatment applied at 650 °C. The standard aged specimen had the highest yield strength of 998 MPa and tensile strength of 1100 MPa, whereas the solution treatment yield strength was around 400 MPa and tensile strength was 700 MPa. Xiaobin Yu at el. [68] examined the influence of post-heat treatment on IN718 fabricated by laser solid formation, which is another name for DLD, by studying aged samples, solution treated samples and as-fabricated samples. The as-fabricated samples mainly consisted of γ columnar dendrites and a small quantity of γ-Laves phases in the interdendritic area. γ'/γ" found around Laves phases after direct ageing. Moreover, δ-phase precipitates existed around and within the Laves phase. The segregation reduced and the distribution of γ'/γ" in the dendrite arm was almost homogeneous.

The mechanical properties of Inconel 718 are known to be harmed by Nb segregation and the formation of the Laves phase. Effective methods to prevent Nb segregation and the creation of the Laves phase are still lacking. An order-of-magnitude increase in the cooling rate and an order-of-magnitude drop in the molten pool solidification time due to the reduced Nb segregation in the PW sample demonstrates the strong effect of the ageing treatment, with higher hardness and more desirable tensile properties. LAM usually results in a finer microstructure and better solute trapping due to rapid cooling and solidification. During solidification, even with fast Nb diffusion at the S/L interface, severe Nb segregation occurs, forming brittle intermetallic and long-chained Laves phases. The formation of the Laves phase

is undesirable because it depletes the matrix of useful alloying elements and promotes the initiation and propagation of cracks [54, 69].

The solidification dendritic structure has a strong influence on the Laves phase. The formation of discrete Laves phase particles is supported by small equiaxed DAS, a high cooling rate, and a low temperature gradient to growth rate ratio. Therefore, either water or liquid nitrogen may be used to cool the substrate [59, 70]. As it is difficult to prevent columnar dendrites with CW, rapid cooling may not fully eliminate the long chain-like Laves phase over the entire volume, even by adjusting operating parameters or by accelerating the cooling of the substrate. The PW laser power mode was used to achieve a smaller heat affected zone, lower dilution rate and a more refined grain structure. A low average heat input and a high cooling rate from PW enabled the elimination of Nb segregation and Laves phase formation [19, 69, 71-74]. Xiao et al. [54] used the two types of power modes, CW and PW, to fabricate Inconel 718 samples using an AM process and then investigated the effects of ageing treatments. Their results show that direct ageing plays a major role in increasing hardness in the samples. Regarding the as-built samples, those produced with CW showed very low hardness, whereas the PW samples showed a slight increase in hardness. In contrast, the aged samples showed a significant increase in hardness; furthermore, the PW samples showed increased hardness compared with the CW samples.

2.1.9 The role of the specific elements within a nickel superalloy

This section considers the effect of each particular element within the alloy, as well as how each element impacts phase formation and mechanical properties. The composition of the nickel superalloy is explored in terms of the main phases' formation and functions within the alloy. Nickel superalloys normally contain about ten constituent components, each of which is used to serve a specific purpose or strengthen a specific property. Some alloying elements can

have a single essential feature, while others have a range of properties and microstructural effects. Figure 2.9 shows the description provided by Donachie [44] of each common element's role: elements with minor beneficial effects are denoted by hatching, while elements with negative effects are denoted by horizontally shading.

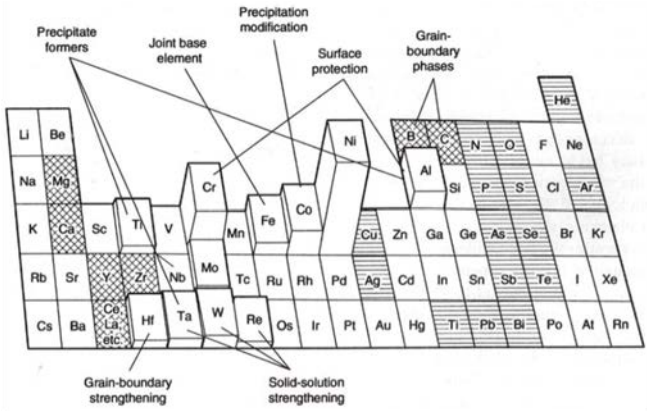

Figure 2.9: An overview of the role of each key element within a typical nickel superalloy [44]

2.1.9.1 The role of chromium (Cr)

Chromium is found in most nickel superalloys, and its primary effect is determined by the composition. The addition of Cr to a precipitate hardenable nickel-based superalloy is primarily to provide hot-corrosion resistance and improve oxidation. Diffusion of Cr from the interdendritic region allows the formation of a protective oxide layer (Cr_2O_3) on the alloy's surface, which prevents the reaction between nickel and sulphurous gases. Superalloys with Cr content between 6 and 22 wt% are considered to be low-Cr content alloys; IN718 contains 18.18 wt% and CM247LC contains 8.29 wt%. Cr also serves as a solid solution strengthener, although this is considered to be a secondary effect. Cr may also be used to shape MC carbides [44, 75, 76].

2.1.9.2 The role of aluminium (Al)

The primary reason for adding Al is to form γ', but it also helps with limiting oxidation and/or corrosion. According to the study of Gordon et al. [77], both Al and Cr oxides form on the

exposed surfaces. Diffusion of Al from the γ' precipitates near the surface under the Cr_2O_3 outer oxide layer allows the formation of Ni_3Al particles. The diffusion of Al from γ' forms a thin γ'-depleted zone between the matrix and the inner oxide layer, Al_2O_3. Cr diffuses through the Al_2O_3 layer, forming an external layer of Cr_2O_3, and TiO_2 can form depending on the alloy composition. Antolovich et al. [78] suggested that oxides act as crack initiator points in Ni-based superalloys. Another study by Boismier and Sehitoglu reported in two different papers [79, 80] stated that during fatigue, the oxide and γ'-depleted layer form a region of weaker material ahead of the advancing crack tip. Furthermore, due to the differing thermal expansion coefficients of the layers under thermal cycling, additional material damage may occur. According to Coffin's research [81], crack blunting caused by the formation of oxides at the crack's tip can reduce localised stresses and even improve fatigue performance under low-frequency fatigue.

2.1.9.3 The role of molybdenum (Mo)

Molybdenum is typically included in nickel-based superalloys in small amounts to provide wet corrosion resistance, and it also acts as a solid solution strengthener and increases γ' volume fraction by raising the solvus temperature. Additionally, Mo increases density, promotes TCP phases (μ, σ) and reduces γ' precipitates [44].

2.1.9.4 The role of titanium (Ti)

Titanium can be used to replace aluminium in phase strengthening depending on the atomic misfit parameter. It is used in nickel-based superalloys in small amounts to provide hot corrosion resistance and remove nitrogen through the formation of TiN [44, 82].

2.1.9.5 The role of tantalum (Ta)

Tantalum has two impacts on nickel superalloys. The first is the carbide composition change. The analysis of Janowski et al. [83] indicated that Ta can be substituted for Hf within carbides,

and that Ta-containing carbides are less stable than Hf-containing carbides, rendering Hf-rich carbides more thermodynamically stable than Ta-rich carbides. Furthermore, Ta has a strong affinity for the γ' phase and promotes its precipitation. It has been recorded that a 1 wt% increase in Ta induces a 2 wt% increase in the γ' phase and a corresponding decrease in the γ phase. According to research by Nathal and Ebert [84, 85], reducing Ta from MAR-M247 to 0 wt% results in a 6% decrease in volume fraction. The second experiment looked at the effects of Ta, Co, and W on superalloy at high temperature. The removal of Ta reduced creep in MAR-M247. Other research by Chakravorty and West [86] found that Ni-Al-Ta-Hf enhances high temperature tensile/creep properties, but the study only looked at mechanical properties and did not consider microstructural effects.

2.1.9.6 The role of tungsten (W)

Tungsten is mainly used as a strengthener [44]. Tungsten segregates the γ' phase, according to Rawling and Staton-Bevan [82], because it can substitute for both Ni and Al in the FCC structure. Furthermore, the enhancement happens as a result of the replacement of W for Al. Analysis by Nathal and Ebert [85] indicated that W-containing alloys have a greater lattice misfit. Furthermore, removing W from the alloy lowers the γ' solvus temperature, which will affect the superalloy's mechanical properties at high temperatures. Another paper by Nathal and Ebert [85] stated that W improves creep resistance resulting in improvements in mechanical properties related to the increased lattice misfit parameter.

2.1.9.7 The role of hafnium (Hf)

Hafnium's role in nickel superalloys is as a refiner of the grain boundary [44]. Heck et al. [87] claimed that no cracking appears in CM247LC with 1.4 wt% Hf compared with the high levels of cracking in IN792 with just 0.5 wt% Hf during casting. When Hf content was increased in IN792 it showed a reduction in cracking susceptibility. Furthermore, the addition of Hf

improves the tensile properties of the alloy, which improves its ability to resist cracking. Other research by Duhl and Sullivan [88] investigated the rupture life and the elongation of MAR-M247LC with 2 wt% Hf and without Hf at four different high temperatures; the results showed that for the alloy with Hf the mechanical properties increased in both tests and at all four temperatures. Dohery and Giamei [89] demonstrated the development of a blocky γ" phase at grain boundaries as a result of Hf segregation during solidification and its affinity for the γ' phase. They also mentioned that the grain boundaries were aligned. The carbides appeared irregular and fine, with a lower probability of creating a thin script-like film. Cr has a clear affinity for the γ phase, which aligns with the grain boundary and decreases the amount of Cr available in the γ' phase in the carbides $M_{23}C_6$. The solid strengthening of Hf inside the blocky γ" phase explains the strengthened mechanical properties due to Hf addition. According to Doherty et al. [90], Hf attachment may be used to create stable sulphides and thereby reduce the effects of sulphur embrittlement. Hf also has harmful effects on nickel-based superalloys; in casting Hf can react with the cast shell and produce inclusions.

2.1.9.8 The role of niobium (Nb)

Niobium is a good strengthener that can be used for both solid solution stabilisation and strengthening by facilitating the precipitation of the γ"-Ni_3Nb form. Roger and Shira [91] stated that the use of Nb instead of Al/Ti as an age hardener in Inconel 718 eliminated SAC but resulted in the formation of the brittle Laves phase in the fusion zone.

2.1.10 Time-temperature-transformation diagram (TTT)

The transformation between phases, such as γ', γ" and δ phases, as a function of time and temperature, are revealed in the TTT diagram of the IN718 superalloy. However, the TTT diagram depends on grain size, extent of homogenisation and, in the case of wrought IN718, the degree of retained dislocations in the material [23, 92]. Figure 2.10 shows the wrought IN718 TTT diagram. The TTT diagram shows that the δ phase can form below 1010 °C, with

first precipitates forming at grain boundaries followed by intragranular precipitation when held at the temperatures indicated for an extended period. The γ'' and γ' phases are stable at lower temperatures. The overlap of γ'' and δ phase transformation curves after longer times illustrates the aforementioned transformation of the metastable γ'' phase into the more stable δ phase [35, 93, 94]. The prevalent conditions in AM are very different, such as the degree of elemental separation, grain size, the number of dislocations, and that could lead to transformation curves that differ from those seen in Figure 2.10 [95, 96]. For instance, wrought IN718 usually consists of equiaxed grains, while grains in AM samples are usually columnar [97].

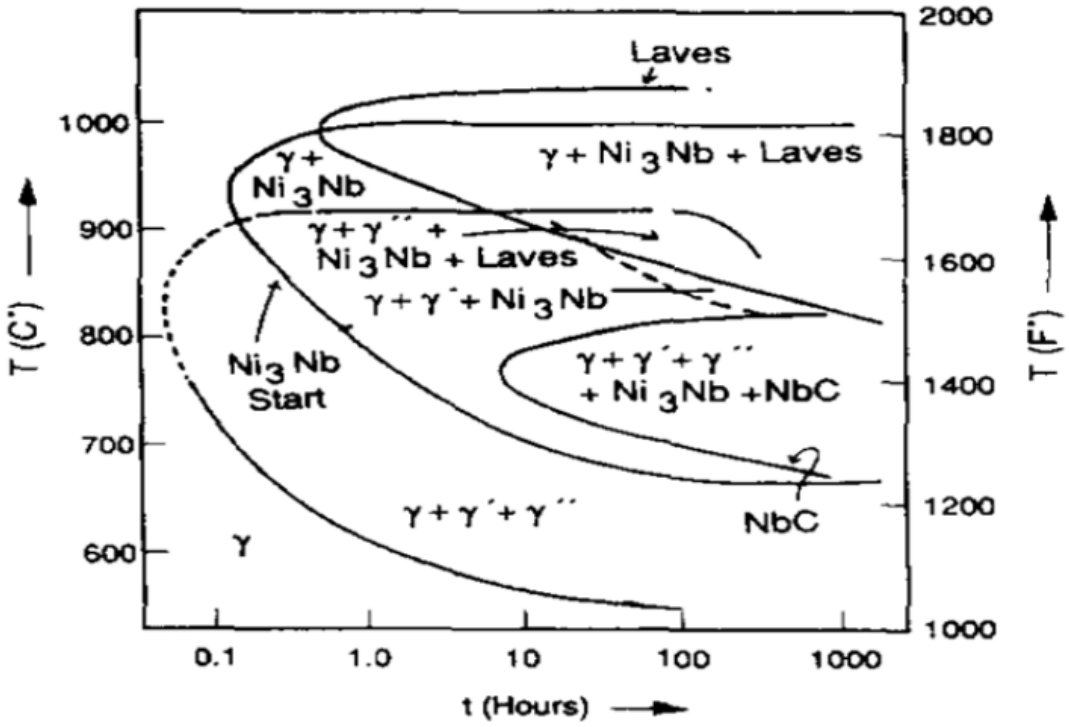

Figure 2.10:TTT diagram for wrought IN718 [93]

2.1.11 Crystallographic orientation

Crack initiation and propagation can be determined by crystallographic orientation and microtexture. The surface controlled slip trace will show the twist misorientation angle within the grain boundary as well as the tilt misorientation angle [98, 99].

2.1.12 Cooling rate

Radhakrishna and Claimed [100] stated that the amount of interdendritic Nb segregation and the amount of Laves phase were reduced when the cooling rate was increased. Zhang et al. [101] showed that higher temperature gradients in directional solidification processing refined the microstructure and reduced micro-segregation. Zhang et al. [102] studied the effects of phosphorus on the precipitation of γ″ and γ′ phases in IN718 at different cooling rates. The amount of γ″ and γ′ particles increased after air cooling as the phosphorus concentration was increased. The accelerating effect of phosphorus on the precipitation of the γ″ and γ′ phases decreased first and then increased as the cooling rate was reduced.

2.2 Additive manufacturing

AM is a collective term for many processes. For example, rapid manufacturing (RM) and rapid prototyping (RP) are terms adopted recently within AM, which broadly refers to manufacturing methods that have the ability to produce components directly from 3D computer-aided design (CAD) data or programmed G-codes by adding material layer-by-layer. Figure 2.11 shows the most common AM methods [15]. In the DLD process, the powder is injected or blown into the melt pool through the laser beam. Using a user-defined tool path, each layer is assembled track-by-track, with a single nozzle or multiple nozzles [103].

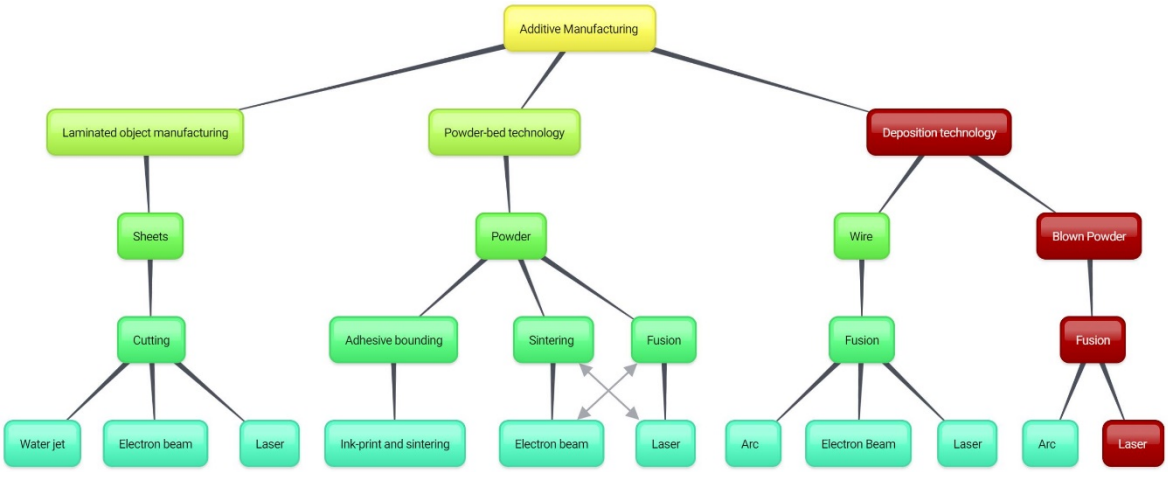

Figure 2.11: Process map of AM methods showing the combinations that AM methods can include. The red windows refer to the DLD method. Modified from [15]

2.2.1 Direct laser deposition

DLD is a member of the AM family that concentrates thermal energy in the form of photons or electrons to melt and bind material in different feed stock forms, such as wire or powder. DLD is also called laser blown powder, as the laser beam hits the substrate where the powder is flowing and forms a molten pool on the substrate [104]. A schematic diagram is shown in Figure 2.12.

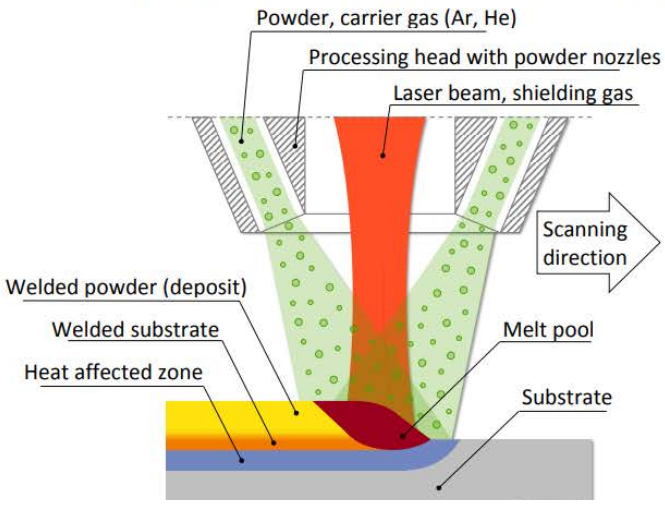

Figure 2.12: The direct laser deposition system [103]

DLD can be used for AM of pure metal components and functionally graded parts, as well as laser cladding and repair. According to Nima et al. [14] it will also be able to manufacture products with specific dimensions for automotive, medical or military applications. Figure 2.13 shows samples of unfinished parts made of direct laser deposition.

Figure 2.13: Unfinished parts made of direct laser deposition [105]

The shielding gas, which is usually argon but could be also helium, protects the molten pool and also controls the powder flow. In the DLD process there are two different nozzle types, which can change the behaviour of the powder feed and how it flows when it hits the laser beam. Both types allow the powder to hit the laser beam above the surface to melt the powder particles and push them into the weld pool in the deposited material. However, the powder concentration of the two types of nozzles varies. These nozzles are usually made from copper or brass, which makes them susceptible to heat exposure and molten particles repelled it. The coaxial nozzle, which has annular outlet cone, is in the form of one cone inside another, and the powder flows from the space between these cones, as shown in Figure 2.14b. The second type is the three-beam nozzle, which is made of a solid piece of material, as shown in Figure 2.14a. The construction makes it more susceptible to heat compared with the coaxial nozzle. The powder used in this nozzle can be coarser, which can generate a bigger powder spot size and a lower deposition efficiency [106, 107].

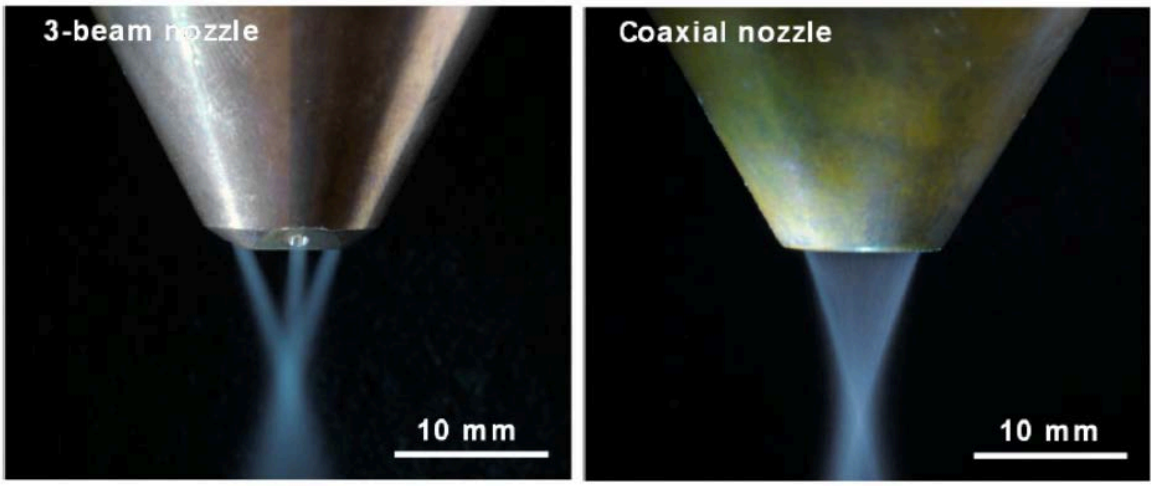

(a) 3-beam nozzle (b) Coaxial nozzle

Figure 2.14:Two types of nozzles used for powder supply in laser blown powder [108]

Figure 2.15 (a) shows powder intensity distribution for three beam nozzle and Figure 2.15 (b) for coaxial nozzle. Figure 2.15 (c) shows powder intensity distribution on the work plane for both three beam nozzle and coaxial nozzle.

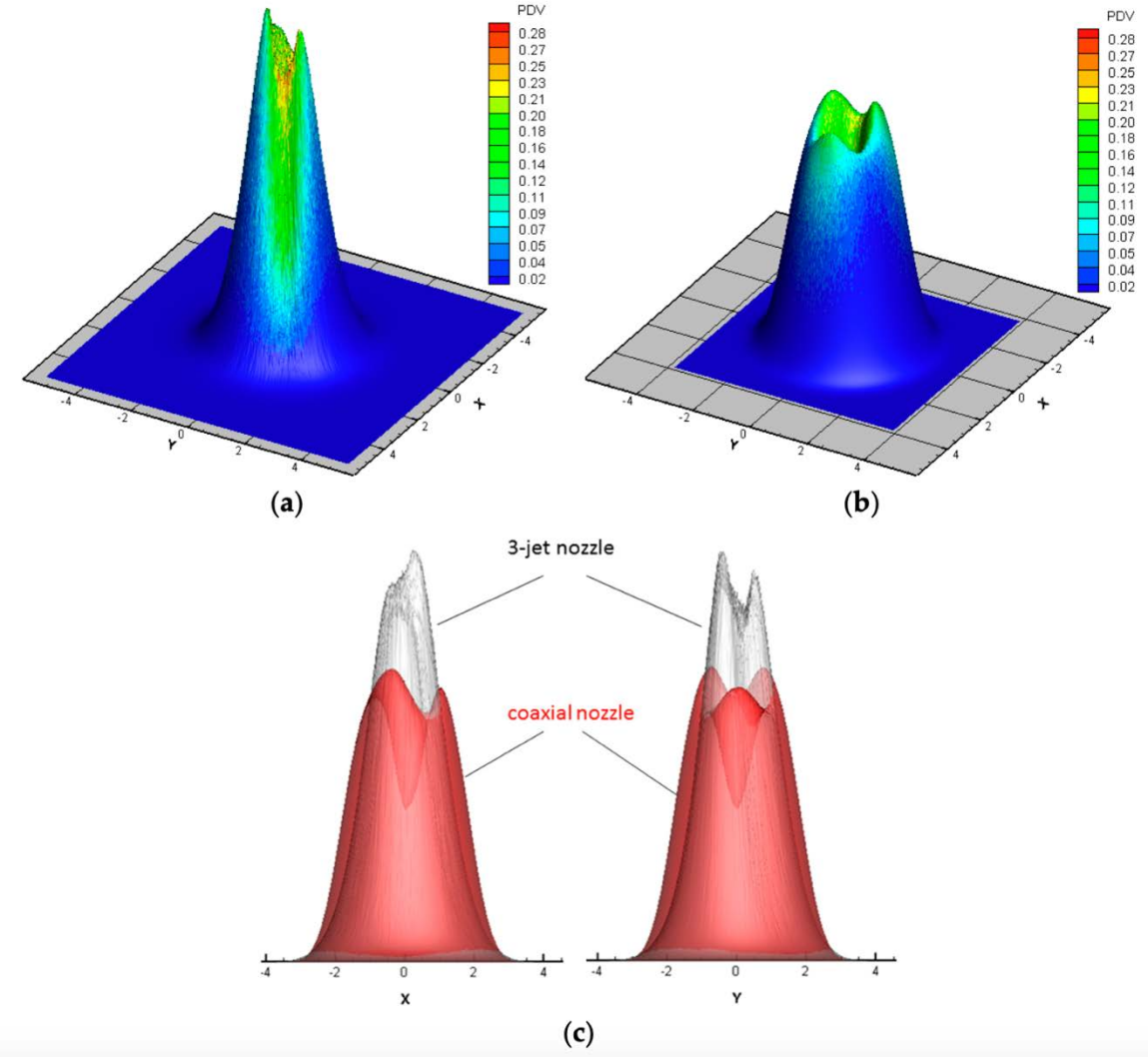

Figure 2.15: 3D-coloured pictures of the powder intensity distribution PIDs: three-beam nozzle (a); and coaxial nozzle (b). The PID on the working plane of the three-jet nozzle (a) and the coaxial nozzle (b) are superimposed with different colours in the two side views (c) [108].

2.3 Critical review of different approaches to modifying microstructure in AM

2.3.1 Laser heat input parameters

The effect of the laser is one of the most important process parameters. This research is mostly focusing on the power manipulation in the DLD process. Changing the laser power affects the heat input and melt pool; therefore, it will affect the geometry, such as the height and width, as

well as the depth of penetration, microstructure, surface finish and mechanical properties of the product. However, the heat input depends on multiple parameters, such as spot diameter and scanning speed, in addition to the laser power [106]. This relationship is described by Equation 2.3

$$E_s = \left| \frac{L_p}{L_d V_l} \right| \qquad \textit{Equation 2.3}$$

where E_s is the energy density, L_p is the laser power (watt), L_d is the laser spot size (mm) and V_l is the scanning speed (mm/min). As stated previously, an increase in laser power will increase heat input; therefore, the thermal gradient will be lowered and the cooling rate will be lowered, giving rise to larger grains [106]. An interesting study by Adegoke et al. [109] claimed that the strongest process parameter influencing the void content was power, while the strongest influence on the crack density depended on the interaction of power and hatch spacing. Moreover, power had the most influence on microhardness.

2.3.2 Laser pulsing

Although there is a lot of research on laser power modes, the area is still suffering with many gaps. In relation to DLD, the continuous wave (CW) laser power mode has been extensively used with various materials, such as nickel-based superalloys [71, 110, 111], steel alloys [112-114] and also titanium alloys [115, 116]. On the other hand, DLD's PW laser power mode breaks the patterns of heat source, melt pool motion, and vary temperature. It has been stated that PW provides many benefits in comparison with CW, including increased hardness, better surface finish, decreased solute diffusion and a more refined microstructure. Moat et al. [16] showed a marked effect on grain morphology and crystallographic orientation when using PW. Shah et al. [117] claimed lower surface ruggedness under PW due to disruption of the melting pool. Pinkerton and Li in two pieces of work [73, 118] found a direct correlation with the pulse frequency and an inverse correlation with the pulse duty ratio with the hardness of fabricated

steel samples. They also claimed that the PW laser leads to lower surface roughness and increased hardness compared with CW. Ravi et al. [74] stated that PW-LAM Ti-6Al-4V can obtain much finer equiaxed grains than CW power mode. Xiao et al. [69] also showed that segregation of Nb can be reduced and the Laves phase morphology regulated by PW laser in LAM from Inconel 718. Sivaprasad and Sundara Raman [119] indicated that welding using current pulsing and magnetic arc oscillation resulted in improved mechanical properties, as pulsing refined and reduced the Laves phase. Table 2.1 Shows a summary of some on the features that pulse power can cause on microstructure and mechanical properties.

Table 2.1: summary of literature of pulsing effect on microstructure and mechanical properties

Pulsing effect	**Cause of pulsing**	**Ref**
Small HAZ	Pulsing reduces HAZ since it reduces heat input and give more time for cool off	[19, 69, 71-74]
Refined grain structure	Grains size is smaller than CW and morphology becomes more equiaxed than CW	[19, 69, 71-74]
Low average heat input	Since pulsing gives time to cool during process the average heat input is lower than CW	[19, 69, 71-74]
High cooling rate	Lower heat input increases cooling rate + cooling during process and also due to cyclic temperature variations	[19, 69, 71-74]
Break dendrites	Pulsing breaks the chain-like long dendrite into small fragments.	[16]
Break melt pool motion	Disruption of the melt pool accrued due to pulsing	[74, 117]
Higher hardness	Pulsing reduces grain size and change the morphology, due to Hall-Petch smaller grains means harder structure	[54, 69]
Better surface finish and surface raggedness	Due to the disruption of the melt pool accrued results to pulsing finer surface	[117]
Nb segregation reduced	Due to the distribution on the long dendrites, it disturbs the segregation process as well and reduce Nb segregation reduced	[120] [54]
Change of weld pool size and shape	Due to the energy input variation and enhanced fluid flow of the weld pool and reduced thermal gradients in the weld pool	[54, 73, 121]

2.3.3 Laser power standoff distance

The standoff distance directly affects the distribution of the power source on the surface of the substrate or the build. There are two types of distribution of laser intensity: the top hat shape and the Gaussian shape. If the focus of the laser is above the surface (standoff distance is positive), the laser intensity will take a Gaussian form and that will prevent the formation of

the keyhole. On the other hand, if the focus of the laser is level with the surface, the laser intensity will take a top hat shape [107]. In an interesting study by Gerstgrasser et al. [122], the SLM of CM247LC was investigated, and it was discovered that by increasing the laser beam intensity and reducing the laser beam diameter in the focus plane, the cracks in the layers below are re-melted, and crack healing occurs which decrease cracks by more than 98 times.

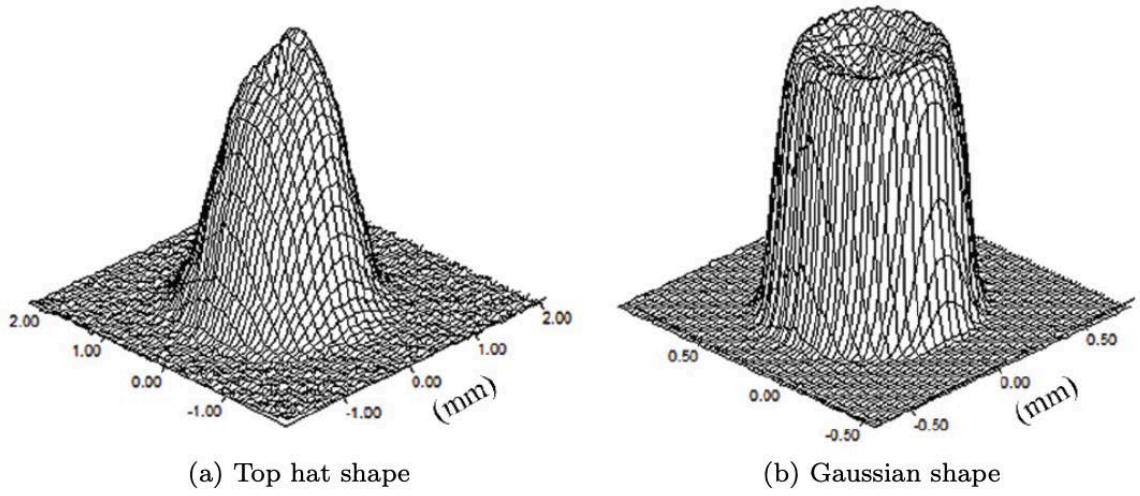

Figure 2.16: If the laser focuses on or slightly below the surface its intensity distribution will take a top hat form (a) and if the laser focus is above the surface it will take a Gaussian form (b) [15]

2.3.4 Melt pool

DLD creates a melt pool similar to a welding melt pool. When the laser hits the powder and melts it into a liquid pool it behaves like a pot of boiling water, except that the heat source is introduced from the top, whereas in the pot, heat is introduced from the bottom. The surface of the liquid melt pool flows from regions of low to high surface tension because the temperature variation of the surface liquid causes fluid surface tension gradients. This type of flow is called Marangoni flow, and it significantly affects the weld pool circulation pattern. When the laser hits the surface of the melt pool the flow will circulate and collide on the surface, pushing hot surface liquid to the bottom of the melt pool and digging into the substrate. Nevertheless, the Marangoni flow could cause gas bubbles within the melt pool instead of pushing them towards

the surface. The melt pool is divided into four sections, as illustrated in Figure 2.17, which describes the different flows within the melt pool. Flow directed downwards enhances the depth of penetration; this does not lie directly underneath the heat input, but it is at the tail of the melt pool because of the continuous sweeping movement of the power source over the surface [123]. A study by Hilal et al. [124] claimed that higher beam speeds resulted in smaller melt track size, while higher beam power tended to give rise to a larger melt pool an inverse relationship was noted for beam power, where higher beam power tended to give rise to tracks area.

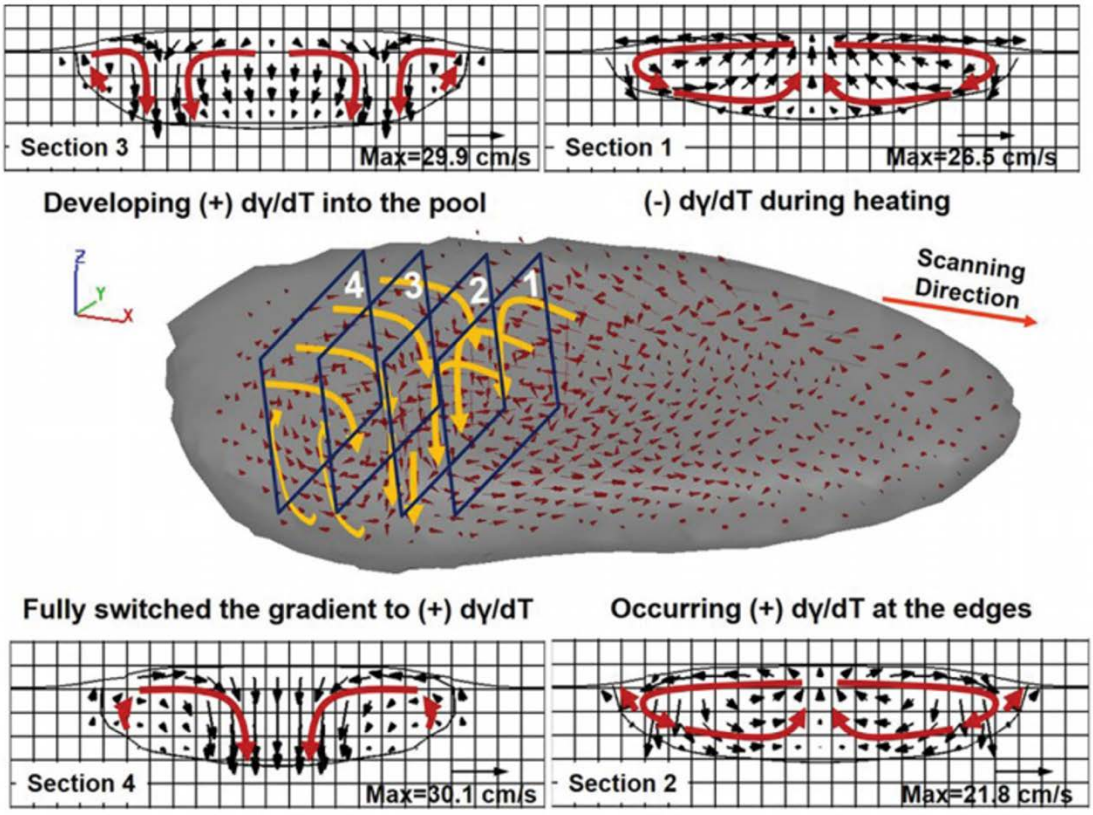

Figure 2.17: 3D and 2D plots showing fluid flow and mixing in the laser clad melt pool [123]

2.3.5 Laser scanning speed and strategies

The DLD process uses a sweeping motion over the substrate and the speed of the motion is called the scanning speed. The scanning speed affects heat intensity as illustrated in the energy Equation 2.3. The scanning speed and heat intensity have an inverse relationship in which a

decrease in scanning speed leads to an increase in heat intensity. Scanning speed is one of the key parameters as it controls the heat intensity, which controls the microstructure and thus the mechanical properties. If the heat intensity is high, the underlying material will be heated, and this will reduce the thermal gradient and so lead to a columnar grain structure. On the other hand, a faster scanning speed can lead to an equiaxed and small grain structure [106].

A study by Ocelı'k et al. [125] into the effect of laser scanning speed on the laser cladding process examined the grains of cobalt-based alloys. The cross sections shown in Figure 2.18 illustrate an increase in elongated grains with increased scanning speed. While the scanning speed increased the heat input was reduced, leading to faster solidification. This allowed the grains to solidify upwards toward the surface. On the other hand, decreasing scanning speed led to a higher heat input that forced the grains to grow more in the scanning direction.

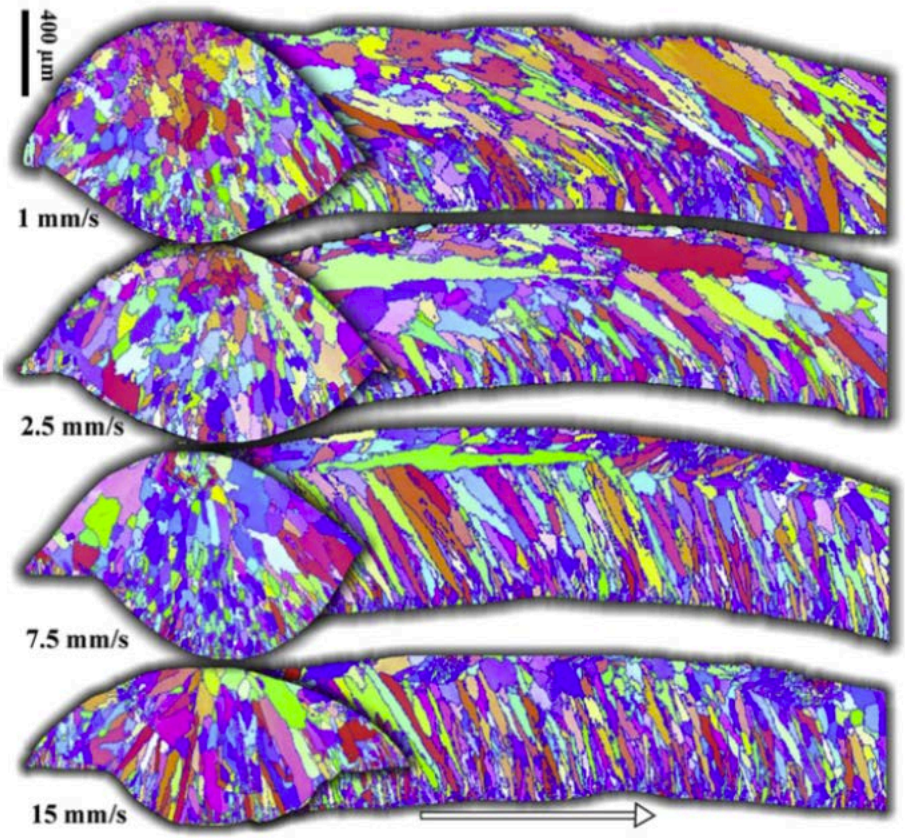

Figure 2.18: Differences in microstructure depending on the scanning speed. The image shows transverse (left) and longitudinal (right) cuts, and the substrate movement direction is shown with an arrow [125]

2.3.6 Powder feed rate

In the DLD process the laser beam is centred within the nozzle and powder particles are shot from the three holes into the beam. The geometry of the deposition is affected by the amount of powder fed into the laser beam. To get a stable bead height, a constant powder feed rate has to be maintained [10]. Moreover, if the feed rate is high, the particles will reach a lower temperature because the laser beam is diffracted, which can result in unmelted particles hitting the substrate, while a lower feed rate will result in the laser hitting more particles and melting them [126, 127]. Kummailil et al. [128] studied the process parameters effects on the deposition of Ti-6Al-4V and found that the deposition can be linked by laser power to the powder feed rate and the energy per unit area and this can help to choose the optimum layer thickness of the deposition. Tang et al. [129] showed that controlling the powder flow rate could keep the track morphology uniform even as the DLD process was decelerated and accelerated. These results also showed that the difference in layer thickness can be reduced significantly compared with parts manufactured with a constant powder flow rate.

2.3.7 Powder standoff distance

The standoff distance is the distance between the tip of the nozzle and the surface of the substrate. The maximum efficiency of the powder flow rate is reached when the powder focus is level with the substrate, which is called zero standoff. If the powder focus moves up or down from the surface, the efficiency will decrease, and the build geometry will be smaller. It can be beneficial to focus the powder slightly below the surface, as that can level out the deposition material, because when the deposited layer encounters a convex or concave part of the substrate the powder efficiency will decrease and the build-up will be smaller [130].

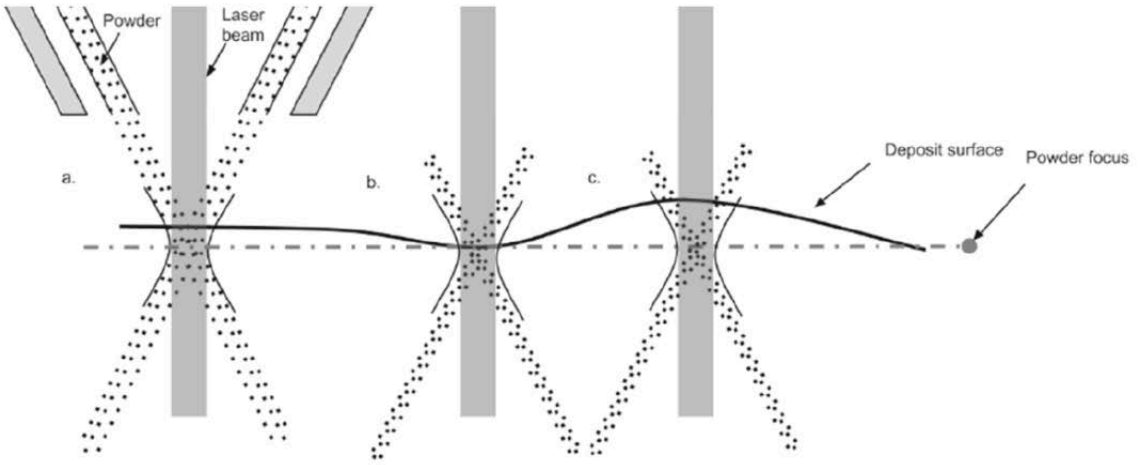

Figure 2.19: An illustration of how the powder efficiency can level out the deposited material. The powder focus in (a) lies below the surface reducing the efficiency while in (b) the focus in right on the surface, increasing the efficiency and level out the height difference. In (c) the focus is very much below the surface reducing the efficiency even more [107]

2.3.8 z-increment condition (Δz)

One of the important parameters that has not been investigated thoroughly is the z-increment, which is the vertical distance the laser nozzle gantry moves between each layer to deposit the next layer. It is necessary that the z parameter is correctly configured, otherwise the powder focal spot will be out of focus and the deposit shape and quality will rapidly deteriorate with each subsequent layer. If the z-increment is too high, the powder nozzle rises more quickly than the deposit can expand. If the nozzle moves further away from the fusion pool, this will lead to a poor capture rate. This effect would worsen with every layer until the nozzle distance became so high that the deposition process could not continue. In contrast, when the z-increment is too small, the nozzle gap decreases steadily, which leads to poor powder capture rate, and, therefore, low build quality, excessive heating and poor surface finish [131, 132]. Pinkerton and Li [133] claimed that good consistency of the layers can be accomplished without the z-increment or, in other words, by fixing the distance between the nozzle and the substrate for more than 20 layers, and poor results are obtained by fixing or regulating the z-increment. Figure 2.20 (A) illustrate the z-increment too high, and the nozzle rises more

quickly than the deposit can expand Figure 2.20 (B) illustrate the z-increment too small, the nozzle gap decreases steadily, which leads to poor powder capture rate.

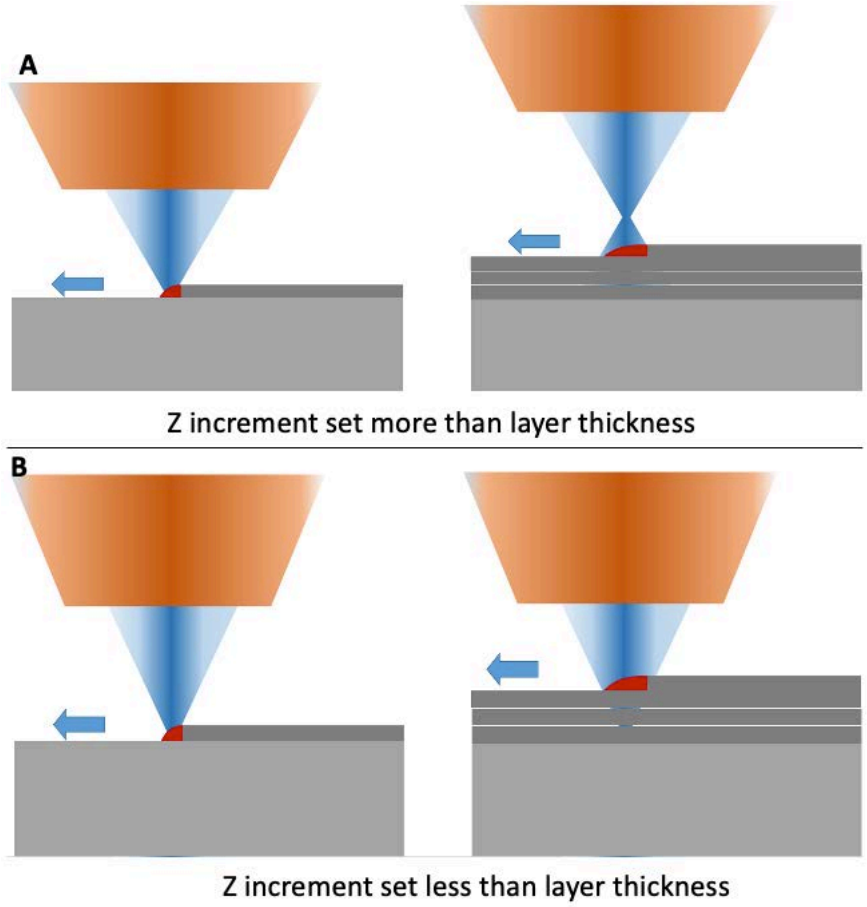

Figure 2.20: Schematic illustration of the effect of Z increment on nozzle standoff distance.

2.3.1 Shielding gas

A study by Manikandan et al. [134] investigated GTAW welding with Inconel 718 using argon and helium. For the combination of helium shielding gas and power pulse mode, the maximum instantaneous weld cooling rate was achieved. This resulted in a decrease in the Laves phase, niobium segregation and DAS in the fusion zone. There is no study that shows the effect of the shielding gas pressure effect on the microstructure.

2.3.2 Texture

The crystallographic orientation of the polycrystalline sample makes the texture. If the crystals in the sample are in an entirely random orientation, then this can be assigned as no distinct

texture. In contrast, if the crystallographic orientation is not random and there is a preferred orientation, then this can be assigned as a strong, weak or moderate texture [135]. Usually in AM, the heat input parameter will affect the thermal gradient and the solidification rate, which vary during the build due to heat accumulation. This results in variations in solidification conditions, leading to differences in solidification microstructures that can be summarised as grain size, morphology and texture that can be manipulated during fabrication by changing process parameters [136]. Moat et al. [16] used PW with varying pulse cooling cycles in DLD processing using the nickel superalloy waspaloy to measure texture. The results show that changes in laser pulsing have a significant effect on the grain size, morphology and microtexture, whereas the cooling cycles showed minor effects on the microtexture.

2.4 Mechanical properties

This section provides a summary of work published about mechanical properties of AM process products, specifically on hardness and tensile testing of both IN718 and CM247LC.

2.4.1 Hardness

Numerous studies of hardness have been conducted into the DLD of Inconel 718 [137-144]. A study of hardness by Amsterdam [145] confirmed that the strength of flat sample walls is higher than that of round samples. Liu et al. [146] performed hardness tests on parts produced by single direction scanning and cross direction scanning. Results showed that, in general, the single direction scanning sample showed greater hardness than the cross direction scanning sample. Parimi et al. [138] found that the hardness of DLD products was lower than that of wrought products due to large grain sizes or segregation of Nb, and the presence of Laves phases instead of sufficient γ" phase. Stevens et al. [139] claimed that hardness decreases as the number of layers deposited or the height of the part increases; moreover, the centre of the AM part is harder than the top, and also the hardness decreases as the energy used during deposition increases. Likewise, overlapping values, the hatching was harder than the surfaces,

in both side and cross sections surfaces. Zhao et al. [137] claimed that the hardness value of heat-treated DLD plasma rotation electrode preparation IN718 powder was the same as that of the heat-treated DLD gas atomised IN718 powder, but the average hardness of as-deposited plasma rotation electrode preparation IN718 powder samples was higher than that of as-deposited gas atomised IN718 powder samples.

Boswell et al. [147] examined a CM247LC rod fabricated by SLM. This rod was then cut into identical pieces and a series of short ageing experiments was carried out at different temperatures. Results showed that samples with post-heat treatment below 600 °C had low hardness. Hardness showed a significant increase between 700 and 900 °C, then started to drop. Divya et al. [148] tested hardness in the as-SLM condition. The hardness was significantly lower than obtained from the sample in the SLM + HT state. Moreover, the hardness of CM247LC in the conventionally cast condition was higher than that obtained from the alloy in the SLM + HT condition. Muñoz-Moreno et al. [149] tested hardness in CM247LC with the SLM process as-built and after solution + ageing in which the solution treatment temperature varied with every sample. The results showed that the hardness of the as-built sample was lower than the solution + ageing sample; however, the variation of solution temperature did not show a noticeable difference.

2.4.2 Tensile properties

Numerous studies have investigated the tensile property behaviour of IN718 manufactured by the DLD process [137, 145, 146, 150-152]. These properties include the tensile strength and the ductility of AM IN718 in the as-built condition and also after post-heat treatment. In the as-built condition, it has been observed that tensile properties can be lower and also higher than for some of the heat-treated alloys. This is because the γ' and γ'' phases of the as-built AM samples lack precipitation hardening. Qi et al. [150] performed tensile testing with vertical coupons and they found that the as-deposited part stayed soft and had poor tensile

strength and good ductility without any heat treatment. Furthermore, the tensile strength was significantly improved and became equal to direct age wrought material due to precipitation during the γ″ and γ′ phases of the matrix strengthening. Zhao et al. [137] performed tensile testing at elevated temperatures and they found that the as-deposited part showed lower UTS and 0.2%YS compared with the heat treated part. However, the as-built part showed a larger reduction in area than the heat-treated parts. A study by Amsterdam [145] used flat and round Inconel 718 samples and claimed that the tensile strength of the thin walls processed with DLD was higher than that of the thicker walls. Liu et al. [146] performed tensile tests on single direction scanning and cross direction scanning parts. Results showed that the UTS was the same for both scanning strategies; however, elongation was higher in the cross direction scanning part. Sui et al. [153] find that the aged IN718 samples with irregular and long-striped Laves phases show the lowest tensile strength and ductility. Hence, a certain amount of small and granular Laves phases are presumably beneficial for the room temperature tensile properties of Inconel 718.

The tensile properties of CM247LC in AM is limited since it is a non-weldable material. Huang and Koo [154] tested cast CM247LC at RT and at high temperature; results showed a smaller grain size at elevated temperatures, with have a higher UTS, YS and elongation than the cast sample with a bigger grain size at room temperature. Kim et al. [155] examined conventional cast and directional solidification cast of CM247LC with two post heat treatments (ageing, and solution + ageing) and the results showed that the aged condition had higher tensile strength than the solution treated + aged condition at low temperature in the conventional cast case. On the other hand, solution + ageing samples at high temperature showed higher strength. The solution + ageing condition showed more strength than the aged samples in the directional solidification samples at all temperatures. Wang et al. [156] examined SLM fabricated and cast CM247LC; the results showed that yield strength of as-

built CM247LC was almost the same as that of conventionally fabricated CM247LC. Moreover, as-built samples had a high strength that is sufficient for it to be used for applications even without any heat treatments.

2.5 Defects on the mechanical properties of AM

2.5.1 Cracks

Cracking is a major issue with AM of CM247LC, during manufacture, heat treatment and service. There are four major mechanisms that cause these cracks.

2.5.1.1 Solidification cracking

Solidification cracking usually happens in the melt pool, particularly in the mushy zone where the material is not fully solidified [44, 157, 158]. As the temperature falls below the coherence temperature, cracks emerge, and the formation of the dendrites follows the heating source direction toward the liquid phase in the interdendritic regions [27]. The residual liquid serves as a stress raiser and crack initiator, allowing the relatively weak S/L boundaries to separate, resulting in an intergranular rupture. This type of cracking is also called hot-tearing.

2.5.1.2 Liquation cracking

Liquation cracking usually occurs in the HAZ where the bulk material is quickly heated to a temperature that is lower than the material's overall liquidus temperature [27]. Grain boundary phases are unable to dissolve fast enough into the solid solution and form phases with low melting points at grain boundaries. These phases eventually melt and form a liquid-grain boundary film. These liquid films have the potential to act as crack initiation points in the fabricated material, forming grain boundary cracks [26, 159-161].

2.5.1.3 Strain-age cracking

SAC predominately occurs in γ' precipitate strengthened alloys, such as CM247LC, during post weld heat treatment (PWHT) in the ageing region, either as part of a stress relief, or during the ramp phase of a solution treatment or high temperature service [44]. This type of cracking can

also be caused by repetitive reheating in AM. Intergranular microcracking appears as a defect in the HAZ or in the deposit itself, with carbides acting as crack initiation sites. Al+Ti contribute to the formation of the strengthening γ' phase. The ageing mechanism increases material strength while decreasing ductility; residual stress and induced stress from the precipitation of the γ' result in strain that exceeds the material's minimal ductility, and failure usually occurs at grain boundaries [26, 44].

2.5.1.4 Ductility dip cracking

Ductility dip cracking (DDC) forms as a result of the lack of ductility in a temperature range below the solidus temperature. This form of cracking occurs as a result of a process known as ductility reduction. This is due to a mixture of macroscopic thermal and solidification stresses produced at high temperatures, as well as microscopic stresses generated within grain boundaries as partly coherent carbide phases precipitate. Although resistant to corrosion and stress corrosion cracking, high chromium nickel superalloys are considered to be especially susceptible to DDC [162, 163].

2.5.2 Surface finish effect on tensile behavior

A small number of studies have investigated the difference in tensile properties between samples with unimproved surface finish. Everhart et al. [164] shows that measurement error in cross-sectional area is the main source of variation between unfinished and machined strength measurements. Results also indicate that a ductile material may demonstrate the same tensile strength regardless of post processing.

study by Rafi et al. [165], cylindrical Ti–6Al– 4V tensile bars were fabricated on both laser and electron beam powder bed systems. Samples were built both vertically and horizontally, and with both unfinished and machined surface finishes. The horizontal bars with unfinished surfaces appear to be constructed without supports and, as a result of melt pool inconsistencies

in unsupported parts, are likely to have some dimensional error and severe surface variation. In this study, it was discovered that vertically oriented components had lower tensile characteristics and that machined bars performed better than unprocessed bars in general. To describe tensile property variance, the authors focused on microstructural variance. Niendorf and Brenne [166] TWIP steel flat tensile bars that were manufactured in a single orientation utilising supports were investigated. After electro-discharge machining to remove supports, surface grinding, and heat treatment, samples were evaluated at different points throughout post processing. The strength and ductility of the samples varied, with the AM portions showing a decrease in strength when compared to traditionally treated sheet material. This discrepancy was ascribed to a measurement error in the sample cross section induced by the rough surface for both unfinished and ground surface samples.

2.5.3 Tensile test orientation

Many of these studies focus on test orientation relative to the build direction, and the results are mixed. Some demonstrate variance in yield strength and tensile strength, while others indicate only a change in ductility. All studies surveyed indicate that samples tested parallel to the build direction have strength less than or equal to samples tested perpendicular to the build direction [167-169]

2.5.4 Fracture morphologies

Deng et al. [170] used SLM to produce IN718 samples and used different conditions (as-built AS, direct ageing DA, solution + ageing SA, homogenization + ageing HA, finally homogenization + solution + ageing HAS.) and different orientations vertical and horizontal. The results shows that the fracture characteristics are not considerably different from one another. The crack propagates in a mixed intergranular and intragranular mode in both horizontally and vertically oriented samples, and in both as-built and heat-treated conditions, as evidenced by the presence of intergranular grain facets and intragranular surfaces; the

fracture occurred in a ductile mode, as evidenced by the presence of the typical dimple feature on the fracture surfaces. Regardless of heat treatment settings, inclusion particles such as Al_2O_3 (inherited from the raw powder) can be detected embedded into the voids on the fracture surfaces. Though the as-manufactured condition's elongations are significantly higher than the DA condition's, their fracture surfaces appear to be quite similar, with intragranular dimples arranged preferentially in a dendrite-like pattern and differentially from grain to grain. Figure 2.21 shows the fractured surfaces morphologies of the different conditions and the different orientations.

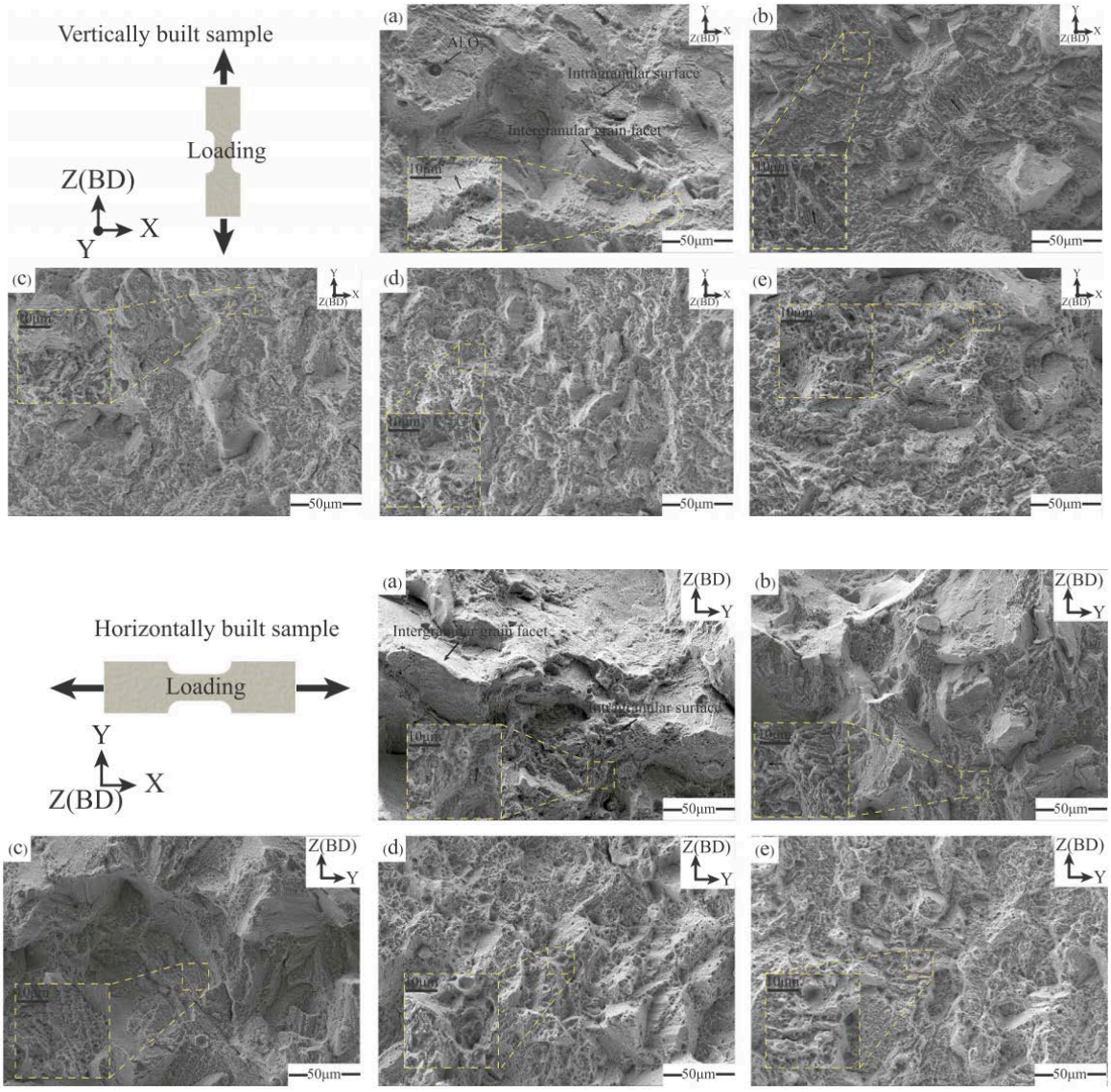

*Figure 2.21Fractured surfaces of **vertically** built SLM IN718 samples in as manufactured and heat-treated conditions: (a) AS, (b) DA, (c) SA, (d) HA, (e) HSA. Note that the alignments of dimples are indicated with the black arrows in (a) and (b). Fractured surfaces of **horizontally** built SLM IN718 samples in as manufactured and heat-treated conditions tested normal to the building direction: (a) AS, (b) DA, (c) SA, (d) HA, (e) HSA. Note that the alignments of dimples are indicated with the black arrows in (a) and (b).*

Li et al. [171] illustrates the fracture morphology of an as-built IN718 tensile sample tested at room temperature. The dendritic morphology is still retained after the room temperature tensile test, according to the findings. In the fibrous zone, there are many dimples with clear directional alignment along the columnar dendrites, which is a hallmark of ductile fracture. Figure 2.22 shows tensile fracture morphology with considerable number of dimples. It also shows laves phase between dendrites which ack as crack initiation.

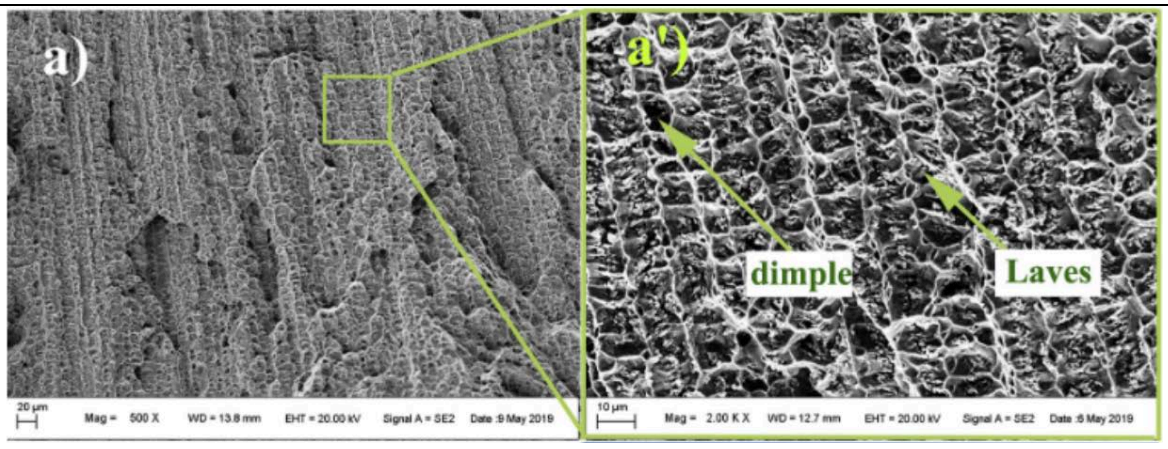

Figure 2.22: Tensile fracture morphology along the tensile direction there is a considerable number of dimples with obvious directional orientation along the columnar dendrites in the fibrous zone, which is the typical characteristic of ductile fracture [171]

2.5.5 Porosity

Ahsan et al. [172] stated that the DLD process allows for a higher deposition rate and that deposits with lower interlayer porosity and surface roughness have a unique epitaxial grain microstructure.

2.6 Research gap

Overall, there are a numerous existing study about IN718 and CM247LC, but they all seem to have the following gaps. Limited literature is available that specifically relates to parameter studies into power pulsing in the DLD process. Most of the existing studies are over a small parameter scale and cannot be used for a wide range of parameters. Moreover, no study was found that discussed the cooling cycle of pulsing and the effect on microstructure. Moreover, no study was found that had managed to produce CM247LC parts with no cracking using the DLD process. The optimisation of build parameters needs to be investigated to enable the matching of the product microstructure to that of the item being repaired to minimise differences in mechanical properties.

2.6.1 Summary of literature: key findings and areas of investigation

A detailed literature review about the control of microstructure using process parameters during DLD of IN718 and CM247LC has been performed, including a consideration of the effect on geometrical accuracy and microstructural development. The following points summarise the current state of knowledge.

- According to the literature, the build quality and microstructure of DLD samples are strongly influenced by process parameters, such as laser intensity, scan speed, powder flow rate and deposition path.
- The majority of research concentrates on two extremes, either low- or high-power intensity, with no experimental evidence for microstructural differences between the upper and lower laser power limits. The effect of layer thicknesses on grain size and morphology is not explained in any of the studies.

- A few studies have looked into the possibility of constructing a functionally graded microstructure by using different laser powers intensity during DLD.
- Most studies concentrate on a GTAW square pulse on butt joint welds rather than AM.
- None of the studies go into detail about the impact of various pulsing effects on grain size and morphology.
- None of the studies take into account the manipulation of pulse length (cooling cycle).
- Most studies concentrate on Inconel phases and not on the relationship between grain size and mechanical properties.
- Current research on power pulsing is incomplete, revealing a variety of information gaps.
- Most of the CM247LC literature on DLD is about cracking.
- None of the research used DLD pulsing to build CM247LC parts.

2.7 Potential for further study

All in all, only a limited amount of information on the development of microstructure, texture, and mechanical properties during DLD has been published. DLD is extremely sensitive to process parameters, and the parameters that are best for geometrical accuracy may not be the best for microstructural and/or mechanical property optimisation. Despite the rapid increase in the number of publications, there are areas that have not been sufficiently addressed in the literature.

- The grain size, morphology, and texture in IN718 single wall builds needs to be investigated with consideration given to the impact of various laser powers on microstructural characteristics, Nb segregation and the resultant mechanical properties.

- The impact of various laser power pulsing modes on microstructural characteristics, Nb segregation and the resultant mechanical properties needs to be investigated.
- The grain size, morphology and texture of thin walls formed by DLD needs to be investigated to understand the impact of different laser pulsing modes on microstructural characteristics, Nb segregation and resultant mechanical properties in depth.
- The laser pulsing technique to achieve crack-free CM247LC needs to be investigated.

As a result, the current study considers the most relevant aspects of these issues, as mentioned in Section 1.3 of the Introduction.

Chapter 3. Experimental Procedure

3.1 Introduction

This chapter describes the experimental techniques used to produce DLD IN718 and CM247LC samples in this research, as well as the sample processing, preparation and characterisation procedures used to assess the powder before processing and the solid structural integrity and microstructural development after processing. Furthermore, the process parameters used in building the samples are detailed. The chapter also includes a description of the microscopic techniques that were used to characterise the samples. An overview of the DLD system set-up located at the University of Birmingham (UoB) is included. This chapter also includes the experimental approach taken to investigate the area of interest identified by the literature review.

3.2 Materials

The materials selected for investigation in this study were the nickel-based superalloys IN718 and CM247LC, and the primary focus of the study was IN718. The materials contained varying levels of the γ′. All investigated powders were produced by argon gas atomisation, and supplied by either Sandvik or the Carpenter Technology Corporation

3.2.1 Powder chemical composition

The chemical composition of the two powders used is shown in Table 3.1, by percentage weight of the alloying elements. The chemical composition of IN718 was determined by AMG Superalloys UK Limited, while that of CM247LC was determined by Incotest UK.

Table 3.1: Powder chemical analysis

Element (Wt%)	Ni	Fe	Cr	Nb	Mo	Ti	Al	C	B	O	Si
IN718	54.45	18.19	18.18	4.88	2.9	0.91	0.42	0.01	<0.02	0.011	0.03
CM247LC	62.2	0.08	8.29	0.05	0.52	0.71	5.55	0.08	20 ppm	<100 ppm	0.11

3.2.2 Powder shape considerations

The gas atomised IN718 and CM247LC powder particles, used in the present study, were examined. The powder particles are not geometrically uniform, having a rough surface finish. It was also observed that very fine satellite powder particles of approximately 5 µm were attached to the large powder particles; this would prevent the particles being dispersed by the argon flow from the nozzles. Further examination of the cross section of powders showed that the as-received powders were not all fully dense. Hollow particles were frequently observed. The pores in these hollow particles were present as a result of entrapped argon or due to shrinkage during atomisation. Thus, the entrapped argon could be present in the finished DLD structures. IN718 powder is discussed in Chapters 4, 5 and 6, whereas CM247LC powder is discussed in Chapter 7.

3.2.3 Base plate

The substrate used was IN718, purchased from Dynamic Metals Ltd as a bar that was cut into discs 25 mm thick and 200 mm in diameter. The disc then was grooved with eight channels; every channel was 16 mm deep and the distance between each groove was 3 mm (the wall building area). Then the substrate was cut using a machine saw.

Figure 3.1:Inconel 718 substrate before machining and the top view layout for the machining process (all is in mm)

The IN718 substrate was then machined to an upside-down T shape and cut into segments of 40 mm length and 20 mm width from each side. Seven 1-mm-deep holes were drilled 2 mm below the substrate surface with a pitch of 5 mm between holes, to be used to insert the K-type thermocouples.

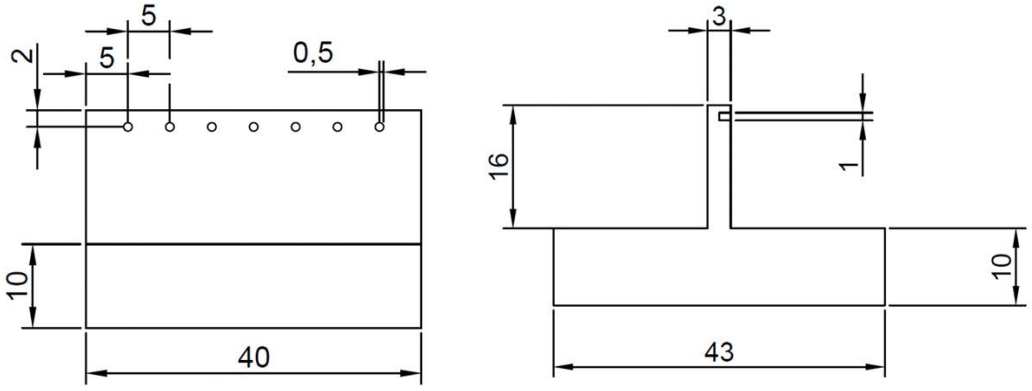

Figure 3.2: Substrate schematic side and front view that shows showing the thermocouple's holes locations (all unite is in mm)

3.3 Concept of laser power source direct laser deposition

A 4-kW diode laser (Trumf TrueDisk 4002) system was used. Diode lasers are a type of solid-state laser, generally made up of a thin disc of ytterbium-doped yttrium aluminium garnet crystal. The diode laser has a wavelength of 1030 nm, similar to that of the Nd:YAG laser. However, the profile of the crystals used in these two types of solid-state laser is different [173]. Figure 3.3 shows the multi-pass pumping diodes in the Trumpf used in this research.

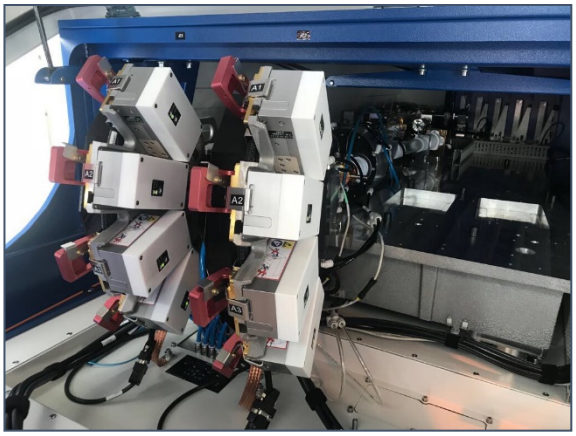

Figure 3.3: End-pumped diode/fibre laser used in the research

3.3.1 Laser energy source

Different thin walls were produced by a Trumpf TrueDisk 4002 equipped with a three-beam nozzle able to move in a Cartesian space (x, y, and z directions). The energy source was placed beside the chamber and the laser was transferred via fibre from the source to the laser optics inside the chamber. The Trumpf provides continuous wave and pulse wave, however, the pulsing in the Trumpf cannot go to complete shut of the power completely, the lowest it can go is 2% of what the powder is set to. The Trumpf also have the ability to vary the pulse cycle time.

3.3.1.1 Powder feeding

A Siemens powder feeding system was used for this study. The powder was positioned on a powder staring hopper on a rotating disc, and the powder feeding rate was determined by the rotation speed. The calibration of the powder feeder was done by setting the rotation to a specific speed on the disc and weighing the amount of powder deposited during a specific length of time. This process was repeated, and the results are recorded in a Table 3.2. The system has 10 levels of powder feed and 10 levels of argon pressure that deliver the powder to the weld pool. The powder feed unit that can be programmed in the G-code is revolutions per minute, which is converted into grams per minute in Table 3.2.

Table 3.2: Approximate conversion from rev/min to g/min

Powder Feed	
rev/min	g/min
1	5
2	8
3	11
4	15
5	18
6	21
7	24
8	25
9	27
10	32

3.3.1.2 Scanning speed and strategy

Scanning speed is programmed in mm/min. Different scanning speeds were used to build the single-walled samples and the single tracks. The scanning speed parameter in most builds was kept fixed at 11.7 mm/s (700 mm/min), whilst the scan strategy was set as bidirectional in most samples with a layer thickness of 0.5 mm.

3.3.1.3 Laser/powder nozzle

The nozzle used in the experiment was a three-beam nozzle, shown in Figure 3.4. Visual inspections were made to ensure that the shape of the powder intercept was correct and that no reflections from the melt pool had damaged the nozzle and disturbed the powder flow.

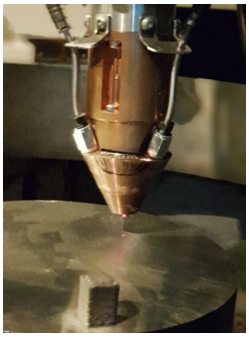

Figure 3.4: The three-beam nozzle used in the experiment

3.3.1.4 Laser set-up

The laser beam focused on a 1.4 mm spot while the standoff distance between the laser head and the surface of the substrate was set to 10 mm. The laser operative system can be set as CW and PW. A three-beam nozzle was used, providing a constant powder flow rate as required, and positioned 10 mm from the substrate in order to achieve a defocusing of the powder stream of 2 mm (shown by D_P in Figure 3.5). The scanning speed strategy was bi-directional Figure 3.7 shows schematisation of the thin wall and the scan strategy. The focus of the laser beam was set in order to attain a positive defocusing of 3 mm above the surface of the substrate (shown by D_L in Figure 3.5). This configuration allowed the triggering of the auto compensation of the deposition during the process in order to avoid uneven horizontal wall surfaces.

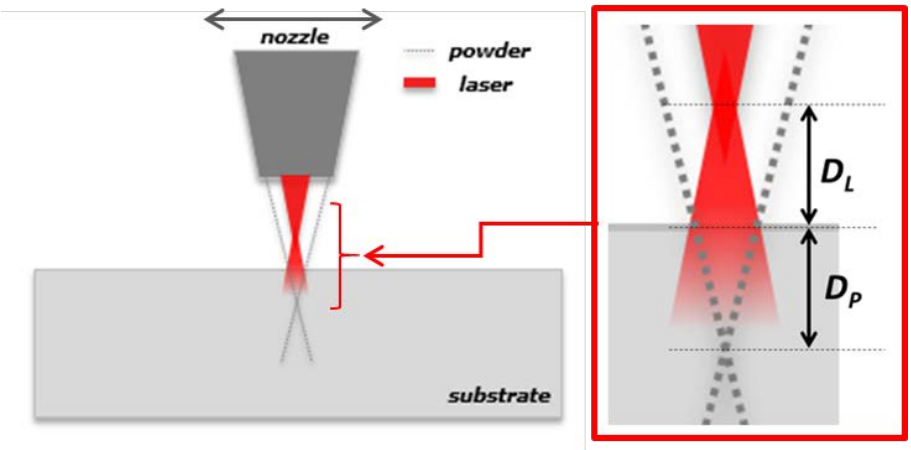

Figure 3.5: 2D schematisation of the powder stream defocusing (DP) and laser beam defocusing (DL) distances.

Figure 3.6 shows the set-up of the experiment. Four K-type thermocouples were inserted into holes located 1 mm below the substrate surface. Two infrared cameras (acquisition filter from 150 °C to 2000 °C) were used to identify the thermal gradient during deposition.

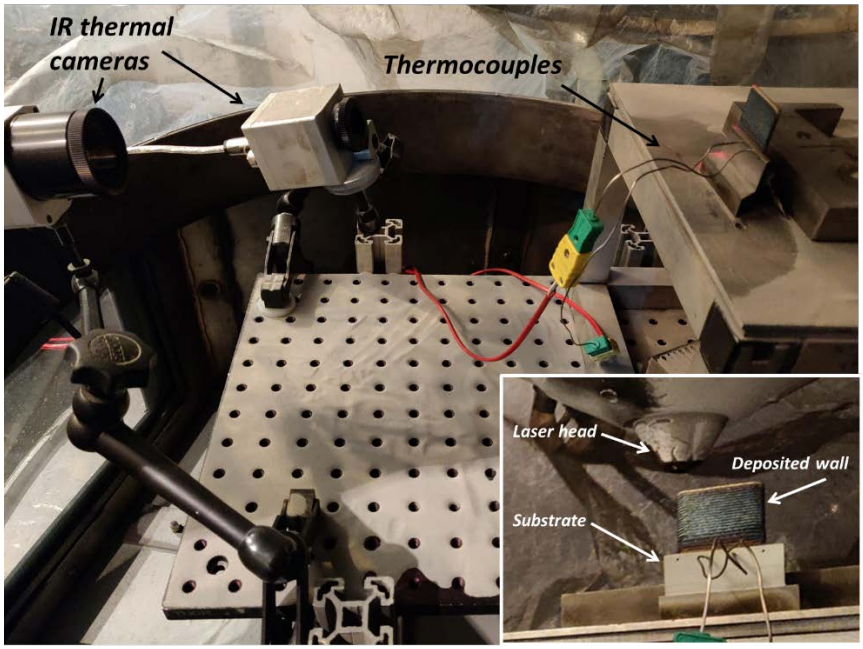

Figure 3.6: Experiment set-up

The heat input H (in J/mm) computed by Equation 3.1, where P in (W) is the power of the laser and V refers to the scan speed in (mm/s).

$$H = {}^{P}/_{V} \qquad \textit{Equation 3.1}$$

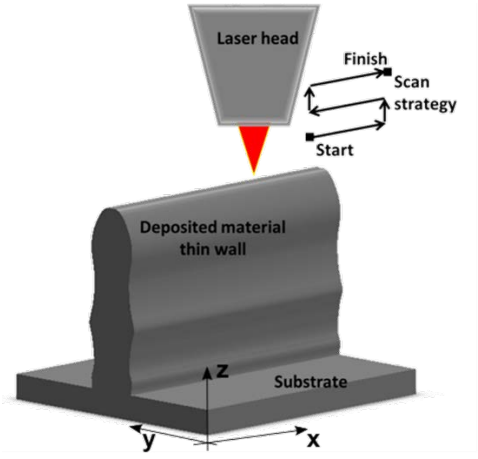

Figure 3.7: Schematisation of the thin wall and the scan strategy

3.3.1.5 Laser power

Five types of laser power modes were used: Continuous wave CW, Pulse wave PW, Partial power wave PPW, Double power pulse wave DPPW and Partial double power pulse wave PDPPW.

3.3.1.5.1 Continuous wave CW

The average and peak power output is the same continuously. CW is discussed in Chapters 4, 6 and 7, and in more detail in Chapter 5.

3.3.1.5.2 Pulse wave PW

The laser power is modulated by a square wave with a duty cycle of 50%; the average power is almost half of the continuous power. However, the maximum (peak) power value is equal to the continuous power, and for the remaining time, the minimum power is 2% of the power. PW is discussed in Chapters 6 and 7.

3.3.1.5.3 Partial power wave PPW

The average power is half that of the CW. Moreover, the peak power is 75% of the continuous power, and for the remaining time, the power is 25% of the continuous power. Figure 3.8 shows a schematic of the power wave modes. PPW is discussed in Chapters 6 and 7.

3.3.1.5.4 Double power pulse wave DPPW

The average power is equal to that of the CW. Moreover, the peak power is double the continuous power or 200% of the continuous power and the bottom peak time is 2% of the continuous power. DPPW is discussed in Chapter 4.

3.3.1.5.5 Partial double power pulse wave PDPPW

The average power is equal to that of the CW. Moreover, the peak power is one and a half times the continuous power or 150% of the continuous power and the bottom peak time is

50% of the continuous power. Figure 3.8 shows a schematic of the five power wave modes. PDPPW is discussed in Chapter 4.

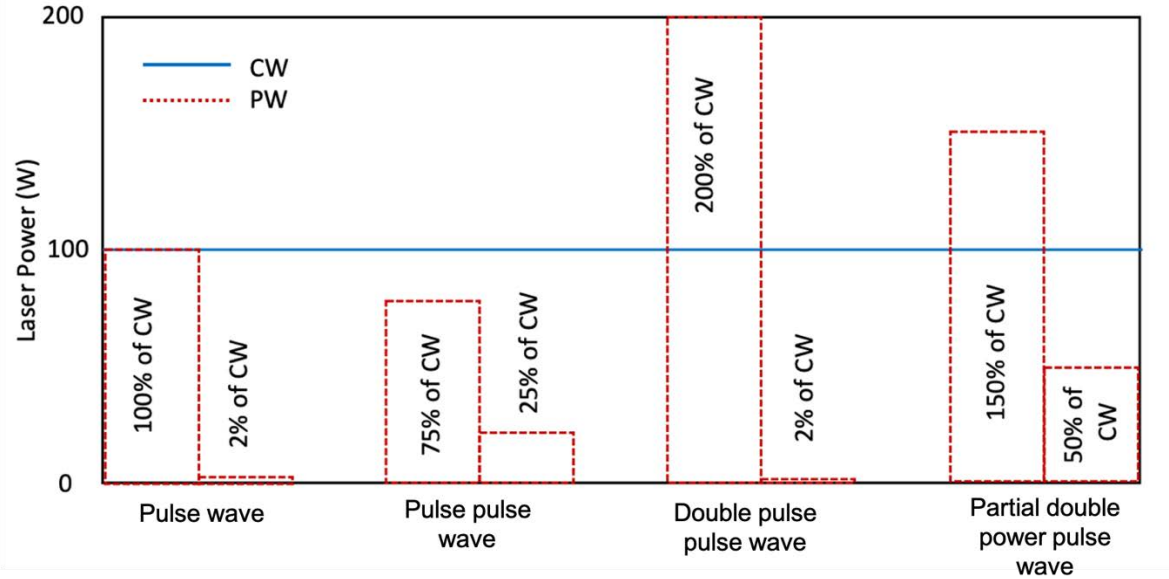

Figure 3.8: The different types of power profile in every mode used

The pulse shapes can be adjusted by controlling the pulse duration, which can be extended allowing improved control over laser processing. Research has proved that alternative pulse shapes reduce spatter, porosity and hot cracking, and improve surface finish [174, 175].

Single wall samples were built using DLD processes. Three different power modes were used, CW, PW and PPW with a 50:50 cycle period (T), as shown in Figure 3.9. Then the lengths of the pulse (T_L) were manipulated to 75:25 and 25:75, as shown in Figure 3.10. In addition, three different conditions were considered: build, solution annealing and ageing.

The pulsing used in this experiment was a square wave, in which the amplitude alternates at a steady frequency between the fixed maximum and fixed minimum value. The duty cycle, which is the ratio of the time at maximum power (high period) to the total period of a pulse wave, was manipulated to 25%, 50% and 75% for PW and PPW.

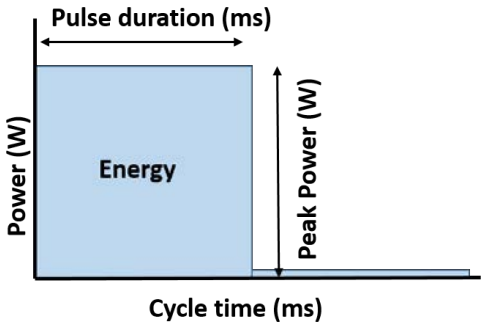

Figure 3.9: Cycle time of pulse wave

In standard pulsing (SP) the pulse duration *t* (ms) is divided equally between maximum and minimum power values. The pulsing duty cycle time was manipulated such that 75% of the time was at peak power and the remaining time was almost off, which is called the pulse wave – low cooling cycle (PW – LCC). In contrast, in the pulse wave – high cooling cycle (PW – HCC), 25% of the time was at peak power and the remaining time almost off. The same approach was taken with the PPW mode. Figure 3.10 illustrates the types of pulse shapes used in this work discussed in Chapter 6.

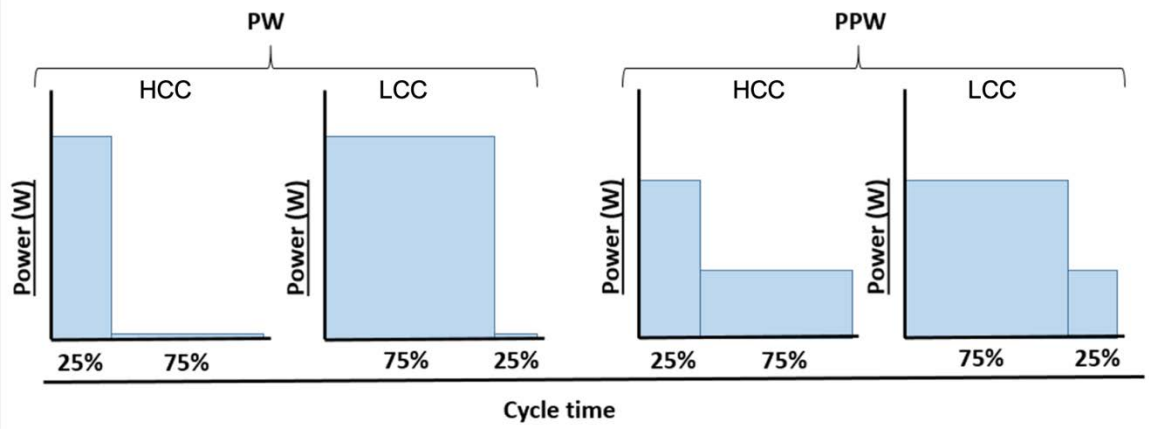

Figure 3.10: Schematic of the pulse cycle with different pulse durations

3.3.2 Experimental set-up

The upside-down T-shape substrate was fixed into position and four thermocouples were inserted. Two thermal camaras were used. The nozzle was placed 10 mm above one end of the substrate and this point was set to be (0,0) on the gantry. A G-code was written to move

the nozzle in the x direction 30 mm back and forth 40 times, with the nozzle moving 0.5 mm in the z direction each time.

3.3.3 Specimen manufacturing details of single wall and single track

Each wall was built by depositing 40 layers with a length of 30 mm along the x direction. The thin walls were produced at a very low oxygen level due to the argon delivered by the laser head in the carrier gas that was flowing from the nozzle. The argon also protected the lens from particles rebounding from the build this is discussed in Chapters 5, 6 and 7. Moreover, multiple single tracks were performed with different parameters to measure the capture rate and depth of penetration; this is discussed in Chapter 4.

3.3.4 Thermal camera and thermocouple measurements

Two thermal infrared cameras from thermo-IMAGER TIM were used. These were positioned in front of the substrate during the deposition. The first camera could measure heat from 150 °C to 900 °C and the second camera could measure heat from 900 °C to 2000 °C. The thermocouple results were used to calibrate the camera results and to adjust the emissivity on the cameras. Three thermocouples (K-type) were located 1 mm beneath the surface substrate. The thermal cameras and thermocouples were utilised for the results discussed in Chapters 5, 6 and 7.

3.3.5 Post processing: sample removal and preparation

The samples were cut from the substrate using an electric discharge machining (EDM) along the build direction. They were then mounted, ground and polished to a 0.05 µm oxide suspension finish (details in Table 3.3). Additionally, the EDM was employed to cut the tensile samples.

Table 3.3:Grinding and polishing procedure used to characterise samples

#	DISC	TIME (MIN)	FORCE (N)	(RPM)	SOLUTION
1	Piano 120	2	15	200	Water
2	Piano 1200	13	20	300	Water
3	Largo	5	35	150	DiaPro
4	MD-Dac	15	50	150	DiaDuo

5	MD-Chem	10	30	Rev 150	OPS

3.3.6 Post processing: heat treatment

The samples were exposed to two kinds of post-heat treatments. In the annealing process, samples were subjected to an increase in temperature to 980 °C for 1 hr then air cooled to room temperature. The second heat treatment was ageing, in which samples were heated up to 720 °C for 8 hr, furnace cooled to 625 °C, then aged a second time at 625 °C for 8 hr, followed by furnace cooling. Figure 3.11 shows the results from the thermocouple inserted next to the samples.

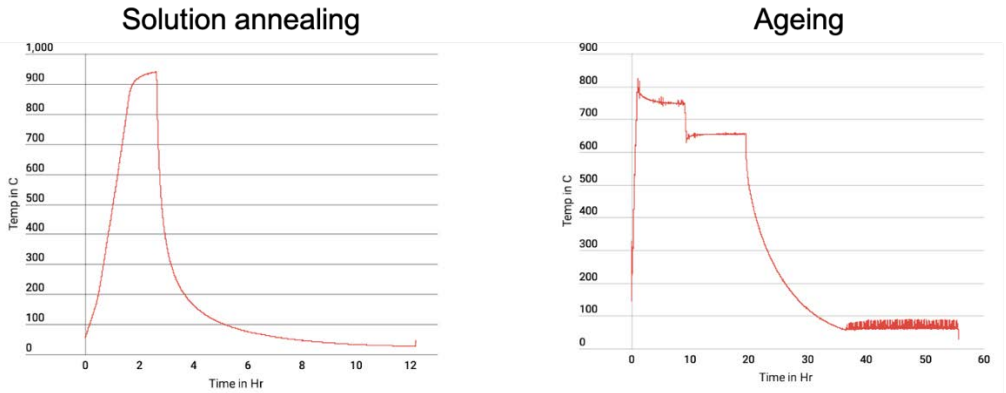

Figure 3.11: Thermocouple readings for post-heat treatment cycles

3.4 Characterisation

3.4.1 Porosity measurements

The porosity analyses were carried out by imaging analysis, for which nine images were taken for every sample. These were analysed with image J (image processing software). For porosity measurements, the image was thresholded to produce a binary image isolating the relevant features.

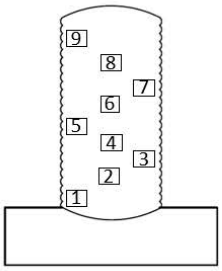

Figure 3.12: The locations of the nine images were taken for every sample.

3.4.2 Scanning electron microscopy

A Hitachi TM3000 scanning electron microscope (SEM) equipped with back scattered electron detector (BSE) and Energy Dispersive X-Ray Analysis (EDX) was used. Also, a Philips XL30 SEM equipped with electron backscattered diffraction (EBSD) were used to examine the microstructure. Image J software was used to perform stereological analysis of optical micrographs on one polished surface in order to quantify the porosity area fraction.

3.4.3 Electron backscattered diffraction

With a step size of 5 μm, EBSD was performed at 20 kV on a Philips XL30 SEM system through an integrated Oxford/HKL EBSD detector. The surface layer of the specimens for the EBSD test was mirror polished to remove any scratches and plastic deformation. The EBSD data was analysed with Oxford Instruments HKL Channel 5 software (HKL Technology, Inc., Connecticut, CA, USA).

3.4.4 Etching

To reveal the solidification microstructure (dendrites and intermetallic phase, etc.), samples were etched by submersion for 5–10 seconds in waterless Kalling's reagent (5 g CuCl2 + 100 ml HCl + 100 ml ethanol), then rinsed with ethanol and dried. To reveal the precipitates and grain boundaries, samples were electrolytically etched in a 10% (by volume) solution of phosphoric acid (H_3PO_4) in H_2O using an EX2020R power supply from Thurlby Thandar Instruments Ltd (TTi)

3.4.5 Melt pool measurements

Spot sizes were measured after a set of single tracks was laid on a substrate and the width of the tracks was measured. Moreover, the weld pools were measured during the deposition of the walls using a CCTV camera placed vertically on the weld pool and were utilised in the study described in Chapter 6.

3.4.6 Grain size measurements

The average grain size was determined using line intercept methods. Nine images were taken from every sample, from bottom to top. From every image, three horizontal lines and three vertical lines were taken to average out the grain width and length to verify the columnarity of the grain using equation 3.2 to find the average grain size.

$$Average\ Grain\ Size = {Line\ Length}/{Number\ of\ Grains} \qquad \textit{Equation 3.2}$$

3.4.7 Columnarity measurements

DLD is dominant generally by a columnar (elongated) microstructure. The columnar grain is quantified by two geometrical features that are length (l) and width (w) of the grains. The term columnarity is the longitudinal access of a grain. This was measured using images from SEM and then analyze them with imageJ software using the average grain size equation 3.2

3.4.8 Aspect ratio

The aspect ratio of a gain is the ratio of its width to its length this is measured using SEM images and analyze them with imageJ software using the average grain size equation 3.2

3.4.9 Grain's geometry

Is another term of the grain morphology or form and structure of a crystal or grain shape. This was observed visually and measured using images from SEM and then analyze them with imageJ software using the average grain size equation 3.2 if the aspect ratio is more than one then the grain is columnar and if that apply on the whole microstructure then it is columnar microstructure.

3.4.10 X-ray diffraction

To characterise the crystal structure and for a rapid assessment of the crystallographic anisotropy, X-ray diffraction (XRD) was performed using a Bruker D2 Advance Diffractometer (Karlsruhe, Germany) with Cu Kα radiation (wavelength, λ = 0.15418 nm), at 40 kV and 40 mA in a 2θ range of 30°–90° using a step size of 0.02° with a Co-tube (Kα radiation, λ=1.79 Ångström). Figure 3.12 shows the XRD used in this research.

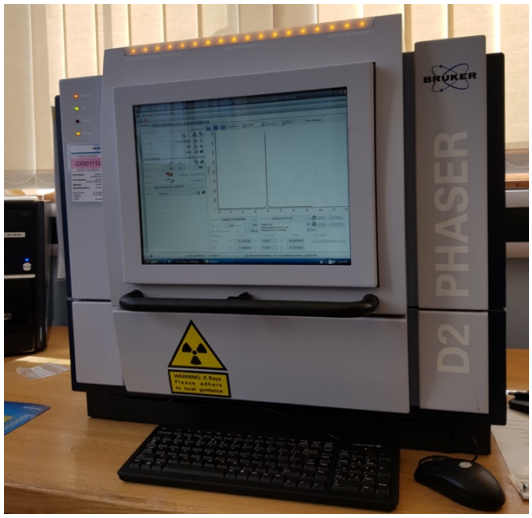

Figure 3.13: D2 Phaser, Bruker Advance Diffractometer

3.4.11 Hardness measurements

The microhardness was measured using a microindenter (Buehler Wilson VH1202), with a load of 500 g and dwell time of 10 s; 10 indentations were carried from bottom to top of the sample analysed. Finally, the average value for each region analysed was determined. All hardness indentations were made on polished horizontal surfaces (parallel to the build plate), and an average value and standard deviation were calculated based on 10 measurements.

3.4.12 Room temperature tensile testing

Multiple single walls were built with a length of 90 mm and a height of 20 mm. These walls then were cut with the EDM in the yz direction to specific tensile test coupon. Then the test coupons were sanded with sandpaper to reduce roughness. The test was performed using a Zwick Roell 1484 universal testing machine, using an extensometer with a gauge length of

20 mm. All the specimens were simultaneously polished by a grinding machine to ensure identical surface quality. Figure 3.13 shows the tensile specimen cut orientation from the wall specimens.

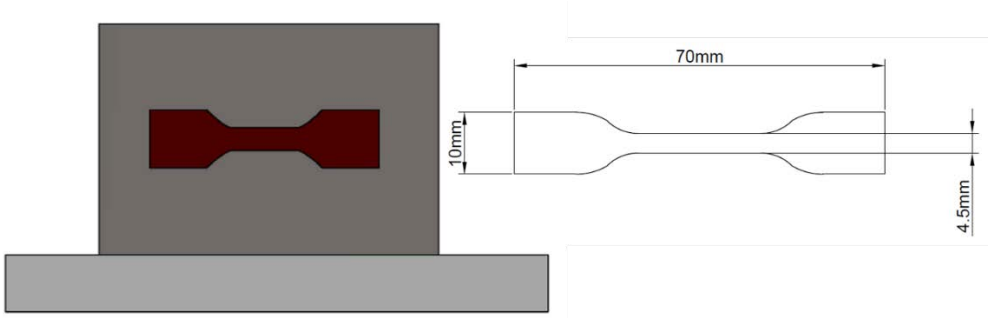

Figure 3.14: Schematic drawing showing the tensile specimen cut orientation from the walls on IN718 and CM247LC

3.4.13 Reciprocating wear test

The wear tests were conducted at room temperature. Al_2O_3 was used as the counter-body material, with a ball diameter of 10 mm and a Vickers hardness value of 1600HV. Under a dry surface, Al_2O_3 balls were used to slide over continuous power waving samples in a reciprocating motion. The load was 20 N, the sliding speed was 10 mm/s, the sliding distance was 5 mm, and the time duration was 30 min. Reciprocating wear tests are discussed in Chapter 4.

Chapter 4. Influence of Direct Laser Deposition Parameters on Geometrical and Microstructural Development

Abdullah Alhuzaim[a, b], Stano Imbrogno[a], Moataz M. Attallah[a]

[a] School of Metallurgy and Material Sciences, University of Birmingham, Edgbaston, Birmingham, B15 2TT, United Kingdom.

[b] Mechanical Engineering Department, Jubail University College, Jubail Industrial City, Kingdom of Saudi Arabia.

4.1 Abstract

The effects of different direct laser deposition laser power modes, continuous wave (CW), double power pulse wave (DPPW) and partial double power pulse wave (PDPPW), have been investigated by measuring the powder capture rate and depth of penetration on single tracks. Additionally, the effects of scanning speed, powder injection rate, carrier gas pressure and z-increment on the geometry of single walls have been examined. A reciprocating wear test was also conducted. Microstructure analysis was performed using scanning electron microscopy and image analysis software. The results indicate that the scanning speed has a clear effect on the capture rate: the capture rate increased with increasing scanning speed. Furthermore, it was found that PDPPW gave rise to the deepest penetration, followed by DPPW and then CW. Scanning speed also plays a big role in depth of penetration, as a low scanning speed gave rise to deeper penetration than a high scanning speed. Moreover, decreasing the powder feed rate decreased the height of the wall, and the height of the wall increased with increasing powder flow rate. Furthermore, the columnarity of the grains increased when the z-increment decreased. Finally, the friction coefficient of the sample produced by the CW laser power mode

in the as-built condition was higher than in the annealed condition and was lowest in the aged condition.

Keywords: Inconel 718, parametric study, power pulsing

4.2 Introduction

To achieve enhanced mechanical properties within direct laser deposition (DLD) processed parts, it is essential to understand and characterise how DLD process parameters (e.g., laser power, scanning speed, powder feed rate, layer thickness, etc.) affect the produced parts.

DLD process performance is extremely sensitive to powder flow rate because the quantity of powder injected into the molten pool and absorbed the energy of the laser will affect the volume of material available to make the product, geometry of the pathway and consistency of deposition. Typical powder flow is controlled by changing the mass powder feed rate and/or standoff distance, nozzle escape rate and shielding gas velocity [14, 133, 176]. On the other hand, the capture rate refers to the amount of powder melted into the welding pool and that becomes part of the build. Experiments show the increase in scanning speed increases the capture rate. The capture rate has a direct effect on the build height, width and layer thickness of a product. Slower scanning results in greater powder flow, which results in high losses that decrease the capture rate, whereas a scanning speed that is too high results in an insufficient amount of powder in the molten pool. The deposition head provides laser light, powder and protective gas. The powder, which is carried by the inert gas through three radially symmetric nozzles at 30° to the vertical axis, is injected into the molten pool created by the laser beam. The powder feed rate ranges from 0.3 to 50 g/min, and is governed by the rotational speed of the powder feeder rotating discs in the powder hopper feeding system [177].

Several attempts have been made to identify powder flow in different nozzles, including both coaxial nozzles and multi-nozzles [177-181]. Christopher et al. [182] used a quadruple nozzle

deposition head for the DLD process, and their results showed that the highest powder concentration was at 11.1 mm stand-off distance from the substrate to the powder nozzle. Wu et al. [183] claimed that reducing the z-increment was beneficial for obtaining a dense build and reducing porosity, while increasing the z-increment was good for suppressing cracking. Kuo and Jeng [184] mapped the depth of penetration for samples created using a Nd-YAG laser wave, and the width of the weld pool ratio resulting from the continuous wave (CW) and pulse wave (PW) laser power modes, and also scanning speed. The results show that, in general, pulsing wave power modes give rise to deeper penetration than CW power modes. In many engineering applications, wear is a life-limiting factor for various safety critical components. Inconel 718 has unsatisfactory wear characteristics. Thus, it is desirable to improve the wear resistance of Inconel 718 without adversely affecting its corrosion resistance [185-187]. Karabulut et al. [188] claimed that an Inconel 718 specimen fabricated by additive manufacturing can have much higher wear resistance than conventionally produced Inconel 718 if it is heat-treated at a certain temperature.

The aim of this study is to:

- To understand the DLD parameters such as laser power, scanning speed and powder feed.
- To investigate the effects of different modes of laser power on the depth of penetration.
- To examine the scanning speed effect on powder capture rate
- To study the influence of laser power modes on capture rate.
- To measure effect of powder feed rate and gas purging pressure on build geometry.
- To understand the z-increment effect on microstructural.

4.2.1 Methodology

In this chapter, three power modes were used and 15 single tracks were deposited to allow investigation of capture rate and depth of penetration. Additionally, seven walls were built using a fixed continuous power of 2000 W, a fixed scanning speed of 275 mm/min and fixed carrier gas at 10 cfh. The powder feed rate was varied from 4 to 10 rev/min (see Table 4.1).

All tracks and walls were produced using a Trumpf TrueDisk 4002 equipped with a three-beam nozzle able to move in cartesian space (x, y and z axes) and a 4-kW diode laser. During deposition, the laser beam was focused to a spot size of 1.4 mm and the standoff distance was set to 10 mm. The laser source was varied between CW, double power pulse wave (DPPW) and partial double power pulse wave (PDPPW) modes, while the laser power was varied from 1000W to 1250 W. The three-beam nozzle provided a constant powder flow rate of 28 g/min. The powder was carried through the system by the argon flow that guaranteed a protective environment during the interaction between the laser and the powder within the melt pool. Three scanning speed parameters were used: 50, 250 and 500 mm/min. Fifteen single tracks were built with a length of 30 mm and a layer thickness of about 0.5 mm.

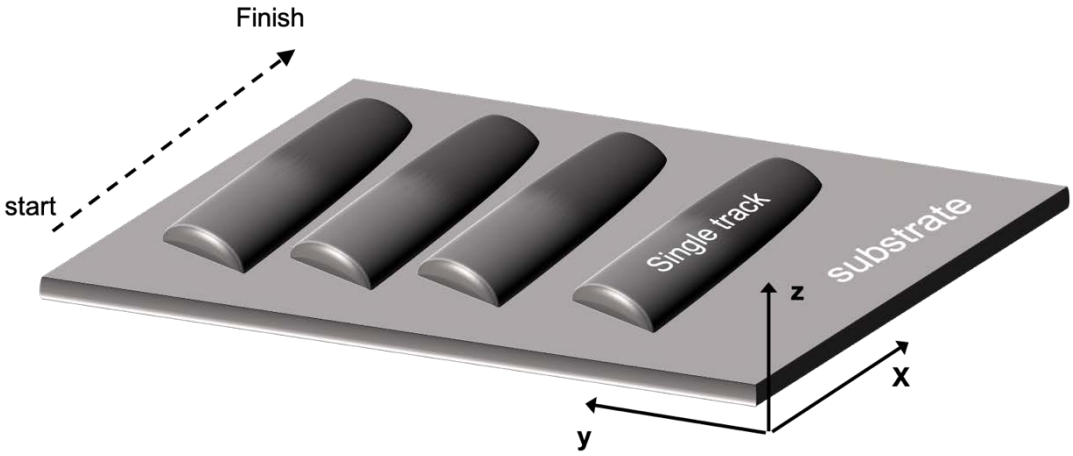

Figure 4.1: Schematic illustration of the single tracks on the substrate

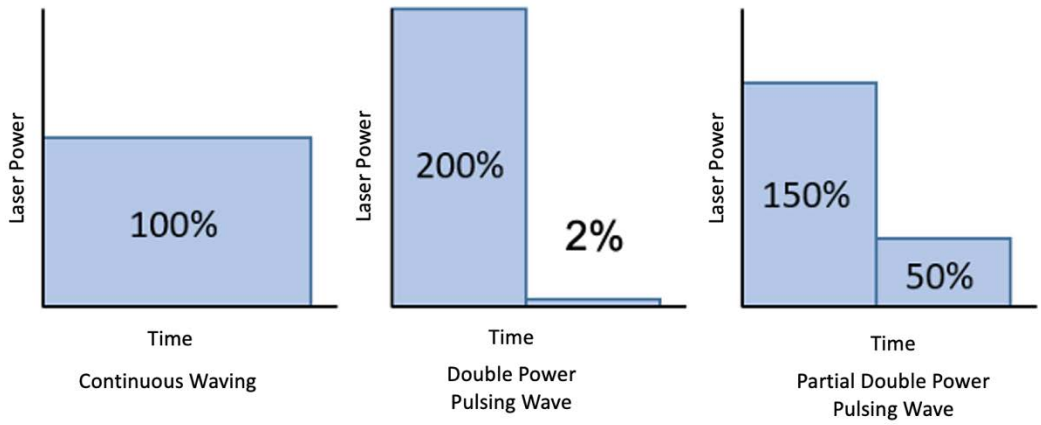

Figure 4.2: The different types of power modes

4.3 Post-deposition heat-treatments

The samples produced by DLD were exposed to two kinds of post-heat treatments. In annealing the samples were kept in a furnace for one hour with the temperature set to 980 °C and subsequently air-cooled to room temperature. The second heat treatment was ageing, in which the samples were kept at 720 °C for eight hours, furnace cooled to 625 °C, then aged again at 625 °C for another eight hours, then furnace cooled.

4.3.1 Single track samples

Fifteen single tracks divided into six groups were produced using different parameters to determine the effect on the capture rate and depth of penetration. The first three groups each consisted of three single tracks, produced with the three different power modes (CW, DPPW and PDPPW) see Figure 4.4. The power was fixed at 1000 W in the first three groups and the scanning speed was varied. The first group of three tracks was produced with a scanning speed of 50 mm/min, the second group used a scanning speed of 250 mm/min and the third group used a scanning speed of 500 mm/min. Groups 4–6 consisted of only two tracks, each made with different power modes (CW and PDPPW). Again, each group had a different scanning speed: 50, 250 and 500 mm/min.

The energy input of the energy beam determines the thermal history, therefore, influences the microstructure and mechanical properties. To calculate the energy density in the linear form [189, 190]

$$Energy\ density\ = \frac{P}{v} \qquad \textit{Equation 4.1}$$

Where P is power in (W) and v is scanning speed in (mm/sec). If the hatch spacing (H) or beam diameter (D) is added to the equation, the equation will become areal energy density Equation 4.2 [191, 192] and Equation 4.3 [193, 194]

$$Energy\ density\ = \frac{P}{vH} \qquad \textit{Equation 4.2}$$

$$Energy\ density\ = \frac{P}{vD} \qquad \textit{Equation 4.3}$$

If the layer thickness (t) added to the areal equations, the equation will become volumetric energy density Equation 4.4 [191, 195] and Equation 4.5 [196]

$$Energy\ density\ = \frac{P}{vHt} \qquad \textit{Equation 4.4}$$

$$Energy\ density\ = \frac{P}{vHt} \qquad \textit{Equation 4.5}$$

Table 4.1: Process parameters used in this study

		Average Power	**Power**		**Scanning Speed**	**Linear Energy Density**
Single Track #		(W)	Low peak	High peak	(mm/min)	J/mm
ST1	Group 1	1000	Continuous		50	1200
ST2		1020	40	2000	50	1212
ST3		1000	500	1500	50	1200
ST4	Group 2	1000	Continuous		250	240
ST5		1020	40	2000	250	242.4
ST6		1000	500	1500	250	240
ST7	Group 3	1000	Continuous		500	120
ST8		1020	40	2000	500	120
ST9		1000	500	1500	500	120
ST10	Group	1250	Continuous		50	1500

ST11	4	1250	585	1755	50	1500
ST12	Group 5	1250	Continuous		250	300
ST13		1250	585	1755	250	300
ST14	Group 6	1250	Continuous		500	150
ST15		1250	585	1755	500	150

4.4 Results and discussion

The metal powder used was gas atomised IN718 and the morphology is shown in Figure 4.3. The powder was mainly spherical with excess satellite formation. Both coarse and fine particles with less spherical shapes were present while the surface texture was rough (Figure 4.3B). The particle size ranged from 53 to 180 µm and the chemical composition is illustrated in Table 4.2.

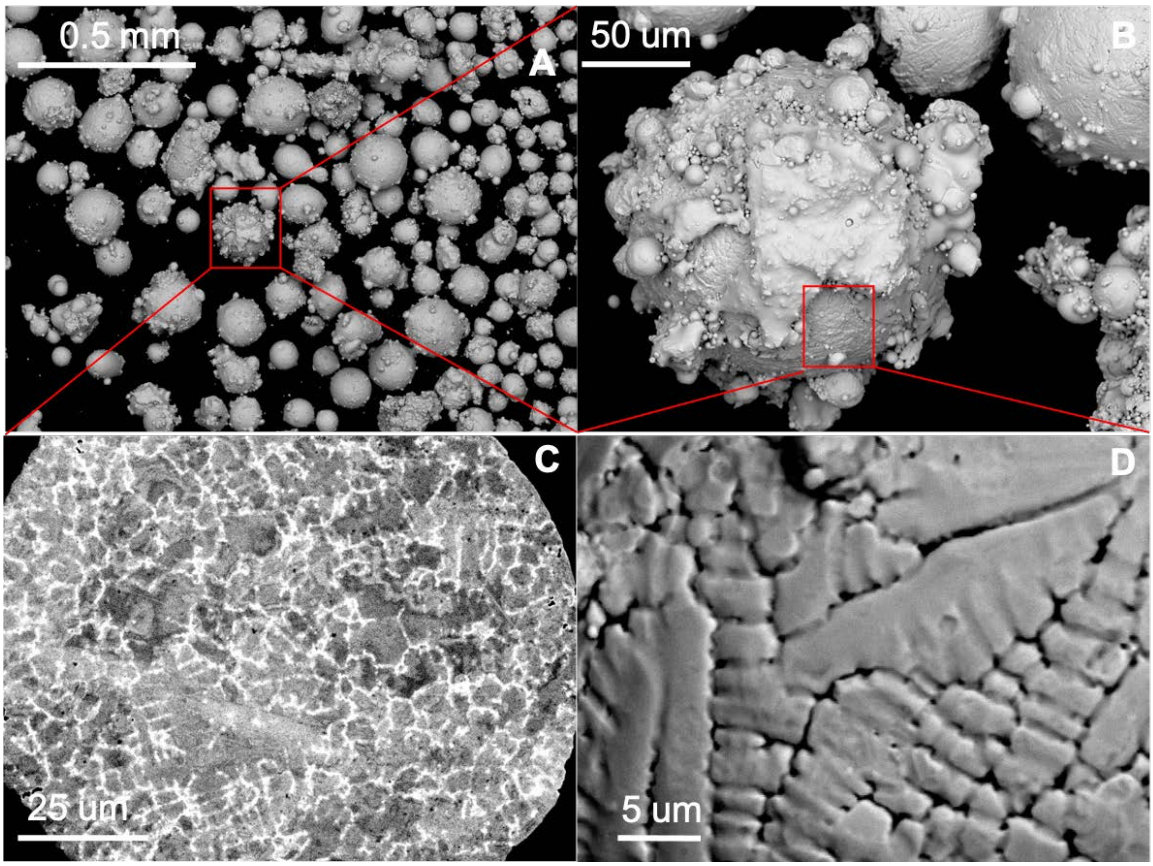

Figure 4.3: IN718 powder particles at four different magnifications in millimetre and micrometre (A)cumulation of IN718 Powder particles (B) a single powder particle with satellite formation (C) cross section view of a powder particle (D) surface view of a powder particle

Generally, the powder exhibits a surface that is visually free from secondary phases and contamination species. However, a few non-metallic inclusions, such as oxide, could be found on the satellites with a size of less than 1 μm. This is compatible with the findings of Gruber et al. [197].

Table 4.2: Powder chemical composition of IN718 (% weight)

Ni	Cr	Fe	Nb	Mo	Ti	Al	Si	N	O	C
54.45	18.18	18.19	4.88	2.90	0.91	0.42	0.03	0.01	0.01	0.01

4.4.1 Powder flow

The flow of powder particles in the hoppers is important in the DLD process. The flow created by the discharge of particles from the hopper is similar to the laminar flow of viscous liquids. Free flowing powders are commonly used because they are simple to handle and do not generally cause problems during the manufacturing process. The opposite is true for cohesive or poorly flowing powders which give rise to unpredictable behaviour [198]. The Hall flowmeter was used to determine the apparent density and flow of metallic powder mixes. 50 g of powder flows through a funnel and the time it takes is registered as the flow rate. The Hall funnel is also widely used for determination of apparent density and flow of metallic powder mixes. Table 4.3 list the three attempt of powder flow on the funnel, the time consumed and the average.

Table 4.3: Calculation of Hall flow rate of IN718 powder

	ATTEMPT	ATTEMPT	ATTEMPT	AVG	HALL FLOW RATE
	1	2	3		(s/50g)
MASS	50.07	50.00	49.99	50.02	0.33
TIME	16.81	16.65	16.69	16.72	

The tapped density is the maximum density achieved when metal powder is vibrated or tapped under specific conditions. The international standard MPIF-46 test method, ASTM B-527 or

ISO 3953 can be used. The tapped density of a powder is the ratio of the powder's mass to the volume occupied by the powder after it has been tapped for a certain amount of time. A powder's random dense packing is represented by its tapped density. Equation 4.6 may be used to find the tapped density.

$$Tapped\ density\ \left(\frac{g}{mL}\right) = \frac{M}{V_f} \qquad \textit{Equation 4.6}$$

$$Carr's\ index = 100\ X\ \left(1 - \frac{\rho_b}{\rho_t}\right) \qquad \textit{Equation 4.7}$$

$$Hausner\ ratio = \frac{\rho_t}{\rho_b} \qquad \textit{Equation 4.8}$$

where M = mass in grams, and V_f = the tapped volume in millilitres. Bulk density was determined using the graduated cylinder method (known mass, 100 mL cup). The tapped density was determined using a tap densitometer. The specific volumes were computed by multiplying the mass by the densities. Equations 4.7 and 4.8 were used to calculate the Carr's index and the Hausner ratio, respectively, where ρ_b is the bulk density and ρ_t is the tapped density of each material. Table 4.4 list the powder with and without tap and the parent and tapped densities.

Table 4.4: Calculation of tapped density and Hausner percentage

	Weight (g)	Volume cm³	Parent Density g/cm³	Tapped Density g/cm³	Hausner %
Cup	138.58	25			
Powder without tap	106.62	25	4.2648		
Powder with tap	121.035	25		4.8414	
					1.1352

Hausner ratios can be used to estimate the flow characteristics of a powder. The Hausner percentage is calculated to be 1.1352%, which is considered to be “good flowability”, and the Carr compressibility index was found to be between 11% and 15% per centimetre, as shown in Table 4.5

Table 4.5: Carr Evaluating flow properties of solids. [199]

Compressibility index (%)	Flow character	Hausner ratio
01-10	Excellent	1.00-1.11
11-15	Good	1.12-1.18
16-20	Fair	1.19-1.25
21-25	Passable	1.26-1.34
26-31	Poor	1.35-1.45
32-37	Very poor	1.46-1.59
> 38	Very, very poor	> 1.60

The powder was also characterised using the shear ring test, which showed that the powder had good flowability. In this research, the powder feed rate used was up to 32 g/min whereas the free flow can only reach up to 19.8 g/min according to the Hall flow rate; this demonstrates the excellent flowability of the powder feed. The increase in the powder feed rate from 19.8 to 32 g/min is due to the argon carrier gas pressure.

4.4.2 Powder size analysis

This analysis allows the determination of the distribution of particles sizes in granular materials. Since many separation processes and reactions depend on the amount of surface area relative to mass and that ratio increases as particle size decreases, knowing the distribution of sizes can be very important.

The IN718 (MIDAS) powder was provided by Sandvik Osprey Powder Company. Particle sizes range from 53 µm - 180 µm as it stated on the container. A sieves analysis was made to a sample of 100g of the provided powder to understand and optimize the range of particle size and compare it with what the company stated. The process equipment consists of Stack of sieves ranging from 25µm– 140µm, The Ban and a led, Mechanical shaker, Digital balance

The results are presented in a graph is percent retained on each sieve and the accumulative percent retained. On the graph the sieve size scale is in (µm). To find the percent of total passing through each sieve, the following equation was used.

$$\%Retained = \frac{Wsieve}{W\ Total} X100 \qquad \textit{Equation 4.9}$$

Where W Sieve is the weight of powder on each sieve and W Total is the total weight of the powder. To find the cumulative percent of the powder retained in each sieve. The following equation was used.

$$\%\text{Cumulative Passing} = 100\% - \%\text{Cumulative Retained} \qquad \textit{Equation 4.10}$$

The graph illustrates the normal distribution of IN718 powder. A clear bell shape is shown between 125 um-25 um. The percentage of particle between 90 µm – 63 µm is almost 60% of the overall weight of the sample. The mass of powder retained on each sieve shows a slight increase in particle size up to 90 µm. This is also reflected on the cumulative curve which indicates that between 90 µm and 63 µm, the percentage of supplements shot up dramatically. Particle sizes range from 180 µm - 53 µm Microns as it stated on the manufacturing container is 98.73%. The percent of error of the experimental is 1.13%

Table 4.6: Powder particle size analysis of the IN718

sieve	Sieves Size	Mass of each sieve	mass of each sieve + retained powder	Mass of Powder retained on each sieve	Percent of Mass Retained on Each Sieve	Cumulative Percent Retained	Percent Finer
No.	um	G	8	g	R_n	$\sum R_n$	$100-\sum R_n$
1	140	263.58	277.49	13.91	13.91	13.91	86.09
2	125	262.53	270.61	8.08	8.08	21.99	78.01
3	106	251.89	265.35	13.46	13.46	35.45	64.55
4	90	248.61	263.85	15.24	15.24	50.68	49.32
5	71	256.02	285.47	29.45	29.45	80.13	19.87
6	63	234.86	248.5	13.64	13.64	93.77	6.23
7	53	252.44	257.4	4.96	4.96	98.73	1.27
8	25	252.01	252.15	0.14	0.14	98.87	1.13
9	pan	354.45	354.45	0	0.00		
			$\sum=W_p$	98.88			
	Mean	252.74	265.10	12.36	%Of error	1.13	
	stan	8.96	12.55	8.69			

Material that is finer than 100 um, dry sieving can be less accurate due to the mechanical energy required to make particles pass through an opening. Since the surface irregularity can hold the particles between the screen opening. Sieve analysis assumes that all particles will be round (spherical) or nearly so and will pass through the square openings when the particle diameter is less than the size of the square opening in the screen.

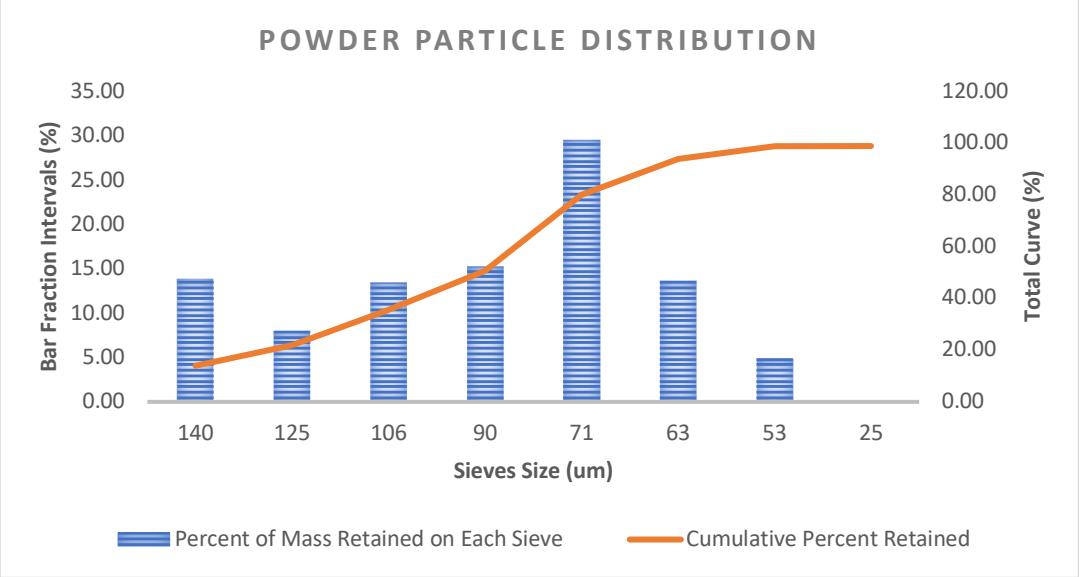

Figure 4.4:Powder particle distribution of the IN718

4.4.3 Capture rate

The powders used for DLD should have a particle size between 20 and 200 µm [177]. The best feeding properties are achieved with spherical particles, which are typical for atomised powders. The powder particles usually remain solid as a result of the very light contact between the laser and the powder particles until they meet the molten pool. Assuming the laser can provide sufficient energy, all particles that enter the pool are melted and then bonded; otherwise, the rest ricochet away and are lost.

The DLD system has 10 levels of powder feed and 10 levels of argon pressure that deliver the powder to the weld pool. The powder feed rate can be programmed in the G-code

in revolutions per minute, and the number of grams the nozzle can inject per minute was manually measured. The conversion is shown in Table 4.6.

Table 4.7: Approximate conversion of the powder feed rate from rev/min to g/min

Powder feed	rev/min	1	2	3	4	5	6	7	8	9	10
	g/min	5	8	11	15	18	21	25	28	30	32

The capture rate per minute in this experiment was measured by calculating the time taken to create a single track, then estimating the amount of powder injected by the nozzle in one minute, then measuring the weight of the track in grams and multiply the total weight of the track by 100 and divide it by the total power injected.

The capture rate due to the different power modes could not be predicted; the different modes did not have a clear effect on the capture rate, as the results were random. However, the scanning speed did have a clear effect on the capture rate. When the scanning speed was 50 mm/min the capture rate was around 0.2 g/min, and when scanning speed increased to 250 mm/min, the capture rate also increased to 0.6–0.8 g/min. Finally, when the scanning speed increased to 500 mm/min, the capture rate increased to an average of 1.4 g/min. To confirm these results, the same experiment was repeated but with the average power increased to 1250 W and the DPPW was eliminated because of the DLD limitation. The lower scanning speed led to a lower capture rate, as was seen in the first group. For group 5, the scanning speed was increased to 250 mm/min and the capture rate also increased to an average of 0.6 g/min. Finally, for the last group, with a scanning speed of 500 mm/min, the capture rate was 1.3 g/min. Figure 4.5 Effect of scanning speed on capture rate for all the six groups

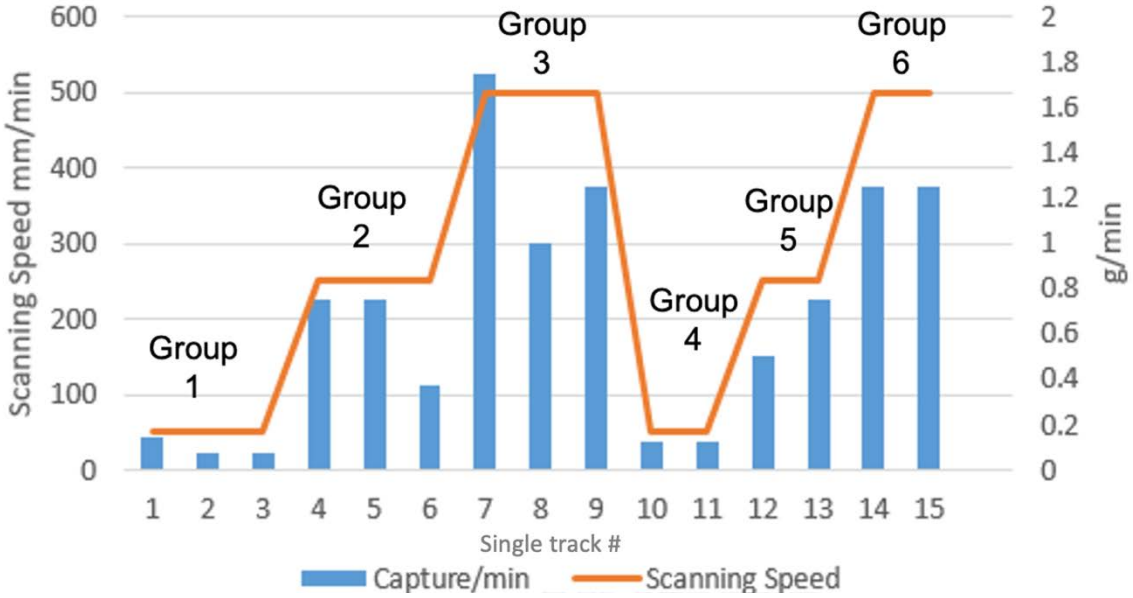

Figure 4.5: Effect of scanning speed on capture rate for three different scanning speeds and two different power values

The single tracks were produced with three different power modes (CW, DPPW and PDPPW) to measure the powder capture rate and determine how it was affected by scanning speed. The other parameters were kept constant with average laser power set to 1000 W. However, in the PDPPW mode, the peak power was set at 1500 W and the minimum power was set at 500 W, and for the DPPW mode, the peak power was 2000 W, and the minimum power was 20 W. The standoff distance was 10 mm from the tip of the nozzle.

The results show a very disappointing capture rate, with less than 1% of the powder captured when the scanning speed was 50 mm/min. It then increased for all power modes when the scanning speed increased to 250 mm/min, with a slight increase for the CW power mode and an increase for DPPW to 3% and to 1.5% for PDPPW. This variation may be due to the bigger diameter of the spot size with the continuous power. Moreover, when the scanning speed increased further to 500 mm/min, the capture rate increased to 7% for the CW power mode, 5% for the PDPPW and 4% for the DPPW mode. Figure 4.6 shows the capture rate percentage with scanning speed for the three different power modes.

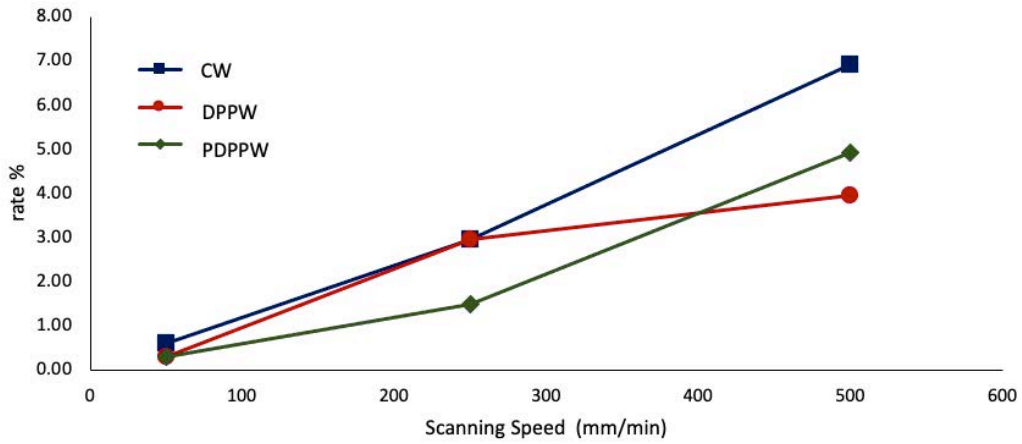

Figure 4.6: Capture rate percentage with scanning speed for three different power modes

4.5 Depth of penetration

The depth of penetration was measured for nine single tracks produced with three different scanning speeds (50, 250 and 500 mm/min) and three laser power modes (CW, DPPW and PDPPW), where the average power was fixed to 1000 W in all nine tracks. Figure 4.7 shows the weld pool with the HAZ and depth of penetration. The depth of penetration was greatest for the PDPPW sample produced with the low scanning speed. Less penetration was observed when the scanning speed increased to 250 mm/min and even shallower penetration was seen when the scanning speed was 500 mm/min. The same behaviour occurred with DPPW, which had a very similar penetration to that of the PDPPW product with the low scanning speed. However, it was clear that shallower depths of penetration appeared for scanning speeds of 250 and 500 mm/min. It is worth remembering that PDPPW and DPPW have an average power equal to the continuous power; however, the DPPW mode has a peak power of twice the CW power, and in the PDPPW mode the peak power is 1.5 times the CW power. Finally, the CW showed the lowest depth of penetration among all power modes. This can be explained by the high peak power of the PDPPW mode, which creates a drilling effect while the melt pool is still liquid. In contrast, in the DPPW mode, which has an even higher peak power than the PDPPW, the metal has time to cool down and partially solidify, which

makes it difficult to penetrate deep into the metal. Moreover, Vasquez et al. [200] showed that high powder feed rates decrease the depth of the melt pool, and Pinkerton and Li [201] showed that high powder feed rates will increase layer thickness. In general, the CW will penetrate up to two layers on average, whereas the DPPW and PDPPW will penetrate up to three layers, which could cause liquation cracking. The results also shows that the range of laser power used in this research is quite high.

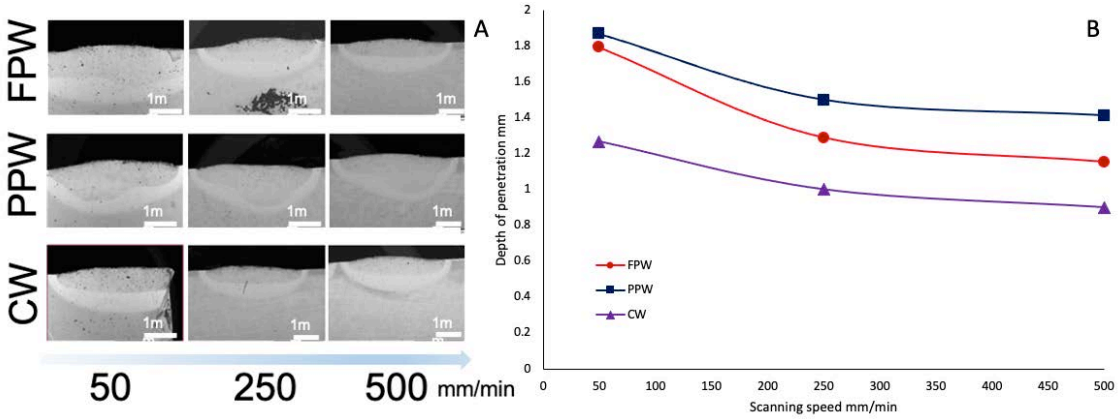

Figure 4.7: Scanning speed effect on depth of penetration for three different scanning speeds and three different power modes (A) the actual depth of penetration morphology for every power mode and scanning speed (B) the measured depth of penetration for every power mode and scanning speed

4.5.1 Layer thickness

The powder feed has a significant effect on the layer thickness and, therefore, the height of the wall. Liu and Dupont [202] proved a linear increase in the layer height as the powder feed rate increases. It was observed that the build height tends to increase with the increase in powder flow. It was also observed that the build width tends to act in the same manner as the build height, but the effect is less intense.

In this experiment, seven samples were manufacture with fixed continuous power of 2000 W and a fixed scanning speed of 275 mm/min and fixed carrier gas at 10 cfh. The powder feed rate was varied from 4 to 10 rev/min (see Table 4.6). The results show that when the powder feed rate was 15 g/min the height was 6 mm; when the powder feed rate increased to 18 g/min the height increased to 10 mm; when the powder feed rate was 21 g/min the height increased

to 14 mm; once the powder feed rate increased to 25 g/min the wall height increased to 16 mm; when the powder feed rate was 28 g/min the height increased to 20 mm; when the powder feed rate was 30 g/min the wall height increased to 20.1 mm; and finally, when the powder feed rate increased to 32 g/min the wall height remind at 20 mm. Moreover, the layer thickness increased every time the powder feed rate was increased until it got to the target height, then it stopped increasing. In contrast, the wall width did not change much; it was almost fixed at 6 mm in all walls. Figure 4.8 shows the powder feed rate effect on wall geometry.

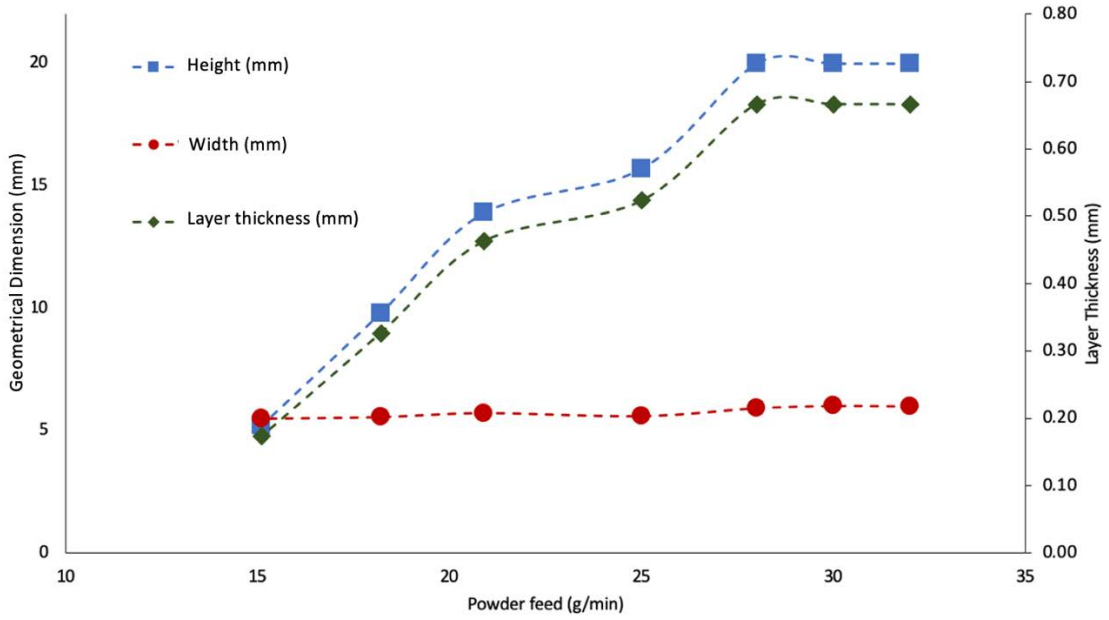

Figure 4.8: Powder feed rate effect on build geometry (height and width) and layer thickness at 275 mm/min and 2000 W

The carrier argon gas pressure had no significant effect on the width or the wall thickness and a slight effect on the height of the walls. Figure 4.9 shows the carrier gas flow rate effect on the build geometry. Naturally, this slight increase in wall height had a minor effect on the layer thickness.

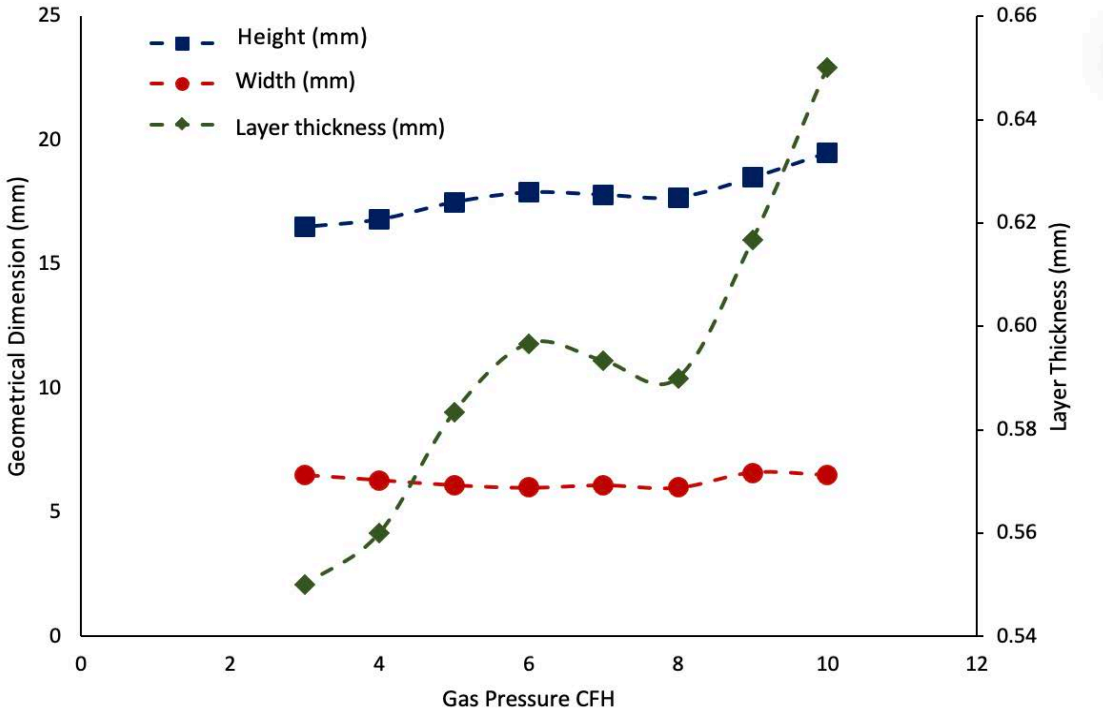

Figure 4.9: Carrier gas pressure effect on geometrical size at 2000W mm/min and 32g/min feed rate

4.6 Standoff distance

The laser beam movement leads to the solidification of the melt pool, and also to the forming of each track, which consists of a full density crack-less deposit with a full fusion bound to the substrate surface under the appropriate process parameter [203]. The standoff distance is a critical process variable; it is the distance between the nozzle and the material deposition point. An interesting study by Pinkerton and Li [133] showed three conditions of standoff distance within a 20-layer wall. The first condition had a fixed standoff distance and z-increment. In the second, each layer was measured, and the z-increment distance set according to the height of the layer. In the third, there was no standoff distance. In other words, the nozzle and the substrate distance were fixed for the entire duration of the build. The results showed the highest wall was the one built with no standoff distance, followed by a wall built with the variable distance and the shortest wall was the fixed standoff.

Powder standoff distance has a significant effect on the dimensional characteristics of the material deposit, as well as the straightness of the top surface and the penetration depth. The laser standoff distance primarily affects the laser spot size, which affects laser energy density. The laser spot radius is related to energy density [15], as shown in Equation 4.11 [107]

$$I = \frac{L_p}{W_o^2 * \pi} \qquad \textit{Equation 4.11}$$

where I is the energy density in watts per square millimeter, L_p is the laser power in watts and W_o is the laser spot radius in millimetres. From the equation, it can be concluded that reducing the standoff distance will increase the laser spot diameter. Additionally, will increase the time of production and length of processing since the number of layers will need to increase to achieve the same height. The normal layer thickness in the DLD used in this experiment is 0.5 mm and so is the z-increment. However, in this experiment the z-increment was set to 0.2, 0.3 and 0.4 mm to study the effect on the grain structure, as shown in Figure 4.10.

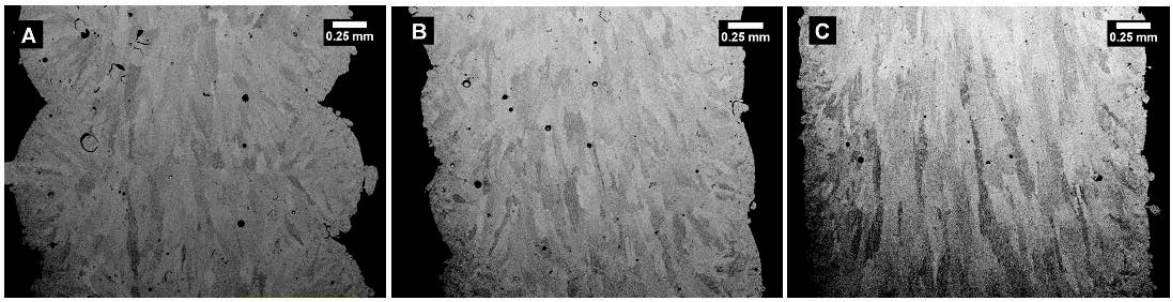

Figure 4.10: Effect of different z-increments on grain size and morphology for three different samples with fix parameter CW 300 W and 700 mm/min and three different z-increments of (A) the z-increment is 0.4 mm, (B) the z-increment is 0.3 mm and (C) the z-increment is 0.2 mm

The columnarity of the grains increased to about 260% when the z-increment decreased from 0.5 to 0.4 mm (26.4 µm increased to 69.3 µm) in the length of grain with the power set at 150 W, and to 507% when the z-increment decreased from 0.5 to 0.3 mm (26.4 µm increased to 134.5 µm). Moreover, it increased to 909% when the z-increment decreased from 0.5 to 0.2 mm (26.4 µm increased to 241 µm). Similarly, with the second sample, which used a power of 200 W, an increase of about 1120% in grain columnarity was seen when the z-increment

decreased from 0.5 to 0.4 mm (34.9 µm increased to 392 µm), a 1303% increase in grain columnarity was seen when the z-increment decreased from 0.5 to 0.3 mm (34.9 µm increased to 456 µm), and a 1416% increase in grain columnarity was seen when the z-increment decreased from 0.5 to 0.2 mm (34.9 µm increased to 495.5 µm). Again, for the third sample, which used 300 W, an increase of about 670% was seen in the grain columnarity when the z-increment decreased from 0.5 to 0.4 mm (80 µm increased to 536 µm), a 935% increase in grain columnarity was seen when the z-increment decreased from 0.5 to 0.3 mm (80 µm increased to 748 µm), and an 1190% increase in grain columnarity was seen when the z-increment decreased from 0.5 to 0.2 mm (80 µm increased to 952 µm). Figure 4.11 shows the increase in grain columnarity due to the change in z-increment.

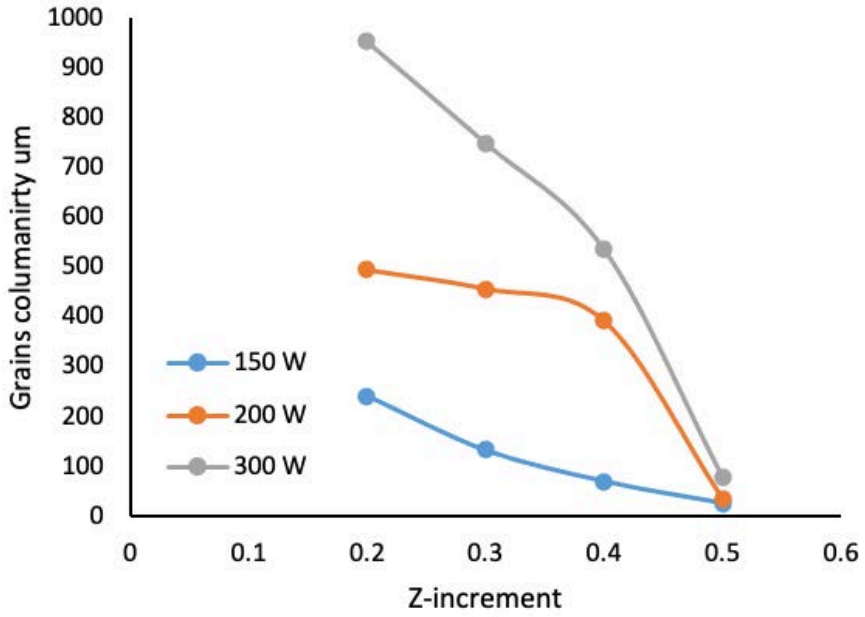

Figure 4.11: Z-increment effect on grain columnarity for three different power values

4.7 Reciprocating wear test

The wear properties of IN718 under three conditions (as-built, aged and annealed) were examined using a reciprocating wear machine with coefficient of friction measuring capabilities. The wear tests were carried out at room temperature. The counter-body material

used was Al_2O_3 with a ball diameter of 10 mm and Vickers hardness value of 1600HV. Al_2O_3 balls were used to slide over continuous power waving flat samples in a reciprocating motion under a dry surface. A load of 20 N, a sliding speed of 10 mm/s, a sliding distance of 5 mm and a time duration of 30 min were used. The worn surfaces were examined using scanning electron microscopy (SEM). Figure 4.12 shows three different samples under three different conditions (as-built, aged and annealed).

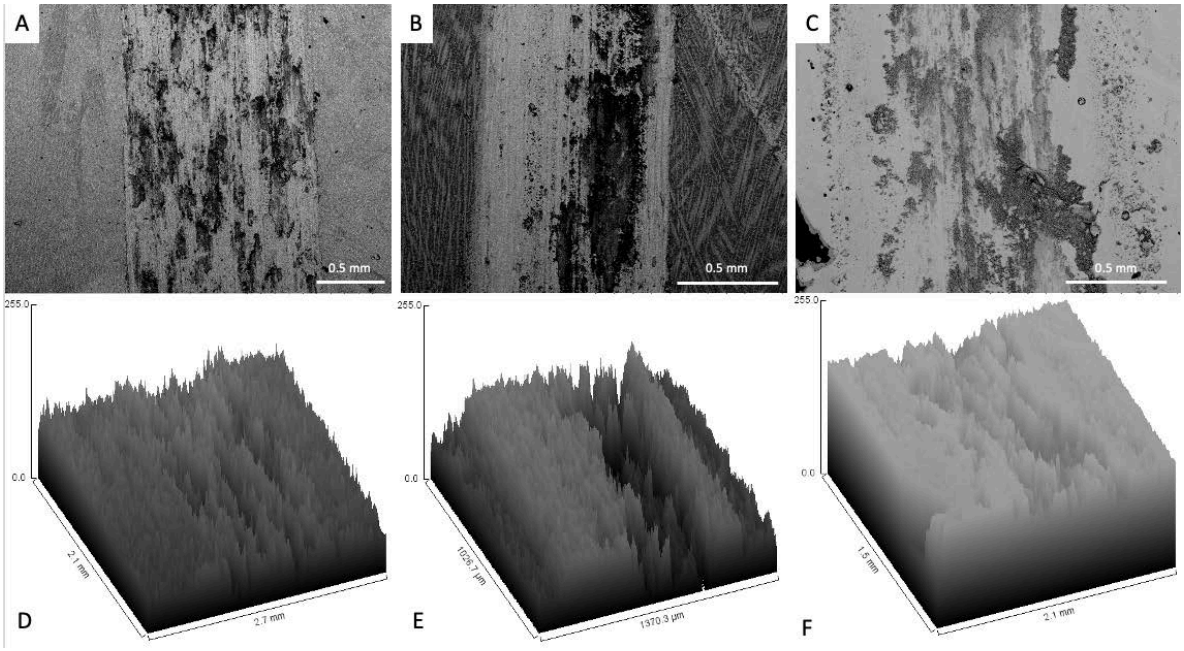

Figure 4.12: Reciprocating wear test for three different conditions (A) and (D) as-built, (B) and (E) aged and (C) and (F) annealed

Figure 4.13 shows how the coefficient of friction depends on the sliding time of the samples under the as-built, aged and annealed conditions. The friction coefficient of the as-built specimen was higher than for then that aged and annealed samples, with an average of 0.971. The friction coefficient of the aged sample was approximately 0.411, and the annealed sample friction coefficient was approximately 0.713. This indicates that heat treatment affects the coefficient of friction. The coefficient of friction of the aged condition is 58% smaller than that of the as-built specimen, and that of the annealed condition is 26% less than the coefficient of

friction of the as-built specimen. This is due to the large amount of Nb segregation in the as-built sample, which prevents the formation of γ'', which is the hardening phase of the IN718.

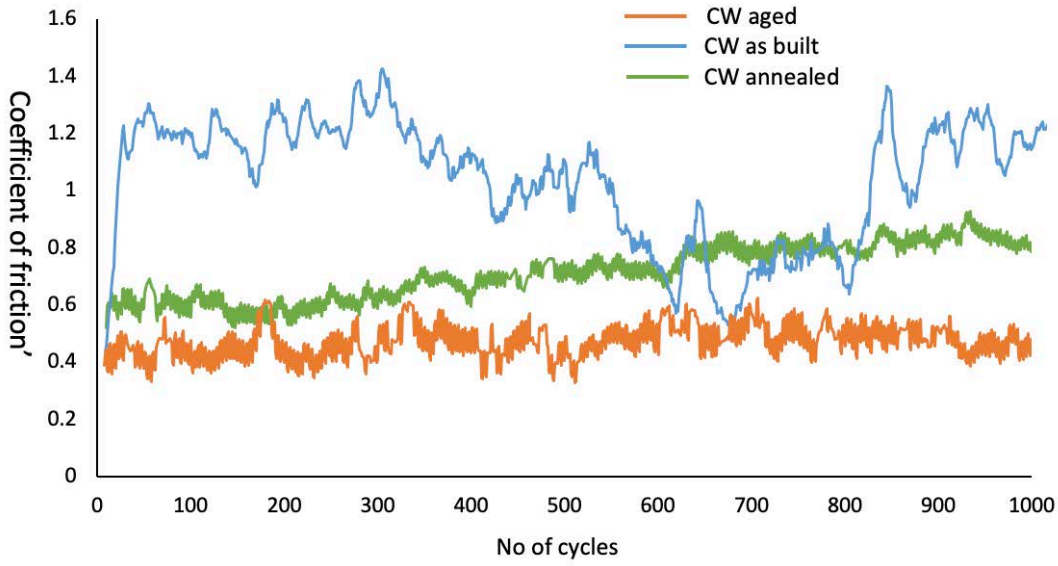

Figure 4.13: Variation of the coefficient of friction with sliding number of cycles for continuous power waving in three conditions: as-built, aged and annealed

4.8 Conclusion

An initial study has been performed to investigate the effect of several DLD parameters on the microstructural development of IN718. The most influential process parameters in DLD were found to be the laser power, scanning speed, powder feed rate and z-increment.

- Increasing the laser power has been shown to significantly affect depth of penetration and capture rate. The laser power modes enhance the depth of penetration by enforcing the drill effect. The PDPPW mode provided the deepest penetration, followed by the DPPW and finally the CW.
- Scanning speed plays a major role in the depth of penetration and the precision of the geometry of the build. A higher scanning speed increased the powder capture rate and, therefore, the layer thickness. If the speed was too high the capture rate decreased. The scanning speed had an inverse relationship with penetration depth.

- Increasing the powder feed rate has been shown to increase capture rate significantly and give more build height accurate geometry.
- Grains can be affected by the z-increment. Decreasing the z-increment increased energy density and time of exposure to heat input, therefore, the grains were larger and more columnar.
- Post-heat treatment can affect the hardness and the coefficient of friction of the samples. Samples with no post-heat treatment had higher coefficient of friction than for the samples that had post-heat processing. Moreover, the ageing process gave rise to a lower coefficient of friction than the annealing post-heat processing. That is because post heat treatment gave time to the Nb to dissolve back into the matrix and form the strengthening phase γ″ even though it might not be fully developed.

CRediT authorship contribution statement
Abdullah Alhuzaim: designed the study and performed the experimental tests and the analysis of the results. Writing – review and editing
Stano Imbrogno: Reviewing the paper.
Moataz Attallah: supervision, support on experimental feasibility and infrastructure.

Chapter 5. Controlling Microstructural and Mechanical Properties of Direct Laser Deposited Inconel 718 via Laser Power

Abdullah Alhuzaim[a, b], Stano Imbrogno[a], Moataz M. Attallah[a,*]

[a] School of Metallurgy and Material Sciences, University of Birmingham, Edgbaston, Birmingham B15 2TT, United Kingdom.

[b] Mechanical Engineering Department, Jubail University College, Jubail Industrial City, Kingdom of Saudi Arabia.

This paper has been published in Journal of Alloys and Compounds, 2021, volume 872

Abstract

The control of grain structure, texture and micro-segregation during additive manufacturing is important due to their impact on the mechanical properties. In this work, multiple single walls were deposited using Inconel 718 powder by the Direct Laser Deposition (DLD) process. The influence of a wide range of laser power (150W-1900W), as well as the thermal gradient, were characterised using electron microscopy and hardness testing. The heat input effect on the microstructural, dendritic morphology, and microhardness was also examined. The results illustrated that a higher thermal gradient due to lower heat input tends to form equiaxed grains and more Nb-segregation, whilst a higher heat input develops columnar grains with low Nb-segregation. The segregations within the interdendritic boundaries increased in size when the heat input was increased, whilst the contribution from precipitation strengthening was not significantly evident in the as-fabricated condition. A wall with two different powers was also

deposited to demonstrate the possibility of creating functionally graded structures through the control of laser power.

Keywords: Ni-Superalloys; Direct Laser Deposition; Microstructure; Segregation.

5.1 Introduction

DLD is a technique where components are built layer-by-layer by blowing powder through a nozzle and melting-with a focused laser beam. It has been used extensively within the aerospace and energy sectors, particularly in repairing turbine and steam engine blades. DLD is also recognised as a process with the ability to produce complex geometric components and with the flexibility to repair damaged or worn parts, with less powder consumption effects compared to laser powder bed fusion [56, 69]. It is considered one of the most rapid near net-shape techniques because of its large spot size, layer thickness and deposition rate. It is known that as-fabricated builds typically have poor mechanical properties compared to the post-deposition heat-treated parts. The focus of this study is to develop as-fabricated structures with best properties of IN718 can be produced, as a quick introduction to the market and the speed of delivering the part can be crucial in some fields.

Turbine blades can be manufactured in multiple ways. The traditional method is conventional casting which usually produces equiaxed crystal structures, providing isotropic mechanical properties, higher tensile strength and fatigue resistance. An alternative production technique is directional solidification which allows the production of large directionally solidified grains in the blade leading to good creep deformation resistance, improved oxidation resistance and enhanced mechanical properties along the solidification direction. In contrast, the fir tree root of the blade requires high tensile strength due to centrifugal loading and high/low cycle fatigue resistance, therefore the microstructure has to show different

characteristics compared with the blade body [204]. The scope of this study is on single-wall deposition due to its potential from a repair perspective, especially in the repair of turbine blade tips and seal segments. The study focused on the laser power impact on the microstructural development, due to the ease of modifying the laser power on the fly (as a single parameter), compared with changing the other parameters (e.g., powder flow rate, laser speed, etc…). Of a greater interest, the study assesses the possibility of matching the grain structure of the substrate or component being repaired through controlling a single parameter.

The Ni-based superalloy Inconel 718 (IN718) is widely used in aerospace applications due to its good formability, high corrosion resistance and excellent mechanical properties up to 650°C [44]. During DLD of IN718, rapid heating, melting, solidification and rapid cooling processes are involved, and these affect the liquid-solid interface during solidification through fast diffusion of the Nb [69]. The different thermal gradients and the growth rate control the morphology and solidification of the grains structure whilst the direction of the growth of the grains usually follows the heat source.

During the deposition process, the heat source is perpendicular to the molten pool towards the previous layer or the substrate since the lower ratio of the thermal gradient (G) and solidification rate (R) near the top surface of the molten pool results in equiaxed grains. Hence, columnar dendrites are observed to grow from the substrate perpendicular to the edge of the welding pool. The solidification velocity and the temperature gradient are responsible for forming columnar or a mixture of columnar and equiaxed dendrites towards the heat source direction [44, 204].

During solidification, several Nb atoms are constantly rejected and segregated into the liquid around the dendrites while the solid γ phase is forming from the liquid phase. After the γ phase formation, the low solubility of Nb results in its continuous ejection and accumulation at the liquid phase. As the solidification proceeds, the chemical composition of the liquid phase

will shift towards the eutectic point. Lastly, the liquid phase transforms into the γ phase and the segregated Nb from the interdendritic phase reaches the eutectic point by a eutectic reaction. [120].

During DLD, the solidification process is comparable with the one observed during welding. Therefore, the expected microstructure is dendritic and characterised by micro-segregation due to the thermal cycle and high cooling rate. Chen *et al.* [205] used DLD to produce single-track thin walls and they claimed that the Laves phase had the highest fraction in the middle of the sample due to high accumulation of heat and a low cooling rate. It had the lowest fraction at the bottom and the top of the sample due to a high cooling rate and less accumulated heat. Therefore, it is clear that the cooling rate can govern the segregation rate during solidification. Furthermore, they also claimed that there is an inverse correlation between the Nb concentration of the Laves phase and the cooling rate since the element diffusion would have insufficient time when the cooling rate increases [65]. However, the effect of different laser powers on the microstructure and mechanical properties was overlooked since they focused their study on liquation crack formation.

Parimi *et al.* [206] found that DLD high laser power generates columnar grains structures with <001> fibre texture along with the build directions and a mixture of fine equiaxed and coarser columnar grains in the low power samples. It was demonstrated that DLD is capable of tailoring the grain structure depending on the process parameters and the deposition strategy. Zhu *et al.* [207] also studied the influence of various parameters on the as-deposited Inconel 718 at different laser power and laser beam diameters. The columnar grains enlarged with increasing laser power and laser beam diameter. Ding *et al.* confirmed that the dendrite core microstructure can be linked to the cooling rate [208]. A high cooling rate showed a fine dendrite core, nearly continuous inter-dendritic regions, whilst a low cooling rate led to coarse dendritic regions and semi-continuous interdendritic regions. On the structural integrity

front, Zhong *et al.* [209] showed that porosity can be reduced by increasing the laser power [25].

The solidification regimes remain the key factor in controlling the microstructure. Raghavan *et al.* [61] showed that control of the crystallographic texture of the components can be achieved, to some extent, by governing the variations of (G) temperature gradient and (R) growth velocity at the liquid-solid interface of the melt pool. The results of the model indicated that by increasing the height of the wall, the rate of the heat removed by conduction by the substrate was decreased, thus leading to higher heat accumulation. This led to an increase in the grain size due to the increase in the height of the wall [210].

There are numerous current studies on DLD of IN718, but they appear to demonstrate the following gaps. Firstly, the majority of the studies focus on two extremes such as low and high power, with no experimental evidence on the microstructural variations between the upper and lower laser power limits. None of the studies explain the effect of the layer thicknesses on grain size and morphology. Moreover, limited studies explored the possibility of using different laser powers during DLD to explore the possibility of creating a functionally graded microstructure. In this study, the development in grains size, their morphology and texture were investigated in IN718 single wall builds. The effect of different laser powers on the microstructural characteristics and Nb segregation and, therefore, mechanical properties were analysed in detail.

The aim of this investigation is to demonstrate the utility of DLD parameters in tailoring the as-fabricated IN718 microstructure through controlling the solidification pathways. The solidified microstructure as demonstrated using the dendrite arm spacing (DAS) can be correlated with the solidification mechanisms and cooling rates. Finally, a strategy for parameter control and prediction of the microstructure and the mechanical properties of the fabricated IN718 superalloy by changing the laser power in the DLD process is also developed

and discussed. Figure 5.1 shows a schematic diagram which illustrates the effect of power on the microstructure and mechanical properties.

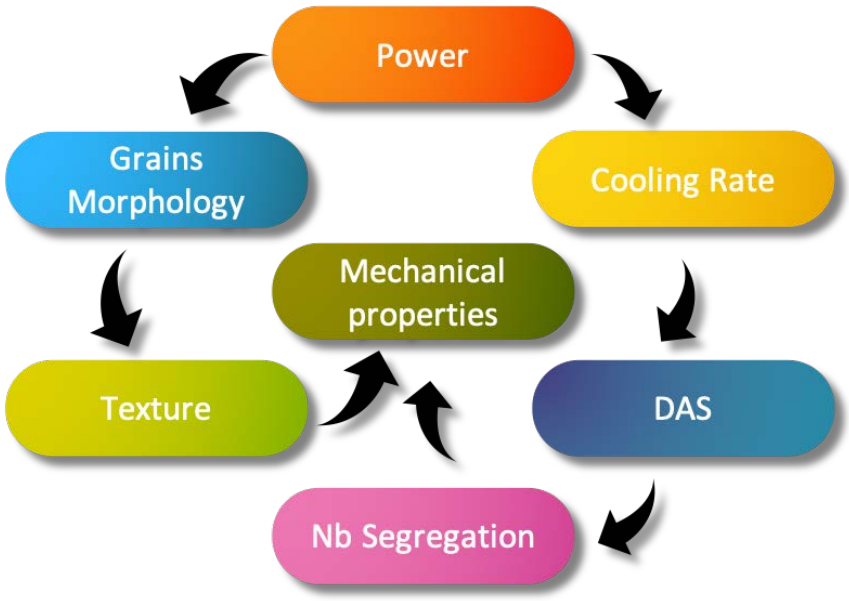

Figure 5.1: Schematic diagrams showing the effect of power on the microstructure and mechanical properties

5.2 Experimental Procedures

Thin walls were produced using the Trumpf TLC 1005 system equipped with a three-beam nozzle able to move on a cartesian space (x, y and z) and a 4-kW diode laser (Trumpf TrueDisk 4002) system. Gas atomised IN718 powder (supplied by Carpenter Additive) with limited satellite formation was used, as shown in Figure 5.2. The powder was sieved in the range from 53 to 180µm, as required by the DLD process due to its ease of flow through the nozzle. The chemical composition was analysed by AMG Superalloys UK Limited using Inductively Coupled Plasma (ICP). The chemical composition is shown in Table 5.1.

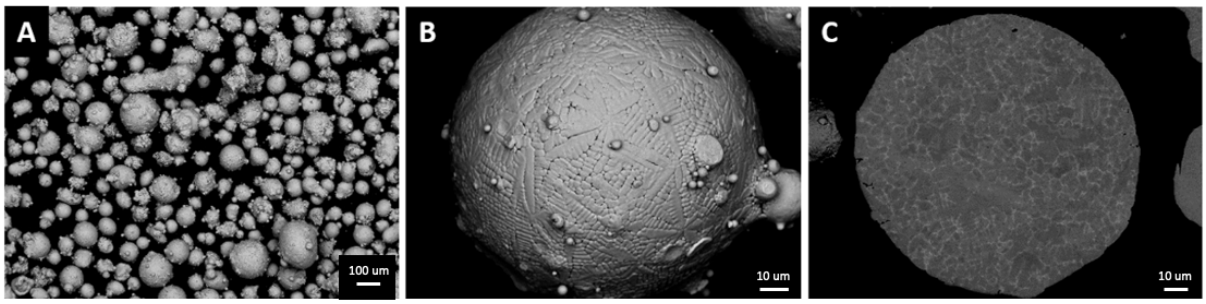

Figure 5.2: A) SEM of the gas atomised IN718 Powder Particles, B) micrograph showing the surface of a large particle, C) dendrite morphology inside powder particle

Table 5.1: Powder Chemical Analysis for IN718 (% weight)

Ni	Cr	Fe	Nb	Mo	Ti	Al	Si	Ta	C	S	N	O
54.45	18.18	18.19	4.88	2.9	0.91	0.42	0.03	0.02	0.01	0.002	0.01	0.011

During deposition, the laser beam focused on a spot size of 1.4 mm while the standoff distance between the laser head and the surface of the substrate was set to 10 mm. The laser operative regime was set as continuous wave (CW). A three-beam nozzle was used, providing a constant powder flow rate of 25 g/min and positioned with a 10mm distance from the substrate, in order to achieve a defocusing distance for the powder stream of 2 mm (D_P in Figure 5.3). The focus of the laser beam was set in order to attain a positive defocusing of 3 mm above the surface of the substrate (suggested by D_L in Figure 5.3). This configuration allowed the triggering of the auto compensation of the deposition during the process in order to avoid uneven horizontal surfaces of the walls.

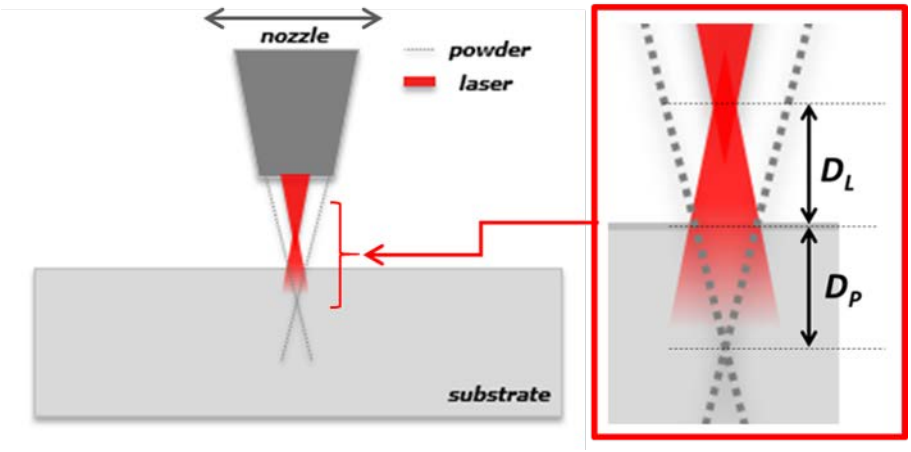

Figure 5.3: Schematic illustration of the powder stream defocusing (D_P) and laser beam defocusing (D_L) distance.

The scanning speed parameter was kept fixed to 11.7 mm/s. whilst the scan strategy was set as bidirectional with a layer thickness of 0.5mm. Each wall was built by depositing 40 layers with a length of 30 mm along the x-direction. The thin walls were produced at a very low oxygen level due to the argon delivered by the laser head in the carrier gas that was flowing from the nozzle. The argon also protected the lens from rebounding particles from the build. The IN718 substrates were machined to an upside-down T shape. Figure 5.4 shows the setup of the experiment. Four K-type thermocouples were inserted into holes located 1mm below the substrate surface. Two infrared cameras (acquisition filter from 150°C to 2000°C) were used to identify the thermal gradient during deposition.

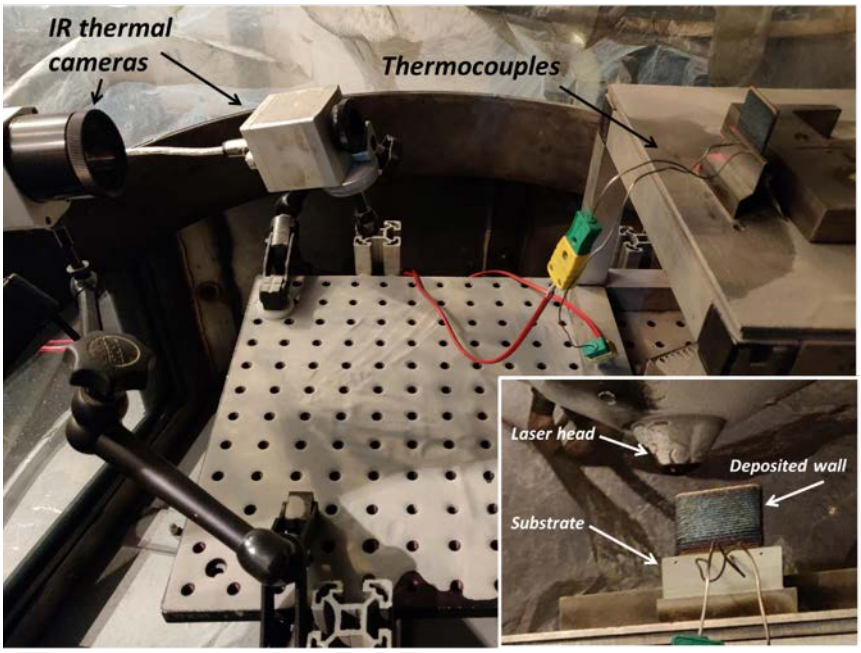

Figure 5.4: Experiment set up using the Trumpf, thermo-cameras and thermocouples

Table 5.2 reports the process parameters used and the energy density E (J/mm^3) calculated using Equation 5.1 where L_P (W) is the power of the laser and V_l refers to the scan speed (mm/s), L_d is the laser spot size (mm).

$$Es = {L_p}/{(L_d\ V_l)} \qquad \textit{Equation 5.1}$$

However, due to the wide range of laser powers that were investigated which will affect the spot size diameter which is fixed to 1.4 mm, a simpler equation (Equation 5.2) was used, where P is the laser power (Watt) and V is the scanning speed (mm/sec) [211].

$$Heat\ input\ (HI) = \frac{P}{V} \qquad \textit{Equation 5.2}$$

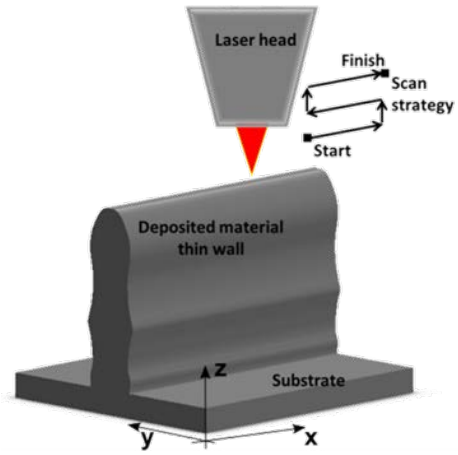

Figure 5.5: Schematization illustration of the laser metal deposition process depositing material of the thin wall and the scan strategy

Table 5.2: Process parameters of single walls

Sample	Power (W)	Scanning Speed (mm/s)	Powder feed (g/min)	Heat input (J/mm)
CW 150	150			12.8
CW 200	200			17.1
CW 300	300			25.6
CW 400	400			34.2
CW 500	500			42.7
CW 700	700	11.7	25	59.8
CW 900	900			76.9
CW 1100	1100			94.0
CW 1300	1300			111.1
CW 1500	1500			128.2
CW 1700	1700			145.3
CW 1900	1900			162.4

As shown in Table 5.2, the different laser power levels were investigated while the scan speed and the powder feed were kept constant in order to study the effect of only the laser power.

5.3 Characterisation methods

After DLD, the thin wall builds were cut using wire electric-discharge machining (EDM) into 3 mm samples in the XY dimension, then they were hot mounted in Bakelite, ground and polished to 0.04μm colloidal silica suspension finish. Subsequently, the samples were electrolytically etched using 10% phosphoric acid (H_3PO_4) and 90% H_2O for 30 seconds using a voltage of 5V. This procedure permitted the revealing of the microstructure that was investigated using a Hitachi 3000 Scanning Electron Microscope (SEM) equipped with a backscattered electron (BSE) detector. The pictures acquired were analysed using ImageJ. A Philips XL-30 SEM equipped with an electron backscatter diffraction detector (EBSD) and operated at 20kV with a spot size of 6 nm was used to reveal the crystallographic texture due to DLD. The EBSD maps were imaged at 120 X magnification and a 3.0μm step size.

Grain size analysis was carried out using the linear intercept method. X-ray diffraction (XRD) was performed using a Bruker D2 Cobalt diffractometer, Co-Kα radiation (λ=1.79 Å) with a step of 0.02° 2θ, a scan speed of 11.7 s/step and 2θ angle ranging from 40° to 120°. Micro-hardness ($HV_{0.5}$) was measured using a micro-Vickers MMT-X from MATSUZAWA.

5.4 Results and discussion

The depth of penetration (DP) and weld pool width (WPW) are normally influenced by the different process variables in DLD. However, in this study, the laser scanning speed, z-increment, stand-off distance and powder feed were fixed. Still, the results showed that both the WPW and DP increase with the increase in laser power, from ~ 0.25-1 mm range at 150 W reaching 1.5-3 mm range at 1.9 kW. Both quantities are useful in assessing the degree of

attachment between the newly added layers and the substrate or the prior layers. Figure 5.6 shows the effect of laser power on depth of penetration and weld pool width.

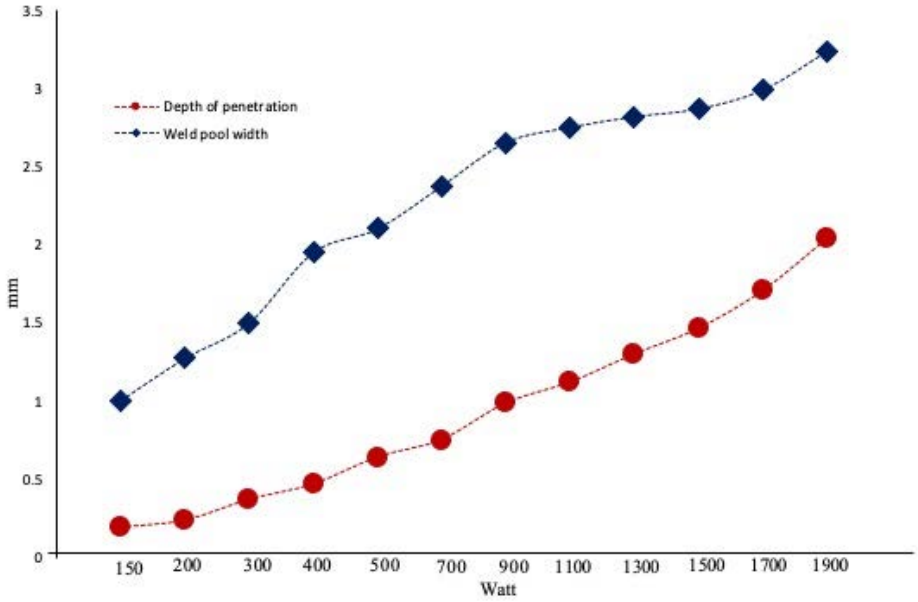

Figure 5.6: Effect of laser power on the depth of penetration and weld pool width

5.4.1 The effects of laser power on microstructure morphology

The columnar-to-equiaxed grains transformation is caused by low solidification velocity and low thermal gradient, while the directionality of the microstructure is a specific characteristic particularly observed when metallic materials are processed using DLD. Columnar-to-equiaxed transition usually occurs when the actual temperature is lower than the equilibrium liquid temperature [212]. During the deposition of the first layer of material on the substrate, the columnar grains start to form, and they grow epitaxially following the direction of the heat source, the laser beam. Subsequently, more layers are deposited, and more columnar grains continue to nucleate and grow epitaxially from the grains formed in the previous layers. Consequently, the elongated epitaxial columnar grains grow continuously through multiple layers [213].

The EBSD maps show the inverse pole figure maps of samples extracted within the middle region of each wall, approximately 10 mm from the bottom of the sample in the cross-section area, Figure 5.7. It is worth highlighting that low laser power (LP) leads to the formation of a microstructure that is characterised by a mixed structure of equiaxed grains and elongated grains along the build direction this is because low power has very high cooling rate which does not give time for grains to expand and grow toward the direction of the heat sources. High laser power (HP), however, leads to a structure with coarse elongated grains that extend columnarly along the build direction which mainly grow following the heat flow path. This is because, when the laser power increases, the weld pool expands which results in a lower thermal gradient and a slower cooling rate compared to the samples with lower power [214]. It can also be observed that the presence of a finer grain structure with random crystallographic orientations leads to a weaker texture intensity in the low power conditions. As concerns the texture, Figure 5.7 illustrates that low laser power produces parts with a weak cubic texture while high laser power produces even weaker cubic texture.

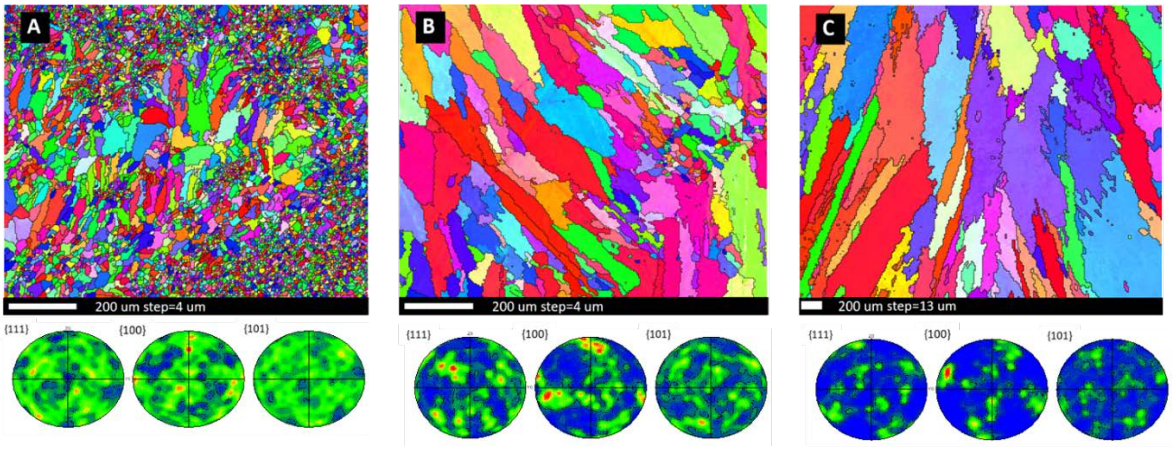

Figure 5.7: EBSD map of IN718 samples produced by a continuous wave in the building direction with no PWHT (A) 150W (B) 500W (C) 1900W. The build direction is the vertical axis of the map.

The grains size distribution (estimated using the equivalent diameter of the grain area) was measured from the EBSD results and is shown in Figure 5.8. shows the frequency percentage of grain size to prove the transformation from equiaxed to columnar. Equiaxed and

columnar grains with different diameters were observed. When using low laser power (150 W), no columnar grains were observed, only fine equiaxed grains were observed with an average diameter of 15 µm. When the laser power was increased to 500 W, columnar grains of different lengths/widths nucleated and grew to an average grain size of 40µm, with the grains extend to ~100 µm in length along the build direction and ~50 µm in width. The highest laser power used 1900 W showed large columnar grains with an average grain size of 70µm.

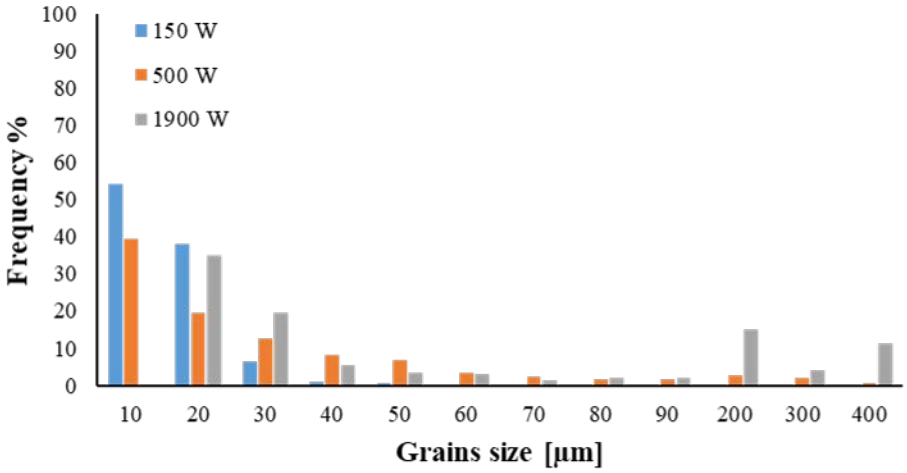

Figure 5.8: Frequency percentage of grain size produced by three different laser powers values

The grain structure of the high laser power samples was characterised by elongated columnar grains that extended across multiple layers. Conversely, the texture observed in the samples produced by low laser power, a mixture of equiaxed and columnar grains with a significant amount of small equiaxed grains in the upper part of the layers and on the side of the build was observed. This was mainly due to the enhanced high cooling rate that affected the solidification rate and thermal gradient, that is compatible with the explanation proposed by Wei *et al.* [213]. Moreover, Wei *et al.* [215] found that epitaxial columnar grain growth occurred from the previously deposited layer or the substrate to the curved top surface and continued to grow because of the cyclic heating and cooling during DLD. The columnar grain area increases by approximately 80% when moving from the edge to the centre of the deposit. This is because of the variable growth directions dependent on the moving molten pool. Due to repeated

thermal cycling and remelting, a gradual increase in grain size is noted between the successive layers, with a 20% increase in grain width from the third to the eighth layers.

5.4.2 The effect of laser power on grain size and growth orientation

Because DLD technology is used to perform repair or coating of already existing metal parts, the control of the crystallographic texture is extremely important. As suggested by the results of this study, some geometrical aspects of the microstructure can be controlled to some extent by manipulating the laser power. Therefore, in order to match the grains of the repaired part to its parent material, understanding the transformation from equiaxed to columnar grain due to the level of laser power must be considered. Generally, a columnar microstructure is dominant in DLD. Generally, the columnar grain is quantified by two geometrical features that are length (l) and width (w) of the grains (Figure 5.9). Figure 5.10 illustrates the grains map that provides an estimation of the length and width of the grains depending on the laser power.

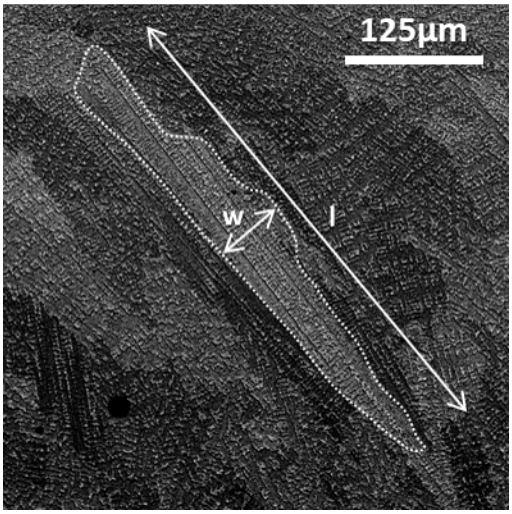

Figure 5.9: Length and width of a columnar grain

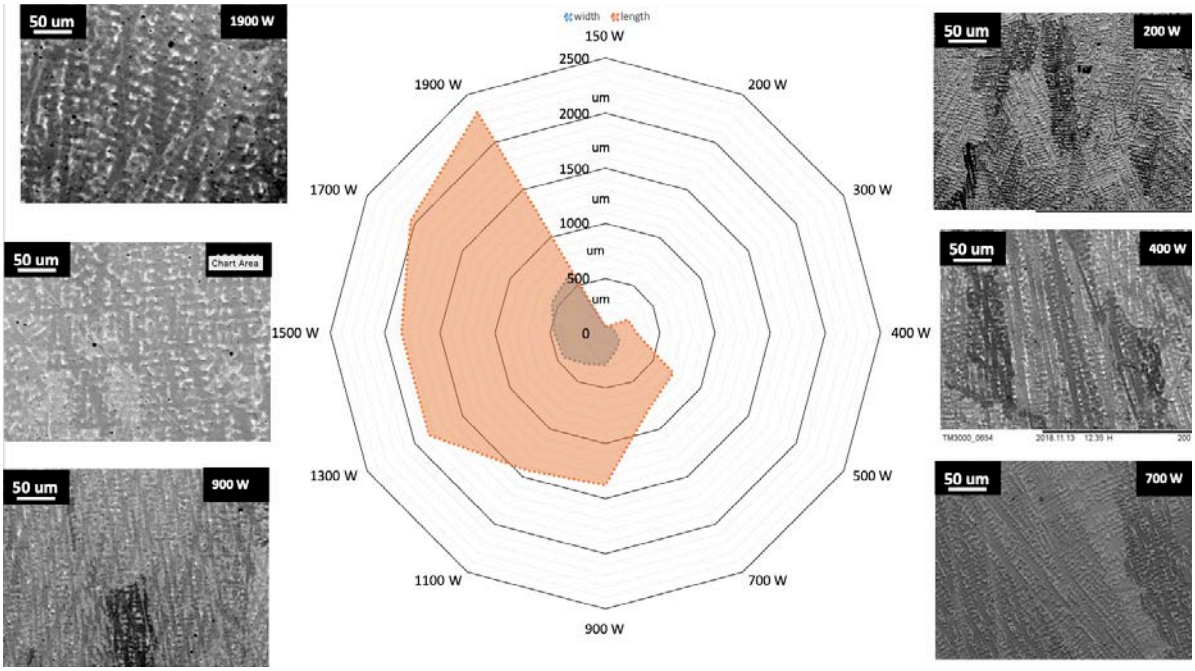

Figure 5.10: Laser power variation effect on the average vertical access of the grains and the horizontal access of the grain, from as low as 150 W to 1900 W

As shown in Figure 5.10, laser power between 150W and 200W gave an aspect ratio close to one, which suggests that the grain structure is approximately equiaxed. The increase of power in the range of 300W to 500W affected the grain morphology, whereby the structure started to become columnar (increasing in length) but still maintaining a similar width of the grains produced with lower laser power. In the range of 500W to 700W, the grains continued to grow longitudinally, but the width started to increase too. In the range of 700W to 900W, the width reached a steady state whilst a slight increase in the length of the grains was still evident. Finally, in the range of 900W to 1900W, the width was still constant, and the length reached a steady state. In particular, it was observed that after every 200W the width increased significantly until it reached a constant value.

Columnar grains provide maximum high-temperature mechanical performance along the loading direction. However, for applications with multidirectional stress applied to the

component, the anisotropy is detrimental [25]. Therefore, microstructure control during the deposition process plays an important role. As showed in Figure 5.10, lower laser powers permitted the achievement of a very low heat accumulation in the deposited material, thus enhancing the cooling rate. Experimental evidence of the different level of accumulated heat using thermal imaging is shown in Figure 5.11. It is possible to observe that increasing laser power will increase the accumulation of heat in the wall and particularly, from the central region up to the top of the wall, it is significantly higher. This result confirms the substrate's impact on reducing the temperature within the first layers deposited, acting as a heat sink. According to Raghavan *et al.* [61], this resulted in having more equiaxed than columnar grains in the microstructure.

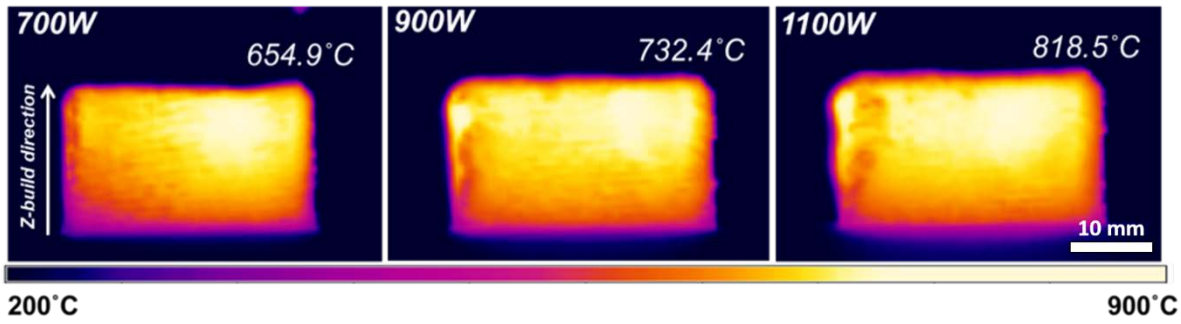

Figure 5.11: Thermal imaging at three different power levels after exactly 1 minute of shouting off heat source

Another microstructural detail is represented by the demarcation, that is, the banded structure caused by rapid cooling. In the produced samples, different angles of demarcation were observed depending on the laser power used. Therefore, the angles were measured as showed in Figure 5.12. The angle was lower than 130° when very low power was used and increased to a constant value (180°) when the power was increased. When laser power higher than 400W was used the demarcation disappeared. Demarcation enhances tensile strength and prevents crack propagation; thus, it is an important feature in DLD microstructures [216].

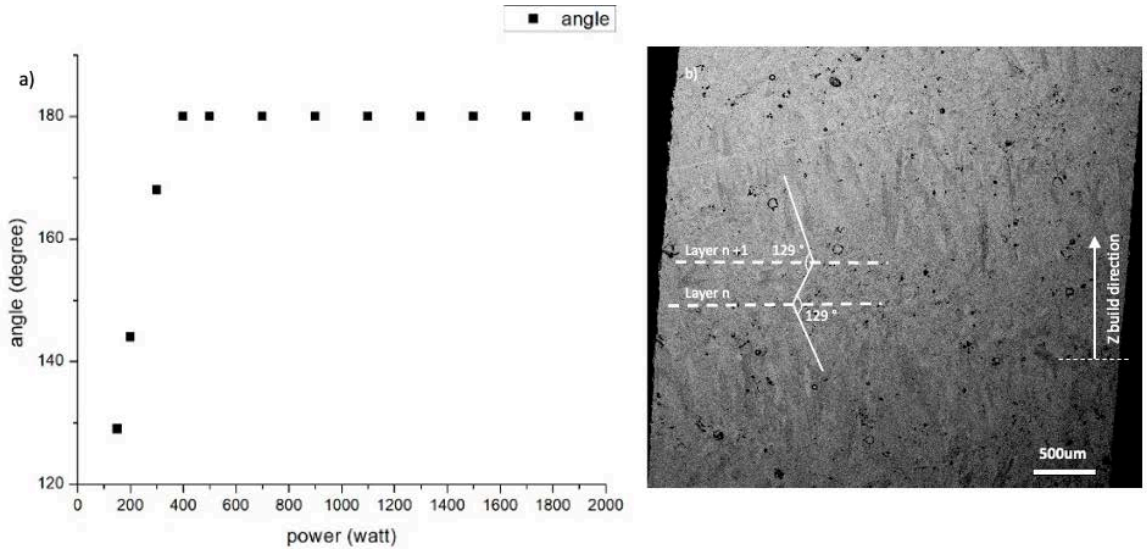

Figure 5.12: Effect of laser power on the demarcation angle.

5.4.3 The effect of laser power on Nb-segregation

SEM analysis was performed on the cross-section of samples (X-Z plane). As shown in Figure 5.13, the austenite matrix γ phase was the dark grey phase, and the interdendritic Laves phase and Nb-segregation were brighter in contrast (mass contrast). The Laves and Nb-rich phases formed a network around dendrite cells.

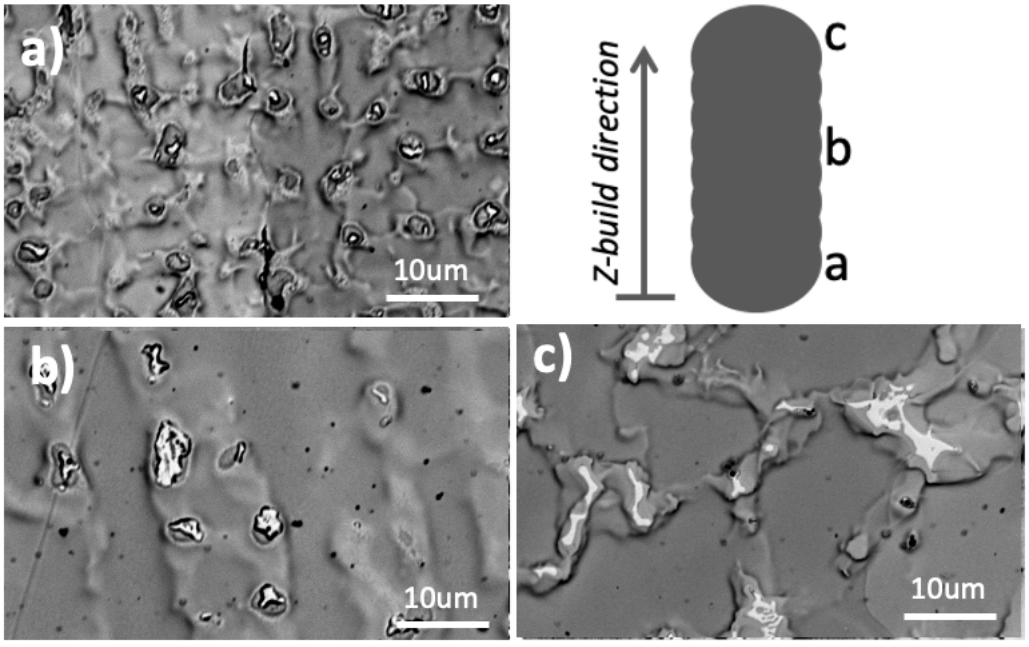

Figure 5.13: Continuous waving single wall sample with laser power of 1100W and scanning speed of 700mm/min (A) Bottom (B) middle (C) top

Nb-segregation is dependent on the cooling rate and the thermal history of the build. The bottom part of the thin wall showed the highest concentration of Laves phase, usually

small and widely distributed. This area was connected to the substrate which acts as a heat sink. Therefore, in this area, a higher cooling rate was observed. The part of the sample in the middle of the build showed a decrease in the Laves phase fraction and a change in their morphology. This area usually experiences an accumulation of the heat cycles during the deposition of the layers. It is contrary to that observed by Chen *et al.* [205] where they claimed that the Laves phase fraction was highest in the middle of the sample due to the lower cooling rate and higher accumulation of heat, whilst the top and the bottom parts of the thin wall experienced higher cooling rate and therefore, lower Laves phase fraction. Moreover, it is important to highlight that in this study the overall Nb-segregation was quantified instead of only the Laves phase since the latter has a different chemistry (Nb, Mo, etc). The top part of the sample showed an increase in Nb-segregated region and percentage compared to the middle section. This area usually experiences very rapid cooling by convection and radiation because it is exposed at the top of the build.

5.4.4 The effect of laser power in Nb-segregation distribution and dendritic microstructure

The microstructure of as-deposited IN718 superalloy shows the different values of dendritic arm spacing (DAS) and Nb segregation with variation of power due to the influence of the cooling rate. The samples produced by low laser power (150W - 300W) experienced a higher cooling rate and, therefore, a higher solidification rate, which produced fine equiaxed dendritic structures with fine and scattered Nb-segregation. The samples produced by higher laser power (400W – 1900W) showed formation of long chain-like Nb-segregation. Figure 5.14 shows the metallographic morphology of dendrites with the different power values.

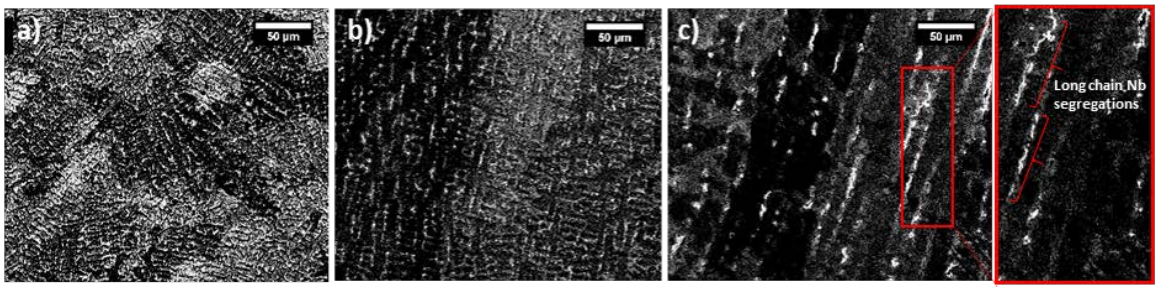

Figure 5.14: SEM Metallographic morphology of dendrites CW (A) 150-Watt (B) 900-Watt (C) 1900 Watt

Figure 5.15 demonstrates variation in DAS and the Nb-segregation (quantified in area %) depending on the laser power used during the tests. The dendrite arm spacing is due to the increase in the heat input and a decrease in the solidification rate. When the heat input was increased from 12.86 J/mm (150W) to 163 J/mm (1900W), the average DAS increased from 7µm to 20µm. The Nb-accumulation on the area fraction reduced from 8% to 2%.

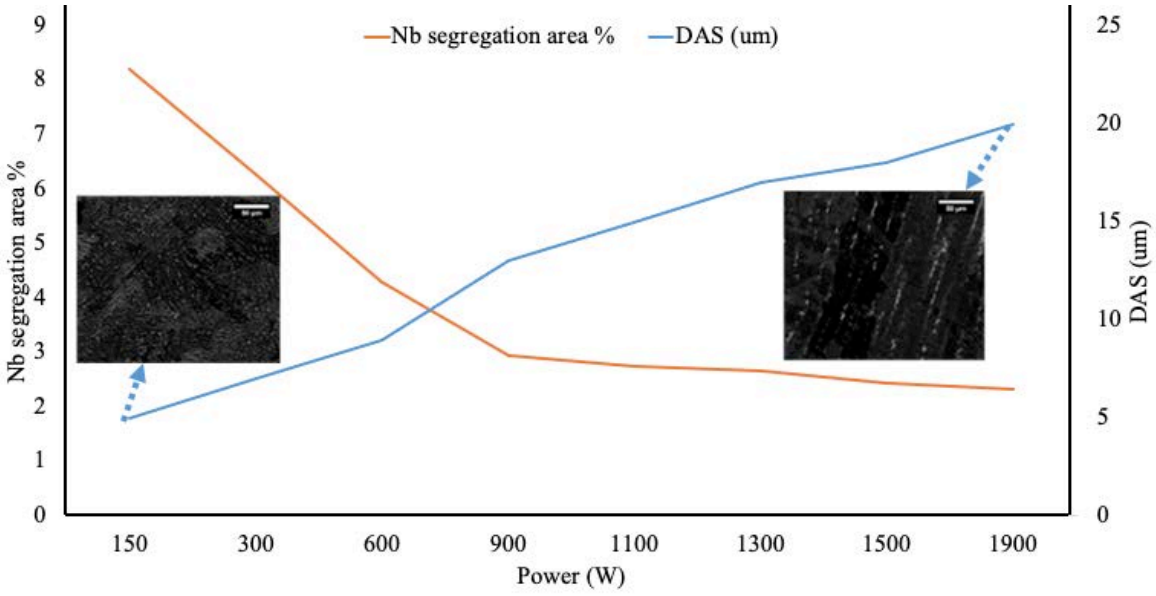

Figure 5.15: Power effect on the percentage of Nb segregation and DAS

5.4.5 Correlating the microstructure and the cooling rate

As observed in the previous results, the heat accumulated is directly related to the laser power used. This is also responsible for the cooling rate of the material during the deposition process. It is also well known that the cooling rate has a direct effect on DAS, and this relation can be described mathematically by Equation 5.3.

$$\lambda = 80\varepsilon^{-0.33}$$ *Equation 5.3*

[217]

Where λ is the primary dendrite arm spacing and ε is the cooling rate in K/s. Equation 5.3 correlates the cooling rate and the DAS considering the calculated solidification rates in relation to the heat input studied in this work [65]. The amount of Nb segregation was higher in the low power samples because of the effect of the cooling rate associated with the heat input. This result was also observed by L. Zhu et al. [207].

As illustrated in Figure 5.10, the grains transform from equiaxed to columnar with an increase of power which inversely affects the thermal gradient and solidification velocity. In DLD the solidification is directed toward the thermal gradient (i.e., in the direction of the heat source) and the solid-liquid interface speed can be controlled by the heat input or by the travel speed. Depending on the power level, a columnar to equiaxed transition may occur and usually, this happens when the temperature is lower than the equilibrium liquid temperature [212].

Figure 5.16 shows the cooling rate values obtained using DAS measurements and Equation 5.3. Moreover, the relation between the DAS and the laser power is also plotted. This graph clearly demonstrates that when laser power is limited to low values (e. g. 150W), very fine DAS can be expected (approximately 5μm) and only a high cooling rate can form smaller microstructures characterised by small DAS.

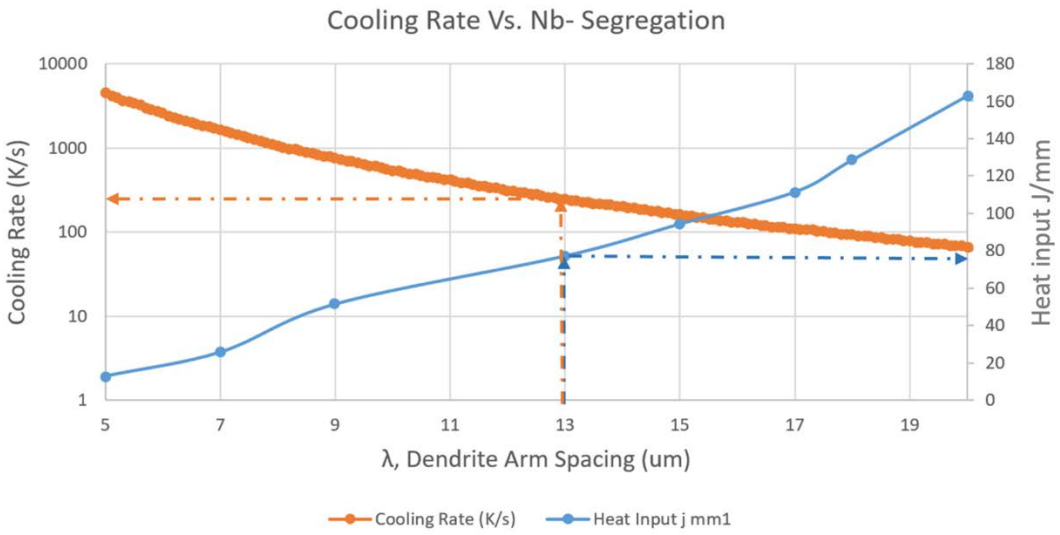

Figure 5.16: The effect of cooling rate and power on dendrite arm spacing

Therefore, it is possible to observe that when the heat input increases, the DAS also increases while the cooling rate decreases. A decrease in the cooling rate usually is due to a decrease of the thermal gradient or a decrease in the velocity of the solidification front. Because the scan speed is kept constant during all the tests, the variation of the cooling rate could be mainly related to the laser power.

5.4.6 The effect of laser power on hardness

The as-fabricated builds typically have poor mechanical properties compared to wrought products due to the presence of detrimental phases and the lack of strengthening phases. However, Qi *et al.* [150] showed that mechanical properties can be improved by performing a homogenisation heat treatment at ~1100 °C for 1–2 h, followed by a solution treatment and ageing to allow the precipitation of the strengthening γ″ and γ′ phases. Although the γ″ phase is the main strengthening phase in IN718, the rapid solidification that occurs during DLD does not enable its formation due to its sluggish nature. It is important to highlight that, in this study, only the as-fabricated condition was investigated due to the study focus on grains size control.

Post heat treatment below the recrystallisation temperature can be used to improve the mechanical properties without affecting the grains size and morphology.

The hardness results of the three specimens with different power levels are plotted in Figure 5.17. The obtained results appear to suggest a possible relationship between hardness and grain size. A primary factor of increasing hardness in IN718 is the precipitation phenomena. In this case, a lower laser power such as 300W led to gentle heating and accumulation of heat, provoking what seems to be limited ageing which may promote the formation of strengthening phases (γ′ and γ″), since γ′ and γ″ phases precipitate between 600 and 900 °C. Moreover, the γ′ can form in a shorter time and requires less heat than the sluggish γ′ [218]. On the contrary, laser power of 1700W led to an extremely high temperature and a significant accumulation of heat, therefore, the Nb tends to dissolve into the matrix. Specially in the middle of the sample where the temperature is the highest due to the low heat lost due to convection or conduction

The grain size might also affect hardness results. In general, the smaller the grain size is, the harder the material is and since lower power produces smaller grain size, the greater hardness could be justified by the finer microstructure.

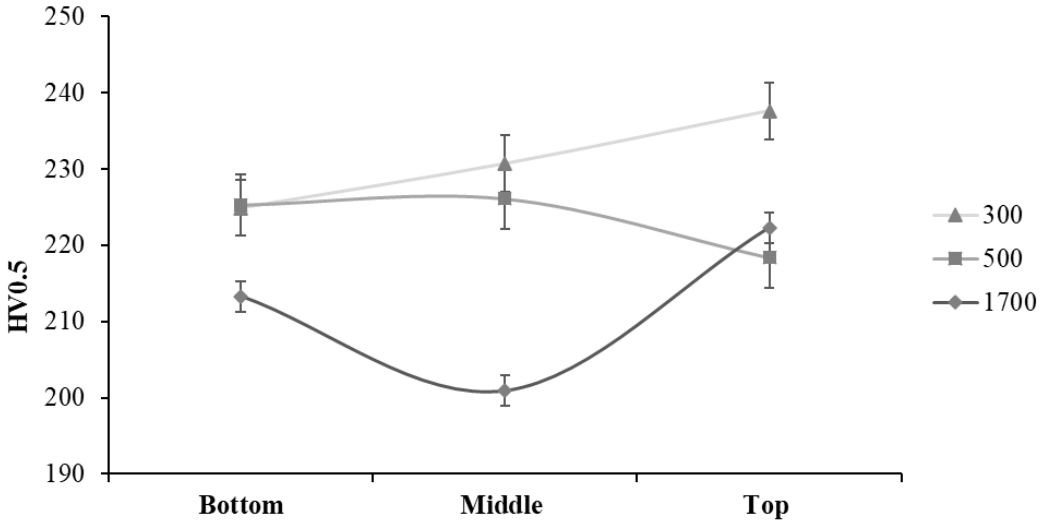

Figure 5.17: The effect of laser power effect on hardness (cross section of the samples)

The third factor is related to the Nb segregation percentage that forms during the deposition. Indeed, lower laser power produced samples with higher Nb segregation and Laves phase as showed in Figure 5.15. This contributes to the greater hardness and lower tensile strength which is compatible with the results obtained by Chen *et al*. [219]. Although, Nb segregation is considered as mainly responsible for the detrimental Laves phase formation that drastically affects the mechanical properties, however, the fine Laves phase formation does show characteristics which can increase the hardness of samples produced by lower laser power.

5.4.7 The effect of laser power on density and porosity

Porosity is formed by the gas that is dissolved in a liquid alloy and it starts to form pores. Usually, pores are created when the pressure within the pores exceeds the pressure within the interdendritic liquid. This a decrease of laser power leads to a decrease of the solubility of the gas elements [220]. It was also observed that high laser power leads to the production of samples that show higher density and reduced porosity than ones produced by lower laser power. This is compatible with the findings of Zhong *et al.* [209]. This trend was experimentally observed in the samples produced and the main results are reported in Figure 5.18. Also, Kobryn *et al.*[11] showed that porosity can be reduced by increasing laser power and scanning speed. Overall, the porosity variations are rather limited due to the high quality of the powder, as evident through the lack of entrapped pores within the powder particles.

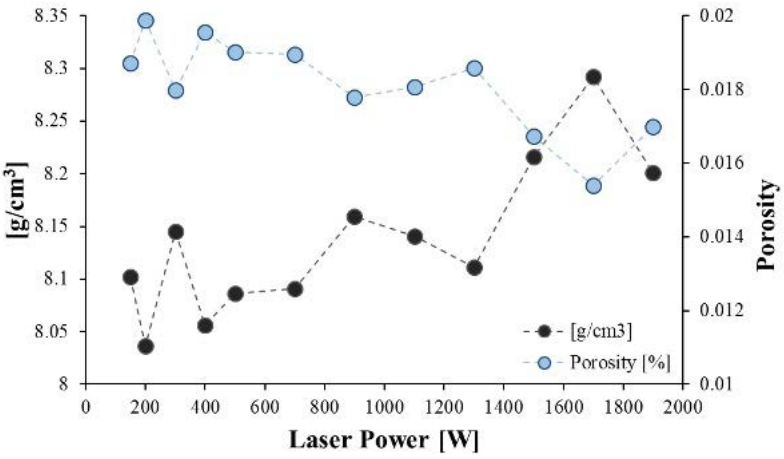

Figure 5.18: Laser power effect on the density and the porosity

5.4.8 The effect of laser power on texture and phases (XRD)

The X-Ray diffraction patterns measured on walls produced by different levels of laser power are reported in Figure 5.19. The section which was analysed on each sample is referred to as the x-z plane. The results of the powder analysis showed major peaks in the correspondence of (111), (200), (022), (311) and (222) with no other minor peaks. At low (400W) and high (1500W) laser power, the dominant peak switched from (111) to (200), which is also the preferred orientation of the material during DLD. However, when a laser power of 900W was used, the intensity of the main peaks was comparable with those observed on the powder. The higher powers, e.g., 900W and 1500W, showed the formation of small peaks and this is because of decreased lattice parameters through depletion of the matrix of Nb and Laves phase formation. Precipitate phases such as γ″ (Ni_3Nb, BCT) and γ' (Ni_3(Al, Ti), FCC) have limited volume fraction, their peaks partially overlap with γ-Ni peaks and indirectly infer with the presence of intermetallic phases. These peaks appear because of thermal stress build-up which leads to Nb-segregation or precipitates formation in the microstructure. Carbides of M_6C or MC types of form at high temperature, which explains the increase in peak intensity at 75° with the increase in laser power. Because of the high laser power and the accumulation of the heat input, which causes the build to be exposed to high temperatures for longer time, this leads to the formation of NbC which forms at ~1250℃ during solidification. δ phase has been

observed emanating from the NbC particles. Generally, MC and δ phase are detrimental for the mechanical properties. The presence of these phases at the grain boundaries could improve the creep property if controlled as stated by Sjoberg et al. [221].

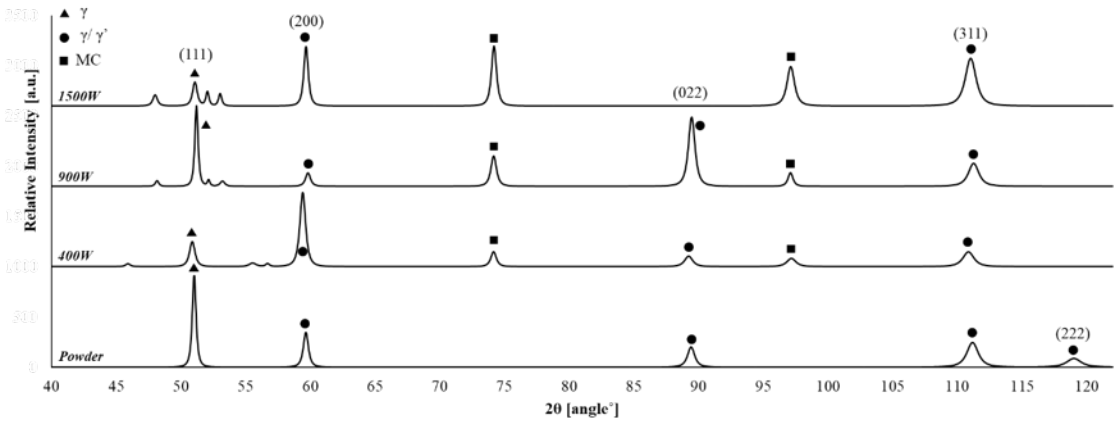

Figure 5.19: X-Ray diffraction patterns comparison of the samples produced by different laser powers

5.4.9 Microstructural Control using Laser Power

To demonstrate the effect of laser power variation in controlling and tailoring the microstructure, two thin walls were built varying the power in real time after a specified number of deposited layers. In detail, the deposition process consisted of two different laser powers. The first was set to 700W for 20 layers and the second, a reduction to 200W was performed. Then the sample was double aged at 720 ºC for eight hours the furnace cooling to 625 ºC, followed by second an ageing to 625 ºC for eight hours with furnace cooling. The microstructural analysis on the thin wall cross-section (y-z plane) showed that the grains columnarity was reduced from 760µm to 242µm. After the heat accumulated, the grains became coarser, and the grain aspect ratio also increased. Higher power tends to produce wider spot sizes, and thus justifies the increase of the wall width when 700W was used. The EBSD mapping was also performed on a cross-section of the samples (y-z plane perpendicular to the build direction) and x-z plane. In Figure 5.20, the EBSD results are reported and suggest a drastic variation of the grain size as well as their morphology.

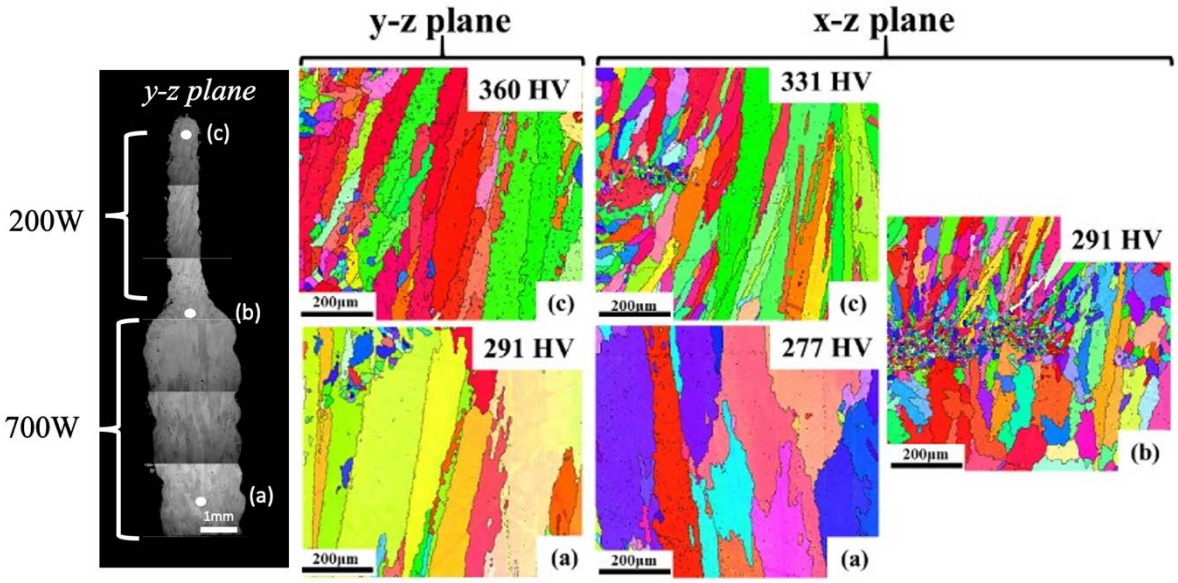

Figure 5.20: EBSD map of IN718 samples produced by two different continuous waving in three different locations (bottom, middle and top) and two different orientations (yz and xz)

It is important to highlight that the grains observed in the region where lower laser power (200W) was used are three times greater than those measured in the single walls (Figure 5.10). The reason for this difference is mainly due to the different heat accumulation evolution. The first 20 layers were produced using higher laser power (700W) which led to a higher accumulation of heat. The hardness was measured in three different locations bottom where the high power was used, in the middle where the power shifted to lower power and in the top where the lower power used. Two indentations were taken for each location and each orientation then the average was taken. Table 5.3 shows hardness calculation indentations value and the mean and stander deviation. Moreover, the grains closer to the top region of the wall were smaller and a higher hardness was measured as expected. Moreover, the grain columnarity and width at the top region of the wall were reduced by 33% and 29% respectively. Finally, as shown in Figure 5.20, the hardness measured on the y-z and x-z plane showed higher value compared with the bottom part and the increment measured in the x-z and the y-z plane is comparable at 23% and 20% respectively. The hardness on its own is insufficient to

understand the mechanical performance at high temperature, which will be explored in a future publication.

Table 5.3: Hardness calculation on three different locations (bottom, middle and top) and two different orientations (yz and xz) the of IN718 samples produced by two different continuous waving

	Bottom		Middle	Top	
	y-z	x-z	x-z	y-z	x-z
Indentation1	283	259	287	355	322
Indentation 2	299	295	295	365	340
Mean	291	277	291	360	331
Standard Deviation	8	18	4	5	9

Notice the average hardness on the yz bottom and the middle section are the same which can be explain by the bottom is close to the substrate which acts as a heat sink. Therefore, in this area, a higher cooling rate was observed, whereas in the middle the heat was reduced which also provides higher cooling rate. The indentations were not exactly measured from the substrate which explains why the xz and yz are slightly different.

5.5 Conclusion

In this research, the microstructural characterisation and the hardness of the IN718 single walls, fabricated using DLD, varying the laser power were investigated. Finally, the following results can be summarised:

- The microstructure and, in particular, the grains can be tailored to an average size by changing the heat input through different laser power values using a constant scan speed.
- An increase of the heat input increases the dendrite arm spacing (DAS) which indicates a decrease of the cooling rate. This is usually due to a decrease of the thermal gradient or a decrease of the velocity of the solidification front.

- Electron microscopy confirmed the transition between equiaxed to columnar dendritic microstructure when the low laser power was increased to high, although no well-defined texture was developed.
- The hardness measured on the samples produced by low laser power showed slightly increased hardness than the samples produced by higher laser power. This is related to the microstructural size as smaller dendrite arms spacing increases hardness.
- Higher laser power led to a decrease of porosity and an increase of the density of the parts produced.
- An increase of laser power led to the formation of carbides due to higher heat accumulation during the DLD process. Their presence was confirmed by the X-Ray diffraction analysis.
- The Nb- segregation behaves differently depending on the location of the build, the cooling rate and the outside influences such as substrate and atmosphere controls the formation of Nb segregation.
- Nb-segregation decreases with an increase of heat input since the lower cooling rate allows the Nb to dissolve in the γ and γ'' phases.

CRediT authorship contribution statement
Abdullah Alhuzaim: designed the study and performed the experimental tests and the analysis of the results. Writing – review and editing
Stano Imbrogno: Reviewing the paper.
Moataz Attallah: supervision, support on experimental feasibility and infrastructure.

Chapter 6. Influence of Power Mode on the Microstructural and Mechanical Properties Development

Abdullah Alhuzaim[a, b], Stano Imbrogno[a], Moataz M. Attallah[a]

[a] School of Metallurgy and Material Sciences, University of Birmingham, Edgbaston, Birmingham B15 2TT, United Kingdom.

[b] Mechanical Engineering Department, Jubail University College, Jubail Industrial City, Kingdom of Saudi Arabia.

6.1 Abstract

The effects of Direct Laser Deposition (DLD) power modes such as Continuous Waving (CW), Pulse Wave (PW) and Partial Power Wave (PPW) by pulse duration changes on the microstructure, has been investigated in a wide range of laser power (500W-1900W). Furthermore, the effects of heat treatments (solution annealed and aged) were investigated using scanning electron microscopy (SEM), electron backscattered diffraction (EBSD) and X-ray diffraction (XRD), which was compared with the as-deposited condition. The results indicated that microstructure morphology can be tailored to an average size, while the Nb segregation can be reduced, modifying the pulse duration. Pulsing duration also plays an important role in reducing segregation, while allowing mechanical properties to be enhanced using short post-processing, thus improving heat treatments.

Keywords:

6.2 Introduction

Direct Laser Deposition (DLD) utilizes relatively high laser power to melt the IN718 powder material to form a part layer by layer. High heat results in a microstructure and continues Nb segregation [54, 212]. Epitaxial columnar grains grow through the layers due to a continuous repeated heating and cooling cycle [215]. Continuous-wave power (CW) develops columnar dendrites, which results in severe Nb segregation leading to the Laves phase to be continuously distributed [69]. Specific characteristics of DLD superalloys are the directionality of microstructure (e.g., columnar grains), detrimental phase formation (e.g., Laves phase, carbides) and anisotropy in strength and hardness. Generally, during the solidification, the Nb atoms are continuously ejected from the dendrites γ-phase into the liquid phase. This results in a lack of Nb solubility in the γ-phase and produces an increase of Nb concentration in the liquid, which forms the conventional Laves phase and Nb concentration phases. DLD laser mode can control the solidification and Nb segregation.

The pulsed laser power has been used effectively to induce grain refinement and to improve the mechanical properties and the solidification cracking resistance. The amount of Laves phase can be significantly reduced, and the use of the laser power pulsed influences the morphology of the grains, improving the tensile properties [58]. The laser wave pulsing refines the Heat Affected Zone (HAZ) solidification structure. The Pulsed laser similarly influences the solidification process in different manners. The energy input variation results in the following: (i) continuous change of weld pool size and shape; (ii) cyclic temperature variations; (iii) enhanced weld metal cooling rates; (iv) enhanced fluid flow of the weld pool; (v) reduced thermal gradients in the weld pool [54, 73, 121].

The energy input generated by the combination of the scanning speed and the laser power intensity influences grain size and morphology, the microstructural homogeneity, and the grain columnarity. The microstructures in DLD vary in appearance, with the heterogeneous

grain aspect ratio occurring over relatively small distances. Moat et al. [16] and Wu [60] et al. reported that large columnar grains in DLD can compromise the mechanical properties. Nevertheless, the grain structure shape can be controlled by manipulating the process parameters [74, 104].

Considerable number of research has been conducted that looked at laser pulsed optimization. L.J. Song et al. [69] claimed using the pulsed laser reduces the Nb segregation and the Laves phase morphology, promoting the formation of fine equiaxed dendrites. Moreover, the mechanical properties of the pulsed samples were slightly higher in the as built than after heat treatments. Ram et al. [58] investigated the GTAW of IN718 and claimed that when the current is pulsed, it provides the following benefits; (i) it refines the fusion zone microstructure, (ii) reduces the amount of the Laves phase and affects its morphology and (iii) improves the response of the fusion zone to post-weld heat treatment and tensile properties. Radhakrishna et al. [100] investigated the formation of segregation and discovered the Laves phase in IN718 during welding can be controlled by the use of; (a) fast weld cooling rates, (b) low weld heat inputs, (c) heat extraction techniques, such as chilling blocks in tooling, (d) steep thermal gradients, (e) pulsing techniques, and (f) low-Nb fillers. Moat et al. [16] studied the role of laser pulse length and duty cycle and claimed long cycle periods and short pulse lengths resulted in a highly columnar microstructure, while specimens produced with short cycle periods and long pulses (high duty cycles), lead to lower aspect ratio grains. Xiao et al. [69] analysed the effect of the continuous wave (CW) and the pulsed wave (PW) laser modes on the microstructure. The CW mode tends to develop columnar dendrites, relatively severe Nb segregation and continuous distributed Laves phase, whereas the PW mode tends to produce fine equiaxed dendrites, less Nb segregations and a fine discrete Laves phase. The refined and equiaxed dendrite microstructure reduces Nb segregation. The fine and discrete Laves phase particles produced, are mainly due to the improved cooling rate with one order of magnitude

and a decreased solidification time of the molten pool. The quasi-continuous wave (QCW) samples show a good response to ageing treatment, with a higher hardness and more desired tensile properties due to the reduced Nb segregation, and the fine discrete Laves phase and microstructure [69, 222, 223]. Work by Mumtaz and Hopkinson [224] investigated the effect of the pulsed laser on the surface quality of the deposited samples. They found that controlling the high peak power reduces the top and side surface roughness, as recoil pressures flatten out the melt pool and reduce the balling formation by increasing wettability of the melt pool. This study aims to obtain experimental data to support a clearer view of grains mapping and reduce the formation of Nb segregation and Laves phase when three different operative laser modes are used.

The current studies on power pulsing literature are insufficient and demonstrate a lack of knowledge. First, the majority of studies focus on a square pulse on butt joint welds, and not on additive manufacture (AM). None of the studies explains the effects of different pulsing with different pulsing types on the grains. Furthermore, neither did they consider the manipulation of pulsing duration or investigate the relationship between the different grain size and mechanical properties. In this study, the grains sizes, their morphology, and texture were all investigated on IN718 thin walls produced by DLD. Furthermore, the effect of different laser pulsing on the microstructural characteristics and Nb segregation and, therefore, mechanical properties were analysed.

This study aims to demonstrate the utility of laser pulsing in controlling the IN718 microstructure and explore the influence of laser pulsing influence on microstructural development (grain morphology, Nb segregation, etc.). Lastly, it will consider the correlation of solidified microstructure (e.g., DAS) with the solidification mechanisms and cooling rates in DLD. Figure 6.1 is schematic of the areas of investigation in this study.

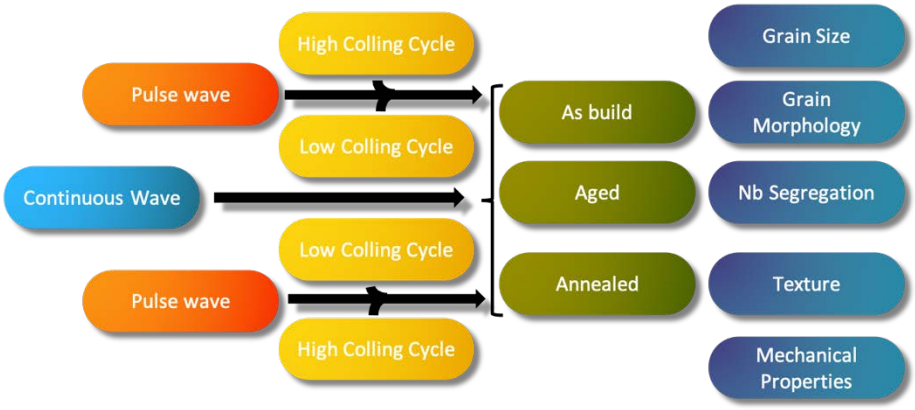

Figure 6.1: schematic of the investigation of this study

6.3 Experiment Procedures

Different thin walls (20mm height, 30mm length and around 1.5mm thick depends on the laser power used) were produced by a Trumpf TLC 1005, equipped with a 3-beam nozzle able to move on a cartesian space (x, y and z) and a 4-kW diode laser (Trumpf TrueDisk 4002) system. The metal powder used was gas atomised IN718, and the morphology showed in Figure 6.2. The powder was mainly spherical without excess satellite formation. Both coarse and fine particles with less spherical shapes were present, while the surface texture was rough (Figure 6.2b). The particle size ranged from 53-180 µm and the chemical composition is illustrated in Table 6.1.

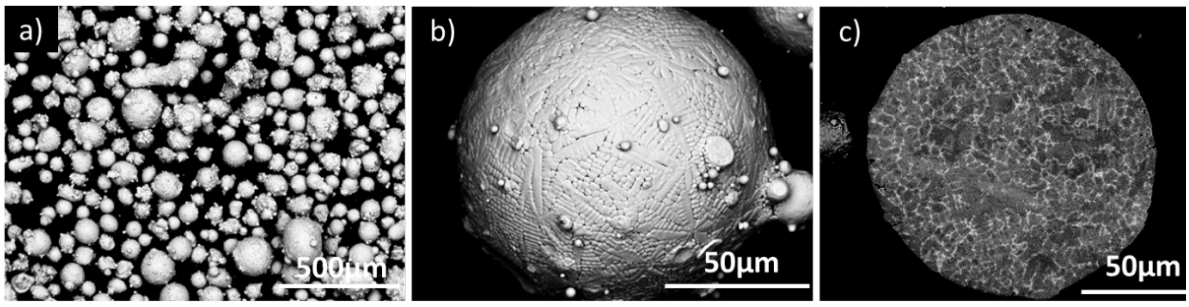

Figure 6.2: A) SEM of the gas atomised IN718 Powder Particles, B) micrograph showing the surface of a large particle, C) dendrite morphology inside powder particle

Table 6.1: Powder Chemical Analysis for IN718 (% weight)

Ni	Cr	Fe	Nb	Mo	Ti	Al	Si	Ta	C	S	N	O
54.45	18.18	18.19	4.88	2.9	0.91	0.42	0.03	0.02	0.01	0.002	0.01	0.011

During the deposition, the laser beam focused to a spot size of 1.4 mm and standoff distance was set equal to 10 mm. The laser source was altered between continuous-wave operative mode (CW), pulse waving (PW) and partial pulse waving (PPW), while the laser power was varied from 500W to 1900W. A three-beam nozzle was used providing a constant powder flow rate of 25 g/min, whilst the focus of the powder stream was set 2 mm below the substrate. The powder stream defocusing and laser beam defocusing, (DP and DL respectively) were adapted to trigger the auto compensation of the deposition during the process, in order to avoid lack of deposition due to the uneven horizontal surface of the walls [225]. The powder was carried through the system by the argon flow, which guaranteed a protective environment during the interaction between the laser and the powder within the melt pool.

The scanning speed parameter was kept fixed to 700 mm/min, with the laser head following a bidirectional path. The single walls were built of 40 layers with a length of 30 mm. The scanning strategy was back and forth, with a layer thickness of 0.5 mm shown in Figure 6.3.

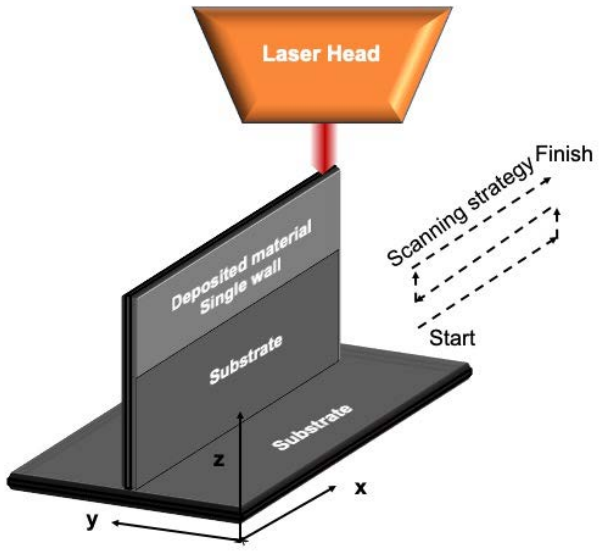

Figure 6.3: Schematisation illustration of the laser metal deposition process depositing material of the thin wall and the scan strategy

The build was not in a controlled atmosphere. Local shielding was done relying on only carrier gas from the nozzle, which also protects the lens from the rebounding particles from the build. Three types of laser power mode were used: a Continuous Waving (CW), Pulse Power Waving (PW) and Partial Power Waving (PPW), while the heat input is defined as reported in Equation 6.1 [211]. Moreover, when the pulsed laser mode (PW or PPW) was used, the frequency of the pulse mode was set equal to 100Hz.

The use of the pulsed laser can also manipulate the energy variation within a single pulse. The Trumpf TLC 1005 allows the user to manipulate the power during the deposition varying from 100% which is the full power signal to 2% which is the minimum power signal. The rectangular pulse shape is the most used, when the power density remains constant.

Continuous Waving (CW)

The average and peak power output is continuously the same.

Pulse Waving (PW)

The laser power was modulated by a square wave with a duty cycle of 50%; when utilised the average power is almost half the continuous power. However, the maximum power

(peak power) value is equal to the continuous power, and remaining time for the minimum power (bottom power) is 2%.

Partial Power Waving (PPW)

The average power is half the continuous waving. Moreover, the peak power is 75% of the continuous power and the remaining time of the single pulse is 25% of the continuous power. Figure 6.4 shows a schematic representation of the three-power mode waving used.

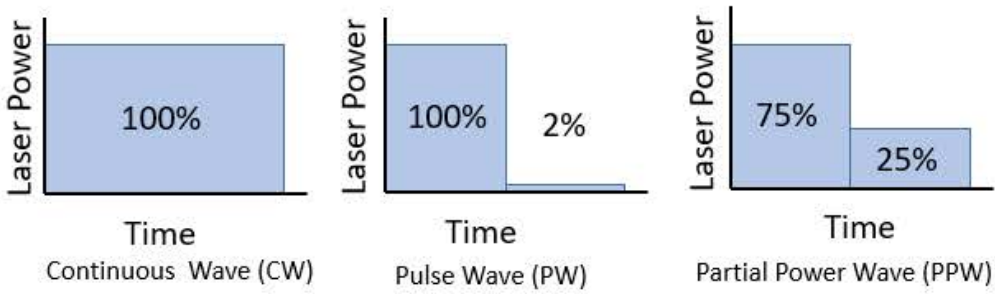

Figure 6.4: Schematic of the three-power mode waving

Pulse shapes can be adjusted by controlling the pulse duration, which can then be extended allowing improved control over laser processing. Research has proven the use of alternative pulse shape reduces spatter, porosity and hot cracking, while improving the surface finish [174, 175].

Therefore, the pulsed wave used in this study has been further manipulated modifying the duty cycle. The duty cycle, which is the ratio of the pulse width (high power) to the total period of a pulse wave, was manipulated between 25%, 50% and 75% considering the PW and the PPW.

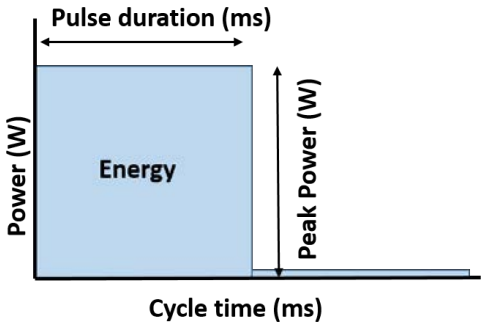

Figure 6.5: cycle time of pulse wave

Standard pulsing (SP) is where pulse duration t (ms) is divided equally between maximum and minimum peaks. The pulsing duty cycle time was also manipulated from the 50/50 to 75% of the time on peak power, and the remaining time (25%) was almost off and that is called pulse waving – low cooling cycle (PW – LCC). Whereas the pulse waving – high cooling cycle (PW – HCC) is 25% of the time on peak power, and for the remaining time the power is reduced to 2%. The identical relationship exists with the partial power waving. Figure 6.6 illustrates the types of pulse shapes used in this work. The parameters used are listed in Table 6.2.

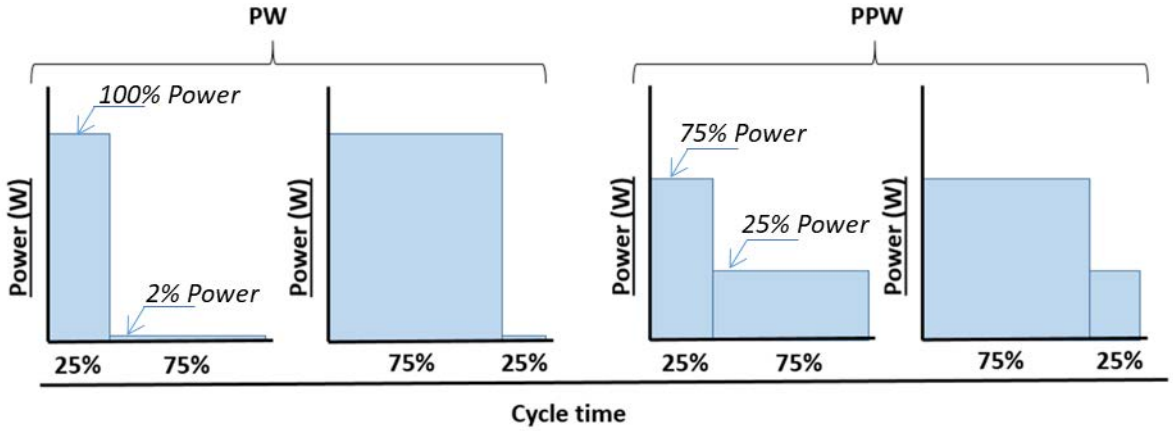

Figure 6.6: Schematic of the pulse cycle with different pulse duration

Thermal measurements were carried out by drilling four holes within 2 mm from the surface of the substrate. The K-type thermocouples were used to measure the temperature during the deposition as shown in Figure 6.7. Moreover, two thermal infrared (IR) cameras

were used. The first camera was equipped with a filter able to allow a temperature acquisition range between 150 °C and 900 °C, while the second camera had a filter for higher temperature acquisition between 900 °C and 2000 °C. The thermocouple results were used to calibrate emissivity used in the IR camera results.

Table 6.2 Process parameters used in this study.

Power mode	Pulsing time	Power max value	Cycle time first half	Power min value	Cycle time the second half
	(ms)	%	%	%	%
CW	∞	100			
PW - SP	100	100	50	2	50
PW - LCC	100	100	75	2	25
PW - HCC	100	100	25	2	75
PPW - SP	100	75	50	25	50
PPW - LCC	100	75	75	25	25
PPW- HCC	100	75	25	25	75

The practical pulse energy E (J) can be defined by the above parameters. Max power p_{peak} (kW) is given by a portion of laser beam energy and pulse duration as follows:

$$p_{peak} = E/t \qquad \textit{Equation 6.1}$$

Equation 6.2 was used to estimate the Weighted Average Power (WAP) used during the deposition, when the pulsed laser mode was involved.

$$WAP = PMax * \left(\frac{tmax}{100}\right) + PMin * \left(\frac{tmin}{100}\right) \qquad \textit{Equation 6.2}$$

In detail, the P_{max} represents the maximum power value (e.g., for the PW this is 100% of the power value, for the PPW this is 75% of the power value), whereas P_{min} represents the minimum power value for example the PW is 2% of the power value, for the PPW is 25% of the power value. The t_{max} and t_{min} represent the maximum and minimum pulse duration according to the representation reported in Figure 6.4 and Figure 6.6. For example, considering the nominal laser power equal to 700W, when PW is considered and the t_{max} is equal to 25% (t_{min} equal to 75%), the WAP can be estimated as:

$$WAP = 700W * (0.25) + 0.02\ x\ 700W * (0.75)$$

That is equal to 175W suggesting that the PW is characterized by less power than the CW (represented by 700W). The entire calculation depending on the PW, PPW and time duration of the pulse is reported in Table 6.3.

Table 6.3: Process parameters with weighted average power

	Power in watt		Scanning Speed	Powder Feed	Weighted Average Power
	P_{max}	P_{min}	mm/min	g/min	WAP
Continuous Waving	500		700	25	500
	700				700
	900				900
	1100				1100
	1300				1300
	1500				1500
	1700				1700
	1900				1900
Pulse Waving-SP	500	10			255
	700	14			357
	900	18			459
	1100	22			561
	1300	26			663
	1500	30			765
	1700	34			867
	1900	38			969
Partial Pulse Waving-SP	375	125			250
	525	175			350
	675	225			450

	825	275			550
	975	325			650
	1125	375			750
	1275	425			850
	1425	475			950
PW-LCC	700	14			528.5
PW-HCC	700	14			185.5
PPW-LCC	525	175			437.5
PPW-HCC	525	175			262.5

Figure 6.7 shows the actual set up for the DLD nozzle and the T-shaped substrate with the thermocouples inserted on it and the thermal camera angles.

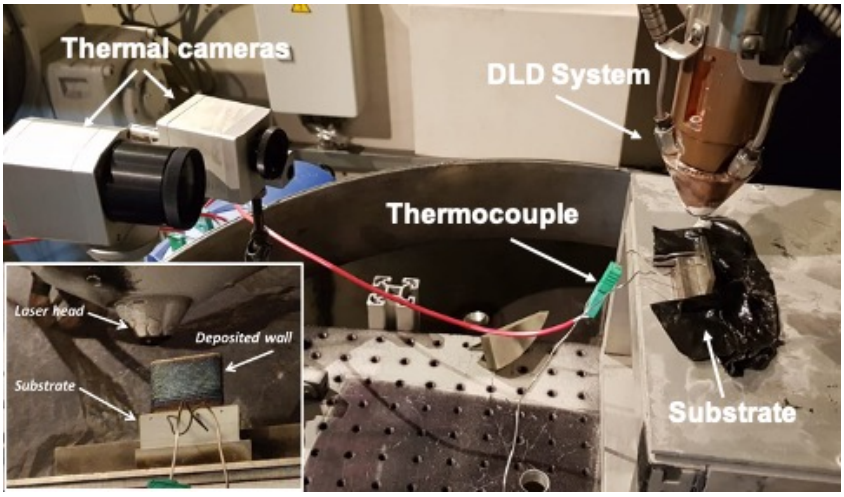

Figure 6.7: experimental set up

Furthermore, the samples produced by DLD were exposed to two kinds of post-heat treatments. Annealing post processing that consisted of keeping the samples for 1h in a furnace with the temperature set to 980°C, and subsequently air-cooled to room temperature. The second heat treatment was ageing which is to keep the samples at a consistent 720°C for eight hours, furnace cooling to 625°C, followed by a second ageing treatment at 625ºC for eight hours with furnace cooling. Figure 6.8 illustrates the reported curves representative of the two heat treatments carried out on the samples.

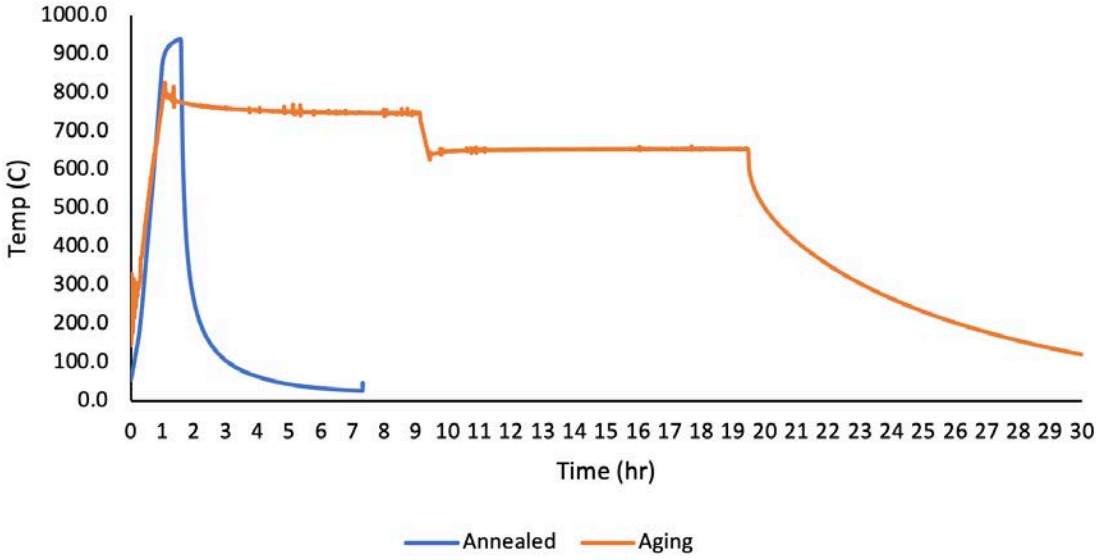

Figure 6.8: Annealing and ageing heat treatments

ImageJ software analysed the microstructure and was able to quantify the Nb content area percentage. In detail, the thresholding operation used for the Nb-segregation usually demonstrates a higher contrast because of the higher Nb density compared to the other materials in the alloy. Several images were taken along the XZ axis considering three regions, namely the bottom, the central and the top of each wall. Figure 6.9 shows SEM for the microstructure with Nb segregation on continuous waving single wall sample on the locations.

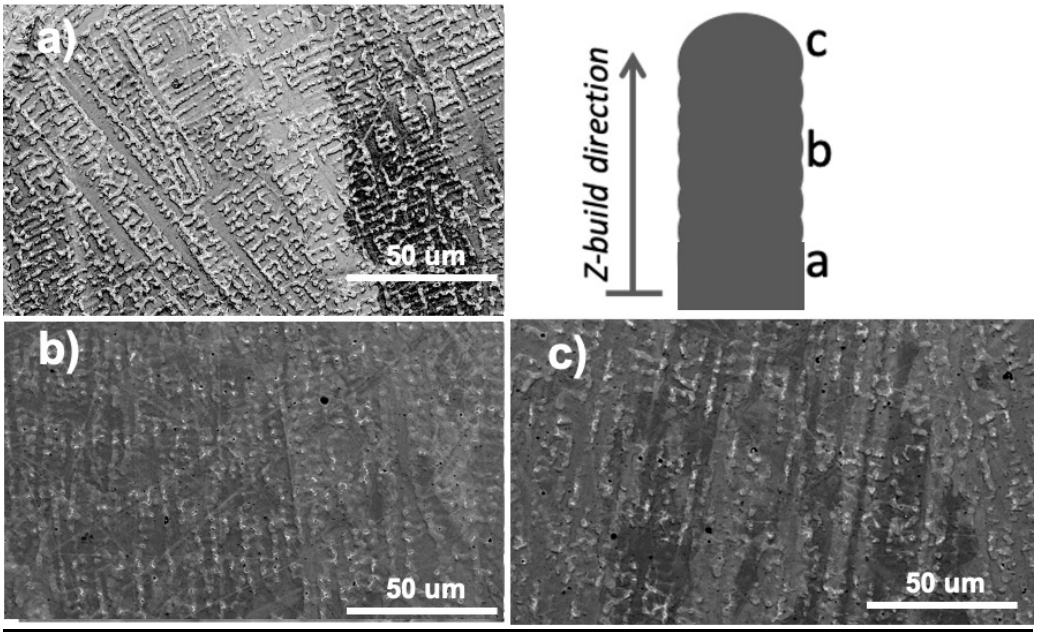

Figure 6.9: Continuous waving single wall sample with laser power of 700W and scanning speed of 700mm/min (A) Bottom (B) middle (C) top

Finally, multiple single walls were built with a length of 90mm and a height of 20 mm. Different tensile specimens were produced and the surfaces ground and polished to reduce the effects of the rough surface during the mechanical properties' characterization.

6.4 Results and Discussion

6.4.1 Effect of the Power Mode on the Thermal Distribution during the Deposition Process

The distribution of the temperatures measured via thermocouple during the entire deposition process are reported in Figure 6.10. The thermocouple reading confirmed that the CW provided the highest heat input during the manufacturing process of the samples. The heat accumulation increased during the deposition, until a certain number of layers and subsequently it started to decrease due to the wider distance from the heat source and position of the thermocouple. The temperature profiles measured by the thermocouple during the PW deposition, showed a significant drop of the heat input and a faster cooling effect. Finally, the PPW showed a comparable trend with the PW during the first thirty seconds of the deposition and subsequently, the temperature raised due to the higher heat accumulation. The temperature partially reached a plateau and finally decreased.

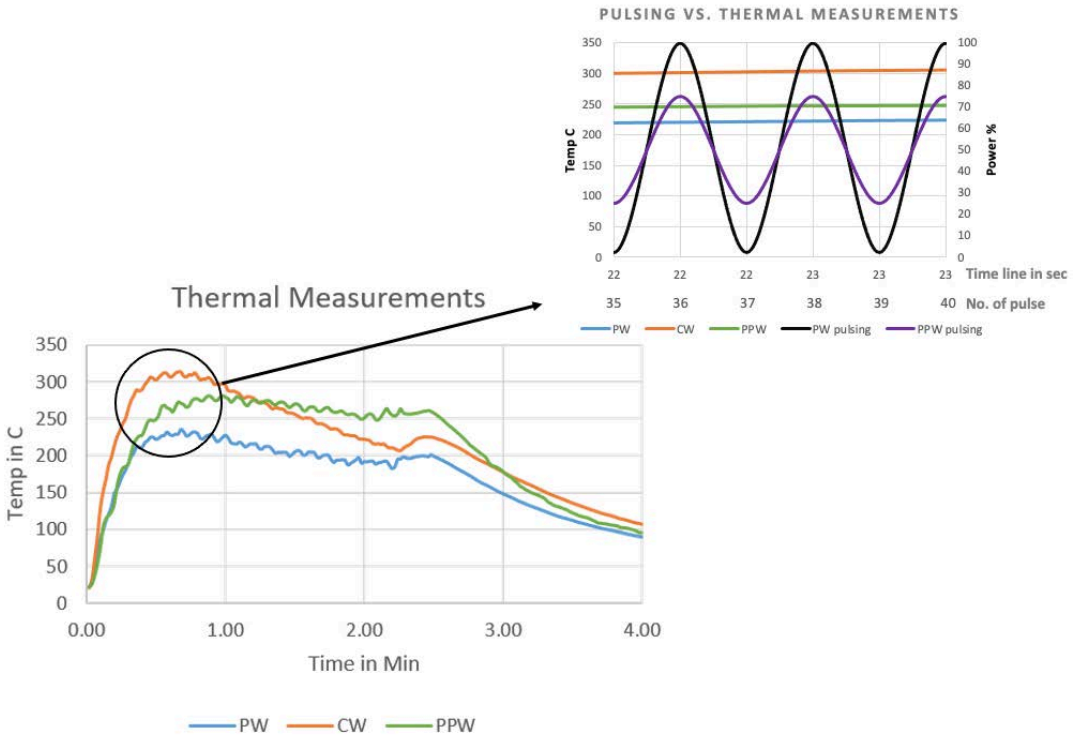

Figure 6.10: Temperature measured by the thermocouple.

Analysing the data reported in Figure 6.10, the temperature measured using the CW laser mode reached the maximum value after 33s, with a temperature equal to 313 °C, which means during the deposition of the 13th layer. The temperature measured during the PW laser mode reached the peak maximum value after 34s, and the temperature was equal to 235 °C again during the deposition of the 13th layer. It is interesting to notice the use of PPW laser mode was characterised by less heat accumulation compared to the CW. Indeed, the maximum temperature reached was equal to 280 °C, and this was achieved after 44s and the 17th deposited layer. It is important to highlight that the thermocouple acquired data every second making the evaluation of the effect of the pulsed frequency used (100Hz that are 100 pulses per second) on the temperature difficult.

Calculating the WAP for the investigated laser modes highlights the possibility to manipulate the amount of heat accumulated during the deposition varying the pulse duration. Indeed, as shown in Figure 6.11, although the laser power selected was 700W, then the PW was set, the

WAP was equal to 357W, 528.5W and 185.5W when the pulse duration (%t_{max}) was set to 50%, 75% and 25%, respectively. The same discussion can be conducted when the PPW was considered as laser operative mode. It is important to highlight that the PPW showed higher power was involved when the minimum power level considered was 25%. According to the results reported in Figure 6.11, it is estimated that the PW induced a higher cooling rate than the PPW and the CW, therefore the expectation is a lower temperature and less heat accumulation. These results were confirmed by the data acquired by the infrared camera (Figure 6.12 and Figure 6.13).

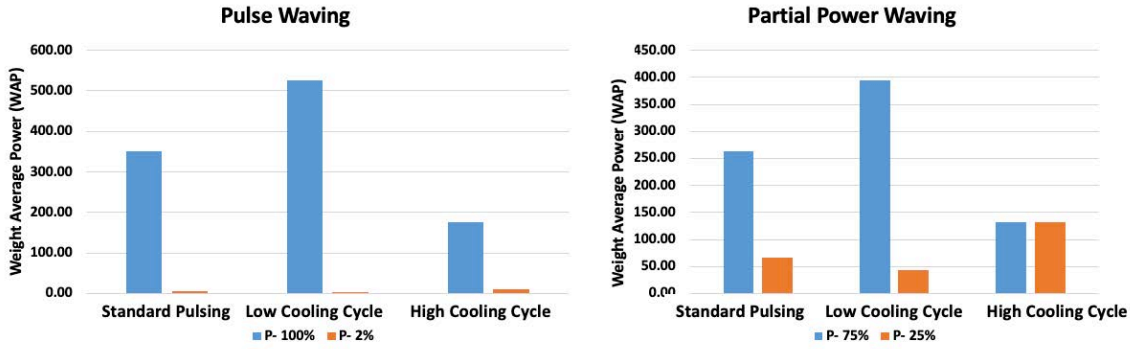

Figure 6.11: WAP calculated depending on the PW, PPW and different time duration (laser power equal to 700W).

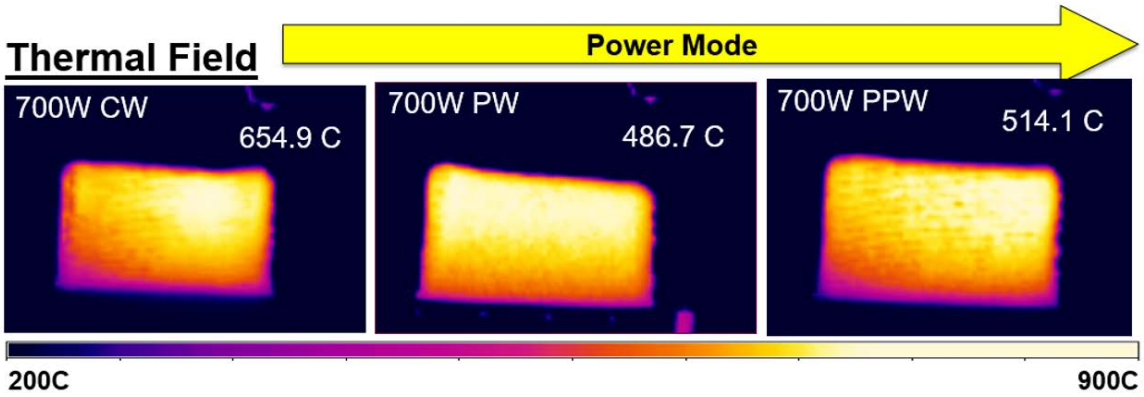

Figure 6.12: Thermal field distribution on the z-x plane of the deposited walls depending on the power mode used

Figure 6.12 shows the thermal field of the longitudinal surface of the deposited walls when different power modes were used. In detail, the frame represented the temperature distribution 60 s after the end of the deposition where the laser was turned off. According to Figure 6.12, when PPW with a standard pulse (SP) was set, the WAP was 350W, while the PW was characterised by a WAP of 357W. The WAP suggested that higher heat should be involved when PW is used, rather than PPW. The 25% of the power involved during the t_{min} when PPW was used, allowed the cooling rate to reduce when the laser was not operating at the maximum power. Power mode strategy allows the cooling rate to be manipulated and, therefore, heat to be accumulated. Indeed, although the WAP suggested a difference of only 7W between the PW and the PPW, the average maximum temperature evaluated was lower when the PW was used. Another interesting comparison is highlighted in Figure 6.13 when the different value of the pulse duration is used is shown. As expected, higher pulse duration characterised by higher power, led to higher heat accumulation within the deposited material as showed in Figure 6.13.

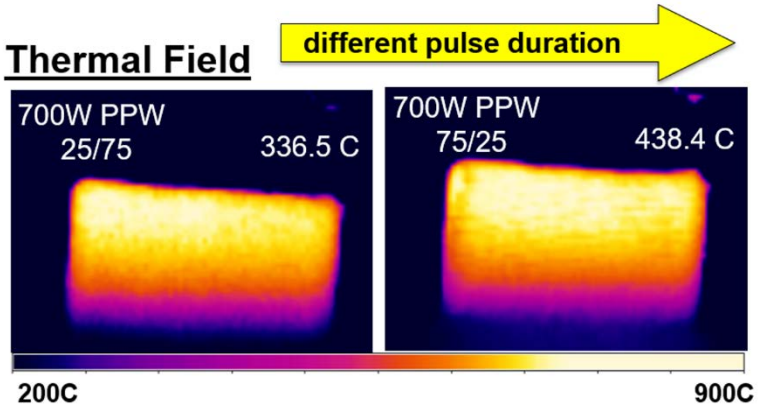

Figure 6.13: Thermal field distribution on the z-x plane of the deposited walls considering the PPW power mode but different pulse duration

1.1. Effect of the Power Mode on the Wall Shape and the Microstructure

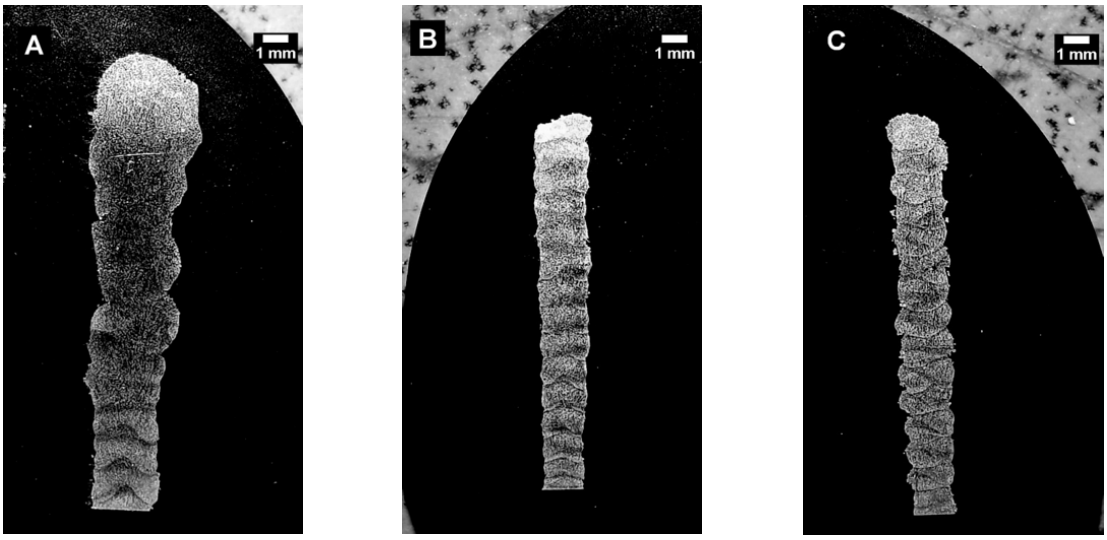

Figure 6.14: Geometry of single walls with same laser power "700 W" and different power modes in the cross-section view xz (A) CW (B) PW (C) PPW

Different power modes and pulse duration led to different thermal cycles and heat accumulation inducing an inevitably different effect on the microstructure. Many studies reported the effect of the power, the scanning speed, the powder feed, the laser focal length and stand-off distance on the microstructure. In this study the above-mentioned process parameters were kept constant. Considering the geometry target of the thin walls (height of 20mm), the analyses carried out on the geometry showed that the CW (the highest heat input) produced walls with the height close to the theoretical one (19.07 mm) and thicker (2.5 - 4.5 mm). The walls produced by PW were the shortest (height of 15.6 mm) and the thinnest (1.8 – 2.0 mm), while the PPW produced the most uniform wall (height of 16.6mm and thickness of 2mm).

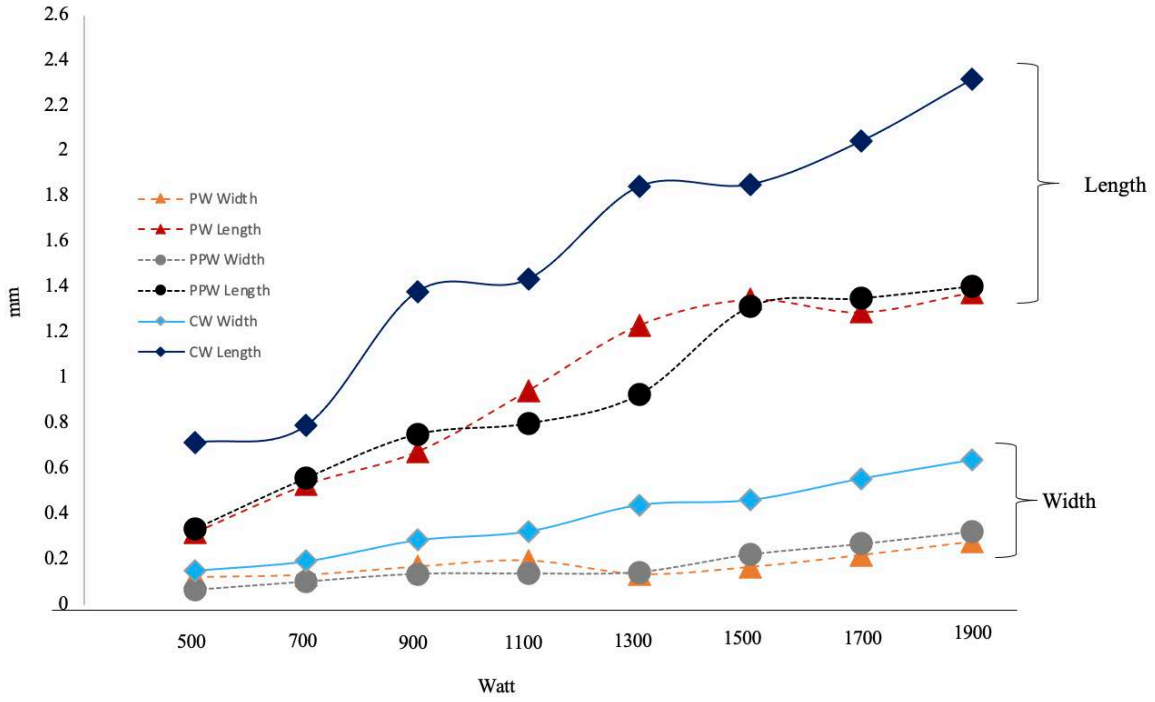

Figure 6.15: Laser power effect on the morphology of the grains

In general, all power modes led to columnar grains formation as shown in Figure 6.15. The use of the CW led to bigger grain morphology. Moreover, the laser power between 500W and 700W for the CW, shows longer grains than the ones produced when the PW and the PPW are used. These latter grains have comparable sizes. The width of the grains showed the same trend as the height, although they were slightly smaller. From 700W to 900W the length and the width of the CW grain increased noticeably. On the other hand, the grains produced when the PW and PPW are used, showed the same morphology with a slight increase in grain length when the PPW was used. Laser power from 900W to 1100W showed a plateau in grain morphology when the CW and PPW are used, while the PW laser mode enhanced the columnarity of the grains. From 1100W to 1300W another increase in the columinarty in the CW and PW was seen, however, PPW goes into plateau. The width of the grains in this power intensity increases in the CW case, whereas PW decreases and in the PW, it remains the same. The use of the laser power from 1300W to 1500W showed significant grain columnarity when the PPW mode was used, while no significant variation was observed when the PW and the

CW were used. The same trend was observed when the width of the grains was evaluated. Power from 1500W to 1900W saw an increase in grain columanirty of CW and a slight increase in grain width. However, the PW and PPW go into a plateau for the grain's length and slight increase in grain width.

The microstructure analysis was carried out through EBSD mapping. The EBSD analysis was performed across the YZ direction, covering an area about 2000μm² of the section of the wall. Figure 6.16 shows the grain size and the crystallographic texture of the samples manufactured using the CW, PW and PPW power mode.

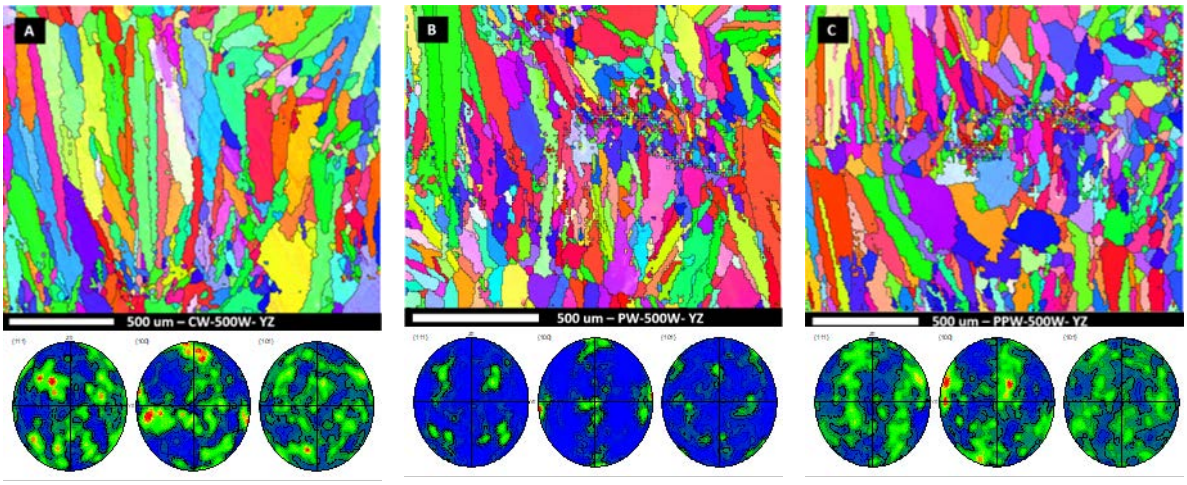

Figure 6.16: EBSD Inverse pole figure (IPF) map of IN718 samples produced by (A) CW 500W and (B) PW 500W (C) PPW 500W in the building direction with no PWHT

Depending on the power mode used, some differences in the microstructure and texture can be observed on the samples produced. In particular, the CW power mode produced samples characterised by a microstructure dominated by columnar grains, with a small percentage of equiaxed grains between the layers. While the PW enhanced the refinement of the grains, the lowest grain columnarity and a high percentage of equiaxed grains can be observed (Figure 6.16b). The PPW power mode produced samples with a mixture of columnar and equiaxed grains (Figure 6.16c). The coarser columnar grains produced using the CW was justified by the significant heat input which was almost twice the heat accumulated by the deposited

material when the PW and the PPW were used. Moreover, it is important to highlight that although the PPW and the PW have a comparable WAP, the cooling rate achieved by the PPW mode was lower than the one experienced by the sample produced by the PW which resulted in a larger grain size (Figure 6.17c). The finer microstructure produced using the PW (higher cooling rate), was also confirmed by the grain size measurements obtained by the EBSD mapping analysis. Indeed, as shown in Figure 6.17b, the samples produced by PW revealed a higher frequency of finer grains around 10µm. The effectiveness of the PW in producing samples characterised by finer and equiaxed microstructure was also confirmed by Imbrogno et al. [226] .

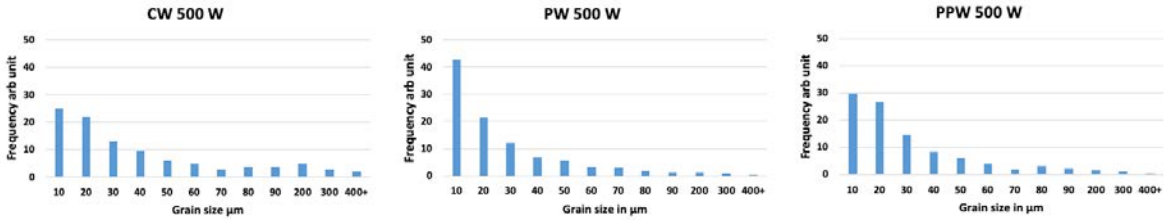

Figure 6.17: grains size statistic in (a) CW (b) PW (c) PPW

Figure 6.17a also highlights the heat accumulation effect on grain size. The highest heat accumulation was observed when the CW power mode was used and this is also highlighted by the highest frequency of grains with a size higher than 200µm, 300µm and 400µm. The samples produced by the PW power mode frequently showed small equiaxed grains mostly nucleated between the layers, while within each layer elongated columnar grains were observed. Although no satisfactory explanation exists in research literature for this microstructure behaviour, the EBSD results suggested that the columnar grains grew immediately after the Heat Affected Zone (HAZ) (Figure 6.18). In this region, multiple layers are affected by the heat source leading to a different effect on the microstructure and mechanical behaviour between the Fusion Zone (FZ)and the HAZs. For example, Huang et al. [227] discovered that the hardness was lower in the HAZ than the FZ. Lakshmi et al. [206]

found out that in the first few layers. Fine grains were expected due to the heat sink effect of the substrate, although the deposited material was subjected to a different thermal cycle. Far from the substrate the presence of fine grains was less evident.

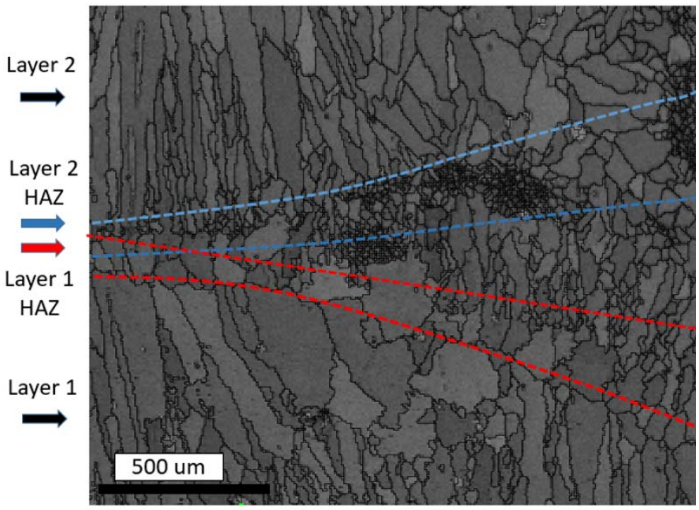

Figure 6.18: Effect of the HAZ between two layers on the microstructure

During the welding process the metallurgical characteristics of the material are subjected to different changes induced by the amount of heat involved. One of the main interesting regions is the FZ, where the grains are generally the largest and their growth direction is driven by the heat source movement.

It is worth noting that the grain size can also be altered and tailored by changing the pulse duration. Indeed, different pulse durations allowed the heat accumulation and the cooling rate to be modified during the deposition process. Different cooling rates effect the growth of the grain differently. According to Lee et al 2014 [123], it is possible to control the growth of the dendrite by controlling the solidification rate and thermal gradient. As highlighted by Figure 6.19a, the grains are significantly bigger and more columnar when the duration of the peak power is longer, and the cooling rate is lower. Whereas the grains become much smaller and less columnar when the duration of the peak power is shorter, and the cooling rate is higher (Figure 6.19b). In this example, the grain columanirty increased in the PPW-LCC by 64%

compared to the PPW-SP, on the other hand, the PPW-HCC decreased in grain columanirty to 57% compared to the PPW-SP.

A study by Mumtaz et. al. [224] investigated different pulsing shape techniques which showed a reduction in spatter ejection during processing and improvement of the surface roughness with minimising melt pool width. Therefore, the use of smaller pulse duration and a higher cooling rate can minimise the melt pool width, and consequently reduce the heat accumulation that leads to finer microstructure.

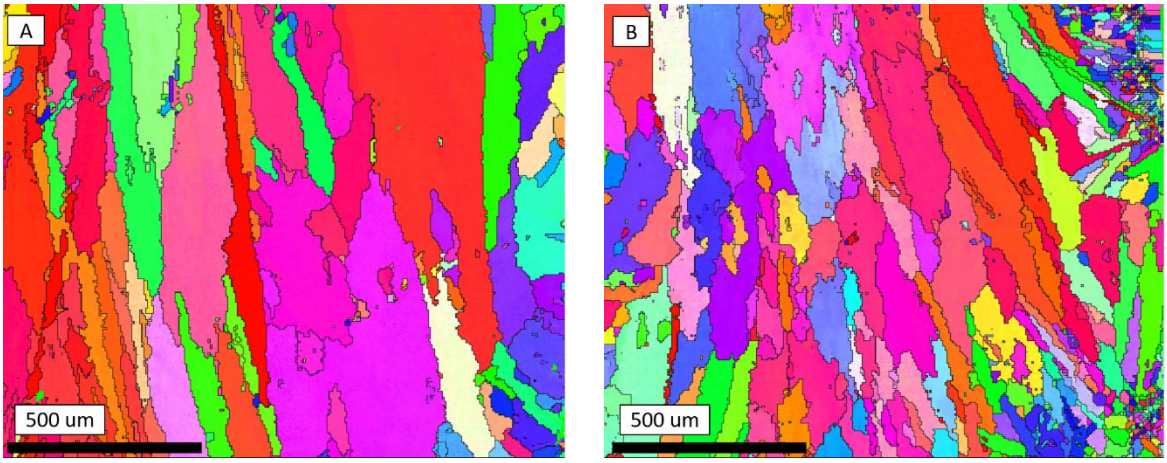

Figure 6.19: EBSD Inverse pole figure (IPF) map of IN718 samples produced by a partial pulsing laser waving in the building direction with no PWHT (A)PPW +75-25 700W (B) PPW -75+25 700W

6.4.2 Effect of the Power Mode on the Segregation

The effect of the power mode on segregation formation and morphology were analysed. Figure 6.20 illustrates the segregation distribution on the cross-section of different samples produced by CW, PW and PPW. As shown in Figure 6.20A, the use of CW promoted the formation of long chain-like dendrites and segregation area, whereas the pulsing generally led to the formation of smaller dendrites, and a relatively finer segregated area (Figure 6.20B and Figure 6.20C).

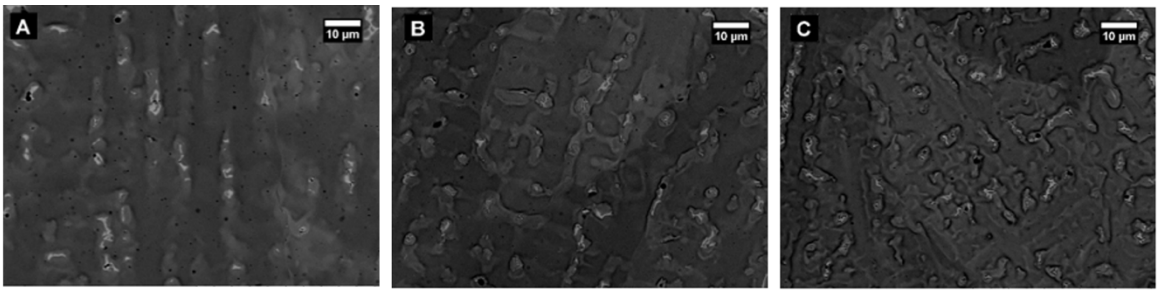

Figure 6.20: power mode effect on the as built samples of 700W 700 mm/min (A) CW (B) PW (C) PPW

Sui et al. [228] reported that long chain-like Laves phase is more crack susceptible, while the use of the pulsed laser allowed a fine Laves phase to form due to the high cooling rate (G·R) and a low ratio of a temperature gradient to the growth rate (G/R). Figure 6.21 reported the percentage of Nb segregation in general, was higher in the samples produced by CW and it decreased when the pulsed power modes (PW and PPW) were used. Almost the same behaviour of the Nb segregation on CW and PPW samples was recorded, with less segregation of the Nb in the PPW. This is because the melt pool did not have time to cool down as the power continues but with less intensity in the low peak of the pulsing cycle. The PW showed less Nb segregation with wide variation in higher powers. However, in general, still behaving with less Nb segregation in higher power samples, Figure 6.21 illustrates the Nb segregation on a wide range of samples were produced with different power modes.

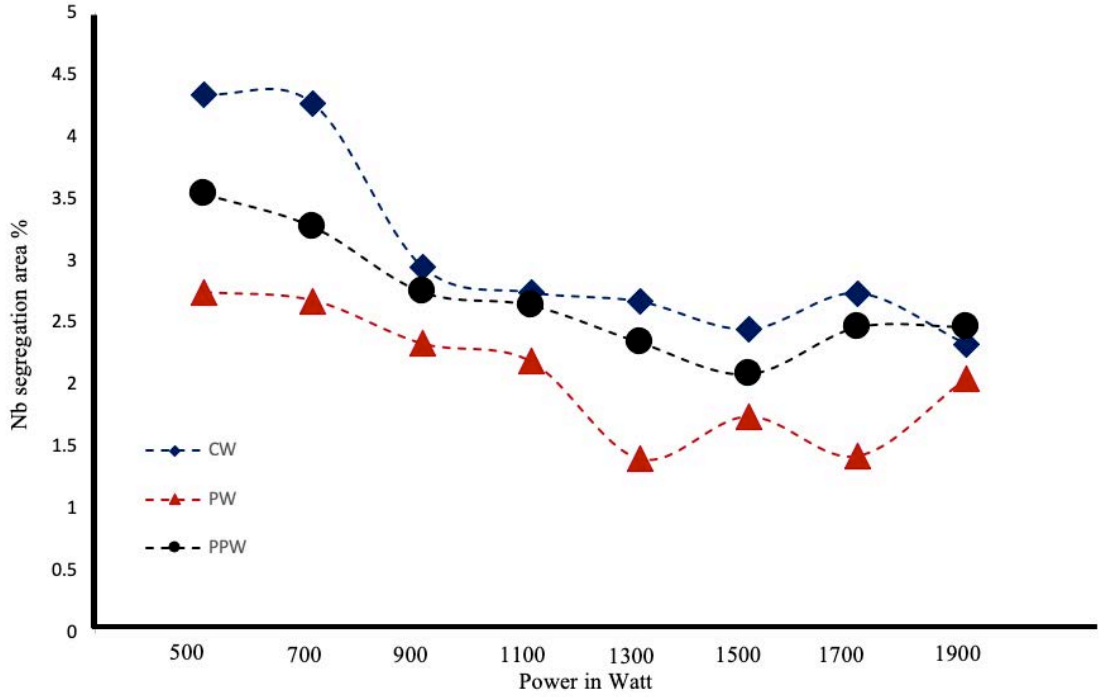

Figure 6.21: power mode effect on Nb segregation behavior

The pulsed laser breaks the continuous growth of the dendrites, disturbing the ejection of the Nb from the core of the dendrite into the liquid phase. Although the PW and PPW are power mode based on pulsed laser, the higher cooling rate provided by the PW, enhanced the formation of small segregation zones with a lower concentration of Nb. Furthermore, the cooling rate in the laser pulsing processes can be enhanced by modifying the duty cycle, increasing the period of low power, and decreasing the period of peak power and vice-versa. Figure 6.22 shows the microstructure of the PW and PPW standard pulse and high cooling cycles and low cooling cycles.

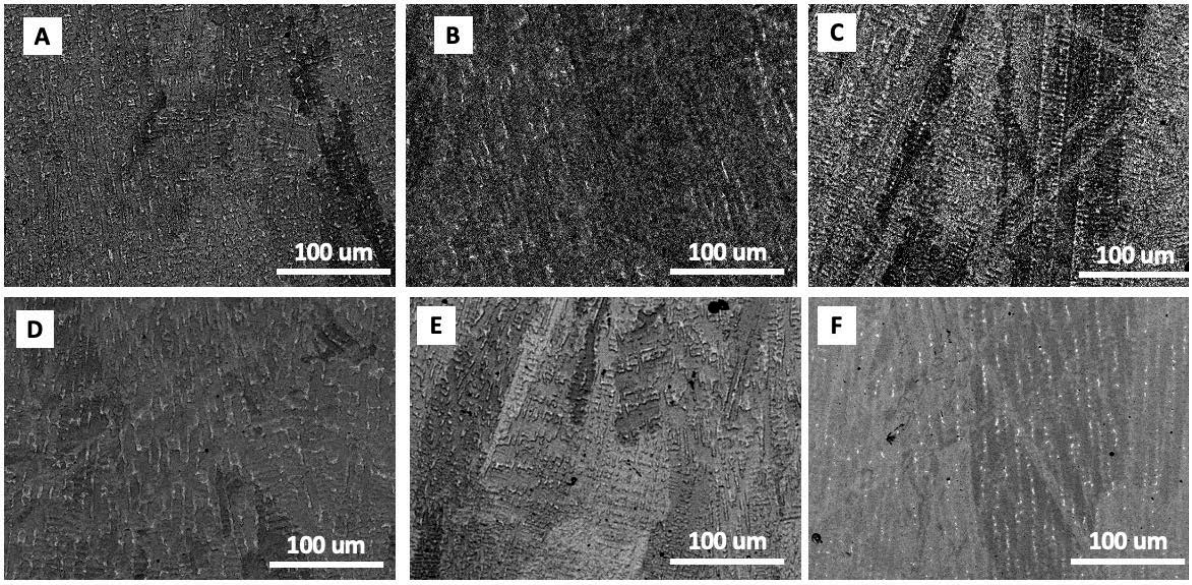

Figure 6.22: 700W (A) PW-SP (B) PW-HCC (C) PW-LCC (D) PPW-SP (E) PPW-HCC (F) PPW-LCC

As mentioned before the highest concentration of Nb in the segregated area was observed on the samples produced by CW. Although PW and PPW have the same average power, they show different Nb segregation results. When the PPW-HCC was used, the lower power and the higher cooling rate led to fine dendrites, and a high percentage of Nb segregation was observed. Moreover, PW-HCC was much lower in heat input and more in Nb segregation because of the high solidification rate that produces fine, equiaxed like structure dendrites with smaller DAS. On the other hand, PW-LCC shows the highest heat input and the lowest Nb segregation. The high heat allowed more Nb to dissolve into the matrix, as well as leading to a higher value of DAS. Dendrite core which injected Nb into the liquid was also large, therefore, the quantity of the dendrite was less. Figure 6.23 shows the Nb segregation behaviour on an as-built sample with different power modes and cooling cycles compared with the continuous power wave.

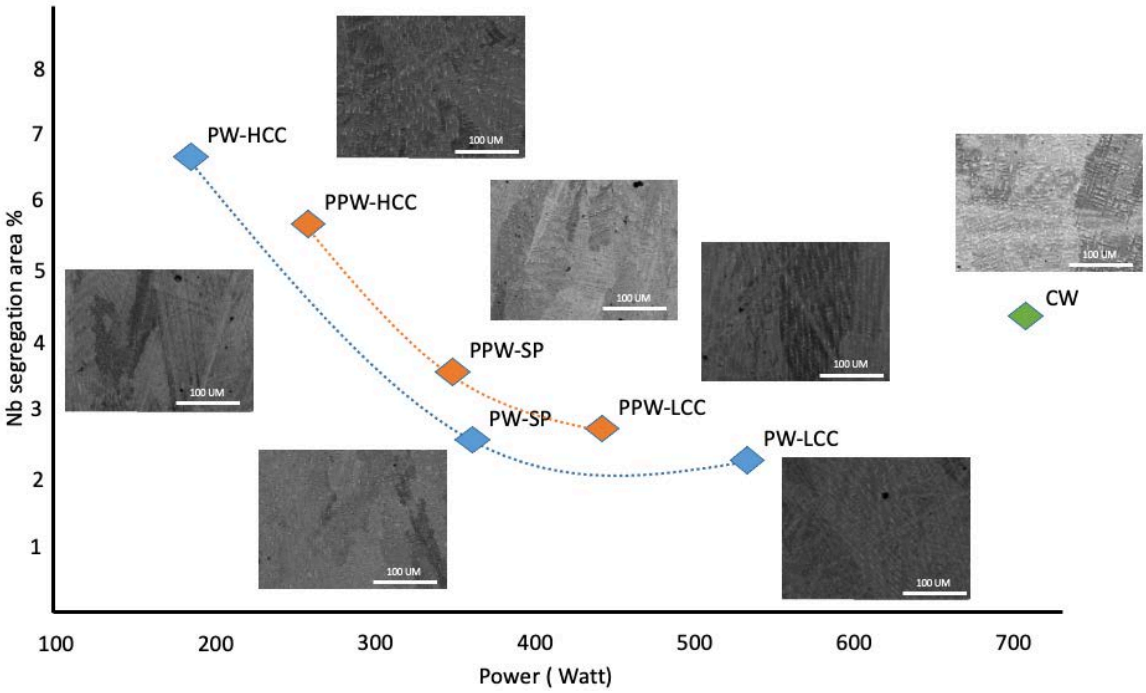

Figure 6.23: Nb segregation on an as-built sample with different power mode and cooling cycle.

The use of the pulsed laser should produce less Nb segregation percent area than the continuous power. This is due to the breaking of the continuous dendrite, and continuous growth of the dendrites disturbing the ejection of the Nb from the core of the dendrite into the liquid phase. However, the PW-HCC and PPW-HCC showed more Nb segregation than the PW SP, PPW SP and the CW. The explanation can be clarified by calculating the WAP for the PW-HCC, which is 185W, and the PPW-HCC which is 262W. As shown in Figure 6.23 the Nb segregation continues to increase with the decrease of laser power. However, the WAP values are not represented in Figure 6.23. Figure 6.24 represents the Nb segregation changes depending on the WAP calculated for the PPW and the CW. Therefore, it is possible to note that considering the same WAP value, the CW led to higher Nb segregation formation than the PPW.

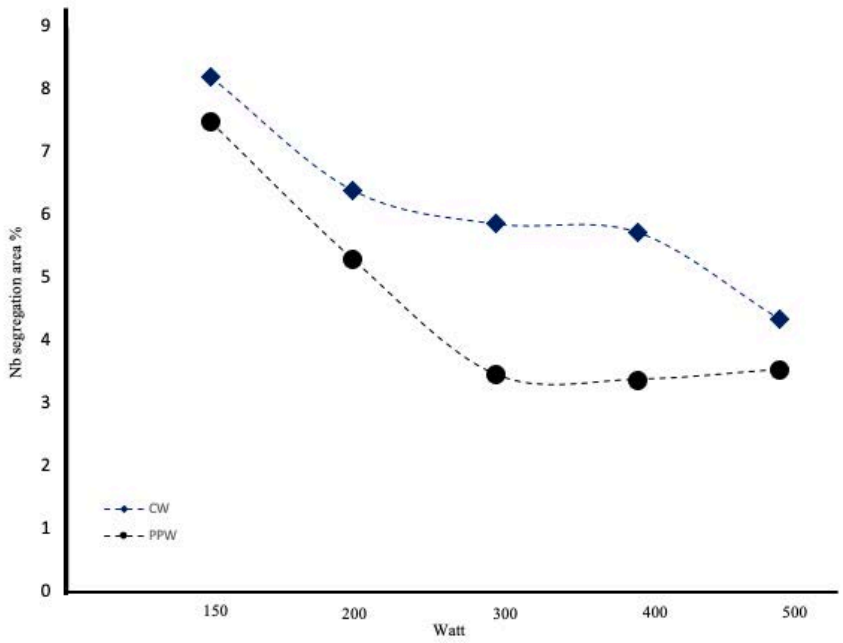

Figure 6.24: low power mode effect on Nb segregation behaviour

6.4.3 Effect of the Power Mode and the Heat Treatments on the Microstructure, Segregation and Mechanical Properties

The effect of the heat treatment combined with the power mode was investigated. The heat treatment, as explained and described in Figure 6.8, are annealing and ageing. Annealed samples were left in a furnace for only one hour at a temperature equal to 980°C. The temperature of static recrystallization of the IN718 alloy is about 1020°C as reported in [229]. It is important to highlight that although the temperature did not reach the recrystallization temperature, the grain size and the morphology slightly changed, resulting in larger grains than the ones observed in the as-deposited samples. Figure 6.25 shows the EBSD map of CW 400W before and after annealing treatment. It is possible to note that the grain size, after the heat treatment, was slightly bigger than the as-deposited ones but the morphology did not show any significant modification. Therefore, the one produced by the deposition process was still dominant.

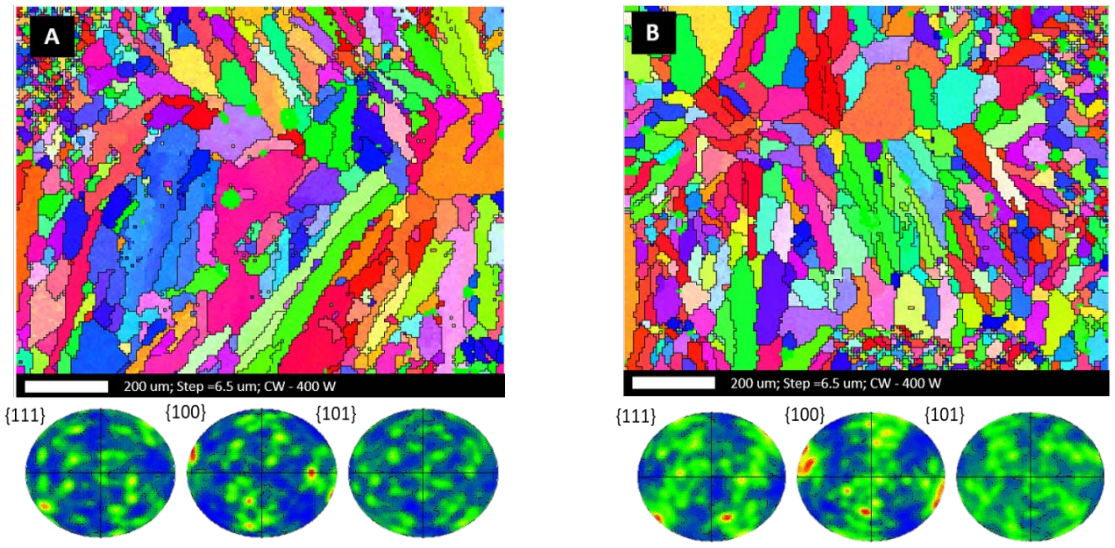

Figure 6.25: EBSD Inverse pole figure (IPF) map of IN718 samples produced by a CW laser power in the building direction (A) As-built (B) Solution annealing

Kashyap et al. and Jin at al. [230, 231] studied the behaviour of the grains with different annealing temperature and different processing time. In general, higher heat triggers grain growth. Prolonged exposure of the samples at high temperature will induce significant grain growth compared with reduced exposure time. However, the annealing treatment performed in this study did not significantly affect the microstructure as highlighted by the EBSD map, and the annealing process was not longer than one hour. Figure 6.26 shows in detail the slight change in grain size due to the annealing process. However, the temperature of the annealing treatment and the exposure time were not able to trigger a significant recrystallization phenomenon on the samples.

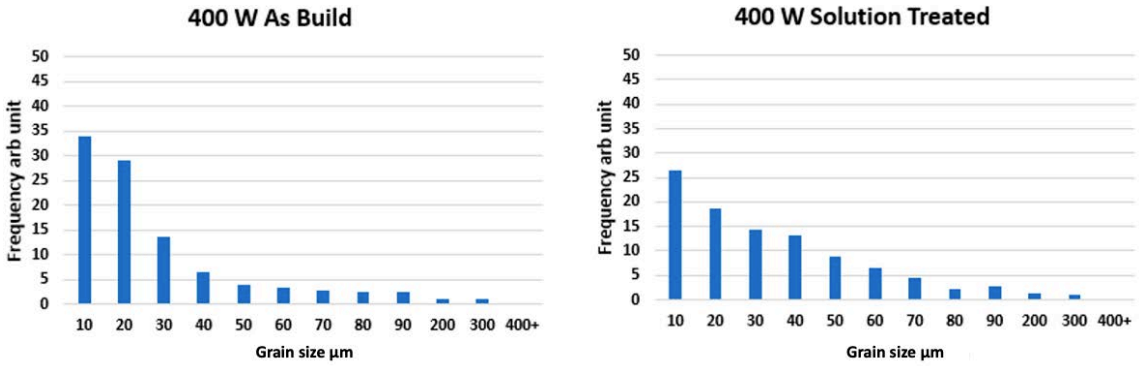

Figure 6.26: Grains size before and after the solution treatment

Figure 6.27 shows the Nb segregation percentage in the three different power modes with three conditions when 700W was used. The Nb segregation is affected by the heat accumulated during the deposition process and the heat applied during the heat treatments (i.e., annealing or ageing). Although, the ageing treatment reduced the Nb segregation, the most significant results were observed when the annealing was performed. The reduction of Nb segregation clearly shows the Laves phase. Zhang et al. [217] claims that the Laves phase will not change their original morphology after ageing, moreover, Nb segregation reduces the quantitative ration after ageing which results in exposing the Laves phase. It was also observed the Nb behaviour reflected on the aged samples with less segregation. The lowest amount of Nb segregation was observed on the samples produced by PW, followed by PPW but CW samples showed higher values. Figure 6.28 shows the reduction on Nb segregation varies in the aged samples. The low power sample has a reduction of Nb segregation at about 58%, compared to the as-built samples and the percentage decreased with the increase of power input. The highest power decrease in Nb segregation was about 46%, compared with the as built. Whereas the annealing treatment reduces Nb segregation by almost 99% or almost eliminate segregation in the lower power and the percentage of Nb segregation increased with the increase of the power, until the highest power shows an 84% reduction on Nb segregation.

The annealing treatment dissolves the Nb, however, the treatment was not long enough to trigger the formation of the γ''strengthening phase. Instead, some δ phase was forming and that shows in the low power samples.

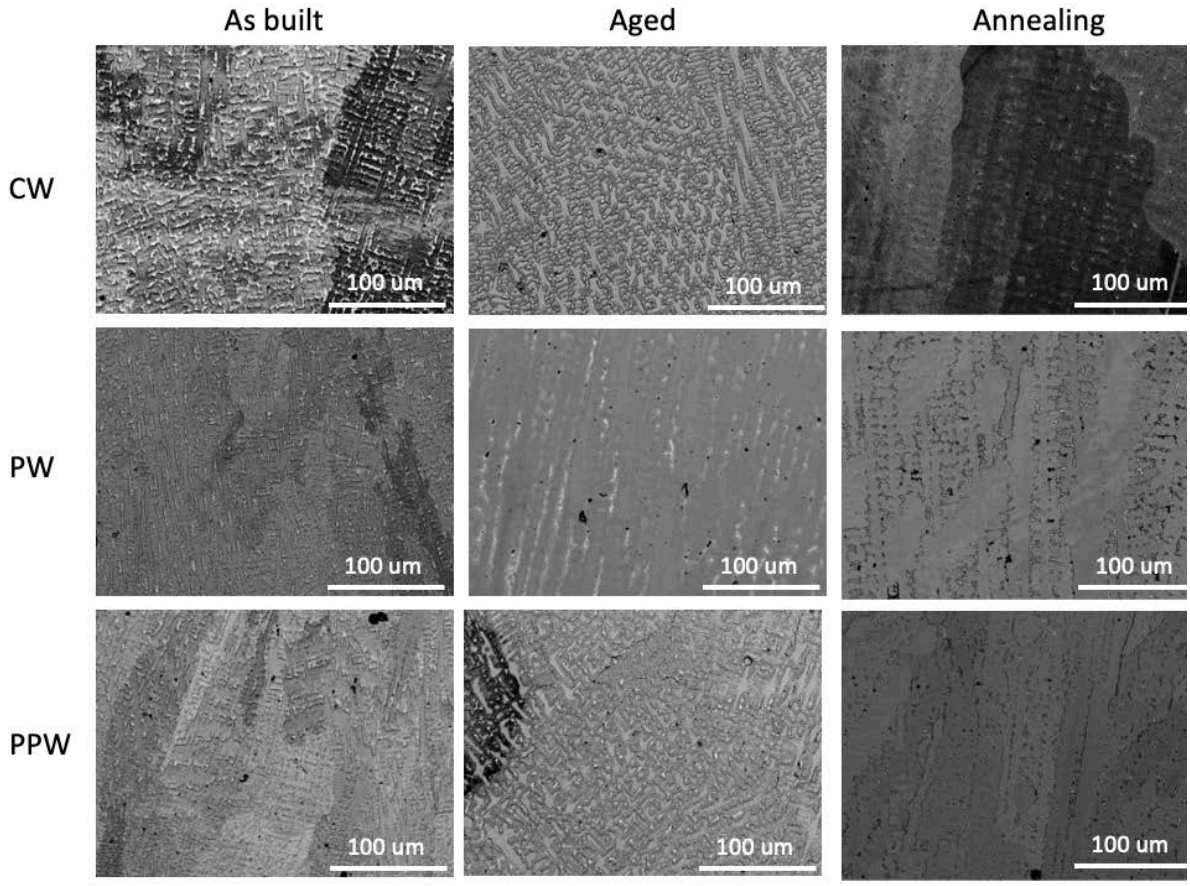

Figure 6.27: Nb segregation percentage in the three different power modes with three conditions for the 700W parameter

Annealing, which is a short post-processing procedure, dissolved a significant amount of the Nb segregation, however most of the Nb dissolves to form the δ phase. The delta phase was noticed in the PPW-SP low power (500 W), while it was difficult to note on the samples produced with higher power (higher heat input). Figure 6.29 shows the δ phase structured.

Multiple power was used and Nb segregation was measured on all three conditions and a map was drawn. Ageing reduced significantly the Nb segregation, compared to the as-built parts. Solution annealing treatment almost eliminates Nb segregation. Figure 6.28 shows Nb segregation percentage on different continuous power value for different sample conditions.

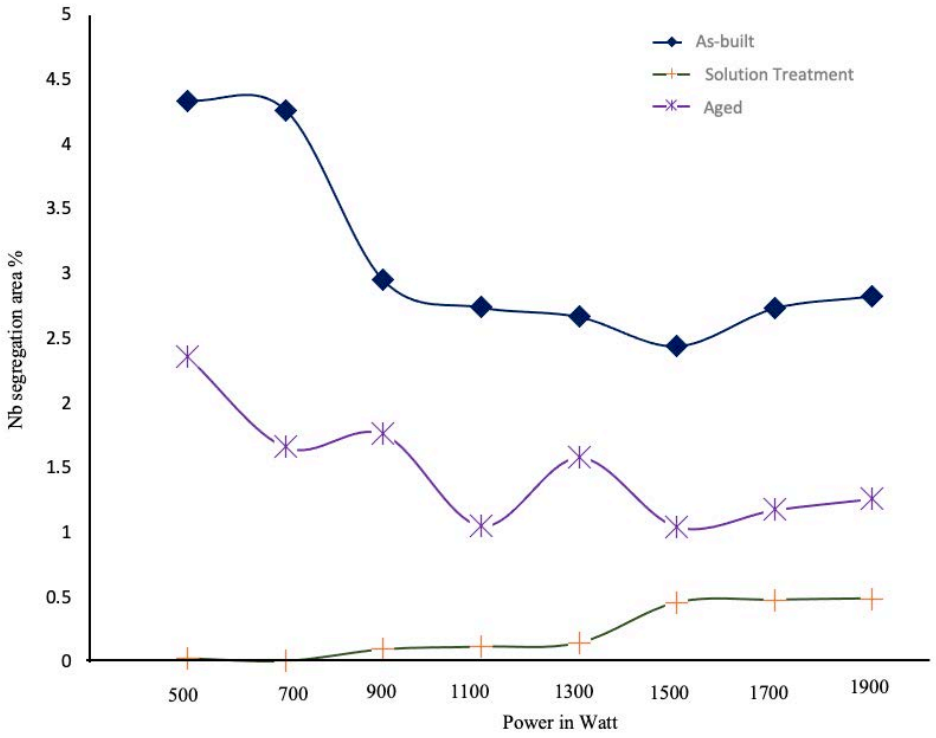

Figure 6.28: Nb *segregation percentage mapping for different power values on CW mode and three different conditions (as-built, Solution Treatment and Aging)*

Annealing treatment dissolves the brittle Laves phase, but due to short post-processing time led to the formation of the δ-phase. Ageing did not dissolve all the Laves phase, however, it was essential to trigger the precipitation strengthening. Azadian et al.[232] showed that the precipitation of δ-phase, due to the one hour annealing treatment, was equal to 2% in volume fraction and this volume increased with the increased exposure time.

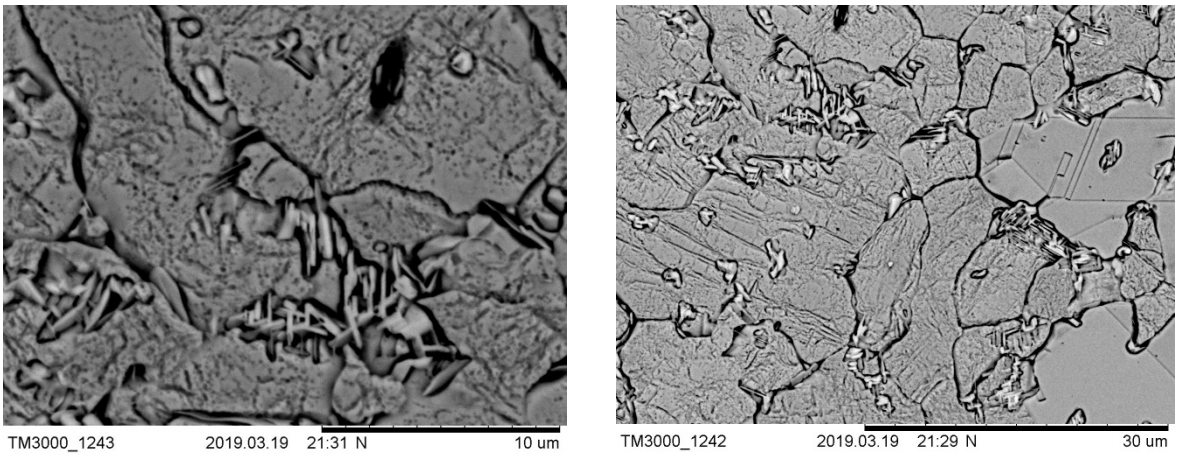

Figure 6.29: delta phase formation after the annealing treatment

EDX was performed on the as-built samples produced with different power modes. In detail, three different locations: matrix, dendrite core and Laves phase were considered. Three measurements were performed, and the average value was considered. In the matrix, the CW Nb content was around the expected percentage. Whereas the PPW was significantly lower than expected this could be due to the low peak power and the reduced heat accumulated that did not allow the Nb to dissolve into the matrix.

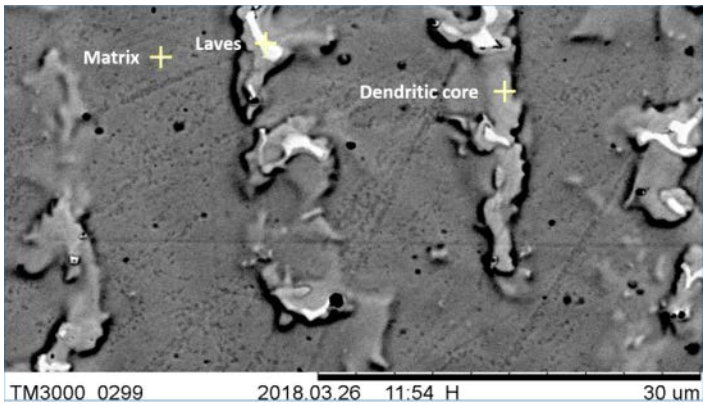

Figure 6.30: the three areas subjected to EDX analysis

In the dendrite core a high accumulation of Nb in the PPW was observed and this result explained the lower percentage in the matrix. The PW shows good distribution of Nb in the three analysed regions, suggesting that the higher cooling rate and the dendrite break contrasted the Nb accumulation within the inter-dendritic region. The use of PW was effective in reducing the accumulation of the Nb within the detrimental Laves phase.

Table 6.4: Energy dispersive spectrometer (EDX) elemental mapping of matrix dendrite core and laves of IN718.

	Nickel %	Iron %	Chromium %	Titanium %	Aluminium %	Molybdenum %	Niobium %
CW Matrix	51.11	18.85	19.02	0.57	0.37	3.12	4.16
PW Matrix	49.74	19.95	19.30	0.46	0.27	3.02	3.37
PPW Matrix	51.63	20.12	18.58	0.54	0.39	3.09	2.91
CW laves	36.63	12.62	12.44	0.89	0.19	4.91	28.79
PW Laves	47.47	16.48	16.04	0.91	0.26	3.16	9.57
PPW laves	42.73	12.37	12.73	1.63	0.39	3.93	22.81
CW dendritic core	49.58	17.25	17.66	0.92	0.32	3.54	8.07
PW Dendrite core	48.87	16.40	17.21	0.85	0.37	3.33	7.90
PPW Dendrite core	48.95	16.49	16.37	1.02	0.38	3.30	9.67

6.4.4 The Effect of Laser Power Mode on Porosity and Density

The samples produced in this research work were characterised by crack free regions and the layers were well bonded. Very small areas were represented by limited pores due to the small gas trapped during solidification. Usually, pores are created when the pressure within the pores exceeds the pressure within the interdendritic liquid. As a result the decrease of the laser power leads to a decrease in the solubility of the gas element [220]. It was also observed that high laser power leads to the production of samples that show higher density, and reduced porosity than the ones produced by lower laser power. This is compatible with the findings of Zhong et al [209] . This trend was experimentally observed in the samples produced and the main results are reported in Figure 6.31. Also, Kobryn et al.[11] showed that porosity can be reduced by increasing laser power and scanning speed. Overall, the porosity variations are rather limited due to the high quality of the powder, as evident through the lack of entrapped pores within the powder particles. The porosity does reduce significantly in the sample produced by pulsing the laser in general. Furthermore, the PW show an increase in density,

therefore, reduction in porosity followed by the PPW. This result is compatible with Andrew et al. [73] who found that a pulsed beam can reduce the porosity found using a continuous beam, but low pulse repetition frequencies give a coarse layer structure.

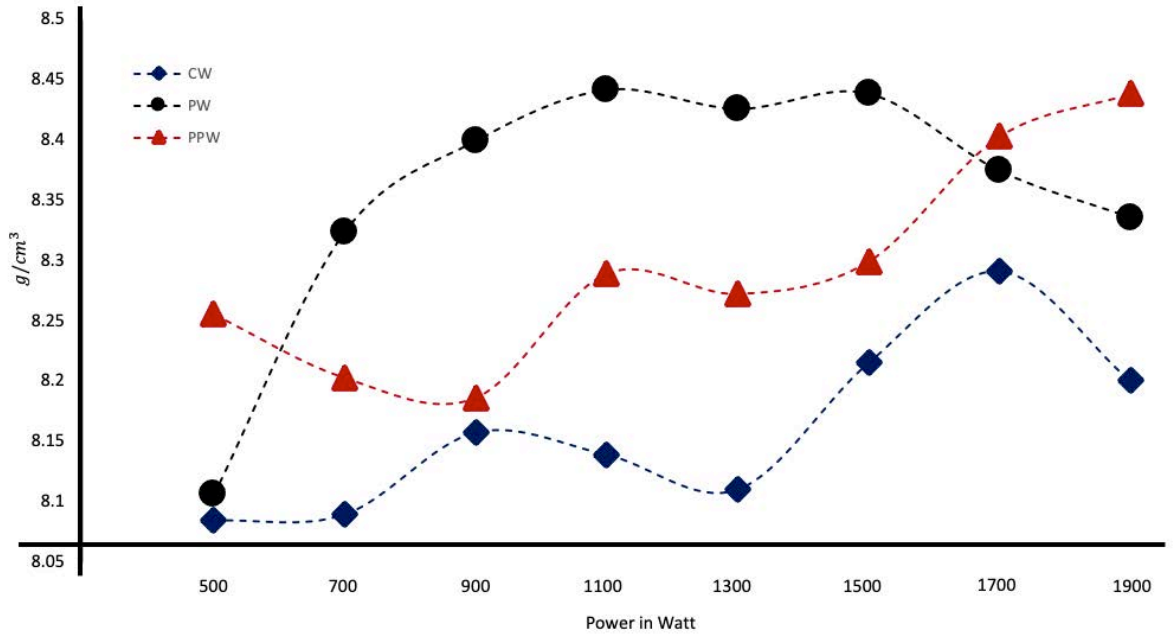

Figure 6.31: Effect of the power mode and the laser power on the density.

The XRD results shown in Figure 6.32 for all the three power modes and three conditions. Coupons show additional peaks that did not exist on the as-supplied powder. In θ angles equal to 75° and 100° small peaks appear on all additive manufacture samples, regardless of the power mode or the post-process. This result is because of decreased lattice parameter by depletion of the matrix due to the precipitate and Laves phase formation. The samples that did not show peaks on the (111) γ are the PW 900W annealed and the higher power sample 1500W as-built. For the preferred orientation (200) the samples that did not show peaks were CW 900W aged and PW 900W as-built. The samples that did not show peaks at (022) are PW 900W annealed and PW 900W as-built, CW 900 aged and CW 1500W.

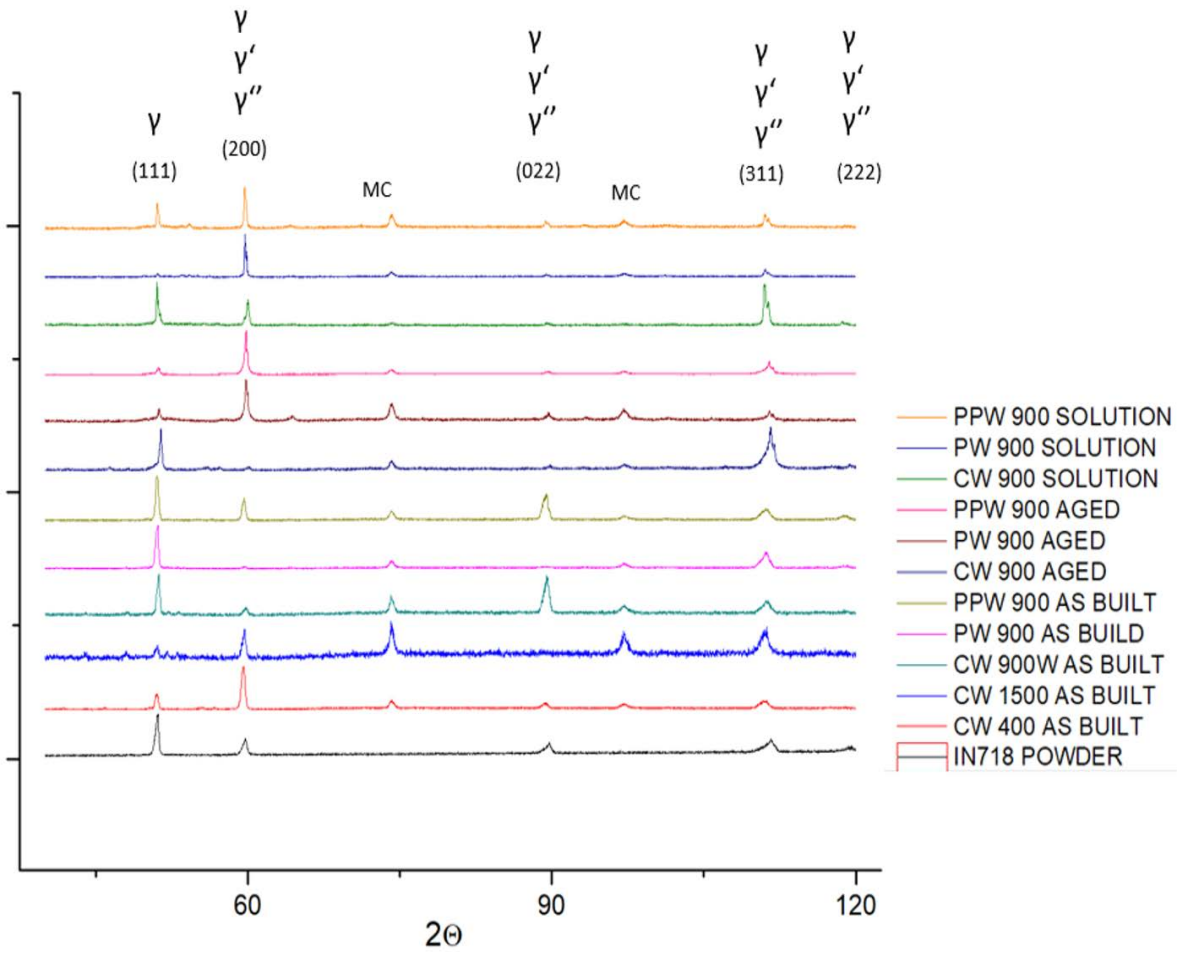

Figure 6.32: XRD results for three power modes and three conditions

The hardness results of the as-fabricated samples with the three power modes are shown in Figure 6.33. The obtained results suggest a possible relationship between hardness, fine dendrites, and the grain size. A primary factor of increasing hardness in IN718 is the precipitation phenomena. In this case, a lower laser power such as 500W-900W led to gentle heating, and accumulation of heat which provide finer dendrite microstructure. This provoked what seems to be limited ageing, which may stimulate the formation of limited strengthening phases (γ′ and γ″), since γ′ and γ″ phases precipitate and increases hardness. The γ′ can form in a shorter time and requires less heat than the sluggish γ″ [23]. The grain size might also affect hardness results. In general, the smaller the grain size, the harder the material and since lower power produces a smaller grain size, the greater hardness could be justified by the finer

microstructure. On the contrary, high power such as laser power of 1500W-1900W led to an extremely high temperature and a significant accumulation of heat. Therefore, the Nb tends to dissolve into the matrix. Andrew et al. found that a finer dendrite microstructure increases hardness [73].

As-fabricated builds typically have poor mechanical properties, compared to wrought products due to the presence of detrimental phases. However, Qi et al. [22] showed that mechanical properties can be improved by performing a homogenisation heat treatment at ~1100 °C for 1–2 h. This is followed by a solution and ageing treatment to allow the precipitation of the strengthening γ′ and γ″ phases. It is important to highlight that in this study, only ageing and annealing as separate cases were investigated to prove the point of control of the grains size and morphology. The post heat treatment below the recrystallization temperature was used to improve the mechanical properties, without affecting the grains size and morphology.

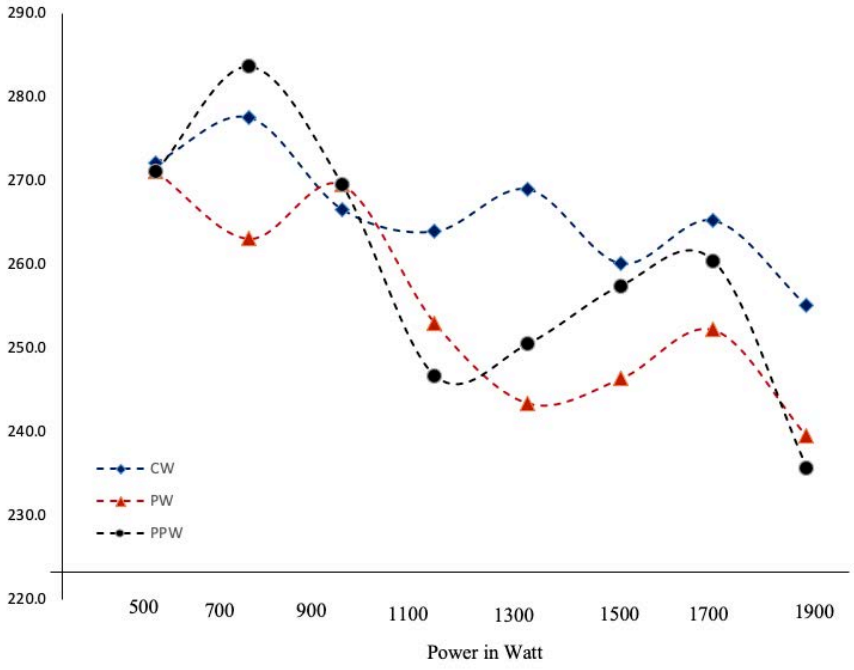

Figure 6.33: The effect of the power mode and the laser power on the hardness.

Hardness was compared between the three-power modes (CW, PW and PPW). For two different power values (700W and 1700W) and for three different conditions (as-built, annealed and aged) in Figure 6.34. The results show that as-built samples show the lowest hardness with less than 225 HV. It also shows that lower power samples have a slightly higher hardness than those at higher power. Liu et al [233] measured the as-built hardness and it was 225 Hv. However, the hardness for the as-built sample for all the three power modes was the same suggesting that the pulsing has no significant effect on hardness. Annealing is a short heat treatment, which increases the hardness significantly from 225 HV to an average of 320 HV considering the pulsed mode. This is due to the dissolution of the Nb into the matrix. However, the short time of the process led the Nb to form the δ phase instead of the strengthening phase γ″. It did not show any increase in hardness in the CW which could be a result of the high Nb segregation that CW had in the as-built condition, and the annealing process does not have enough time to dissolve the Nb. The aged samples show the highest hardness among all three cases with an average of 375 HV. Sundararaman et. al. [234] explained the increase in hardness was due to the carbide precipitation which seemed to be confined almost exclusively to the austenite grain boundaries. Liu et al [233] also measured the hardness of the IN718 samples with a standard double ageing process and the results were about 450 HV. It is worth mentioning that the results of hardness in this study are lower than Liu et al. which uses higher power (laser surface annealing).

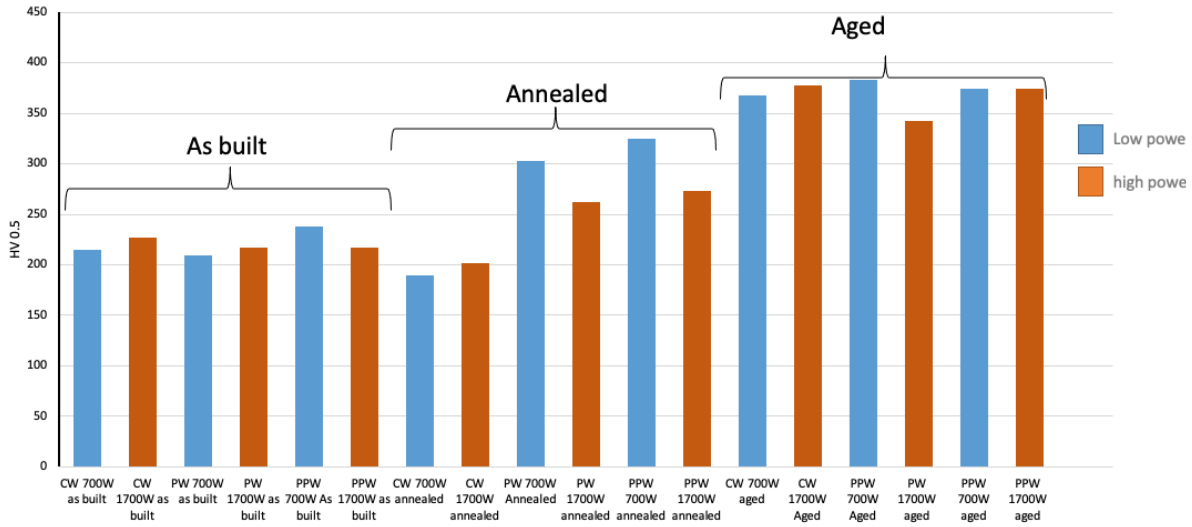

Figure 6.34: hardness results for the three power modes and three conditions.

The single-walled sample was made with 900W and 700 mm/min scanning speed and 28 g/min powder feed with different power mode. The sample cut in XZ dimension showed the grains grow perpendicular to the tensile samples (Figure 6.35). The sample surface was subsequently smoothed by sanding to perform the tensile tests. Brinkman and Korth [235] measured the tensile test at room temperature and at 650 C° for solution annealed and double aged samples. They showed that the UTS was approximately 250 Ksi at room temperature (1723 MPa), whereas, at 650 °C the UTS is 210 Ksi (1448 MPa). The true stress-strain at 650°C could be described by the Ludwik [236] equation:

$$\sigma = \sigma p + K\varepsilon p^{\eta} \qquad \text{Equation 6.3}$$

Where σp, K, and η are constants for a given material heat treatment and temperature, and σ (in ksi) and εp are the true stress and true plastic strain values. Respectively σp was found to be approximated by the expression:

$$\sigma p = A - BT \qquad \text{Equation 6.4}$$

Where T is temperature, °C. The elastic portion of the stress-strain curve is described by σp /E, where E is the elastic modulus.

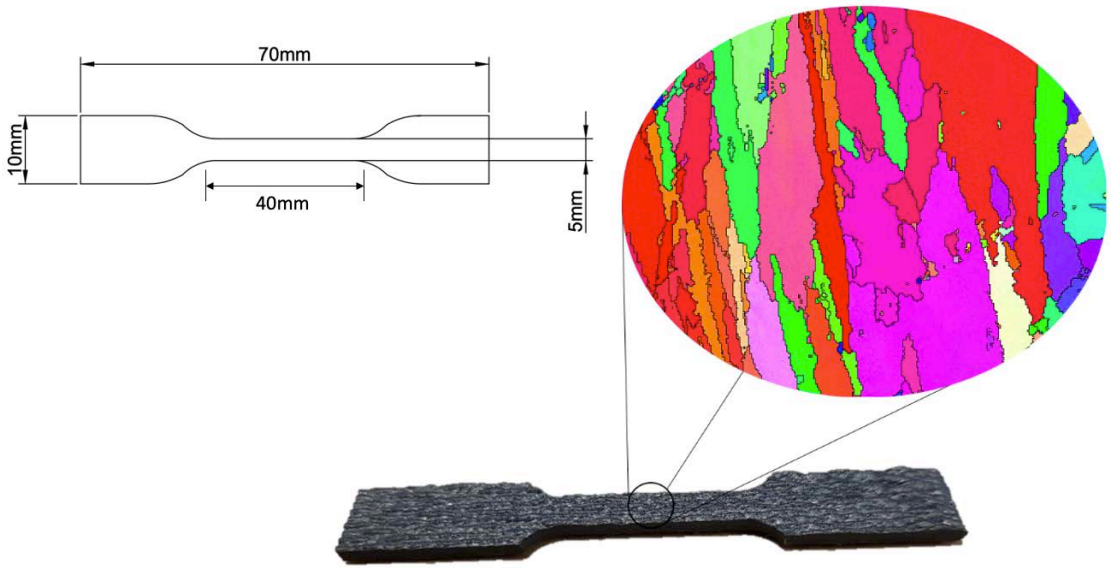

Figure 6.35: The ordination of the grains morphology and the dimensions of the test coupons of the tensile samples

The engineering tensile test curves of IN718 alloy in the aged conditions are shown in Figure. 6.36. Three samples from each condition were done except the CW 900W two tensile samples. The higher results from each condition were used to be compared with other conditions. All tests were done in a room temperature. The engineering stresses of all the power modes are almost similar, however, the PPW has an increase in elongation because using pulsing decreasing cooling time which gives Nb more time to dissolve. In this study the material was characterised by a UTS value of 1200MPa and 1100MPa for samples produced by CW and PW. Figure 6.36 (B) shows decreasing cooling time to 25% of the pulse duration (PPW LCC), an increase in the tensile results and showed less ductility than the PPW-SP. Figure 6.36 (C) shows that increasing CW power will have no effect on tensile results although it will affect the elongation. More power creates more elongation and that is due to more heat, Nb segregation has more time to merge back into the matrix and reduction of laves phase which is brittle. Figure 6.36 (D) also shows that decreasing the cooling cycle time increases elongation. Table 6.5 list the details of each sample.

Table 6.5: Tensile test parameters

Specimen ID	F_{max}	dL at F_{max}	F_{Break}	dL at break	a_0	b_0	S_0
	N	mm	N	mm	mm	mm	mm^2
PW 900W 700SS 75/25 1	11711.73	1.60932	11311.33	1.629	2.08	5	10.4
PW 900W 700SS 75/25 2	11724.52	1.541039	11617.76	1.560799	2.09	4.97	10.3873
PW 900W 700SS 75/25 3	11739.79	1.47444	11192.33	1.49976	2.02	5.05	10.201
CW 900W 700SS aged 1	9982.368	0.493199	9927.792	0.495481	2.02	5.03	10.1606
CW 900W 700SS aged 2	9811.415	0.4496	9666.795	0.465959	1.96	5.26	10.3096
PW 100hz 900W 700SS 50/50 aged 1	10105.18	0.45336	9398.948	0.49664	2.02	5.01	10.1202
PW 100hz 900W 700SS 50/50 aged 2	10494.46	0.68732	9561.082	0.755517	1.97	5.03	9.9091
PPW 100hz 900W 700SS 50/50 aged 1	10809.3	0.67544	10457.04	0.710319	2.53	4.64	11.7392
PPW 100hz 900W 700SS 50/50 aged 2	9495.007	0.26336	9229.213	0.26636	2.4	4.6	11.04
PW 100hz 900W 700SS 50/50 aged 3	10115	1.343559	10044.98	1.37532	1.82	5.07	9.2274
PPW 100hz 900W 700SS 50/50 aged 3	9897.883	0.3642	9596.722	0.380519	2.49	4.69	11.6781
PPW 100hz 900W 700SS 75/25 aged 1	11976.56	0.507721	11678.86	0.52788	2.9	4.75	13.775
PPW 100hz 900W 700SS 75/25 aged 2	11607.85	0.322079	11291.32	0.372879	3.99	2.77	11.0523
PPW 100hz 900W 700SS 75/25 aged 3	11409.95	0.536199	10962.92	0.56528	3.99	4.71	18.7929
PPW 100hz 900W 700SS 25/75 aged 1	8732.476	0.542559	8561.514	0.561599	1.97	4.59	9.0423
PPW 100hz 900W 700SS 25/75 aged 2	8796.569	0.357159	8563.422	0.376479	1.97	4.64	9.1408
PPW 100hz 900W 700SS 25/75 aged 3	8784.942	0.575799	8475.707	0.576282	2.1	4.65	9.765

Where F_{max} is maximum force and dL is the change in length F_{Break} if force at the breaking point, a_o is the thickness of the original cross section, b_o with of the original cross section and s_o is cross section area. Figure 6.36 (E) shows that the PPW-SP samples with the same young's modulus and slightly different in the ultimate strength and different elongation between 9% to 11%. In Figure 6.36 (F) shows that the PW-SP samples with the same young's modulus and almost same ultimate strength and different elongation between 3.5% to 9%. Figure 6.36 (G) shows that the PW-LCC samples with almost same young's modulus and same ultimate strength and almost same elongation between 10% to 11%. Figure 6.36 (H) shows that the PPW-LCC samples with the different young's modulus (slope) and different in the ultimate strength between 700MPa and 900 MPa also, different elongation between 2.5% to 3.7%. Figure 6.36 (I) shows that the CW samples with the slightly different in young's modulus and almost the same ultimate strength and elongation between. Figure 7.36 (J) shows that the CW high power samples with slightly different in young's modulus and almost same ultimate strength and different elongation between 8% to 13%. Figure 6.36 (K) shows that the PPW-

HCC samples with the different young's modulus and different in the ultimate strength and different in elongation between 2.5% to 3.8%.

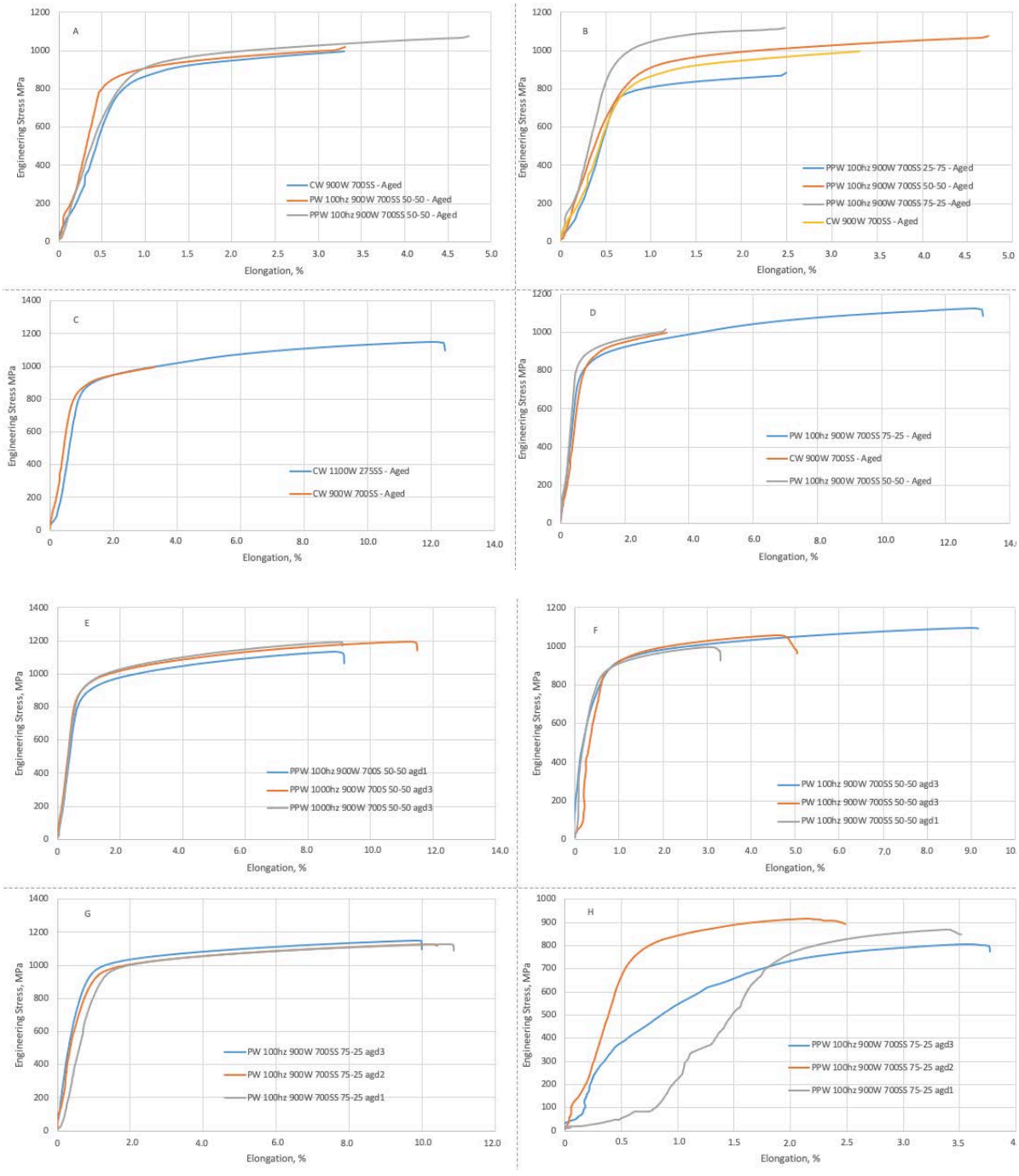

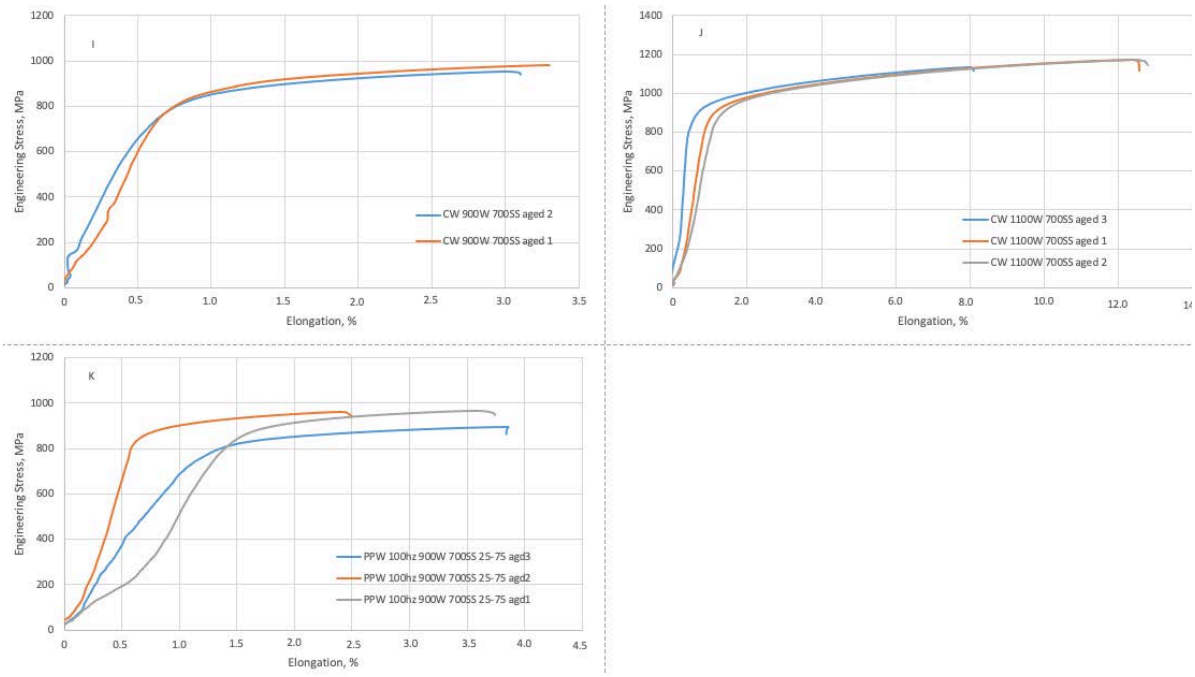

Figure 6.36: Engineering stress-strain curves of IN718 at various power modes (A) All three power modes. (B) CW and PPW (SP, LCC (25-75) and HCC (75-25)) (C) CW high power at 900W and low power at 700W (D) CW with PW (LCC (25-75) and SP) (E) The results of all three samples of PPW-SP (F) The results of all three samples of PW-SP (G) The results of all three samples of PPW-LCC (H) The results of all three samples of PPW-LCC (I) The results of all two samples of CW low power (J) The results of all three samples of high power (K) The results of all three samples of PPW-HCC.

Figure 6.37 shows the tensile samples fracture surface post-mortem analysis. The samples show no necking effect which suggests the material was brittle. The fracture can nucleate and propagate in two ways, the crack starts from all sides as suggested by C and E which shows flat surface in the middle of the crack. The crack starts from one side as indicated by the V shape towards the crack edge as shown in B and F. When the CW was used, the fracture surface suggested the presence of particles that did not melt properly (A). Signs of dendrites can be seen on (B), porosity open up is shown on (E), sign of inclusion clearly shown on (C), oxide, because samples are made in-air, can be seen clearly on (D). The surface of the sample was rough and not machined which can contain many stress raising points.

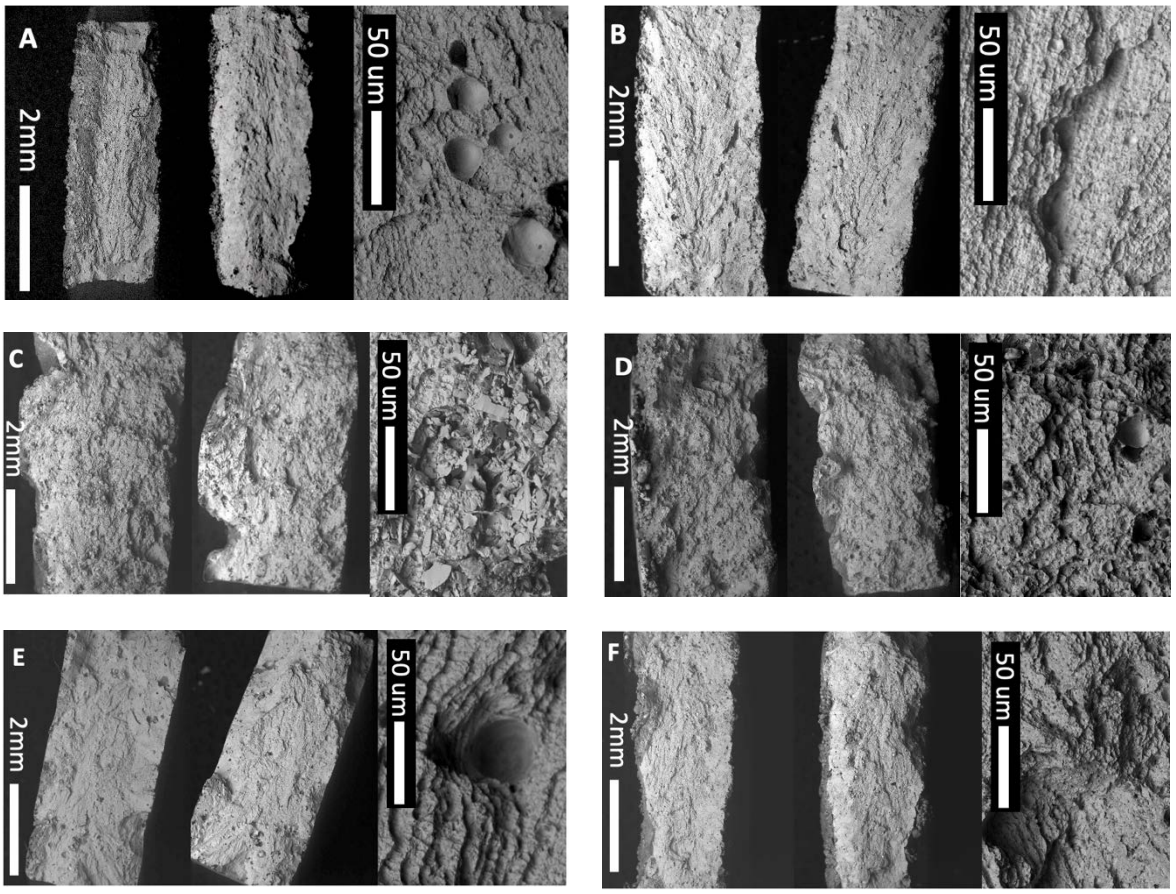

Figure 6.37: Tensile samples (A) CW (B) PPW-LCC (C) PPW-SP (D) PPW-HCC (E) PW-LCC (F) PW-SP

6.5 Conclusion

The outcomes provided in this manuscript highlight the following achievements:

- The use of the pulsed laser mode allowed a better stability of the melt pool to be achieved and consequently a good geometry uniforming the wall profile.
- The pulse waving shows the smallest grain size due to the breaking of dendrite and the cooling time pulsing provides.
- The PPW provides a mixture of columnar and equiaxed grains due to lowering the heat input with every pulse which allows the melt pool to cool down.
- The Nb segregation can be controlled by pulsing which produces fine and broken dendrites. PW produces the lower area percentage of Nb segregation that can be

enhanced by lowering the cooling rate, which will reduce the segregation even more. Same applies to the PPW which slightly increases the Nb segregation area percentage.

- The ageing treatment decreases the percentage of Nb segregation and allows Nb to dissolve into the matrix. However, the heat input is not high enough to melt the Laves phases or dissolve all the Nb segregation. The annealing is a short post-processing treatment with a higher heat input that dissolves most of the segregation. However, due to the short duration. The Nb will not have enough time to form γ'' in the matrix, therefore, it will convert to form the δ-phase. It was also proven that the pulsed laser mode enhances the distribution of Nb and decreases the Nb volume % in the interdendritic region and in the Laves phase.
- The grains columnarity increases with the intensity of the power, while the pulsed laser mode reduces the grain columnarity. PW did not show a significant effect in texture modification when compared with CW. PW in the as-built form was slightly harder than the CW. The annealed samples show approximately 45% increase in hardness compared to the as-built samples. Ageing shows the best hardness properties, with an increase of approximately 72% compared to the as-built samples. However, the PPW shows significant elongation compared to CW and PW. Furthermore, there was no significant difference in elongation considering the PPW (LCC and HCC). Different levels of power when the CW laser mode was used did not affect the tensile strength. However, the elongation was significantly affected by the power.

CRediT authorship contribution statement
Abdullah Alhuzaim: designed the study and performed the experimental tests and the analysis of the results. Writing – review and editing
Stano Imbrogno: Reviewing the paper.
Moataz Attallah: supervision, support on experimental feasibility and infrastructure.

Chapter 7. Direct laser deposition of crack-free CM247LC thin walls: mechanical properties and microstructural effects of heat treatment

Abdullah Alhuzaim[a, b], Stano Imbrogno[a], Moataz M. Attallah[a,*]

[a] School of Metallurgy and Material Sciences, University of Birmingham, Edgbaston, Birmingham B15 2TT, United Kingdom

[b] Mechanical Engineering Department, Jubail University College, Jubail Industrial City, Kingdom of Saudi Arabia

Abstract

CM247LC is classified as a non-weldable Ni alloy due to the high Ti + Al content, which makes it susceptible to cracking. It is particularly prone to microcracking when processed by direct laser deposition (DLD). In this work, multiple single walls were manufactured by DLD in CM247LC using two different laser modes: continuous wave (CW) and pulse wave (PW). The manufactured walls were studied during processing and post-processing, and characterised by scanning electron microscopy, electron backscattered diffraction, thermal analysis and X-ray diffraction. The results indicate that crack-free conditions during the deposition process

and the subsequent thermal processing can be achieved using the PW laser mode and that this can also lead to outstanding mechanical properties.

Keywords: Nickel Superalloy, CM247LC, Direct Laser Deposition, Microstructure, Mechanical properties.

7.1 Introduction

Parts for submarine, aerospace and gas turbine engines, and nuclear reactors that need to withstand high temperatures while maintaining good mechanical properties and performance are usually manufactured using nickel-based superalloys. Among the materials that belong to this family, CM247LC is a valid choice due to its unique properties, like excellent resistance to chemical and mechanical degradation under thermal exposure [43]. The excellent mechanical properties at high temperature are also explained by the high γ′ content of up to 67% volume fraction in the fully heat-treated condition. CM247LC has a chemical composition that is modified from that of MAR M247, and it is specifically designed for making directionally solidified turbine blades; however, it is one of the most difficult alloys to process by conventional fusion welding due to its crack susceptibility [237].

Additive manufacturing (AM) has become an innovative and valid manufacturing method owing to potential advantages such as waste reduction and enhanced design freedom, which consequently leads to a significant decrease in the buy-to-fly ratio. Moreover, the possibility of enhancing the efficiency and performance of components, such as turbine blades, has made AM a valid choice for industry, thanks to the ability to redesign components with geometrical and metallurgical features (e.g., internal cooling channels, gradual microstructure variation) [214, 238-242]. Among the AM technologies, direct laser deposition (DLD) shows

outstanding results in manufacturing components at small or large scales, as well as in repairing parts. DLD uses a high energy focused laser beam that melts blown powder flowing through a nozzle. Therefore, the designed component is manufactured by melting the powder layer-by-layer. DLD has advantages over selective laser melting (SLM), including a high deposition rate and faster production, thanks to technological features such as a bigger laser spot size and the ability to deposit thicker layers [56, 69].

Several studies have highlighted that the nickel superalloys (e.g., IN718, CM247LC) manufactured by AM are generally crack susceptible; therefore, it is fundamental to understand the effect of the process parameters and their combinations to avoid triggering the phenomena that may promote crack formation [147, 243, 244]. Generally, the formation and propagation of cracks in the AM of CM247LC is an issue not only during the manufacturing step, but also during the subsequent heat treatment (post-weld heat treatment; PWHT) or during the service. Crack formation mechanisms can be broadly classed into four main typologies.

- Solidification cracking

This type of crack usually occurs within the melt pool (mushy zone) where the material in not fully solidified (partial solid state). Cracks form when the temperature drops below the coherence temperature; the formation of the dendrites follows the heat source direction toward the liquid phase in the interdendritic regions. The residual liquid phase acts as a stress raiser and crack initiator and the relatively weak solid-liquid boundaries separate to create an intergranular rupture. This type of cracking is also known as hot-tearing. [27, 44, 157, 158]

- Liquation cracking

This usually happens in the heat affected zone (HAZ) where the bulk material is heated rapidly to a temperature that is lower than the overall liquidus of the material [27]. Generally, the rapid heating due to the welding operation leads to the dissolution of certain grain boundary phases (e.g., γ-γ′ in Ni superalloys) and other metallurgical phases such as carbides that are

characterised by lower melting temperatures. Therefore, these liquid films between the grain boundaries potentially act as crack initiation points during welding in combination with the residual stresses [26, 159-161].

- Strain age cracking (SAC)

This type of crack mainly occurs in γ′ precipitate strengthened alloys during PWHT within the ageing region either as part of stress relief or during the ramp phase of a solution treatment or high temperature service [44]. Repeated reheating during AM because of the layer-by-layer melting technique can also cause this form of cracking. During the ageing process the Al and Ti contribute to forming the γ′ strengthening phase and the material increases its strength whilst reducing ductility; therefore, the residual stress and the induced stress from the precipitation of the γ′ result in internal strain that exceeds the limited ductility of the material leading to crack formation, usually at the grain boundaries [26, 44].

- Ductility-dip cracking (DDC)

This kind of crack occurs due to a reduction in ductility (referred to as severe ductility drop) within a certain temperature range below the solidus temperature, and usually occurs along the grain boundaries [245]. This is due to a combination of the macroscopic thermal and solidification stresses generated at elevated temperatures, and the microscopic stresses generated within the grain boundaries due to the precipitation of partially coherent carbide phases. High chromium nickel superalloys, while resistant to corrosion and stress corrosion cracking, are known to be particularly susceptible to DDC [162, 163].

The majority of CM247LC literature related to DLD refers to cracking issues. CM247LC is more susceptible to cracking than other nickel-based superalloys, such as IN718 and IN738, due to the higher γ′ fraction or slower precipitating γ″ phase [1, 246, 247].

This article proposes an alternative technique to manufacture crack-free thin geometries by DLD of CM247LC. The study of the cracks detected in some samples allowed the

understanding of crack formation during the deposition leading to the realisation of a process parameter map that shows the crack-free operative area. Moreover, CM247LC requires heat treatment like other Ni superalloys in order to develop the strengthening phase and to improve the mechanical properties. Therefore, conventional heat treatments and their effects on crack formation were also investigated. Finally, the mechanical property characterisation of the samples produced with optimal parameters was carried out. The overall outcomes reported in this article not only highlight the fundamental role of the appropriate process parameters, but also explain how they affect crack formation in combination with heat treatments.

7.2 Experimental procedure

Thin walls were produced using a Trumpf TLC 1005 equipped with a 4-kW diode laser (Trumpf TrueDisk 4002) and a three-beam nozzle. During the deposition, the laser beam focused to a spot size of 1.4 mm and the standoff distance (distance between the substrate and the laser head) was set to 10 mm. For each test, an IN718 substrate, preliminarily sanded and cleaned with ethanol to remove any contamination, was used to deposit the thin walls. Before each deposition, four pre-heating scan lines were carried out to warm up the surface of the substrate and reduce the thermal shock between the substrate and the powder being delivered and melted by the laser head. In contrast with most of the research presented in the literature, this study also investigated the effect of the laser mode, continuous wave (CW) or pulse wave (PW), on the deposition process and its ability to produce crack-free thin geometries. The three-beam nozzle provided a constant powder flow rate of 25 g/min, while a defocusing of the powder stream (powder stream focus was below the substrate) was set at 2 mm. The powder and laser defocusing values were selected in order to compensate for any lack of deposition due to the uneven horizontal surface of the walls. An inert environment was created by filling the building volume with argon, and the oxygen level during deposition was always lower than 300 ppm. A pre-heating scan with the laser (no powder was delivered during this step) was

conducted to reduce the accumulation of residual stresses during the build process and reduce the risk of delamination between the deposited wall and the substrate. Although the literature reports work in which the pre-heated bed was used to mitigate the residual stress effect and reduce the cooling rate, in this study the local pre-heating by the laser was considered to be effective in reducing the residual stress. Indeed, a local pre-heating by the laser offers several advantages, such as a simplified experimental set-up (no heat bed is required) and can also be applied when repairing components. Regarding the two types of laser mode, CW was characterised by having the same average and peak power during the deposition, while PW was represented by a modulated square wave with a 50% duty cycle and frequency of 80 Hz. Although, the PW maximum power was equal to the CW maximum power, the minimum power was set at 2% of the maximum power. A similar approach was used in another work and has been reported by Stano et al. [226].

The process parameter details are listed in Table 7.1. Multiple single walls with lengths of 45 mm and heights of 20 mm were produced. Subsequently, further thin walls of 90 mm in length and 20 mm in height were produced to extract tensile specimens for mechanical property characterisation. The walls were deposited at different power values (300, 400, 600 and 800 W), different laser modes (CW, PW) and different scanning speeds (300, 500 and 700 mm/min). It is important to highlight that during the deposition of the walls using the CW laser mode, only the process parameters characterised by laser power of 300 W with scanning speeds of 300, 500, 700 mm/min, and laser power of 400 W with a scanning speed of 700 mm/min allowed thin walls to be built without macro-cracks. The use of CW with laser powers of 600 and 800 W with scanning speeds between 300 and 700 mm/min, and laser power of 400W with scanning speeds of 300 and 500 mm/min were not considered in the analyses owing to the significant amount of cracking that appeared after the deposition process.

The heat input or energy density (J/mm) related to the CW mode can be defined as shown in Equation 7.1 [211], in which P represents the power while V is the scanning speed of the laser head.

$$Heat\ input = P/V \qquad \textit{Equation 7.1}$$

Equation 7.2 was used to estimate the weighted average power (WAP) used during deposition using the PW laser mode. P_{max} is the maximum power, P_{min} is 2% of the maximum power, and t_{min} and t_{max} are both equal to 50% since the pulse shape is symmetric.

$$\text{WAP} = P_{\max}\left(\frac{t_{\max}}{100}\right) + P_{\min}\left(\frac{t_{\min}}{100}\right) \qquad \textit{Equation 7.2}$$

Finally, Equation 7.1 and Equation 7.2 were combined to estimate the energy density when the PW mode was used (Equation 7.3).

$$Heat\ input = \left[P_{\max}\left(\frac{t_{\max}}{100}\right) + P_{\min}\left(\frac{t_{\min}}{100}\right)\right]/V \qquad \textit{Equation 7.3}$$

Table 7.1: Process parameters and energy density

Sample	Laser mode	Peak power	Power 2%	Scanning speed		t_{max}/t_{min}	WAP	Heat input
		(W)		(mm/min)	(mm/sec)	ratio	(W)	(J/mm)
CW300/700	CW	300	-	700	11.67	-	300	25.71
CW300/300	CW	300	-	300	5.00	-	300	60.00
CW300/500	CW	300	-	500	8.33	-	300	36.00
CW400/700	CW	400	-	700	11.67	-	400	34.29
PW300/300	PW	300	6	300	5.00	50	153	30.60
PW300/500	PW	300	6	500	8.33	50	153	18.36
PW300/700	PW	300	6	700	11.67	50	153	13.11
PW400/300	PW	400	8	300	5.00	50	204	40.80
PW400/500	PW	400	8	500	8.33	50	204	24.48

PW400/700	PW	400	8	700	11.67	50	204	17.49
PW600/300	PW	600	12	300	5.00	50	306	61.20
PW600/500	PW	600	12	500	8.33	50	306	36.72
PW600/700	PW	600	12	700	11.67	50	306	26.23
PW800/300	PW	800	16	300	5.00	50	408	81.60
PW800/500	PW	800	16	500	8.33	50	408	48.96
PW800/700	PW	800	16	700	11.67	50	408	34.97

During the deposition process, an infrared (IR) camera was used to monitor the thermal field distribution. The scanning strategy was unidirectional: the laser moved along the x axis for 90 mm (first layer), the laser was switched off then moved rapidly in the z direction by the specific height of the layer thickness, and then moved back along the x direction by 90mm; then the laser was switched on again to deposit the second layer.

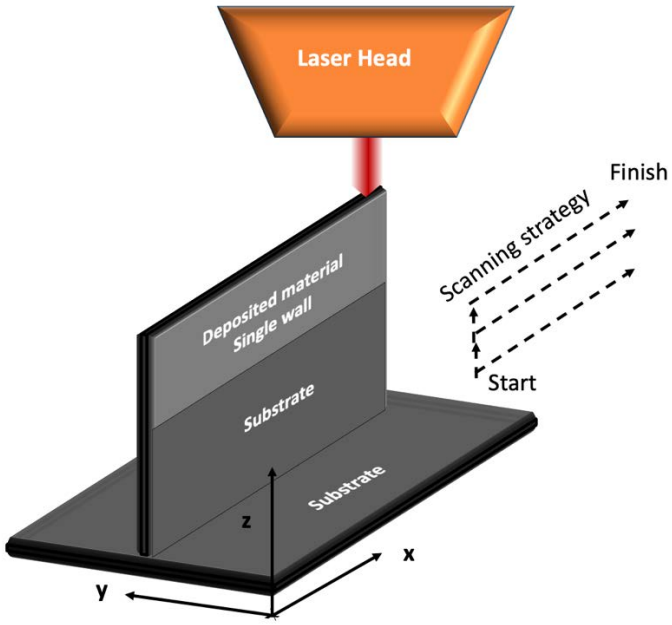

Figure 7.1: Schematic illustration of the DLD process; deposition of the thin wall and the scanning strategy

The CM247LC powder with particles ranging from 53 to 180 µm was analysed using scanning electron microscopy (SEM). The produced samples that did not show particular defects (e.g., excessive porosity, solidification cracks) were heat treated. The successfully

manufactured walls were cut by the EDM and tensile test coupons (in the yz direction) were obtained to assess the mechanical properties after the heat treatments. The surfaces of the tensile specimens were ground and polished to reduce the effect of the surface roughness on the mechanical properties. The walls were also cut and metallographically prepared in order to evaluate the microstructure by SEM, electron backscattered diffraction (EBSD) and energy dispersive X-ray spectroscopy (EDX). Moreover, X-ray diffraction (XRD) analyses were carried out to evaluate the presence of the different phases. The SEM images were analysed by ImageJ processing software by Fiji to characterise the cracks and to evaluate the porosity.

7.3 Results and discussion

7.3.1 Powder characterization

The metal powder used in this work was argon gas atomised CM247LC (53–180 μm) with almost no satellite formation, supplied by Sandvik Osprey Ltd. Figure 7.2 shows the cross sections of CM247LC powder particles analysed by backscattered SEM. The powder was hot mounted within resin and the sample was ground, polished and electro-etched to reveal the microstructure. The results show that the powder was predominantly spherical with limited satellites, while the microstructure was near fully dense with an equiaxed grain structure characterised by submicron precipitates. Chemical composition analysis was performed by Exova [248] using inductively coupled plasma optical emission spectrometry and the results are provided in Table 7.2.

Table 7.2: The chemical compositions of CM247LC powder

Element	**Ni**	**W**	**Co**	**Cr**	**Al**	**Ta**	**Hf**
wt%	Bal.	9.34	8.73	8.29	5.55	3.11	1.23
Element	**Ti**	**Mo**	**Si**	**Fe**	**C**	**Nb**	**O**
wt%	0.71	0.52	0.11	0.08	0.08	0.05	<100ppm

The SEM micrographs of CM247LC cross sectioned powder particles show the fine cellular grain structure and evidence of carbide formation between the cell boundaries. The

dendritic structure is also evident [Figures 7.2(b) and 7.2(c)] although it is very limited. The very fine white particles located in the interdendritic regions are likely to be Hf or Ta, since this is found to vary the most when conducting EDX.

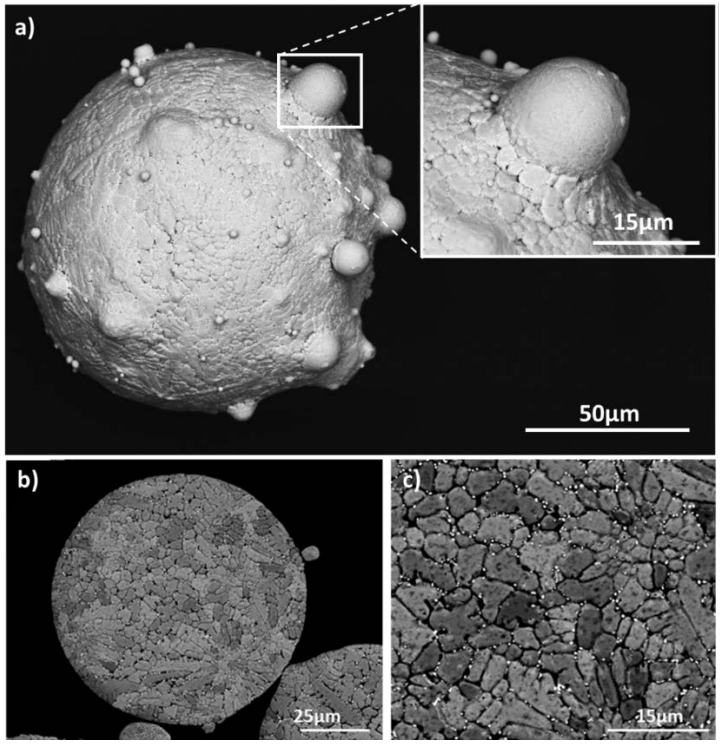

Figure 7.2: (a) SEM micrograph of as-received CM247LC powder particles. (b) and (c) SEM micrographs showing cellular particle topography and presence of precipitates on the powder surface.

7.3.2 Effect of the process parameters on defect and crack formation

Different process parameters and laser operative modes (CW and PW) led to the production of thin walls with several types of defects (e.g., pores, micro- and/or macro-cracks) as well as crack-free thin walls that had been successfully manufactured. It is important to point out that the type of cracks observed via SEM after the deposition originated and propagated along the grain boundaries, as highlighted in Figure 7.3. The SEM analysis of the longitudinal and cross section of each wall helped define the map of the process parameter effects to establish the crack-free domain (Figure 7.3). In particular, the process parameter map was

populated using the SEM analysis of the samples to allow an easy comparison of the defects depending on the scan speed, power and laser operative mode. The entire surface of the map was divided into three separate regions, as shown in Figure 7.3. In general, the areas enclosed by the red circle and rectangle are characterised by process parameters that allowed the building of thin walls without visible cracks, but the presence of cracks (micro-scale or extended) as well as pores and lack of fusion were revealed by SEM analyses. Within the green area, the process parameters used led to the manufacture of thin walls with limited pores (PW only).

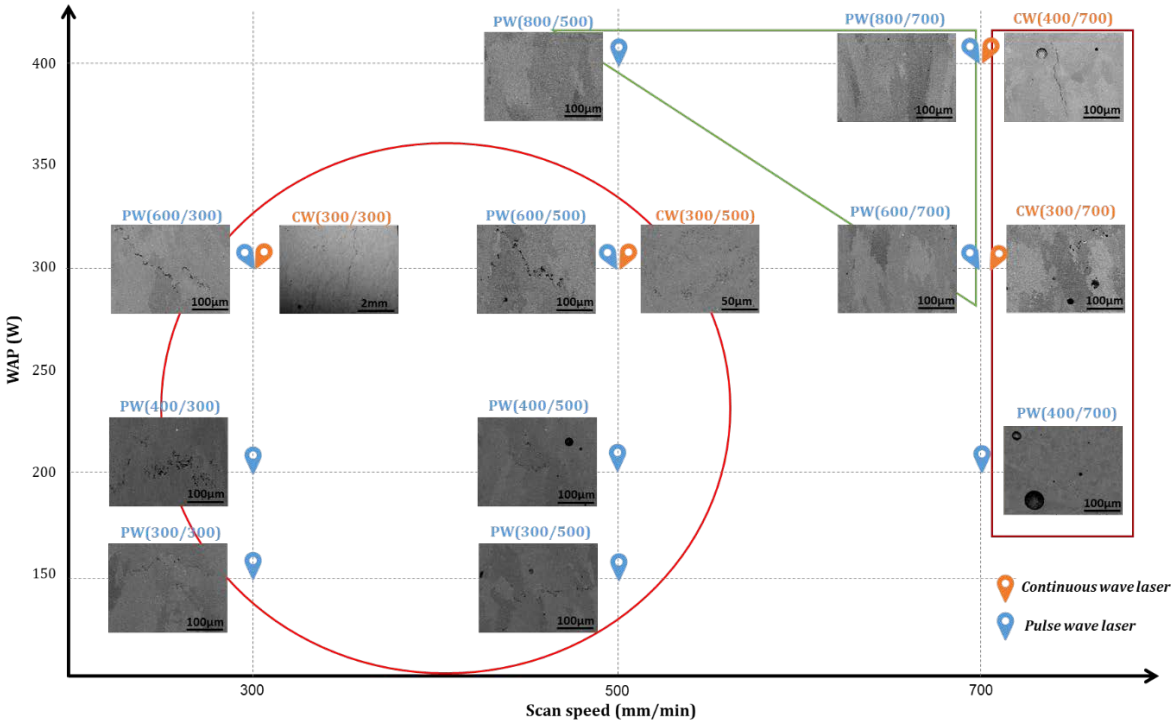

Figure 7.3: Comparison in terms of process parameters and resultant microstructural characteristics

7.3.2.1 Red circle area analysis (low scanning speed and low power)

As previously mentioned, the red circle area is characterised by the combination of process parameters and laser operative modes that manufactured thin walls affected by cracks, pores and lack of fusion. In detail, PW300/300 had small to medium pores, lack of fusion and micro-cracks, whereas PW400/300 had small to medium pores, no lack of fusion and micro-

cracks. Comparing PW300/300 with PW400/300, an increase in power led to more micro-cracks and a decrease in pore numbers. The WAP (153 W, 204 W) was too low for the scanning speed (300 mm/min), which resulted in the formation of stress cracks. PW300/300 had small to medium pores, no lack of fusion and micro-cracks. Compared with PW400/300, PW600/300 showed a reduction in crack number and severity. CW300/300 had small to medium pores, no lack of fusion, and micro- and macro-cracks. Compared with PW600/300, PW600/500 had a macro-crack in the bulk, but no significant differences in pore size and numbers. PW300/500 had small to medium pores, as well as a few large pores, no lack of fusion and one observable micro-crack. Compared with PW300/300, the increase in the scanning speed eliminated some of the stress, which resulted in a reduced number of cracks. PW400/500 had small to medium pores and a few large pores, small lack of fusion in bulk (approximately 40 μm) and one observable micro-crack. PW600/500 had small to medium pores and a few large pores, no lack of fusion and one observable micro-crack. CW600/500 had very small pores, small lack of fusion and visible cracks. PW600/500 showed no lack of fusion when compared with PW400/500 and very similar characteristics when compared with PW300/500. When comparing PW600/300 with PW600/500, the increase in the scanning speed while keeping the power constant resulted in an increase in the pore size, but a decrease in crack numbers.

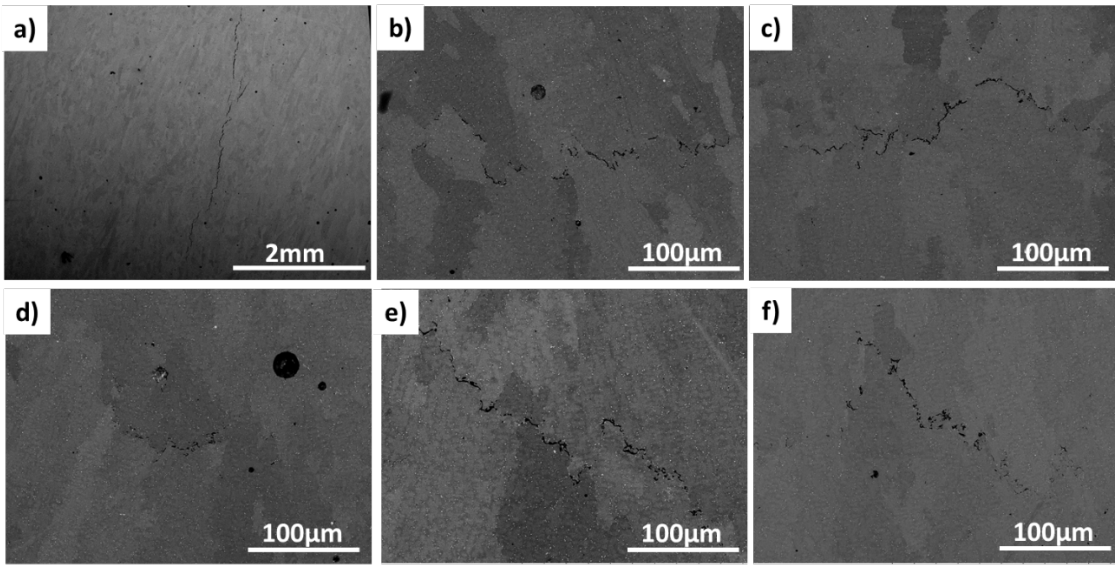

Figure 7.4: (a) CW300/300, (b) PW300/500, (c) PW400/300, (d) PW400/500, (e) PW600/300, (f) PW600/500

7.3.2.2 Red rectangle area analysis

CW300/700 had small to medium pores, lack of fusion and one observable micro-crack. CW400/700 had small to medium pores, lots of micro-cracks and one macro-crack. PW800/700 had small to large pores, lack of fusion in bulk and no visible cracks. Although, the decrease in power and increase in scanning speed (compared to PW800/500) did not result in stress cracking, it led to a lack of fusion in the bulk material. Moreover, an increase in the size and number of pores was observed. The high power and scanning speed led to stress cracking for samples manufactured via CW, but not for those manufactured via PW (Figure 7.5).

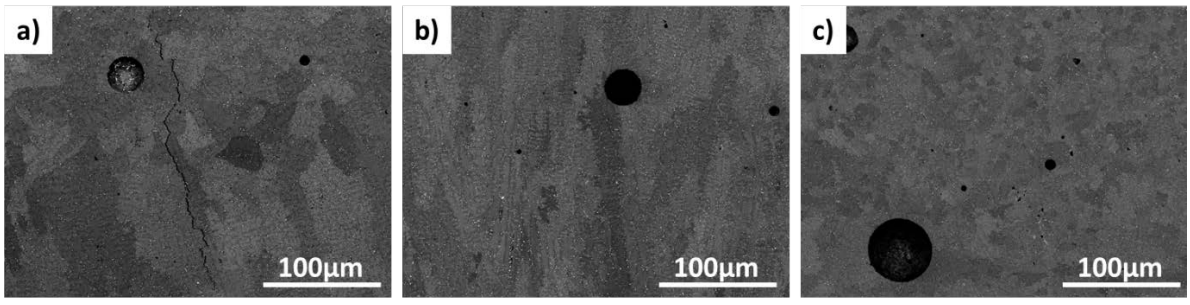

Figure 7.5 (a) CW400/700, (b) CW300/700, (c) PW400/700

7.3.2.3 Green triangle analysis

PW800/500 had limited small to medium pores, and no lack of fusion or visible cracks were detected. PW600/700 had small to medium pores, and no lack of fusion or visible cracks were observed. The higher power of PW600/700 compared with PW400/700 resulted in a reduced size and number of pores and prevented the lack of fusion. PW800/700 showed small to medium pores, no lack of fusion and no visible cracks. The higher power and scanning speed enabled more gas to be trapped during the deposition and, therefore, the pores were larger. Compared with PW600/700, the pores had increased in size, but decreased in numbers. When comparing PW800/500 with PW800/700, the increase in the scanning speed at a constant power resulted in an increase in the pore size and numbers and no lack of fusion (Figure 7.6).

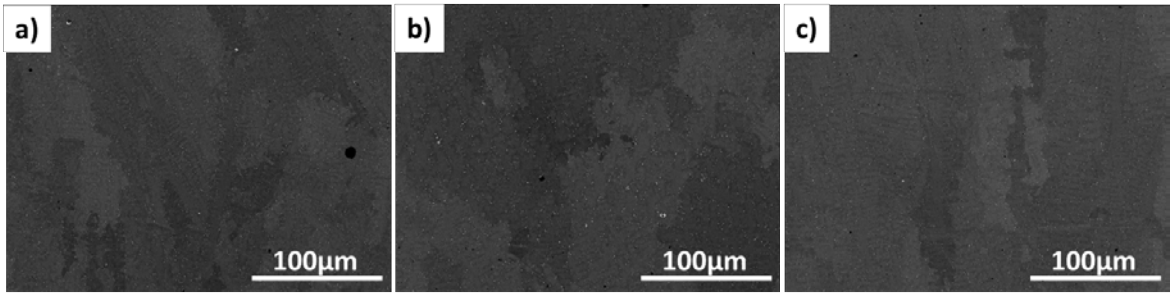

Figure 7.6: (a) PW600/700, (b) PW800/500, (c) PW800/700

Both CW and PW beams were able to produce consolidated parts; however, all the CW parts showed cracks, some porosity and lack of fusion. On the other hand, some of the parts produced by PW were crack-free, had no lack of fusion and showed very limited porosity, suggesting reliability for manufacturing or repairing components. Therefore, it is clear that the use of the PW mode affects the final properties of the material. Figure 7.7 summarises the discontinuities observed in the samples produced using a variety of parameters.

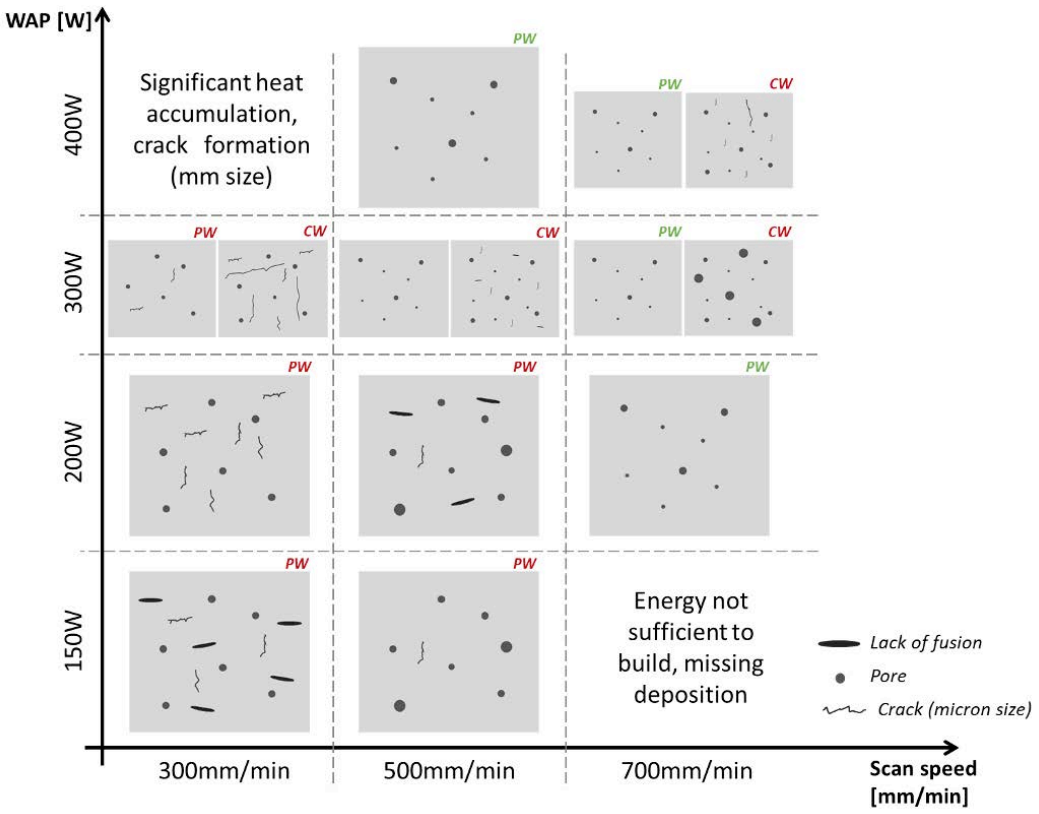

Figure 7.7: Summary of samples' discontinuities and resultant microstructural characteristics

7.3.3 Monitoring solidification cracking during the DLD process

The advantage of using the IR camera was mainly in the detection of the cracks formed during the deposition process. Figure 7.8 shows the formation of the wall produced by CW at 600 W with a scanning speed of 500 mm/min. Although the crack formation is the most interesting result, it is possible to observe that as the number of layers deposited increases there is an accumulation of heat in the wall, and particularly from the central region up to the top of the wall. This result confirms the role of the substrate in reducing the temperature within the first layers deposited, as it acts as a heat sink. According to Raghavan et al. [249], this leads to more equiaxial than columnar grains in the bottom of the microstructure. During the deposition of the 20th layer a small crack appeared and subsequently more cracks formed and propagated while new layers were deposited. These cracks occurred in the mushy zone where the material was not fully solidified. The cracks formed when the temperature dropped below the coherence

temperature, and the formation of the dendrites followed the direction of the heat source toward the liquid phase in the interdendritic regions. The liquid regions that remained acted as stress concentration and crack initiator sites and the relatively weak solid-liquid boundaries separated to form an intergranular rupture [27]. This result was also confirmed by the SEM analysis; indeed, the main macro-cracks were particularly vertically orientated in the dendritic growth direction and the cracks were nucleated and propagated between the dendrites.

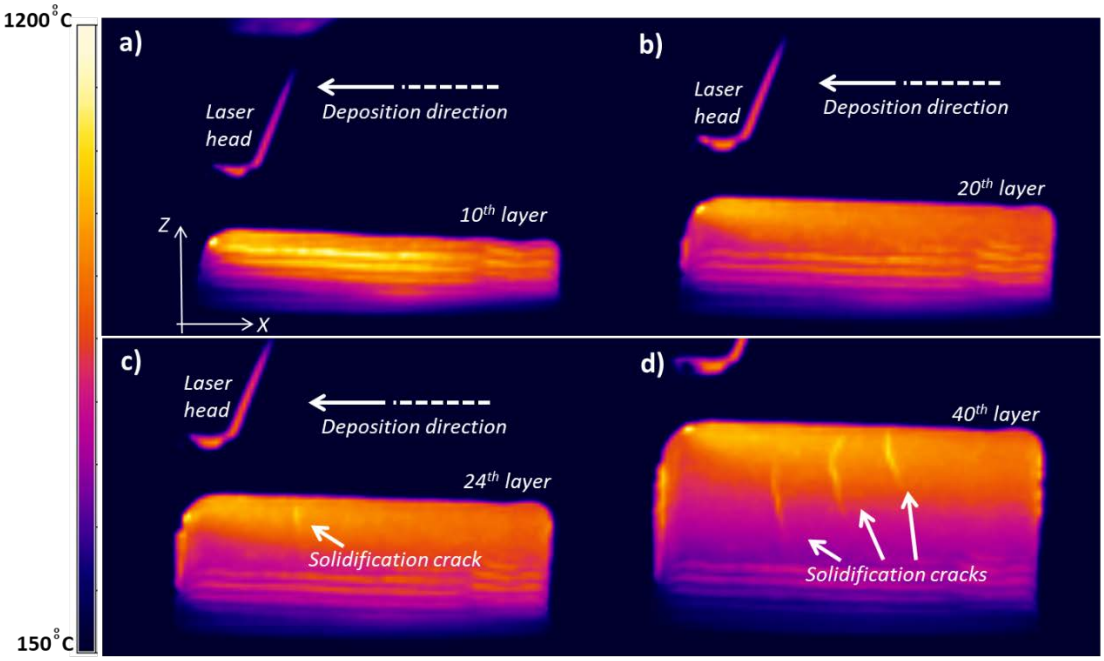

Figure 7.8: Thermal field distribution on the z-x plane of the CW600/500 deposited walls showing crack formation by layer

Figure 7.9 represents the thermal field distribution during the deposition of the thin wall using the PW laser mode at 800 W with a scanning speed of 500 mm/min. This picture shows immediately that the heat accumulation was lower than that evaluated during the CW laser mode deposition (Figure 7.8). The PW laser mode enhanced the cooling rate and consequently lowered the temperature, such that a reduced heat accumulation characterised the entire deposition process. Moreover, no macro-cracks were detected, highlighting the benefit of using

the PW to avoid failures in the manufacturing process. Finally, the PW showed a significant advantage in producing crack-free thin components with CM247LC.

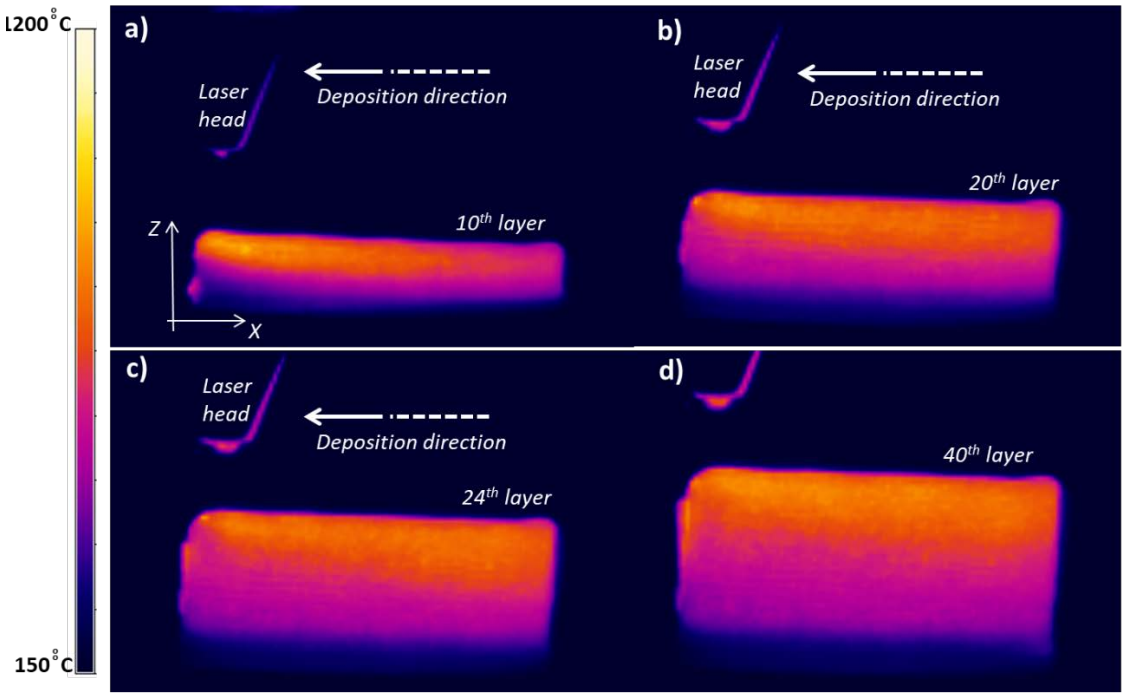

Figure 7.9: Thermal field distribution on the z-x plane of the PW800W/500 deposited wall showing no cracks

7.3.4 Strain age cracking during heat treatment

Heat treatment was carried out on the samples that had been successfully produced without any cracks (micro- or macro-cracks). However, one sample that showed some solidification cracks was also included in the treatment to evaluate its effect on the SAC susceptibility of the sample. A double ageing heat treatment was performed on the samples: 980 °C for 5 h followed by furnace cooling to 870 °C for 20 h followed by furnace cooling to room temperature. The ageing process increases the material's strength while reducing its ductility. Figure 7.10 shows a thin wall characterised by solidification cracks before and after heat treatment. It is possible to observe that new cracks appeared, and these can be classified as SAC; in this case, the carbides acted as stress raiser or crack initiation sites. Moreover, the

residual stress and the induced stress due to the precipitation of the γ′ resulted in strain that exceeded the limited ductility of the material and provoked the formation of cracks, usually at the grain boundaries. Figure 7.11 shows walls successfully produced without cracks. It is possible to observe that the heat treatment did not affect the part in terms of crack formation; therefore, the process parameters used during the DLD process produced a component with a very low SAC susceptibility.

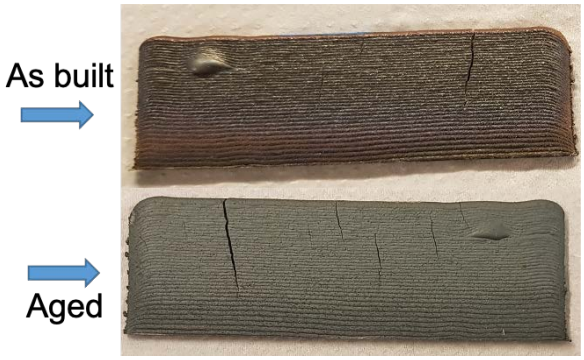

Figure 7.10: Failed samples that cracked during deposition, before and after heat treatment

In particular, the three samples produced by the PW laser that were in the green triangle (no cracks, no lack of fusion and small porosity) passed the ageing post heat treatment with no visible defects, except the sample PW800/500, in which a small horizontal crack appeared immediately after heat treatment [Figure 7.11(B)].

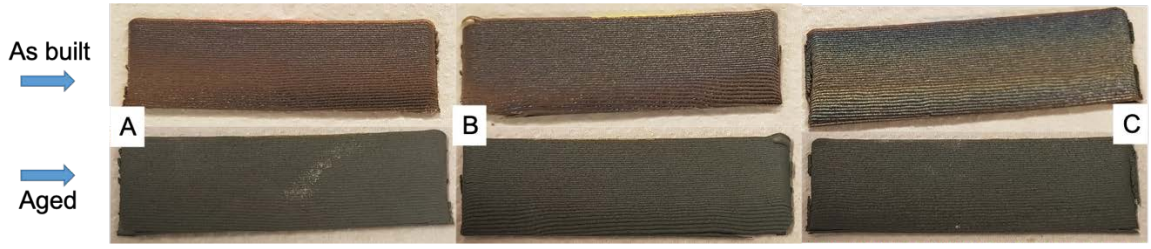

Figure 7.11: Green triangle samples before and after heat treatment: (A) PW600/700, (B) PW800/500, (C) PW800/700

7.3.5 Microstructure and chemical composition

Figure 7.12 shows the microstructure observed by BSE microscopy on the cross section of the sample PW800/500 before heat treatment. The peculiar microstructure usually observed on Ni-superalloy parts produced by DLD is also noted in this study. The elongated columnar dendritic microstructure was developed through the build direction (z) and the orientation was due to the heat source movement [Figure 7.12(a)]. The use of the secondary electron detector allowed observation of the γ′ formed due to the DLD process. The size as well as the shape of the γ′ are clearly comparable with those observed in the Ni superalloys manufactured by conventional processes and heat treated. The strengthening phase formed was characterised by a spherical shape with a submicron size [Figures 7.12(d) and 7.12(e)].

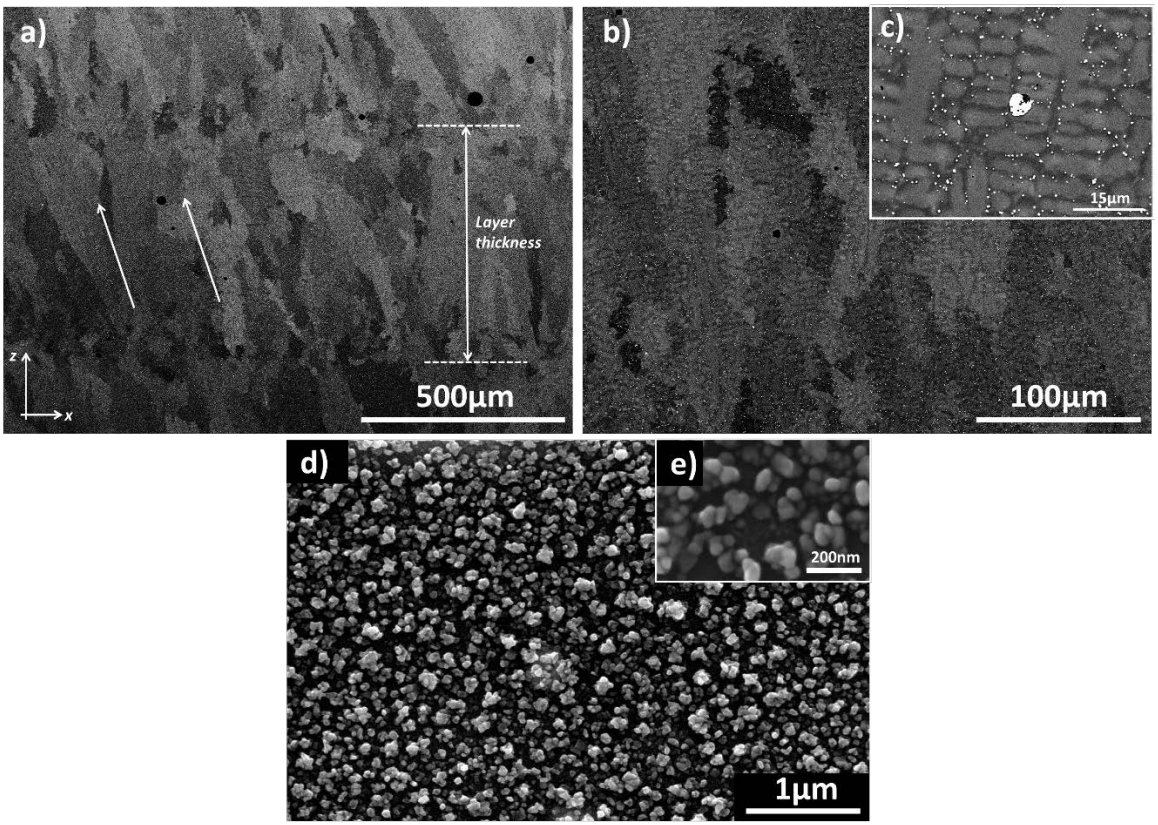

Figure 7.12: Microstructure of the as-deposited PW800/500 sample; (a) zx side of the sample, (b) and (c) details of the interdendritic region; (d) and (e) precipitation strengthening phase γ′.

The interdendritic region was characterised by submicron precipitates [white colour represented in the BSE Figure 7.12(c)]. EDX measurements were carried out to confirm the

chemical elements of the precipitates. The elemental concentration maps showed that the area surrounding the precipitates was rich in Al, Ti, W, Co, Cr and Ni. The white particles (precipitates) were found to be rich in Hf and Ta and they were the MC carbides. The alloying elements Hf and Ta are known to form MC-type carbides that replace Ni, Cr and Co. Generally, carbides appeared to be 1 μm in size, although a finer type of carbide was also observed more frequently. A homogenous distribution of carbides is necessary for good properties, hence carbide precipitation at grain boundaries can provide grain boundary strengthening via pinning effects, while fine carbides precipitated throughout the matrix can provide dispersion strengthening effects [250].

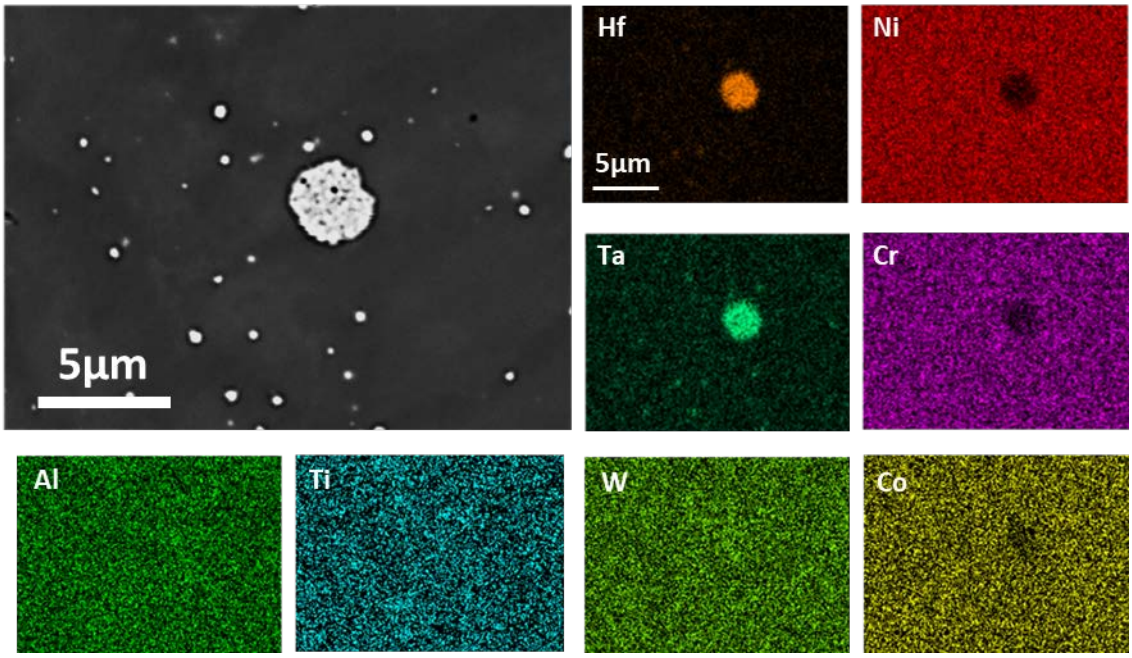

Figure 7.13: EDX images of the segregations detected within the interdendritic region.

Kikel and Parker [251] stated that crystallographic orientation had an effect on the susceptibility to DDC cracking; the strain threshold for DDC reduced from 2.5% strain to 1% strain in the presence of high angle grain boundaries. The first stages of recovery involve rotations of low angle grain boundaries [252]. Local variations in crystallographic orientation

have been identified by Muñoz-Moreno et al. [253]. Therefore, both the increase in DDC cracking and the change in young's modulus indicate the onset of recovery at lower temperatures.

The EBSD analysis allowed to be distinguished grains that were difficult to properly detect by SEM analysis, and their orientation has also been revealed. In detail, Figures 7.14(A) and 7.14(B) show the orientation of the inverse pole figure (IPF) map of the cross section and longitudinal section, respectively, of the sample produced by PW at 800 W with a scanning speed of 700 mm/min. The use of the PW allowed the development of a microstructure with a random texture. The kernel average misorientation map [Figures 7.14(C) and 7.14(D)] confirm the presence of misorientation angles within grains that are typically lower than 5°, although more isolated regions of higher misorientations were also observed. The yz side (build direction or cross section) and xz side (bulk direction) did not contain dislocation arrays or dislocations recovered deformed, as shown in Figures 7.14 (C) and 7.14 (D).

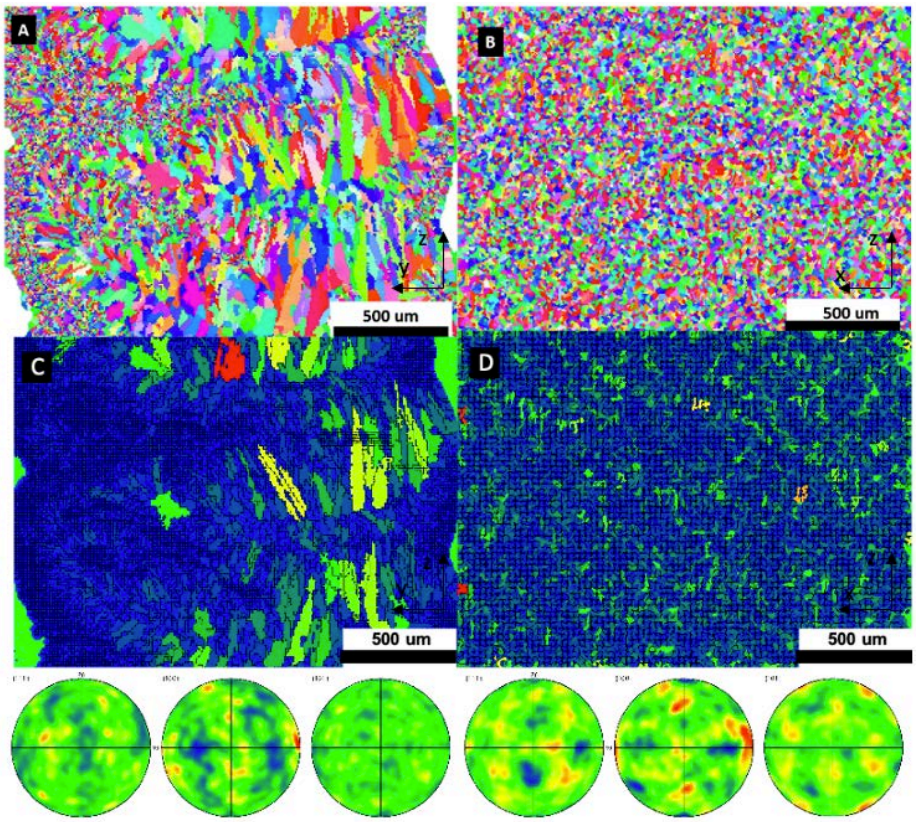

Figure 7.14: EBSD of CM247LC samples produced with PW at 800 W and 700 mm/min. IPF map (A) yz, the build direction and (B) xz, the side direction. Kernel average misorientation map (C) yz, the build direction and (D) xz, the side direction.

Further metallographic analyses were carried out on the heat-treated samples. In detail, the heat treatment enhanced the dissolution of the γ/γ′ and the grain boundaries were more visible with carbides embedded in the γ′. The interior of the grains was characterised by the γ′ particles, as shown in Figure 7.15. It is worth noting that the shape and the size changed due to the heat treatment. The particles were initially more spherical [Figure 7.12(d)], and after the heat treatment they started to assume a more cuboidal appearance, although this was not fully developed [Figure 7.15(c)]. Usually, CM247LC γ′ particles look like split cubes after solution treatment and ageing; however, in this study only double ageing (980 °C for 5 h followed by 870 °C for 20 h) without a previous solution treatment was performed. Therefore, the temperature of the ageing treatment and the duration were not high enough to form the cube-

type primary γ′ with size usually close to 1 μm, as reported by [248]. It is important to highlight that the coarse γ′ particles at the grain boundaries can help to pin the grains. Furthermore, the irregular morphology of the grain boundaries, which arises due to particles pinning the boundary, can help to inhibit grain boundary sliding. In this case, the resultant γ′, although not fully developed into the cube-like shape, was coarser and denser than the one observed in the as deposited samples.

The microstructure after the ageing treatment was more irregular in its morphology, especially regarding the grain boundaries, which could potentially inhibit grain boundary sliding. According with the results reported in [248], the grain boundaries were characterised by a necklace structure and the γ′ observed in the as-deposited and the heat-treated samples resulted in an ultra-fine γ′ that generally appeared within the channels between the cuboidal γ′. Therefore, the high temperature during the deposition process allowed the formation of the γ′ but the drastic cooling rate forced the strengthening phase to reach the nanometre scale. Although the long exposure to high temperatures during the heat treatment promoted the growth of the γ′, its size was still submicron; therefore, it is still considered to be ultra-fine γ′.

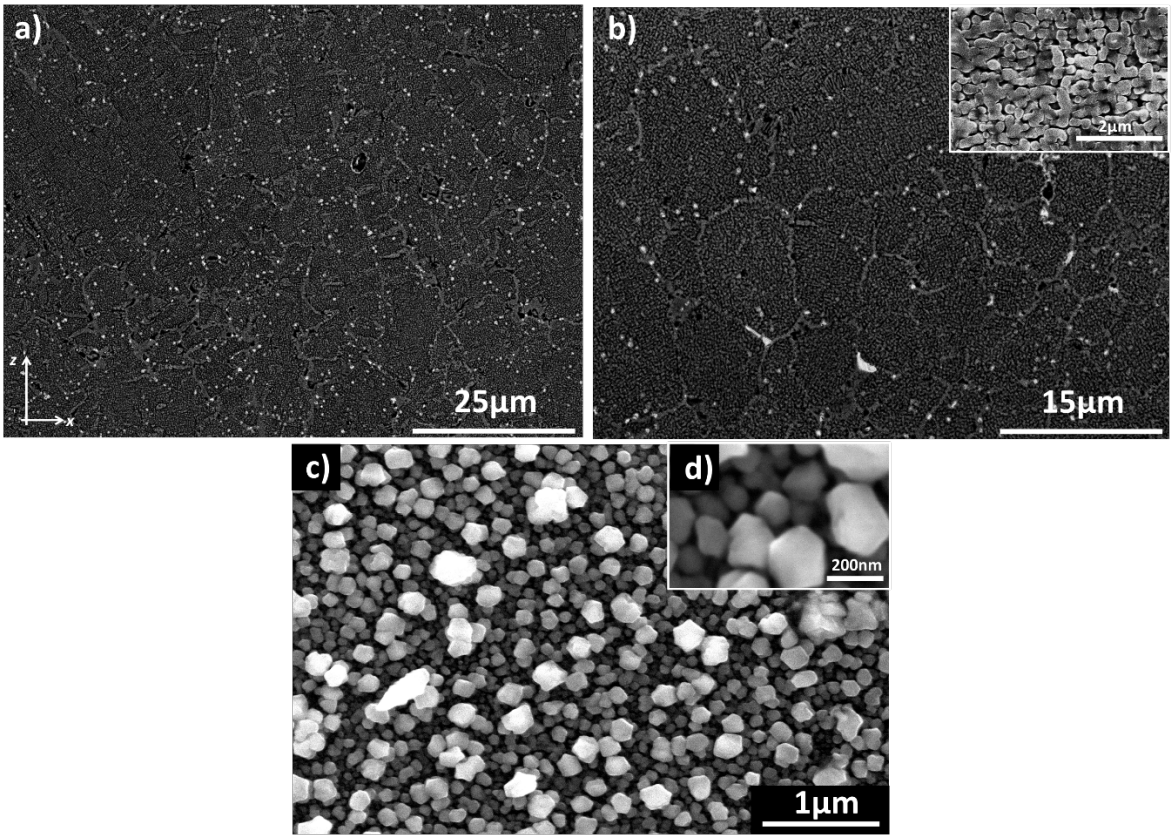

Figure 7.15: Microstructure of the heat-treated CM247LC PW800/500 sample: (a) zx side build direction of the sample, (b) detail of the microstructure showing grains boundary; (c) and (d) ultra-fine strengthening phase γ'.

7.3.6 Texture and phases of the CM247LC: XRD analysis

The results of the powder XRD analysis showed major peaks corresponding to (111), (200), (220) and (311) with no other minor peaks. Moreover, the XRD patterns for CW and PW samples in the cross-section direction (xz) show additional peaks that did not exist on the as-supplied powder. Small peaks appeared at θ = 55° and 75° for all AM samples regardless of the power mode or the post-processing because the lattice parameter was decreased by depletion of the matrix due to the precipitate and the Laves phase.

The samples shifted by a couple of degrees for the peaks on the (111) γ compared with the powder. For both power modes the bulk orientation (yz) showed a higher intensity in the preferred orientation (200). Moreover, CW showed a higher intensity in the (220) and (311) peaks in the yz direction.

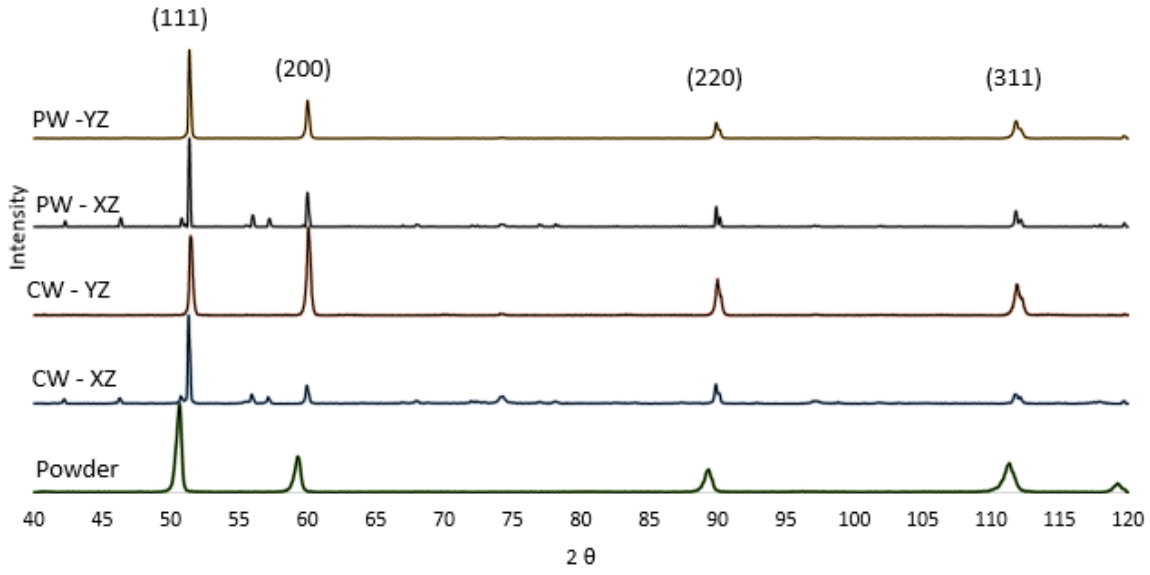

Figure 7.16: XRD results of CM247LC in two laser modes CW and PW in the aged condition, in two different direction, the bulk direction and cross section direction

7.3.7 Mechanical properties and hardness analysis

The mechanical properties were evaluated through microhardness measurements and tensile tests at room temperature. The hardness analysis was carried out on the three successful builds that were crack free after deposition and heat treatment (PW600/700, PW800/500 and PW800/700). The measurements were carried out on the as-deposited and aged samples. It is obvious that the heat-treated samples showed a higher hardness compared with the as-deposited condition. The results show that the as-deposited samples showed the lowest hardness with values slightly less than 450 HV. The heat treatment increased hardness: almost 100 HV more was measured on each sample compared with the as-deposited condition. The measured hardness of the PW600/700 and PW800/500 samples was almost comparable. It is interesting to note that the increase of the power from 600 W to 800 W while the scan speed was kept at 700 mm/min led to a slight increase in hardness. The increase was also observed when comparing the post heat-treated samples. This increase could be related to the higher heat that the sample experienced during the deposition leading to a slightly higher formation of the

strengthening phase. These results are consistent with the trend suggested by the literature. Indeed McNutt [254], who used DLD to perform CM247LC cladding, reported that the hardness increased after performing hot isostatic pressing (HIP) on the manufactured parts. In particular, the hardness was measured in the HAZ from the centre of the deposit to the peripheral region and the variation was from 299 HV to 408 HV, respectively. Yuanbo et al. [255] measured the hardness of a heat-treated sample processed by SLM and the results showed an average value of 455 HV.

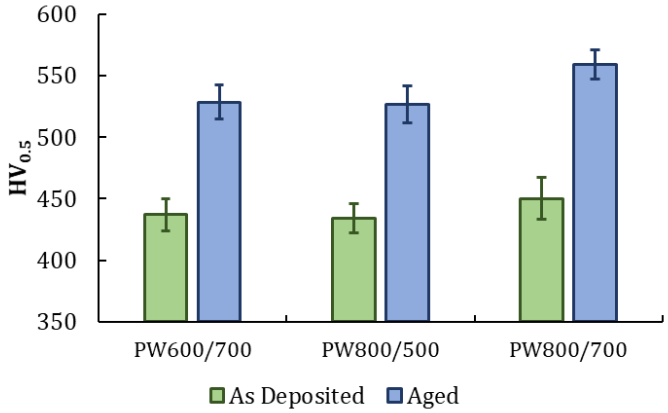

Figure 7.17: Hardness results for the CM247LC before and after ageing for various parameters

Mechanical tests were performed on the heat-treated samples. The engineering tensile test curves of the CM247LC alloy in the ageing conditions are shown in Figure 7.18. A wide comparison with what was already reported in literature was carried out in order to understand the impact of DLD on the mechanical performance in relation to the other near-net-shape manufacturing techniques. Therefore, the mechanical properties reported by Wang et al. [256] after HIP of CM247LC samples produced by SLM and those reported by MacDonald et al. [257] after HIP of CM247LC powder were considered. In particular, Wang et al. [256] measured the ultimate tensile strength at room temperature to be equal to 950 MPa, whereas yield stress was close to 750 MPa while the elongation was approximately 5.5%. MacDonald et al. [257] measured an ultimate tensile strength of 1350 MPa and a yield strength of 815 MPa

with an elongation close to 12.7%. It is also important to point out that the powder used in this work was comparable with the one employed by [257]. In this work the highest ultimate tensile strength of 1120 MPa was measured for the PW800/500 sample, followed by the ultimate tensile strength of 980 MPa for the PW600/700 sample. These results were higher than those reported by Wang et al. [256] for the samples produced by SLM that subsequently underwent HIP; on the other hand, they are smaller than the values reported in [257]. It is interesting to highlight that the yield stress, which in this case was equal to 820 MPa and 980 MPa for PW800/500 and PW600/700, respectively, was comparable with the values reported by Wang et al. [256] and MacDonald et al. [257]. Finally, the elongation results (1.6%–4.6%) were significantly lower than those reported in [257], but still slightly higher than the results of Wang et al. [256].

Table 7.3: Tensile test parameters

Specimen ID	F_{max}	dL at F_{max}	F_{Break}	dL at break	a_0	b_0	S_0
	N	mm	N	mm	mm	mm	mm²
PW600/700-1	7626.582	0.70988	7506.418	0.724639714	1.45	4.67	6.7715
PW600/700-2	7522.954	0.28856	7217.551	0.300159156	1.65	4.67	7.7055
PW800/500-1	6927.313	1.240599	6803.408	1.239361405	1.25	4.67	5.8375
PW800/500-2	6824.494	0.09024	6646.054	0.090799786	1.65	4.67	7.7055
PW800/700-1	5640.734	0.33104	5628.604	0.337320149	1.2	4.67	5.604

Where F_{max} is maximum force and dL is the change in length F_{Break} if force at the breaking point, a_o is the thickness of the original cross section, b_o with of the original cross section and s_o is cross section area

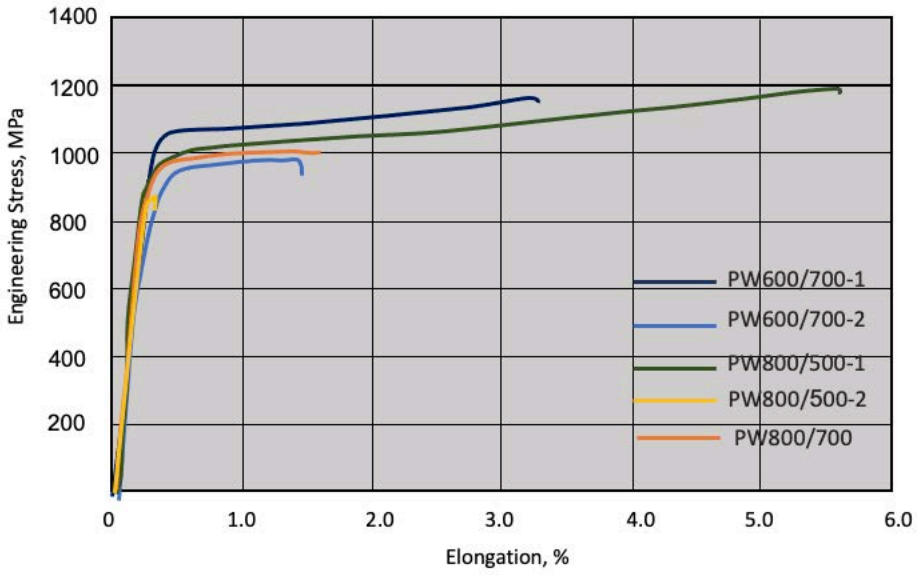

Figure 7.18: Engineering stress-strain curves on CM247LC on the ageing condition of the three successful builds

The fracture surfaces of the tensile specimens produced with a laser power of 800 W and 600 W with scanning speed of 700 mm/min and the PW laser mode were analysed by SEM as shown in Figure 7.19. The characteristics of the surface were revealed through the use of the secondary electron detector [Figures 7.19(a), (b), (c), (d) and (e)], while the backscattered detector was used to detect inclusions [Figure 7.19(f)]. Considering Figures 7.19(a) and 7.19(b), the fracture surface was characterised by an irregular shape [Figure 7.19(c)] and randomly distributed pores were visible [Figure 7.19(e)]. Regardless of the power used to produce the samples, the fracture surface showed similarities: both pores and uneven regions were detected, and the use of the backscattered detector highlighted inclusions that were mainly due to the presence of Hf and Ta. The presence of these inclusions that were usually formed between the grain boundaries during the heat treatment (Figure 7.15) suggested that the intergranular fracture was the preferred path. Figure 7.19(d) shows the presence of microvoid coalescence (dimples). Generally, these types of microvoids nucleate in regions of localised strain discontinuity, usually caused by the presence of inclusions, second phase particles, grain boundaries, etc.

[258]. The reduced ductility shown by the PW800/700 sample, compared with the other samples produced with different process parameters could be related to the different percentage of inclusions that could potentially affect the plastic deformation and the formation of the microvoid coalescence.

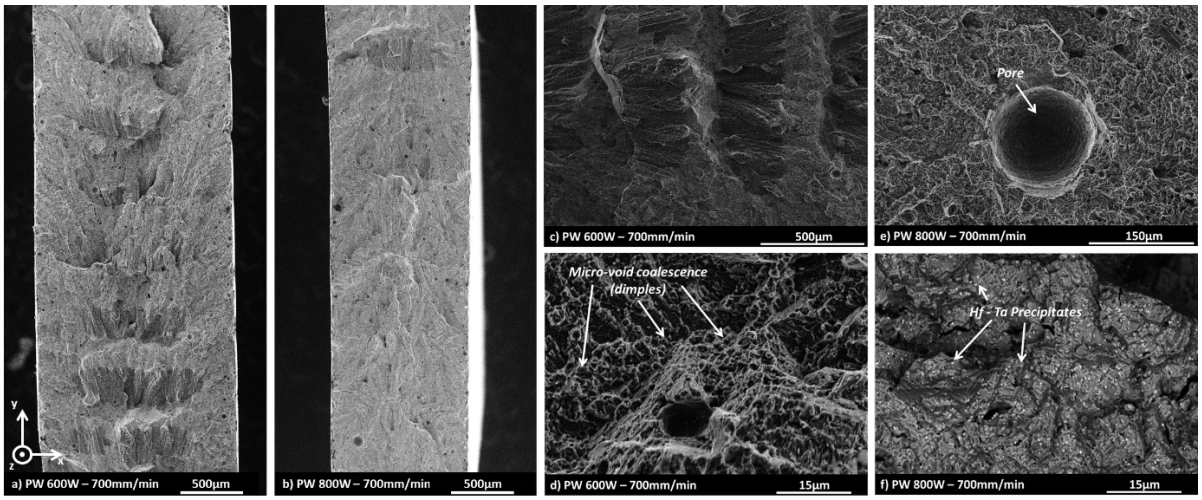

Figure 7.19: (a) and (b) cross section of the fracture surfaces; (c) and (d) fracture surface details of the sample produced with laser power of 600W; (d) and (e) fracture surface details of the sample produced with laser power of 800W.

7.4 Conclusion

In this research, a parameter study of DLD processing using CW and PW to produce CM247LC dense and crack-free single walls was performed, and microstructural characterisation and mechanical properties of the CM247LC were investigated. Moreover, the following results can be summarised:

- CW enhanced the formation of the dendrites in directional solidification. The liquid phase that remained acted as a stress raiser and crack initiator and the relatively weak solid-liquid boundaries separated to form an intergranular rupture. In contrast, PW broke the formation of the dendrites and somewhat perturbed the directional solidification.

- Some process parameters tested with the PW laser mode led to crack formation during the deposition, as did the use of the CW mode. On the other hand, a limited window of process parameters with the PW laser led to the deposition of crack-free thin walls.
- DLD + ageing as the heat treatment was not enough to enable the CM247LC alloy to form the cuboidal microstructure. However, it formed ultra-fine γ_t' that usually appears in the channels between the cuboidal γ_p'.
- The residual stress and the induced stress increased with the ageing process, and this resulted in the precipitation of the γ' resulting in the propagation of existing cracks and possibly forming new cracks.
- DLD + ageing succeeded in providing higher hardness than DLD + HIP and SLM with full heat treatment, whereas the UTS gave a result between those of SLM and HIP. YS was higher, and elongation was lower than with SLM and HIP. The fracture surface analysis suggests that the material showed a ductile behaviour, although limited elongation was observed from the tensile tests.

CRediT authorship contribution statement

Abdullah Alhuzaim: designed the study and performed the experimental tests and the analysis of the results. Writing – review and editing Stano Imbrogno: Reviewing the paper.

Moataz Attallah: supervision, support on experimental feasibility and infrastructure.

Chapter 8. Conclusion, Evaluation and Future Work

The work in this thesis aimed to improve and tailor the microstructure and mechanical properties of the Ni-superalloy by optimising the DLD process parameters. This involved the DLD of IN718 using a wide range of continuous power and pulse power modes. Pulsing can be manipulated to be standard pulse, where the power is at its maximum and minimum levels for equal times in the cycle, or partial power, which in this study had a peak power set at 150% and 75% of the set power and the minimum power was 50% and 25% of the set power. Moreover, manipulation of the pulse cooling time was also studied, in which the time at peak power was increased to 75% of the pulse period and the time at minimum power decreased to 25% of the period, and vice versa. Additionally, the effects of the scanning speed, powder feed and z-increment were studied. Moreover, the DLD process parameter associated with the power mode used to prevent the CM247LC from cracking and to produce a sound and dense build was investigated. This chapter briefly summarises the main conclusions presented in Chapters 4, 5, 6 and 7.

8.1 Summary of chapter 4 effect of laser parameters on geometrical and microstructure development

Essential process parameters directly influence the microstructure and, therefore, the mechanical properties. Laser power, scanning speed, powder feed and layer thickness have been investigated. The findings show that scanning speed has a clear effect on the capture rate: the capture rate increased as the scanning speed increased. Furthermore, the depth of penetration can be affected by the power modes. The PDPPW penetrate the deepest due to the drilling effect applied on the melt pool, followed by the DPPW, and finally the CW penetrates the shallowest. Scanning speed also affected penetration depth: slower scanning speeds resulted in deeper penetration than faster scanning speeds. Furthermore, lowering the powder

feed rate lowered the wall's height, while increasing the powder feed rate raised the wall's height. Additionally, as the z-increment decreased, the columnarity of the grains increased. Finally, the as-built friction coefficient resulting from the CW laser power mode was higher than in the annealed condition, and the annealed condition was higher than in the aged condition.

Increasing laser power has been shown to have a significant impact on penetration depth and capture area. By reinforcing the drill effect, the laser power modes increased penetration depth. The depth of penetration and the geometry of the build were both influenced by scanning speed. The higher the speed, the greater the rate of powder capture and, as a result, the layer thickness. The capture rate was reduced if the speed was too high. Scanning speed had an inverse relationship with penetration depth. Increasing the powder feed rate resulted in a significantly higher capture rate and more precise geometry. The z-increment had an effect on the grain's morphology, decreasing the z-increment increased energy density, making the grains larger and more columnar. The hardness of a sample was affected by post-heat treatment. As a result, the friction coefficient of the sample without post-heat treatment was higher than that of the sample with post-heat treatment. Furthermore, the ageing process produced a lower friction coefficient than annealing.

8.2 Summary of chapter 5 laser power effect on microstructure and mechanical properties

The laser power directly affected the cooling rate, which decreased when laser power increased. The cooling rate affected the formation and the arm spacing of dendrites, which also increased as the cooling rate decreased. In addition, dendrites arm spacing played a major role in Nb segregation, which reduced with increasing DAS, and the mechanical properties reflected this. In addition, laser power impacted on grain size and morphology, thereby affecting the mechanical characteristics. The laser power increased the width and depth of the weld pool.

With the increase in laser power that resulted in reduced thermal gradients and a lower cooling rate, the weld pool increased, leading to a structure with coarse, elongated grains that extended columnarly along the build direction and mainly grew along the thermal flow path.

In contrast, with low laser power, a microstructure was formed that was characterised by a mixed structure of equiaxed and elongated grains along the build direction. The low laser power texture was a combination of equiaxed and columnar grains, consisting of a large amount of small, equiaxed grains on the top and sides of the layers. In addition, rapid cooling demarcation occurred only at low power. Depending on the laser power used, various demarcation angles were observed. Thus, when very low power was used, the angles were measured from 130° and increased to a constant value of 180°, or there was no demarcation at increased power.

Nb segregation is dependent on the cooling rate and the thermal history of the build, and it behaves in a single build as follows. The bottom part had the highest concentration of Nb segregation and Laves phase; the middle of the build showed a decrease in Nb segregation and Laves phase fraction; and the top part of the sample showed an increase again in Nb segregation. However, with builds resulting from different power levels, low power produced a higher cooling rate and, therefore, a higher solidification rate, which produced fine equiaxed dendritic structures with fine and scattered Nb segregation. In contrast, higher laser power formed long, chain-like Nb segregation.

The grain size affected the hardness results: the smaller grain size from the lower laser power gave rise to samples that were slightly harder than those from the higher laser power, which produced a larger grain size. Lower laser power also produced samples with fine Laves phase formation, which can increase the hardness. It was also observed that high laser power leads to the production of samples that show higher density and reduced porosity compared with ones produced by lower laser power. In summary, the microstructure and, in particular,

the grains can be tailored to a particular average size by changing the heat input through different laser power values using a constant scan speed.

8.3 Summary of chapter 6 laser power mode effect on microstructure and mechanical properties

A variety of laser power modes (CW, PW and PPW) and cooling cycles (LCC and HCC) were used along with three conditions (as-built, annealed and aged). Thermocouple results confirmed that the CW provided the highest heat input and PW showed a significant drop of the heat input and a faster cooling effect, while the PPW showed a heat input in between CW and PW. Different power modes and different pulse durations led to different thermal cycles and heat accumulations inducing inevitably different effects on the microstructure. Regarding the geometry of the walls, those produced by PW were the shortest and thinnest, while PPW permitted the production of the most uniform wall. CW produced walls with a height close to the theoretical calculated value. In general, the pulsing decreased the width and length of the grains compared with the same power with the CW mode. Moreover, the CW power mode produced a microstructure dominated by columnar grains with a small percentage of equiaxed grains between the layers, while the PW enhanced the refinement of the grains, producing the lowest grain columnarity and a high percentage of equiaxed grains. Grain size could also be tailored by changing the pulse duration. Different pulse durations allowed modification of the heat accumulation and the cooling rate during the deposition process. Different cooling rates had different effects on grain growth. The grain columnarity increased in the PPW-LCC by 64% compared with the PPW-SP. In contrast, the PPW-HCC decreased grain columnarity by 57% compared with the PPW-SP. A smaller pulse duration and, therefore, higher cooling rate can minimise the melt pool width and consequently reduce the heat accumulation that leads to a finer microstructure.

The use of CW promoted the formation of long chain-like dendrites and increased the segregation area, whereas pulsing led to the formation of smaller dendrites and a relatively finer segregated area. There was less segregation of the Nb in the PPW because the melt pool did not have time to cool down as the power continued but with less intensity during the minimum of the pulsing cycle. The PW showed less Nb segregation, with wide variation at higher powers. PPW-HCC, where power is low and the cooling rate is high, produced fine dendrites and a high percentage of Nb segregation. Moreover, PW-HCC had a much lower heat input and more Nb segregation because the high solidification rate produced fine equiaxed-like structure dendrites with smaller DAS. In contrast, PW-LCC showed the highest heat input and the lowest Nb segregation. The high heat input gave insufficient time for much of the Nb to dissolve back into the matrix and a relatively big DAS. The dendrite core that injects Nb into the liquid was also large; therefore, the segregation was reduced. Pulsing should produce a smaller area of Nb segregation than the CW, because of the breaking of the continuous dendrite formation, and continuous dendrite growth disrupts the ejection of Nb from the dendrite core into the liquid phase. However, PW-HCC and PPW-HCC showed more Nb segregation, not only compared with the PW and PPW standard pulse, but also compared with the CW due to the low heat input.

Usually, lengthy exposure of the samples to high temperatures induces significant grain growth compared with reduced exposure time. However, the annealing treatment performed in this study did not significantly affect the microstructure. The ageing treatment reduced the Nb segregation, but the most significant results were observed with annealing. The annealing treatment dissolved the brittle Laves phase and Nb segregation; however, due to the short post-processing time to dissolve back into the matrix, it didn't form γ'' and that was reflected in the strength of the material. It formed δ instead and that was clearly shown in the low power

samples. Ageing on the other hand, did not dissolve all of the Laves phase, but it was essential to fully precipitate strengthening.

All power modes produced a metallurgically sound build with no signs of cracks, and the layers were well bonded, except in areas with small amounts of gas trapped during solidification. High laser power led to the production of samples of higher density and reduced porosity compared with ones produced by lower laser power. Moreover, the PW showed increased density and, therefore, reduced porosity compared with the PPW. Ageing promoted the formation of strengthening phases (γ' and γ''), since γ' and γ'' phases precipitated and increased hardness. The γ' can form in a shorter time and requires less heat than the sluggish γ''. Lower power produced a slightly harder build than a higher power; however, the hardness of the as-built sample for all three modes was the same, which means the pulsing had no significant effect on hardness. Moreover, annealing increased the hardness significantly and the aged samples showed the highest hardness among all three power modes. The young modulus of all the power modes were similar. However, PPW showed a progressive increase in elongation using pulsing and with decreasing cooling time. Decreasing cooling time to 25% of the pulse duration increased the tensile results, and vice versa, and reduced ductility compared with the PPW-SP. Increasing CW power had no effect on tensile results, although it did affect elongation. The samples showed no necking, which means they were brittle.

8.4 Summary of chapter 7 laser power mode effect on eliminating cracking in CM247LC

High heat input led to porosity, micro- and macro-stress cracking and a lack of fusion. However, there is a small parametric window that can achieve a sound, dense build.

PW beams produce consolidated parts; however, all the CW products displayed porosity, lack of fusion and solidification cracking. These cracks occurred in the mushy zone

where the material had not fully solidified. The cracks form when the temperature drops below the coherence temperature. In contrast, some of the PW products were crack-free, did not lack fusion and were less porous, making them suitable for applications.

The ageing process increased the material strength whilst reducing ductility. Most failed samples cracked during deposition. Moreover, after heat treatment, old cracks propagated, and new cracks also appeared; these cracks are classified as strain age cracking (SAC). In this case the carbides acted as stress raisers or crack initiation sites. The residual stress and the induced stress from the precipitation of the γ' resulted in strain that exceeded the limited ductility of the material and failures in the form of cracks usually occurred at the grain boundaries. However, ageing for at 870 °C for 20 hr without solution treatment was not enough to form the cube-type primary γ'. The microstructure after ageing showed an irregular morphology of the grain boundaries, which could help inhibit grain boundary sliding. Ageing alone did not form a cuboidal microstructure; however, it formed ultra-fine γ_t' instead, which usually appeared in the channels between the cuboidal γ_p'.

Hardness results show that as-built samples had the lowest hardness. Moreover, ageing increased the hardness by about 23%. The CM247LC obtained through DLD was more yield strength than that produced by SLM and less so than that of HIP. The 0.2% strain observed in the DLD process was greater than SLM and HIP produced. Moreover, elongation in CM247LC was greater than the SLM process produced and less than the HIP produced.

8.5 Overall conclusion

This study explores the laser power fixability to its full potential and demonstrated that control the microstructure and control solidification, mitigation of defects, using laser power control via pulsing and partial pulsing.

- Microstructure if Inconel superalloy can be tailored using power parameters.
- Pulsing can change the morphology of the grains and reduce segregation.

- Pulsing control cooling rate therefore the solidification which control microstructure and mitigate defects.
- The control of the microstructure allows us to improve mechanical properties.
- Functionally graded material parts can be achieved using only laser power.
- IN718 is one of material that have the potential to produce a lot of dense conditions with diffract microstructure, the different microstructure gives the potential to tailor the microstructure for properties and reduce the defects

8.6 Future work

Based on the research conducted and discussed in previous chapters in this thesis, the main factor in the DLD of IN718 and CM247LC to reduce segregation, tailor the microstructure and eliminate cracking is the cooling rate. However, the columnar grain structure and Nb segregation was not eliminated from the DLD process at this stage. The following subsections present the future work proposed and potential issues that need to be solved for considering DLD of IN718 and CM247LC for practical industrial applications.

8.6.1 Improve substrate cooling

This proposed work has been considered by a number of researchers. However, the combination of the pulsing laser modes, cooling cycles and frequencies can make a difference. Yuan et al. [59] improved the effectiveness of the substrate by imposing a continuous water flow on the back of the substrate during DLD AM of IN718. Results showed highly ordered columnar dendrites were established, and a mono-crystalline texture was constructed. Zhang et al. [70] used liquid nitrogen to cool down the substrate in the DLD process using IN718. The results showed that the liquid nitrogen provided an ultrarapid cooling rate during laser cladding. The Laves phase in the ultrarapid cooled clad coating was refined and Laves concentration and dendritic space were decreased. Moreover, another idea that can be studied involves surrounding the substrate with a cooling medium, such as water, that increases in height as the build height increases such that each layer is cooled at the same rate throughout the entire build.

8.6.2 The use of a magnetic field during DLD

A number of academics have reported on using a magnetic field to control the microstructure. However, the use of pulsing laser modes, cooling cycles and frequencies could change the microstructure and mechanical properties. Li et al. [259] used a low voltage pulsed magnetic

field to investigate the effect on cast IN718 of the pulsing magnetic field to refine solidified grains. Wang and Shi [260] used the magnetic-field-assisted laser AM method in the DLD of IN718. The results indicated that the magnetic field changed the inter-dendritic micro-segregation pattern from a continuous chain to a discrete morphology.

8.6.3 More complicated shapes

The influences of pulsing modes, cooling cycles and frequency on the microstructure and mechanical properties of multi-track and layer builds (thick walls and solid blocks) need to be investigated, with thermal analysis and monitoring of weld pool behaviour.

8.6.4 Other parameters

The DLD process has many parameters that can have direct and indirect effects on the microstructure and mechanical properties that can be investigated alongside the pulsing modes, cooling cycles, frequency, scanning speed and powder feed, such as scanning strategies, spot size, deposition direction and overlap between layers.

8.6.5 Mechanical testing and modelling

Distortion and residual stress development can be studied and correlated with cooling rates, and modelling can be employed to predict the temperature profile, distortion, resulting thermal stresses and mechanical properties. In addition, fatigue or stress rupture behaviour, particularly at high temperature can be investigated.

References

[1] L. X. Jianyin Chen, Sheng-Hui Wang, "Experimental studies on process-induced morphological characteristics of macro- and microstructures in laser consolidated alloys," vol. 46, pp. 5859–5875, 2011, doi: 10.1007/s10853-011-5543-3.

[2] X. Wang, X. Gong, and K. Chou, "Review on powder-bed laser additive manufacturing of Inconel 718 parts," *Journal of Engineering Manufacturing,* 2015.

[3] Clyde O. Brown, Edward M. Breinan, and M. Bernard H. Kear, "Method for fabricating articles by sequential layer deposition," USA Patent Appl. 88,808, Apr. 6, 1982.

[4] B. Baufeld, Erhard Brandl, and O. v. d. Biest, "Wire Based Additive Layer Manufacturing: Comparison of Microstructure and Mechanical Properties of Ti–6Al–4V Components Fabricated by Laser-Beam Deposition and Shaped Metal Deposition," *Journal of Materials Processing Technology,* pp. 1146-1158, 2011.

[5] A. E. Abdullah Mohammed, Pooya Sareha, Mahmoud Elsayed, Hany Hassanin, "Additive Manufacturing Technologies for Drug Delivery Applications," *International Journal of Pharmaceutics,* vol. 580, 2020.

[6] T. Masuch, "Consumer Products & Electronics increasingly important for AM market," Wohlers Report 2020 illustrates current trends in the industry and numerous applications 2020. [Online]. Available: https://fon-mag.de/industry-news/2020/05-wohlers-report/?L=1

[7] "3D printing: a threat to global trade," ING Economic and Financial Analysis, 2017.

[8] M. Petch, "ING report claims 3D printing will make over $6 trillion of goods within 40 years," 2017. [Online]. Available: https://3dprintingindustry.com/news/ing-report-claims-3d-printing-will-make-6-trillion-goods-within-40-years-122100/

[9] M. AM. *Analysis of Additive Manufacturing materials from Wohlers and Senvol Database*. [Online]. Available: https://www.metal-am.com/analysis-of-additive-manufacturing-materials-from-wohlers-and-senvol-database/

[10] H. Qi, M. Azer, and P. Singh, "Adaptive toolpath deposition method for laser net shape manufacturing and repair of turbine compressor airfoils," *Int J Adv Manuf Technol* vol. 48, pp. 121-131, 2010.

[11] P.A. Kobryn, E. H. Moore, and S. L. Semiatin, "The effect of laser power and traverse speed on microstructure, porosity, and build height in laser-deposited Ti-6Al-4V," *Scripta mater.,* vol. 43, pp. 299–305, 2000.

[12] N. R. O. P.A. Kobryn, L.P. Perkins and J.S. Tiley, "Additive Manufacturing of Aerospace Alloys for Aircraft Structures," *Net-Shape Processing,* pp. 3-1 – 3-14, 2006.

[13] S. M. K. a. S. L. KAMPE, "Microstructural Evolution in Laser-Deposited Multilayer Ti-6Al-4V Builds: Part I. Microstructural Characterization," *METALLURGICAL AND MATERIALS TRANSACTIONS A,* 2002.

[14] N. Shamsaei, A. Yadollahi, L. Bian, and S. M. Thompson, "An overview of Direct Laser Deposition for additive manufacturing; Part II: Mechanical behavior, process parameter optimization and control," *Additive Manufacturing,* vol. 8, 2015.

[15] A. Segerstark, "Additive Manufacturing using Alloy 718 Powder," MS, University West, Sweden, 2015.

[16] R.J. Moat, A. J. Pinkerton, L. Li, P. J. Withers, and M. Preuss, "Crystallographic texture and microstructure of pulsed diode laser-deposited Waspaloy," *Acta Materialia,* vol. 57, pp. 1220-1229, 2009.

[17] G. P. Dinda, A. K. Dasgupta, and J. Mazumder, "Laser aided direct metal deposition of Inconel 625 superalloy: Microstructural evolution and thermal stability," *Materials Science and Engineering A,* vol. 509, pp. 98-104, 2009.
[18] A. P. D. Zhang *et al.*, "Grain Refinement of Alloys in Fusion-Based Additive Manufacturing Processes," *Metallurgical And Materials Transactions,* 2020.
[19] F. Liu *et al.*, "Microstructural changes in a laser solid forming Inconel 718 superalloythin wall in the deposition direction," *Optics&LaserTechnology,* pp. 330-335, 2013.
[20] "High-Performance Alloys, Special Metals Corporation (SMC)." http://www.specialmetals.com/products/index.php. (accessed.
[21] E. Akca and A. Gursel, "A review on superalloys and IN718 nickel-based INCONEL superalloy," *Periodicals of Engineering and Natural Sciences,* vol. 3, 2015.
[22] M. M. D. Locq, A. Walder, P. Caron, "Development of New PM Superalloys for High Temperature Applications," *Intermetallics and Superalloys,* vol. 10, 2000.
[23] C. T. Sims, Stoloff, N. S., and Hagel, W. C., *Superalloys II*. New York: Wiley, 1986.
[24] I. S. B. Paper, "Nickel-Based Super Alloys," *No.20,* April 2013.
[25] T. M. Pollock and S. Tin, "Nickel-Based Superalloys for Advanced Turbine Engines: Chemistry, Microstructure, and Properties," *Journal of Propulsion and Power,* vol. 22, 2006.
[26] D. A. M. B. Henderson, R. Larsson, M. Heobel & G. Marchant, "Nickel based superalloy welding practices for industrial gas turbine applications," *Science and Technology of Welding and Joining,* vol. 9, 2004, doi: 10.1179/136217104225017099.
[27] o. H. a. r. C. R. D. Dye, "Numerical analysis of the weldability of superalloys," *Acta Material,* vol. 49, pp. 683–697, 2001.
[28] T. E. C. BY G. A. YOUNG, M. A. PENIK, B. W. MORRIS, AND J. J. McGEE, "The Mechanism of Ductility Dip Cracking in Nickel-Chromium Alloys," *WELDING JOURNAL,,* 2008.
[29] M. Sundararaman, P. Mukhopadhyay, and S. Banerjee, "Some Aspects of the Precipitation of Metastable Intermetallic Phases in Inconel 718 " *Metallurgical Transactions A,* 2015.
[30] P. H.J. Frost and M.F. Ashby, "Deformation-mechanism maps: The plasticity and creep of metals and ceramics," *Applied Science Publishers,* 1982.
[31] J. A. Dutton. "Face Centered Cubic Structure (FCC)." PennState. https://www.e-education.psu.edu/matse81/node/2133 (accessed.
[32] W. K. H. B. REPPICH, G. MEYER, D. PUPPEL, M. SCHULZ$ and G. SCHUMANN, "Duplex γ' Particle Hardening of the Superalloy Nimonic PE 16 " *Materials Science and Engineering,* pp. 45-63, 1986.
[33] H. K. D. H. Bhadeshia. "Nickel Based Superalloys." University of Cambridge. https://www.phase-trans.msm.cam.ac.uk/2003/Superalloys/superalloys.html (accessed.
[34] P. M. M. SUNDARARAMAN, and S. BANERJEE, "Some Aspects of the Precipitation of Metastable Intermetallic Phases in INCONEL 718 " *METALLURGICAL TRANSACTIONS A,* 2015.
[35] R. Cozar and A. Pineau, "Morphology of γ' and γ" Precipitates and Thermal Stability of Inconel 718 Type Alloys " *Metallurgical Transactions,* vol. 4, 1973.
[36] D. F. P. J. M. OBLAK, AND D. S. DUVALL, "Coherency Strengthening in Ni Base Alloys Hardened by D022 Precipitates," *METALLURGICAL TRANSACTIONS,* vol. 5, pp. 143-153, 1974.

[37] "Nb-Ni (Niobium–Nickel) Section III: Supplemental Literature Review," *Journal of Phase Equilibria and Diffusion* vol. 29, 2008.
[38] W. A. B. I. a. D. E. NELSON, "Morphology of Weld Heat-Affected Zone Liquation in Cast Alloy 718," *METALLOGRAPHY* 1986.
[39] R. Y. Zhang *et al.*, "Using Variant Selection to Facilitate Accurate Fitting of γ″ Peaks in Neutron Diffraction," *Metallurgical And Materials Transactions A,* vol. 50A, pp. 5421- 5432, 2019.
[40] S. Azadian and L.-Y. Wei, "Precipitation in spray-formed IN718," *The Minerals. Metals & Materials Society,* 2001.
[41] G. Sjoberg and N.-G. Ingesten, "Grain Boundary δ-phase Morphologies, Carbides and Notch Rupture Sensitivity of Cast Alloy 718 " *The Minerals, Metals & Materials Society,* pp. 603-620, 1991.
[42] M. P. J. R.C. REED, and Y.S. NA, "Characterization and Modeling of the Precipitation of the Sigma Phase in UDIMET 720 and UDIMET 720LI," *METALLURGICAL AND MATERIALS TRANSACTIONS A,* vol. 30A, 1999.
[43] R. C. Reed, *The Superalloys - Fundamentals and Applications*. Cambridge University Press 2006.
[44] M. J. Donachie and S. J. Donachie, *Superalloys A Technical Guide*. ASM International, 2002.
[45] J. N. Dupont, C. V. Robino, and A. R. Marder, "Solidification and Weldability of Nb-Bearing Superalloys." [Online]. Available: http://img2.aws.org/wj/supplement/dupont/dupont.html.
[46] S. Kou, "Welding metallurgy," *John Wiley & Sons,* 2003.
[47] W. Kurz and D. J. Fisher, *Fundamentals of Solidification*, Fourth Revised Edition ed. 1998.
[48] D. A. Porter, K. E. Easterling, and M. Y. Sherif, *Phase transformations in metals and alloys*. FL: Boca Raton, 2009.
[49] S. A. David and J. M. Vitek, "Correlation between solidification parameters and weld microstructures," *International Materials Reviews,* 2013.
[50] A. Mitchell and T. Wang, "Solidification and Precipitation in IN718 " *Superallys,* 2001.
[51] E. Vandersluis, A. Lombardi, C. Ravindran, A. Bois-Brochu, F. Chiesa, and R. MacKay, "Factors influencing thermal conductivity and mechanical properties in 319 Al alloy cylinder heads," *Materials Science & Engineering A,* vol. 648, 2015.
[52] Y. Shi, Q. Xu, R. Chen, B. Liu, Q. Wu, and H. Yang, "A microstructure-strength calculation model for predicting tensile strength of AlSi7Mg alloy castings. ," *In 2nd World Congress on Integrated Computational Materials Engineering, Somerset,,* 2013.
[53] M. G. umann, S. Henry, F. C.́ton, J.-D. Wagnie`re, and W. Kurz, "Epitaxial laser metal forming: analysis of microstructure formation," *Materials Science and Engineering* vol. A271, pp. 232 – 241, 1999.
[54] H. Xiao, S. Li, X. Hana, J. Mazumder, and L. Song, "Laves phase control of Inconel 718 alloy using quasi-continuous-wave laser additive manufacturing," *Materials and Design,* vol. 122, pp. 330-339, 2017.
[55] F. L. Yuan Chen, Ke Zhang, Pulin Nie, Seyed Reza Elmi Hosseini, Kai Feng**, Zhuguo Li*, "Dendritic microstructure and hot cracking of laser additive manufactured Inconel 718 under improved base cooling," *Journal of Alloys and Compounds,* vol. 670, pp. 312-321, 2016.

[56] E. Schlienger *et al.*, "Near Net shape Production of metal Components using LENS," 1998.
[57] J. J. Schirra, R. H. Caless, and R. W. Hatala, "The Effect of Laves Phase on The Mechanical Properties of Wrought and Cast + Hip Inconel 718 " *The Minerals, Metals & Materials Society,* 1991.
[58] G. D. J. Ram, A. V. Reddy, K. P. Rao, and G. M. Reddy, "Control of Laves phase in Inconel 718 GTA welds with current pulsing," *Science and Technology of Welding and Joining,* 2013.
[59] Y. Chen, F. Lu, K. Zhang, P. Nie, S. R. E. Hosseini, and Z. L. Kai Feng, "Dendritic microstructure and hot cracking of laser additive manufactured Inconel 718 under improved base cooling," *Journal of Alloys and Compounds,* vol. 670, pp. 312-321, 2016.
[60] X. Wu, R. Sharman, and W. V. J. Mei, "Direct laser fabrication and microstructure of a burn-resistant Ti alloy," *Materials and Design,* vol. 23, pp. 239-247, 2002.
[61] N. Raghavan *et al.*, *Numerical modeling of heat-transfer and the influence of process parameters on tailoring the grain morphology of IN718 in electron beam additive manufacturing*. (in English), 2016.
[62] Connor and P. Leonard, *Welding Handbook*. American Welding Society, 1989.
[63] A. F. Alhuzaim, "Investigation in the use of plasma arc welding and alternative feedstock delivery method in additive manufacture," Master of Science General Engineering, General Engineering, Montana Tech of the University of Montana, Congriess libraby, 2014.
[64] V. A. Popovich, E. V. Borisov, A.A.Popovich, V. S. Sufiiarov, D. V. Masaylo, and L. Alzina, "Functionally graded Inconel 718 processed by additive manufacturing: Crystallographic texture, anisotropy of microstructure andmechanical properties," *Materials and Design,* 2017.
[65] Z. Wang, T. A. Palmer, and A. M. Beese, "Effect of processing parameters on microstructure and tensile properties of austenitic stainless steel 304L made by directed energy deposition additive manufacturing," *Acta Materialia,* vol. 110, pp. 226-235, 2016.
[66] L. Nastac, J. J. Valencia, M. L. Tims, and F. R. Dax, "Advances in the solidification of IN718 and RS5 alloys," *The Minerals Metals Society,* 2001.
[67] J. X. Z. Z.S. Yu, Y. Yuan, R.C. Zhou, H.J. Zhang, H.Z. Wang "Microstructural evolution and mechanical properties of Inconel 718 after thermal exposure," *Materials Science & Engineering A,* vol. 634, pp. 55-63, 2015.
[68] X. L. Xiaobin Yu, Fencheng Liu, Lilin Wang, Yao Tang, Jiacong Li, Shuya Zhang, Weidong Huang, "Influence of post-heat-treatment on the microstructure and fracture toughness properties of Inconel 718 fabricated with laser directed energy deposition additive manufacturing," *Materials Science & Engineering A,* vol. 798, 2020.
[69] H. Xiao *et al.*, "Effects of laser modes on Nb segregation and Laves phase formation during laser additive manufacturing of nickel-based superalloy," *Materials Letters,* vol. 188, pp. 260-262, 2017.
[70] Y. C. Zhang, Z. G. Li, P. L. Nie, and Y. X. Wu, "Effect of ultrarapid cooling on microstructure of laser cladding IN718 coating," *Surface Engineering,* vol. 29, pp. 414 - 418, 2013.
[71] G.P.Dinda, A.K.Dasgupta, and J.Mazumder, "Texture control during laser deposition of nickel-based superalloy," *Scripta Materialia,* vol. 76, pp. 503-506, 2012.

[72] D. Verdi, M. A. Garrido, C. J. Múnez, and P. Poza, "Mechanical properties of Inconel 625 laser cladded coatings: Depth sensing indentation analysis," *Materials Science and Engineering: A,* vol. 598, pp. 15–21, 2014.
[73] A. J. PinkertonLin and L. Li, "An investigation of the effect of pulse frequency inlaser multiple-layer cladding of stainless steel," *Applied Surface Science* vol. 208-209, pp. 405-410, 2003, doi: 10.1016/S0169-4332(02)01420-4.
[74] G. A. Ravi, C. Qiu, and M. M. Attallah, "Microstructural control in a Ti-based alloy by changing laser processing mode and power during direct laser deposition," *Materials Letters,* vol. 179, pp. 104–108, 2016.
[75] "Connon-Muskegon." www.c-mgroup.com (accessed.
[76] S. CT, "Comtemporary view of nickel-base superalloys," *jornal of metals*, doi: 1966;18:1119.
[77] M. D. T. Ali P. Gordon, Richard W. Neu, Thomas J. Sanders Jr, David L. McDowell, "Corrosion kinetics of a directionally solidified Ni-base superalloy," *Acta Material,* vol. 55, 2007.
[78] S. L. STEPHEN D. ANTOLOVICH, AND R. BAUR, "Low Cycle Fatigue Behavior of Ren6 80 at Elevated Temperature," *METALLURGICAL TRANSACTIONS A,* 1981.
[79] D. A. B. Huseyin Sehitoglu, "Thermo-Mechanical Fatigue of Mar-M247: Part 2—Life Prediction," *ASME,* vol. 80, 1990.
[80] H. S. D. A. Boismier, "Thermo-iechanical Fatigue of Mar-M247: Part 1—Experiments " *ASME,* vol. 68, 1990.
[81] J. L. F. COFFIN, "The Effect of Frequency on the Cyclic Strain and Fatigue Behavior of Cast Ren6 at 1600~ F," *METALLURGICAL TRANSACTIONS,* vol. 5.
[82] A. E. S.-B. REES D. RAWLINGS, "The alloying behaviour and mechanical properties of polycrystalline Ni3AI (y" phase) with ternary additions " *JOURNAL OF MATERIALS SCIENCE,* vol. 10, pp. 505-514, 1975.
[83] R. W. H. G.M. JANOWSKI, and B.J. PLETKA, "The effects of tantalum on the microstructure of two polycrystalline nickel-base superalloys: B-1900 + Hf and MAR-M247," *METALLURGICAL TRANSACTIONS A,* 1986.
[84] N. L. E. Michael V, "INFLUENCE OF COBALT, TANTALUM, AND TUNGSTEN ON THE HICROSTRUCTURE AND
WECHANlCAL PROPERTIES OF SUPERALLOY SINGLE CRYSTALS."
[85] L. E. MV Nathal, "influence of cobalt tantalum and tungsten on the elevated temperature mechanical properties of single crystal nickel base superalloys metallurgical and materials transaction " 1985.
[86] D. R. F. W. s. Chakravorty, " High-temperature strength of nickel alloys based on Y'-phase," *Metals Technology* 1980.
[87] J. R. B. K. Heck, and R. F. Singer, "Castability of directionally solidified nickel base superalloys," *Materials Science and Technology,* vol. 15, 1999.
[88] D. N. D. a. C. P. Sullivan, "Some effects of hafnium additions on the mechanical properties of a columnar-grained nickel-base superalloy," *OURNAL OF METALS,* 1971.
[89] B. H. K. J.E.Doherty, and A. F. Giamei "On the origin of the ductility enhancement in Hf-doped Mar-M200," *JOURNAL OF METALS,* vol. 59, 1971.
[90] G. A. Doherty je, Kear BH., "The importance of grain boundary morphology and cohesion on intergranular strength," 1974.
[91] Prager and Shira, "Welding of precipitation hardening nickel based alloys," *Welding Research Council, Bulletin* vol. 128, 1968.

[92] J. W. Brooks and P. J. Bridges, "Metallurgical Stability Of Inconel Alloy 718 " *Superalloys* pp. 33-42, 1988.
[93] J. R. D. A. D. E. M. R. G. Thompson, "The Effect of Heat Treatment on Microfissuring in Alloy 718 " *Welding Research Supplement,* pp. 299-304, 1986.
[94] A. Oradei-Basile and J. F. Radavich, "A Current T-T-T Diagram For Wrought Alloy 7 18 " *superallys,* pp. 325-335, 1991.
[95] G. Lindwall *et al.*, "Simulation of TTT Curves for Additively Manufactured Inconel 625," *Metallurgical And Materials Transactions A,* vol. 50A, pp. 457-467, 2018.
[96] W. Huang, J. Yang, H. Yang, G. Jing, Z. Wang, and X. Zeng, "Heat treatment of Inconel 718 produced by selective laser melting: Microstructure and mechanical properties," *Materials Science & Engineering A,* vol. 750, pp. 98-107, 2019.
[97] W. J. Sames, K. A. Unocic, R. R. Dehoff, T. Lolla, and S. S. Babu, "Thermal effects on microstructural heterogeneity of Inconel 718 materials fabricated by electron beam melting," *Materials Research Society,* pp. 1920-1930, 2014.
[98] T. Zhai, A. J. Wilkinson, and J. W. Martin, "A Crystallographic Mechanism For Fatigue Crack Propagation Through Grain Boundaries," *Acta Mater,* vol. 48, pp. 4917–4927, 2000.
[99] B. Larrouy, P. Villechaise, J. Cormier, and O. Berteaux, "Grain boundary–slip bands interactions: Impact on the fatigue crack initiation in a polycrystalline forged Ni-based superalloy," *Acta Materialia,* vol. 99, pp. 325-336, 2015.
[100] C. Radhakrishna and K. P. Rao, "The formation and control of Laves phase in superalloy 718 welds," *Materials science,* vol. 32, p. 1977—1984, 1997.
[101] Z. Weiguo *et al.*, "Effect of cooling rates on dendrite spacings of directionally solidified DZ125 alloy under high thermal gradient " *Rare Metals,* vol. 28, pp. 633-638, 2009.
[102] A. Zhang *et al.*, "Effect of cooling rate on phosphorus segregation behavior and the corresponding precipitation of and phases in IN718 alloy," *Journal of Materials Science & Technology,* vol. 35, pp. 1485-1490, 2019.
[103] F. Wirth, S. Freihse, D. Eisenbarth, and K. Wegener, "Interaction of powder jet and laser beam in blown powder laser deposition processes: Measurement and simulation methods," *Lasers in Manufacturing Conference,* 2017.
[104] D. Bourell *et al.*, "Materials For Additive Manufacturing," *CIRP Annals - Manufacturing Technology,* vol. 66, pp. 658-681, 2017.
[105] Y. C. Shin. "Research on Additive Manufacturing." Purdue Research Foundation. https://engineering.purdue.edu/LAMPL/research_AM.html (accessed.
[106] T. DebRoy *et al.*, "Additive manufacturing of metallic components – Process, structure and properties," *Progress in Materials Science,* vol. 92, pp. 112-224, 2018.
[107] A. Segerstark, "Laser Metal Deposition using Alloy 718 Powder Influence of Process," PhD, University of West, 2017.
[108] C. Zhong, N. Pirch, A. Gasser, R. Poprawe, and J. H. Schleifenbaum, "The Influence of the Powder Stream on High-Deposition-Rate Laser Metal Deposition with Inconel 718," *metals,* vol. 443, 2017.
[109] O. Adegoke, J. Andersson, H. Brodin, and R. Pederson, "Influence of Laser Powder Bed Fusion Process Parameters on Voids, Cracks, and Microhardness of Nickel-Based Superalloy Alloy 247LC," *Materials* vol. 3770, 2020, doi: :10.3390/ma13173770.
[110] Y. Chen *et al.*, "Investigation of dendritic growth and liquation cracking in laser melting deposited Inconel 718 at different laser input angles," *Materials and Design,* vol. 105, pp. 133-141, 2016.

[111] Y. Wang, J. Choi, and J. Mazumder, "Laser-Aided Direct Writing of NickelBased Single-Crystal Super Alloy (N5)," *The Minerals, Metals & Materials Society and ASM International,* 2016, doi: 10.1007/s11661-016-3755-5.
[112] B. AlMangour and J.-M. Yang, "Improving the surface quality and mechanical properties by shot-peening of 17-4 stainless steel fabricated by additive manufacturing," *Materials and Design,* vol. 110, pp. 914-924, 2016.
[113] X. Ran, D. Liu, A. Li, H. Wang, H. Tang, and X. Cheng, "Microstructure characterization and mechanical behavior of laser additive manufactured ultrahigh-strength AerMet100 steel," *Materials Science & Engineering A,* vol. 663, pp. 69-77, 2016.
[114] G. Sun, R. Zhou, J. Lu, and J. Mazumder, "Evaluation of defect density, microstructure, residual stress, elastic modulus, hardness and strength of laser-deposited AISI 4340 steel," *Acta Material,* vol. 84, pp. 172-189, 2015.
[115] J. Yao *et al.*, "Influence of heat-treatment on the dynamic behavior of 3D laserdeposited Ti–6Al–4V alloy," *Materials Science & Engineering A,* vol. 677, pp. 153-162, 2016.
[116] A. Reichardt *et al.*, "Development and characterization of Ti-6Al-4V to 304L stainless steel gradient components fabricated with laser deposition additive manufacturing," *Materials and Design,* vol. 104, pp. 404-413, 2016.
[117] K. Shah, A. J. Pinkerton, A. Salman, and L. Li, "Effects of Melt Pool Variables and Process Parameters in Laser Direct Metal Deposition of Aerospace Alloys," *Materials and Manufacturing Processes,* vol. 25, pp. 1372–1380, 2010, doi: 10.1080/10426914.2010.480999. Taylor & Francis Group, LLC.
[118] A. J. Pinkerton and L. Li, "The effect of laser pulse width on multiple-layer 316L steel clad microstructure and surface finish," *Applied Surface Science,* pp. 411-416, 2003.
[119] K. Sivaprasad and S. G. S. Raman, "Influence of magnetic arc oscillation and current pulsingon fatigue behavior of alloy 718 TIG weldments," *Materials Science and Engineering A* vol. 448, pp. 120–127, 2007.
[120] C. Radhakrishna and R. Claimed, "The formation and control of Laves phase in superalloy 718 welds," *Journal of Materials Science* vol. 32, p. 1977 — 1984, 1997.
[121] C. P. Paul, H. Alemohammad, E. Toyserkani, A. Khajepour, and S. Corbin, "Cladding of WC–12 Co on low carbon steel using a pulsed Nd:YAG laser," *Materials Science and Engineering A,* pp. 170–176, 2007.
[122] M. Gerstgrasser, M. Cloots, J. Stirnimann, and K. Wegener, "Focus shift analysis, to manufacture dense and crack-free SLM-processed CM247LC samples," *Journal of Materials Processing Tech. ,* vol. 289, p. 116948, 2021.
[123] Y. S. Lee, M. Nordin, S. S. Babu, and D. F. Farson, "Influence of Fluid Convection on Weld Pool Formation in Laser Cladding," *Welding Journal,* vol. 93, pp. 292-300, 2014.
[124] H. Hilal, R. Lancaster, D. Stapleton, and G. Baxter, "Investigating the Influence of Process Parameters on the Structural Integrity of an Additively Manufactured Nickel-Based Superalloy," *Metals,* vol. 9, 2019.
[125] V. Ocelı´k, I. Fura´r, and J. T. M. D. Hosson, "Microstructure and properties of laser clad coatings studied by orientation imaging microscopy," *Acta Materialia,* 2010.
[126] X. C. Wang, T. Laoui, J. Bonse, J. P. Kruth, B. Lauwers, and L. Froyen, "Direct Selective Laser Sintering of Hard Metal Powders: Experimental Study and Simulation," *The international advanced manufacturing technology,* vol. 19, pp. 351–357, 2002.

[127] J. Ibarra-Medina and A. J. Pinkerton, "Numerical investigation of powder heating in coaxial laser metal deposition," *Surface Engineering,* vol. 27, pp. 754-761, 2011.
[128] J. Kummailil, C. Sammarco, D. Skinner, C. A. Brown, and K. Rong, "Effect of Select LENS™ Processing Parameters on the Deposition of Ti-6Al-4V," *Journal of Manufacturing Processes,* vol. 7, pp. 42-50, 2005.
[129] L. Tang, J. Ruan, R. G. Landers, and F. Liou, "Variable Powder Flow Rate Control in Laser Metal Deposition Processes," *Journal of Manufacturing Science and Engineering,* vol. 30, p. 041016, 2008, doi: 10.1115/1.2953074.
[130] G. Zhu, D. Li, A. Zhang, G. Pi, and Y. Tang, "The influence of laser and powder defocusing characteristics on the surface quality in laser direct metal deposition," *Optics & Laser Technology,* vol. 44, pp. 349-356, 2012.
[131] L. Costa and R. Vilar, "Laser powder deposition," *Rapid Prototyping Jurnal* pp. 264-279, 2009, doi: 10.1108/13552540910979785.
[132] E. Fearon and K. G. Watkins, " Optimisation of layer height control in direct laser deposition," *Journal of Laser Applications,* vol. 1708, 2004, doi: 10.2351/1.5060232.
[133] A. J. Pinkerton and L. Li, "The significance of deposition point standoff variations in multiple-layer coaxial laser cladding (coaxial cladding standoff effects)," *International Journal of Machine Tools & Manufacture* vol. 44, pp. 573–584, 2004.
[134] S. G. K. Manikandana, D. Sivakumar, K. P. Rao, and M. Kamaraj, "Effect of weld cooling rate on Laves phase formation in Inconel 718 fusion zone," *Journal of Materials Processing Technology,* vol. 214, pp. 358-364, 2014.
[135] S. R. Agnew, *Crystallographic Texture*. Encyclopedia of Condensed Matter Physics, 2005.
[136] J. P. Oliveira, T. G. Santos, and R. M. Miranda, "Revisiting fundamental welding concepts to improve additive manufacturing: From theory to practice," *Progress in Materials Science,* vol. 107, 2020.
[137] X. Zhao, J. Chen, X. Lin, and W. Huang, "Study on microstructure and mechanical propertiesof laser rapid forming Inconel 718," *Materials Science and Engineering A* vol. 478, pp. 119–124, 2008.
[138] L. L. Parimi, M. M. Attallah, J. C. Gebelin, and R. C. Reed, "Direct Laser Fabrication Of Inconel-718: Effects On Distortion And Microstructure " *International Symposium on Superallys,* 2012.
[139] E. L. Stevens, J. Toman, A. C. To, and M. Chmielus, "Variation of hardness, microstructure, and Laves phase distribution indirect laser deposited alloy 718 cuboids," *Materials and Design,* vol. 119, pp. 188-198.
[140] E. Amsterdam and G. A. Kool, "High Cycle Fatigue of Laser Beam Deposited Ti-6Al-4V and Inconel 718," *ICAF Symposium – Rotterdam* pp. 1261-1262, 2009.
[141] Y. Zhang, L. Yang, T. Chen, W. Zhang, X. Huang, and J. Dai, "Investigation on the optimized heat treatment procedure for laser fabricated IN718 alloy," *Optics and Laser Technology,* vol. 97, pp. 172-179, 2017.
[142] Y. Tian *et al.*, "Rationalization of Microstructure Heterogeneity in INCONEL 718 Builds Made by the Direct Laser Additive Manufacturing Process," *The Minerals, Metals & Materials Society and ASM International,* vol. 45A, pp. 4470-4483, 2014.
[143] Z. Minlin, Y. Lin, L. Wenjin, H. Ting, and H. Jingjiang, "Laser rapid manufacturing of special pattern IN718 nickel-based alloy component," *The International Society for Optical Engineering,* pp. 511–519, 2005.
[144] Z. Qun-Li, Y. Jian-Hua, and J. Mazumder, "Laser Direct Metal Deposition Technology and Microstructure and Composition Segregation of Inconel 718

Superalloy," *Journal of iron and steel research, international,* vol. 18, pp. 73-78, 2011.
[145] E. Amsterdam, "Evaluation of the microstructure and mechanical properties of laser additive manufactured gas turbine alloys Ti-6Al-4V and Inconel 718," *National Aerospace Laboratory NLR* 2010.
[146] F. Liu *et al.*, "The effect of laser scanning path on microstructures and mechanical properties of laser solid formed nickel-base superalloy Inconel 718," *Journal of Alloys and Compounds,* vol. 509, pp. 4505-4509, 2011.
[147] J. H. Boswell, D. Clark, W. Li, and M. M. Attallah, "Cracking during thermal post-processing of laser powder bed fabricated CM247LC Ni-superalloy," *Materials and Design,* vol. 174, 2019.
[148] V. D. Divya *et al.*, "Microstructure of selective laser melted CM247LC nickel-basedsuperalloy and its evolution through heat treatment," *Materials Characterization,* vol. 114, pp. 62-74, 2016.
[149] R. Muñoz-Moreno *et al.*, "Effect of heat treatment on the microstructure, texture and elastic anisotropy of the nickel-based superalloy CM247LC processed by selective laser melting," *Materials Science & Engineering A,* vol. 674, pp. 529-539, 2016.
[150] H. Qi, M. Azer, and A. Ritter, "Studies of Standard Heat Treatment Effects on Microstructure and Mechanical Properties of Laser Net Shape Manufactured INCONEL 718," *The Minerals, Metals & Materials Society and ASM International,* vol. 40A, pp. 2410-2422, 2009, doi: 10.1007/s11661-009-9949-3.
[151] Y.-L. Kuo and K. Kakehi, "Influence of Powder Surface Contamination in the Ni-Based Superalloy Alloy718 Fabricated by Selective Laser Melting and Hot Isostatic Pressing," *Metals,* vol. 367, 2017, doi: 10.3390/met7090367.
[152] P. L. Blackwell, "The mechanical and microstructural characteristics of laser-deposited IN718," *Journal of Materials Processing Technology,* vol. 170, pp. 240-246, 2005.
[153] S. Sui *et al.*, "The influence of Laves phases on the room temperature tensile properties of Inconel 718 fabricated by powder feeding laser additive manufacturing," *Acta Materialia,* vol. 164, pp. 413-427, 2019.
[154] H.-E. Huang and C.-H. Koo, "Characteristics and Mechanical Properties of Polycrystalline CM247LC Superalloy Casting," *Materials Transactions,* vol. 45, pp. 562-568, 2004.
[155] I. S. Kim, B. G. Choi, S. M. Seo, D. H. Kim, and C. Y. Jo, "Influence of heat treatment on microstructure and tensile properties ofconventionally cast and directionally solidified superalloy CM247LC," *Materials Letters* vol. 62, pp. 1110–1113, 2008.
[156] X. Wang, L. N. Carter, B. Pang, M. M. Attallah, and M. H. Loretto, "Microstructure and yield strength of SLM-fabricated CM247LC Ni-Superalloy," *Acta Materialia,* vol. 87, pp. 87-95, 2017.
[157] J. N. DuPont, J. C. Lippold, and S. D. Kiser, *Welding Metallurgy And Weldability Of Nickel-Base Alloys*. New Jersey.: John Wiley & Sons, Inc., Hoboken, 2009.
[158] S. Kou, "Solidifi cation and Liquation Cracking Issues in Welding," *JOM,* 2003.
[159] H. S. Minlin Zhong, Wenjin Liu, Xiaofeng Zhu, Jinjiang He, "Boundary liquation and interface cracking characterizationin laser deposition of Inconel 738 on directionally solidifiedNi-based superalloy," *Scripta Materialia,* vol. 53, pp. 159–164, 2005.
[160] o. A. O. R.K. Sidhu, and m.C. Chaturvedi, "Microstructural Response of Directionally Solidified Rene´ 80 Superalloy to Gas-Tungsten Arc Welding," *METALLURGICAL*

AND MATERIALS TRANSACTIONS A, vol. 40A, 2009, doi: 10.1007/s11661-008-9700-5.
[161] R. A. B. A.T. Egbewande, O.A. Ojo, "Analysis of laser beam weldability of Inconel 738 superalloy," *MATERIALS CHARACTERIZATION* vol. 61, pp. 569 – 574, 2010.
[162] Y. M. Arata, Fukuhisa; Katayama, Seiji, "Solidification Crack Susceptibility in Weld Metals of Fully Austenitic Stainless Steels (Report II) : Effect of Ferrite, P, S, C, Si and Mn on Ductility Properties of Solidification Brittleness," no. Osaka University, 1977.
[163] N. E. N. J.C. Lippold, "Further investigations of ductility-dip cracking in high chromium, ni-base filler metals," *Welding in the World,* vol. 51, no. The Ohio State University, 2007.
[164] W. Everhart, E. Sawyer, T. Neidt, J. Dinardo, and B. Brown, "The effect of surface finish on tensile behavior of additively manufactured tensile bars," *J Mater Sci,* vol. 51, pp. 3836–3845, 2016, doi: 10.1007/s10853-015-9702-9.
[165] H. K. Rafi, N. V. Karthik, H. Gong, T. L. Starr, and B. E. Stucker, "Microstructures and Mechanical Properties of Ti6Al4V Parts Fabricated by Selective Laser Melting and Electron Beam Melting," *JMEPEG,* vol. 22, pp. 3872–3883, 2013, doi: 10.1007/s11665-013-0658-0.
[166] T. Niendorf and F. Brenne, "Steel showing twinning-induced plasticity processed by selective laser melting — An additively manufactured high performance material," *Materials Characterization,* vol. 85, pp. 57-63, 2013.
[167] N. Hrabe and T. Quinn, "Effects of processing on microstructure and mechanical properties of a titanium alloy (Ti–6Al–4V) fabricated using electron beam melting (EBM), Part 2: Energy input, orientation, and location," *Materials Science & Engineering A,* vol. 573, pp. 271-277.
[168] B. S. Bass, "Validating the Arcam EBM Process as an Alternative Fabrication Method for Titanium-6Al-4V Alloys," Master of Science, Materials Science and Engineering, North Carolina State University, 2007.
[169] A. A. Antonysamy, "Microstructure, Texture and Mechanical Property Evolution during Additive Manufacturing of Ti6Al4V Alloy for Aerospace Applications," Doctor of Philosophy, Engineering and Physical Sciences, University of Manchester, 2012.
[170] D. Deng, R. L. Peng, H. Brodin, and J. Moverare, "Microstructure and mechanical properties of Inconel 718 produced by selective laser melting: Sample orientation dependence and effects of post heat treatments," *Materials Science & Engineering A,* vol. 713, pp. 294-306, 2018.
[171] Z. Li, J. Chen, S. Sui, C. Zhong, X. Lu, and X. Lin, "The microstructure evolution and tensile properties of Inconel 718fabricated by high-deposition-rate laser directed energy deposition," *Additive Manufacturing,* vol. 31, 2020.
[172] M. N. Ahsan, A. J. Pinkerton, R. J. Moat, and J. Shackleton, "A comparative study of laser direct metal deposition characteristics using gas and plasma-atomized Ti–6Al–4V powders," *Materials Science and Engineering A,* vol. 528, pp. 7648–7657, 2011.
[173] *What is a disk laser*, the welding institute. [Online]. Available: https://www.twi-global.com/technical-knowledge/faqs/what-is-a-disk-laser/.
[174] A. Matsunawa, S. Katayama, H. Ikeda, and K. Nishizawa, "Effect of pulse shaping on defect reduction in pulsed laser welding," *Laser Institute of America,* vol. 547, 1992, doi: 10.2351/1.5058527.
[175] S. Katayama, *Handbook of Laser Welding Technologies*. Woodhead Publishing, 2013.

[176] J. Mazumder, "Laser assisted surface coatings," *Metallurgical and Ceramic Protective Coatings,* pp. 74-111, 1996, doi: doi:10.1007/978-94-009-1501-5_5
[177] S. Zekovic, R. Dwivedi, and R. Kovacevic, "Numerical simulation and experimental investigation of gas–powder flow from radially symmetrical nozzles in laser-based direct metal deposition," *International Journal of Machine Tools & Manufacture* vol. 47, pp. 112-123, 2007.
[178] A. J. Pinkerton and L. Li, "Modelling Powder Concentration Distribution From a Coaxial Deposition Nozzle for Laser-Based Rapid Tooling," *Journal of Manufacturing Science and Engineering,* vol. 126, pp. 33-41, 2994.
[179] J. Lin, "Numerical simulation of the focused powder streams in coaxial laser cladding," *Journal of Materials Processing Technology* vol. 105, pp. 17-23, 2000.
[180] J. Ibarra-Medina, M. Vogel, and A. J. Pinkerton, "A CFD model of laser cladding: From deposition head to melt pool dynamics," *Journal of Laser Applications,* vol. 378, pp. 378-386, 2011, doi: 10.2351/1.5062261.
[181] N. Yang, "Concentration model based on movement model of powder flow in coaxiallaser cladding," *Optics & Laser Technology,* vol. 41, pp. 94-98, 2009.
[182] C. Katinas, W. Shang, Y. C. Shin, and J. Chen, "Modeling Particle Spray and Capture Efficiency for Direct Laser Deposition Using a Four Nozzle Powder Injection System," *Journal of Manufacturing Science and Engineering,* vol. 140, 2018.
[183] D. Wu, D. Zhao, Y. Huang, F. Niu, and G. Ma, "Shaping quality, microstructure, and mechanical properties of melt-grown mullite ceramics by directed laser deposition " *Journal of Alloys and Compounds* vol. 871, 2021.
[184] T. Y. Kuo and S. L. Jeng, "Porosity reduction in Nd–YAG laser welding of stainless steel and inconel alloy by using a pulsed wave," *Journal of Physics D: Applied Physics,* 2005.
[185] V. Singh and E. I. Meletis, "Synthesis, characterization and properties of intensified plasma-assistednitrided superalloy Inconel 718," *Surface & Coatings Technology,* vol. 201, pp. 1093-1101, 2006.
[186] Y. Sun, "Kinetics of layer growth during plasma nitriding of nickel based alloyInconel 600," *Journal of Alloys and Compounds* vol. 351, pp. 241–247, 2003.
[187] C. Leroy, T. Czerwiec, C. Gabet, T. Belmonte, and H. Michel, "Plasma assisted nitriding of Inconel 690," *Surface and Coatings Technology,* vol. 142-144, pp. 241-247, 2001.
[188] Y. Karabulut, E. Tascioglu, and Y. Kaynak, "Heat treatment temperature-induced microstructure, microhardness and wear resistance of Inconel 718 produced by selective laser melting additive manufacturing " *Optik,* vol. 227, 2021.
[189] D. Gu *et al.*, "Selective laser melting additive manufacturing of TiC/AlSi10Mg bulk-form nanocomposites with tailored microstructures and properties," *Physics Procedia,* vol. 56, pp. 108 – 116 2014.
[190] D. Gu and Y. Shen, "Effects of processing parameters on consolidation and microstructureof W–Cu components by DMLS," *Journal of Alloys and Compounds,* vol. 473, pp. 107–115, 2009.
[191] J. C. Nelson, N. K. Vail, and J. W. Barlow, "Laser Sintering Model for Composite Materials," *The University of Texas at Austin,* vol. DepartmentofChemical Engineering, 1993.
[192] H. C. H. Ho, I. Gibson, and W. L. Cheung, "Effects of energy density on morphology and properties of selective laser sintered polycarbonate," *Journal of Materials Processing Technology,* vol. 89, pp. 204–210, 1999.

[193] V. E. Beal, R. A. Paggi, G. V. Salmoria, and A. Lago, "Statistical Evaluation of Laser Energy Density Effect on Mechanical Properties of Polyamide Parts Manufactured by Selective Laser Sintering," *Journal of Applied Polymer Science,* vol. 113, pp. 2910–2919 2009.
[194] N. Hopkinson, C. E. Majewski, and H. Zarringhalam, "Quantifying the degree of particle melt in Selective Laser Sintering," *CIRP Annals - Manufacturing Technology,* vol. 58, pp. 197–200, 2009.
[195] H. Gong, K. Rafi, H. Gu, G. D. J. Ram, T. Starr, and B. Stucker, "Influence of defects on mechanical properties of Ti–6Al–4 V componentsproduced by selective laser melting and electron beam melting," *Materials and Design,* vol. 86, pp. 545-554, 2015.
[196] J. Ciurana, L. Hernandez, and J. Delgado, "Energy density analysis on single tracks formed by selective laser melting with CoCrMo powder material," *Int J Adv Manuf Technol,* vol. 68, pp. 1103–1110, 2013.
[197] H. Gruber, M. Henriksson, E. Hryha, and L. Nyborg, "Effect of Powder Recycling in Electron Beam Melting on the Surface Chemistry of Alloy 718 Powder," *Metallurgical And Materials Transactions A,* vol. 50A, pp. 2410-2422, 2019, doi: doi.org/10.1007/s11661-019-05333-7.
[198] R.Aoki and M.Suzuki, "Effect of particle shape on the flow and packing properties of non-cohesive granular materials," 1970, doi: doi.org/10.1016/0032-5910(71)80008-6.
[199] R. L. Carr, "Evaluating flow properties of solids," *Chem Eng,* vol. 72, pp. 163–168, 1965.
[200] F. Vásquez, J. A. Ramos-Grez, and M. Walczak, "Multiphysics simulation of laser–material interaction during laser powder depositon," *Int J Adv Manuf Technol,* vol. 59, pp. 1037–1045, 2012, doi: 10.1007/s00170-011-3571-4.
[201] A. J. Pinkerton and L. Li, "Modelling the geometry of a moving laser melt pool and deposition track via energy and mass balances," *Journal of Physics D: Applied Physics,* 2004.
[202] W. Liu and J. N. Dupont, "In-Situ Reactive Processing of Nickel Aluminides by Laser-Engineered Net Shaping," *Metallurgical and Materials Transactions A,* vol. 34A, pp. 2633-2641, 2003.
[203] M. Gremaud, I. D. Wagnière, A. Zryd, and W. Kurz, "Laser Metal Forming: Process Fundamentals," *Surface Engineering,* 2013, doi: doi.org/10.1179/sur.1996.12.3.251.
[204] H. B. Dong and P. D. Lee, "Simulation of the columnar-to-equiaxed transition in directionally solidified Al-Cu alloys," *Acta Material,* vol. 53, pp. 659-668, 2005.
[205] Y. Chen, K. Zhang, J. Huang, S. R. E. Hosseini, and Z. Li, "Characterization of heat affected zone liquation cracking in laser additive manufacturing of Inconel 718," *Materials and Design,* vol. 90, pp. 586-594, 2016.
[206] L. L. Parimi, G. A. Ravi, D. Clark, and M. M. Attallah, "Microstructural and texture development in direct laser fabricated IN718," *Material Characterization,* vol. 89, p. 102.111, 2014.
[207] L. Zhu, Z. F. Xu, P. Liu, and Y. F. Gu, "Effect of processing parameters on microstructure of laser solid formingInconel 718 superalloy," *Optics and Laser Technology,* vol. 98, pp. 409–415, 2018.
[208] R. G. Ding, Z. W. Huang, H. Y. L. I.Mitchell, G. Baxter, and P. Bowen, "Electron microscopy study of direct laser deposited IN718," *Materials Characterization* vol. 106 pp. 324–337, 2015.

[209] C. Zhong, A. Gasser, T. Schopphoven, and R. Poprawe, "Experimental study of porosity reduction in high deposition-rate LaserMaterial Deposition," *Optics & Laser Technology,* vol. 75, pp. 87–92, 2015.
[210] A. Alhuzaim and R. B. Madigan, "Measurement and Simulation of Low Carbon Steel Alloy Deposit Temperature in plasma Arc Welding Additive Manufacturing," *International Journal for Innovation Education and Research,* vol. 2-06, pp. 113-127, 2014.
[211] D. Gibson, R. Plume, E. Bergin, S. Ragan, and N. Evans, "Molecular Line Observations Of Infrared Dark Clouds. Ii. Physical Conditions," *The Astrophysical,* pp. 123–134, 2009.
[212] L. Zhu, Z. Xu, and Y. Gu, "Effect of laser power on the microstructure and mechanical properties of heat treated Inconel 718 superalloy by laser solid forming," *Journal of Alloys and Compounds,* vol. 746, pp. 159-167, 2018.
[213] H. L. Wei, T. Mukherjee, and T. DebRoy, "Grain Growth Modeling For Additive Manufacturing of Nickel Based Superalloys " presented at the 6th International Conference on Recrystallization and Grain Growth, 2016.
[214] D. D. Gu, W. Meiners, K. Wissenbach, and R. Poprawe, "Laser additive manufacturing of metallic components: materials, processes and mechanisms," *International Materials Reviews* vol. 57, pp. 133-164, 2012.
[215] H. L. Wei, G. L. Knapp, T. Mukherjee, and T. DebRoy, "Three-dimensional grain growth during multi-layer printing of a nickel-based alloy Inconel 718," *Additive Manufacturing,* vol. 25, pp. 448-459, 2019.
[216] O. Miyagawa, M. Yamamoto, and M. Kobayashi, "Zig-zag grain boundaries and strength of heat resisting alloys," *Superalloys,* pp. 245-254, 1976.
[217] Y. Zhang, Z. Li, P. Nie, and Y. Wu, "Effect of Heat Treatment on Niobium Segregation of Laser-Cladded IN718 Alloy Coating," *Metallurgical And Materials Transactions,* vol. 44A, pp. 708-716, 2013, doi: 10.1007/s11661-012-1459-z.
[218] S. Azadian, "Aspects of Precipitation in the Alloy Inconel 718 ", Department o f Applied Physics and Mechanical Engineering, Division of Engineering Materials Luleå University o f Technology, 2004.
[219] Y. Chen *et al.*, "Study on the element segregation and Laves phase formation in the laser metal deposited IN718 superalloy by flat top laser and gaussian distribution laser," *Materials Science & Engineering A,* vol. 754, pp. 339-347, 2019.
[220] P. K. Sung, D. R. Poirier, S. D. Felicelli, E. J. Poirier, and A. Ahmed, "Simulations of microporosity in IN718 equiaxed investment castings," *Journal of Crystal Growth* vol. 226, pp. 363-377, 2001.
[221] G. Sjoberg and N.-G. Ingesten, "Grain Boundary S-phase Morphologies, Carbides and Notch Rupture Sensitivity of Cast Alloy 718," *Superalloys 718, 625 and Various Derivatives,* pp. 603-620, 1991.
[222] b. Hui Xiao a, Simeng Li a,b, Xu Hana,b, Jyoti Mazumder a,b,c, Lijun Song a, "Laves phase control of Inconel 718 alloy using quasi-continuous-wave laser additive manufacturing," *Materials and Design,* vol. 122, pp. 330-339, 2017.
[223] B. Attard, S. Cruchley, C. Beetz, M. Megahed, Y. L. Chiu, and M. M. Attallah, "Microstructural control during laser powder fusion to create graded microstructure Ni-superalloy components," *Additive Manufacturing,* vol. 36, 2020.
[224] K. A. Mumtaz and N. Hopkinson, "Selective Laser Melting of thin wall parts using pulse shaping," *Journal of Materials Processing Technology,* vol. 210, pp. 279–287, 2010.

[225] G. Zhu, D. Li, A. Zhang, G. Pi, and Y. Tang, "The influence of standoff variations on the forming accuracy in laser direct metal deposition," *Rapid Prototyping Journal,* vol. 17/2, pp. 98–106, 2011, doi: 10.1108/13552541111113844.
[226] S. Imbrogno, A. Alhuzaim, and M. M. Attallah, "Influence of the laser source pulsing frequency on the direct laser deposited Inconel 718 thin walls," *Journal of Alloys and Compounds,* vol. 856, 2020, doi: https://doi.org/10.1016/j.jallcom.2020.158095.
[227] C. A. Huang, T. H. Wang, C. H. Lee, and W. C. Han, "A study of the heat-affected zone (HAZ) of an Inconel 718sheet welded with electron-beam welding (EBW)," *Materials Science and Engineering A,* vol. 398 pp. 275–281, 2005.
[228] S. Sui *et al.*, "Microstructures and stress rupture properties of pulse laser repaired Inconel 718 superalloy after different heat treatments," *Journal of Alloys and Compounds,* pp. 125-135, 2019.
[229] H. Y. Zhang, S. H. Zhang, M. Cheng, and Z. Zhao, "Microstructure evolution of IN718 alloy during the delta process," in *International Conference on the Technology of Plasticity, ICTP 2017,* , 17-22 September 2017, : Procedia Engineering.
[230] B. P. Kashyap and M. C. Chaturvedi, "The effect of prior annealing on high temperature flow properties of andmicrostructural evolution in SPF grade IN718 superalloy," *Materials Science and Engineering* vol. 445–446, pp. 364–373, 2007.
[231] Y. Jin *et al.*, "Evolution of the Annealing Twin Density during δ-Supersolvus Grain Growth in the Nickel-Based Superalloy Inconel™ 718," *Metals,* 2016, doi: 10.3390/met6010005.
[232] S. Azadian, L.-Y. Wei, and R. Warren, "Delta phase precipitation in Inconel 718," *Materials Characterization,* vol. 53 pp. 7 – 16, 2004.
[233] L. Liu, A. Hirose, and K. F. Kobayashi, "A numerical approach for predicting laser surface annealingprocess of Inconel 718," *Acta Materialia,* vol. 50, pp. 1331–1347, 2002.
[234] M. Sundararaman, P. Mukhopadhyay, and S. Banerjee, "Carbide Precipitation In Nickel Base Superalloys 718 And 625 And Their Effect On Mechanical Properties," *The Minerals, Metals & Materials Society* pp. 367-378, 1997.
[235] C. R. Brinkman and G. E. Korth, "Strain Fatigue and Tensile Behavior of Inconel 718from Room Temperature to 650°C " *Journal of testing and evaluation,* pp. 249-259, 1974.
[236] D. P. Moon, R. C. Simon, and R. J. Favor, *The elevated-temperature properties of selected superalloys*. American Society For Testing And Materials, 1968.
[237] K. Harris, G. L. Erickson, and R. E. Schwer, "Mar m 247 derivations - CM247LC DS alloy CMSX single crystal alloys properties & performance " *Cannon-Muskegon Corporation* pp. 221-230.
[238] K. V. Wong and A. Hernandez, "A Review of Additive Manufacturing," *International Scholarly Research Network,* vol. 2012, p. 10, 2012.
[239] J.-P. Kruth, M. C. Leu, and T. Nakagawa, "Progress in Additive Manufacturing and Rapid Prototyping," *Annals of the ClRP,* vol. 47, pp. 525-540, 1998.
[240] G. N. Levy, R. Schindel, J. P. Kruth, and K.U.Leuven, "Rapid manufacturing and rapid tooling with layer manufacturing (lm) technologies, state of the art and future perspectives," *CIRP Annals,* pp. 589–609, 2003.
[241] X. Wu, "A review of laser fabrication of metallic engineering components and of materials," *Materials Science and Technology,* vol. 23, pp. 631-640, 2013.
[242] X. Wu and J. Mei, "Near net shape manufacturing of components using direct laser fabrication technology," *Journal of Materials Processing Technology,* vol. 135, pp. 266–270, 2003.

[243] P. Kontis *et al.*, "Atomic-scale grain boundary engineering to overcome hot-cracking in additively-manufactured superalloys," *Acta Materialia,* vol. 177, pp. 209-221, 2019.
[244] W. Zhou *et al.*, "Inhibition of cracking by grain boundary modification in a non-weldable nickel-based superalloy processed by laser powder bed fusion " *Materials Science & Engineering A* vol. 791, p. 139745, 2020.
[245] D. Qian *et al.*, "Statistical study of ductility dip cracking induced plastic deformation in polycrystalline laser 3D printed Ni-based superalloy," *Scientific Reports* vol. 7, p. 2859, 2017, doi: 10.1038/s41598-017-03051-x.
[246] X. L. Fencheng Liu, Gaolin Yang, Menghua Song, Jing Chen, Weidong Huang "Microstructure and residual stress of laser rapid formedInconel 718 nickel-base superalloy," *Optics & Laser Technology,* vol. 43, pp. 208-213, 2011.
[247] X. L. Fencheng Liu, Chunping Huang, Menghua Song, Gaolin Yang, Jing Chen, Weidong Huang, "The effect of laser scanning path on microstructures and mechanical properties of laser solid formed nickel-base superalloy Inconel 718," vol. 509, pp. 4505-4509, 2011.
[248] J. E. MacDonald, "Hot Isostatic Pressing of A High Temperature Ni-Superalloy CM247LC: Processing-Microstructure-Properties," Doctor of Philosophy, School Of Metallurgy and Materials, University of Birmingham, 2016.
[249] S. Raghavan and S. S. Sahay, "Modeling the grain growth kinetics by cellular automaton," *Materials Science and Engineering A,* vol. 445–446, pp. 203-209, 2007.
[250] Q. Zhang, "The microstructure and properties of powder hipped nickel-based superalloy CM247LC," Metallurgy and Materials, University of Birmingham 2011.
[251] J. M. Kikel and D. M. Parker, "Ductility dip cracking susceptibility of filler metal 52 and alloy 690," *Trends in Welding Research,* pp. 757–762, 1998.
[252] A. J. Haslam, S. R. Phillpot, D. Wolf, D. Moldovan, and H. Gleiter, "Mechanisms of grain growth in nanocrystalline fcc metals by molecular-dynamics simulation," *Materials Science and Engineering,* vol. A318, pp. 293–312, 2001.
[253] V. D. D. R. Muñoz-Moreno, S.L. Driver, O.M.D.M. Messé , T. Illston, S. Baker, M.A. Carpenter, H.J. Stone, "Effect of heat treatment on the microstructure, texture and elastic anisotropy of the nickel-based superalloy CM247LC processed by selective laser melting " *Materials Science & Engineering A,* vol. 674, pp. 529–539, 2016.
[254] P. A. McNutt, "An investigation of cracking in laser metal deposited nickel superalloy CM247LC," Department of Metallurgy and Materials, University of Birmingham, 2015.
[255] Y. T. Tang *et al.*, "Alloys-by-design: Application to new superalloys for additive manufacturing," *Acta Materialia,* vol. 202, pp. 417-436, 2021.
[256] X. Wang, L. N. Carter, N. J. E. Adkins, K. Essa, and M. M. Attallah, "Novel Hybrid Manufacturing Process of CM247LC and Multi-Material Blisks," *Micromachines,* vol. 492, 2020, doi: 10.3390/mi11050492.
[257] J. E. MacDonald, R. H. U. Khan, M. Aristizabal, K.E.A.Essa, M. J. Lunt, and M.M.Attalla, "Influence of powder characteristics on the microstructure andmechanical properties of HIPped CM247LC Ni superalloy," *Materials and Design,* vol. 174 2019.
[258] *ASM Handbook Fractography*. 2004.
[259] L. Ying-ju, M. Xiao-ping, and Y. Yuan-sheng, "Grain refinement of as-cast superalloy IN718 under action of low voltage pulsed magnetic field " *Trans. Nonferrous Met. Soc,* vol. 21, pp. 1277-1282, 2011.

[260] Y. Wang and J. Shi, "Texture control of Inconel 718 superalloy in laser additive manufacturing by an external magnetic field," *Metals,* pp. 9809-9823, 2019, doi: 10.1007/s10853-019-03569-7.

Appendix

Influence of the Laser Source Pulsing Frequency on the Direct Laser Deposited Inconel 718 Thin Walls

Stano Imbrogno[a], Abdullah Alhuzaim[a,b], Moataz M. Attallah*[a]

[a]School of Metallurgy and Material Sciences, University of Birmingham, Edgbaston, Birmingham B15 2TT, United Kingdom

[b]Mechanical Engineering Department, Jubail University College, Jubail Industrial City, Kingdom of Saudi Arabia.

*Corresponding author contact: m.m.attallah@bham.ac.uk , University of Birmingham.

This paper has been published in Journal of Alloys and Compounds, 2021, volume 856

Abstract:

The Direct Laser Deposition (DLD) process has shown significant results in manufacturing due to its relevant flexibility to refurbish high-performance components (e.g., turbine blades or disks) or fabricating complex shaped parts. The solidification microstructure during the DLD process, is known to be controllable using different process parameters that induce changes in the grain structure, micro-segregation, and phase transformations. This work focuses on the effect the frequency of the pulsed laser has on the metallurgical characteristics of deposited thin walls. More specifically, the effect of three different pulsing rates (10Hz, 100Hz, 1000 Hz) during the deposition of the Nickel-based superalloys Inconel 718 has been studied and the results compared with parts produced by continuous wave laser mode. This work highlights how the pulsing rate significantly affected the thermal history, melt pool shape, grain size and its morphology, segregation region (Nb-enriched), and hardness. Finally, the microhardness

was also evaluated and a correlation between the metallurgical characteristics and the pulsing rate was established.

Keywords: Direct Laser Deposition; pulsing laser; Inconel 718; microstructure

Introduction

Additive Manufacturing (AM) processes are creating interesting opportunities in producing high-performance structures, together with specifically designed metallurgical features. Among all the AM process, the Direct Laser Deposition (DLD) technique has been widely used for repairing or cladding mechanical components (e.g., turbine blade and blisks, hard coating for complex tools for mining). Moreover, the DLD also enables the fabrication of 3D near-net-shape parts directly from CAD models [1–3].

Generally, the process consists of a laser source that creates a melt pool on a substrate, while the metallic powder is delivered from a nozzle into the melt pool and fully melted. The laser head can be mounted on a cartesian system able to move on x, y, and z directions, coupled with rotational support, in order to have 5-axis of degree of freedom, alternatively it is simply positioned at the end of an arm robot. In this contest, the Nickel base superalloy Inconel 718 is widely used in aerospace applications to produce high-performance components because of its good formability, high corrosion resistance, and excellent mechanical properties up to 650°C [4,5]. The Inconel 718 typically consists of a matrix, the γ phase (face-centered cubic FCC) structure that provides appropriate ductility and toughness at high temperatures. Furthermore, the strengthening of the alloy is guaranteed by the presence of the precipitation phase gamma prime γ’ (Ni_3Al with spherical morphology) and gamma double prime γ’’ (Ni_3Nb with disc morphology). This later has a metastable body-centred tetragonal structure that can be transformed into a coarse platelet stable orthorhombic δ phase, if exposed for a certain time at temperatures above 650 °C [6]. During the DLD process, the material undergoes rapid cooling

and solidification, resulting in a refined dendritic microstructure. Concerning the Inconel 718, the fast Nb diffusion at the interface between the liquid and the solid phase during solidification leads to the formation of significant interdendritic Nb segregation regions. These spots in the material are characterized by brittle intermetallic, and usually undesirable Laves phase (eutectic Laves phase/γ in the last stage of the solidification) [7]. The presence of the microsegregation is unavoidable during the welding process of the Inconel 718, as reported by Radhakrishna and Prasad Rao 1997 [8]. Indeed, the formation of the Laves phase is easier due to the microsegregation of elements present in the alloy, such as Nb, Ti, and Mo because of the non-equilibrium solidification conditions. The Laves phase is characterized by a hexagonal close-packed crystallographic structure and is usually represented by a concentration of Nb ranging from 10%-30%. It is generally known that the presence of this phase is not particularly desired due to the deleterious effect on the mechanical properties [9]. Different studies have shown that the formation and the presence of the Laves phase in the alloy deplete the matrix of the principal alloying elements (e.g. the Nb), which strongly contributes to the formation of the strengthening phases (e.g. γ' and γ'') of the material [4,9,10]. Moreover, the Laves phase, and in particular the interface region between this later and the matrix ,represents a nucleation point of cracks leading to the failure of the material when subjected to high or low cycle fatigue [11]. Due to the important role of the DLD process in the industrial environment, several studies were conducted to define a process strategy able to reduce and control the microsegregation formation. Antonsson and Fredriksson in 2003 studied the effect of the cooling rate on the solidification of Inconel 718, focusing their attention on the solidification sequence and the microstructural changes, as well as the Nb segregation. They discovered that the cooling rate has a significant effect on the type of microstructure that develops from the liquid phase, as well as on the segregation of the Nb. In detail, the coarseness of the matrix structure (γ phase) decreased when the cooling rate was increased, and the morphology

changed from dendrites to cells. They also measured the Nb segregation depending on the cooling rate, and showed that the percentage of Nb was lower at this higher cooling rate due to the improved solubility of this phase into the γ matrix [12]. Zhang et al. 2013 investigated the effect of ultrarapid cooling on the microstructure when the Inconel 718 alloy was used in the cladding process. They observed that the high cooling rate led to a reduction of the Laves phase and a variation in its morphology which was clearly refined and widely dispersed. In detail, the ultrarapid cooling induced a significant reduction of the constitutional supercooling, limiting the Nb segregation into the Laves phase [13]. Other researchers, such as Qi et al. 2009 and Zhang et al. 2013 analysed the effect of the different heat treatment on the microstructure, mechanical properties, and Nb segregation of the Inconel 718 produced by laser cladding. Qi et al. 2009 observed that the direct age could improve the strength of the material, due to the formation of the strengthening phases, but the ductility was strongly compromised due to the presence of the Laves phase. The homogenized solution treatment and ageing were able to completely dissolve the Laves phase into the matrix, but these treatments compromised the microstructure due to the significant grain growth [14]. Zhang et al 2013 obtained similar results which also showed the amount of the Laves phase was different from the region close to the substrate, and the top region of the deposited material [13]. As highlighted by Ma et al. 2015, and Zhai et al. 2019, the process parameters such as scan speed and the power can affect the microstructure and the microsegregation [15,16]. Zhai et al. 2019 showed that a combination of power and scan speed could change the cooling rate, leading to fast cooling and an exceptionally fine microstructure with lower Nb segregation. Ma et al. 2015 defined a map that showed the morphology changes from cells to dendritic microstructure, depending on the power and scan speed, as well as the hardness variation depending on the energy density. Kong et al. 2019 studied the effect of different Nb-content in the IN718 alloy on the metallurgical characteristics and the mechanical properties. They noticed that if the Nb content

within the alloy is lower than 3-4%, there is no formation of Laves phase and significant segregation regions. Moreover, the increase in the Nb content enhanced the formation of finer microstructure as well as the presence of the Laves phase improving thus the strength of the material [17]. New studies revealed the effectiveness of the pulsed laser during the laser metal deposition in terms of Nb segregation modification, as well as the surface roughness in the produced parts. Gharbi et al. 2014 analysed the use of pulsed regime laser, versus the continuous regime on the surface showing that the use of a pulsed laser can generate smoothing effects and improve the surface finish [18]. They did not provide any information about the effect of the pulsed regime of the laser on the microstructure, and segregation as well as mechanical properties. Xiao et al. 2017 studied the effect of the laser modes (continuous and pulsed waves) on Nb segregation and Laves formation during laser deposition of Inconel 718. They claimed that the pulsed regime promoted the formation of fine equiaxed dendrites, reduced Nb segregation, and fine discrete Laves phase due to the high cooling rate [19]. Further studies of Xiao et al. 2017 of the continuous and pulsed regime of the laser during metal deposition, highlighted that the samples produced via QCW responded better to the heat treatment and, therefore, higher hardness values were achieved [20]. Recently, Xiao et al. 2020 investigated the effects of two different frequencies when the pulsed laser was used to deposit the Inconel 718. They noticed finer microstructure and more randomly distributed segregated regions when low frequencies were used. In particular, two values of frequencies were investigated but no comparison was carried out with the continuous wave laser mode [21]. Janaki Ram et al. 2013 showed that the current pulsing during the Inconel 718 Gas Tungsten Arc Weld can control the Laves phases, and in particular its morphology (long chains of interconnected Laves phase versus smaller and well separated interdendritic region) [22]. Wang et al. 2017 observed a higher ultimate tensile strength of the samples produced by pulsed regime laser metal deposition, than the ones produced by the continuous wave laser mode.

They also tested different values of duty cycle (interval of time in which the pulse is on or off), however, the results are related to stainless steel (AISI 316L) [23]. Finally, an interesting study has been carried out by Li et al. 2017 that describe, through numerical simulation, how the pulsed or continuous laser affects the thermal field, as well as the melt pool, its shape, and the microstructure [24]. Although the study showed interesting results in terms of microstructure changes and hardness due to the different laser regime, no results depending on the different frequency of pulsed laser were reported. In the previously mentioned works, the authors used a pulsed regime, but the process parameters were different and although they observed similar phenomena, the results were slightly different from each other suggesting that the pulsing parameters affect the process. Therefore, this work aims to assess the effect of different pulse frequencies of the laser on the microstructure, as well as on the segregation distribution of the Inconel 718 thin walls produced by DLD. A comprehensive analysis of the morphology and texture of the grains carried out by electron microscopy is reported and discussed. The results obtained by the thermal analysis are used to discuss the surface roughness, and the melt pool changes due to the process parameter modification (pulsed laser frequency). Moreover, the mechanical properties in terms of microhardness analysis are shown and correlated with the microstructure and the pulse frequency.

Material and Methods

The gas-atomised IN718 powder supplied by LPW (Carpenter Technology Corporation) was employed in this experimental work, and the certified chemical composition is reported in Table 1. The average particle size of the powder is 85μm, with 90% of the particles falling within the size range of 43–106μm. As showed in Fig. 1a, the powder particles are mostly spherical, showing some fine satellite particles. Analysing the cross-section (Fig. 1b), some internal porosities were also observed, and this is typically due to the production process (gas

atomisation). The analysis of the cross-section is shown in Fig. 1b, and the microstructure was revealed and characterized by dendritic morphology. The powder was characterized by fine dendritic networks, which was caused by the rapid solidification experienced by the material during the gas atomisation process. Moreover, through the Energy Dispersive X-ray (EDX) analysis, the white regions were mainly formed by Nb and Mo, suggesting that the segregated regions already existed in the powder (Fig. 1c). The DLD process has been performed to produce single thin-walled samples of dimensions 20mm×25mm along z and x directions respectively and 1.4mm thickness (y direction) on an Inconel 718 substrate (Fig. 2a). The choice of the material substrate was related to the possibility to test the process parameters for repairing actions usually performed on aerospace components.

Table12.1. IN718 powder chemical element (w%).

Ni	Cr	Fe	Nb	Mo	Ti	Al	Si	Ta
54.45	18.18	18.19	4.88	2.9	0.91	0.42	0.03	0.02

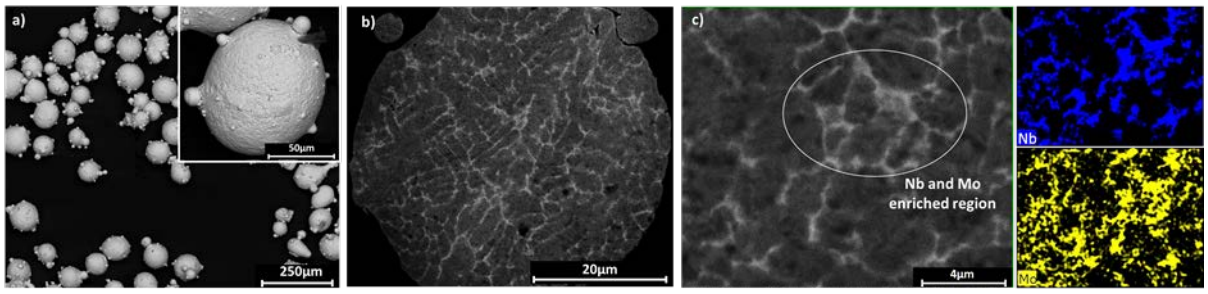

Figure 12.1: SEM of the IN718 powder (a); SEM of the cross-section of the powder(b); EDX of the cross-section of the powder (c).

The Trumpf TLC 1005, equipped with an Nd: YAG laser and 1064nm wavelength (maximum power of 4kW) was used to deposit the thin walls in an argon atmosphere within a plastic customized box. During the deposition, the O_2 level was monitored, and a constant flow of argon was used inside the deposition area to keep the O_2 level under 50 ppm value. The layer thickness was kept equal to 0.5mm throughout the build. The argon was also delivered as a

carrier gas with a flow rate of 10L/min, and a nozzle gas protected the lens from the rebounding particles from the build. The laser beam was focused to have a spot size of 0.9mm, with a focal length of 127 mm and the power set was equal to 300W. A three-beam nozzle assembly was used for powder feeding, where the distance of the powder focus was set at 2mm under the surface of the substrate, while the laser beam focus was set 2mm above from the substrate. This configuration of the laser and powder focus achieved an auto-compensation of the deposited material, therefore possible irregular deposited layers were avoided [25].

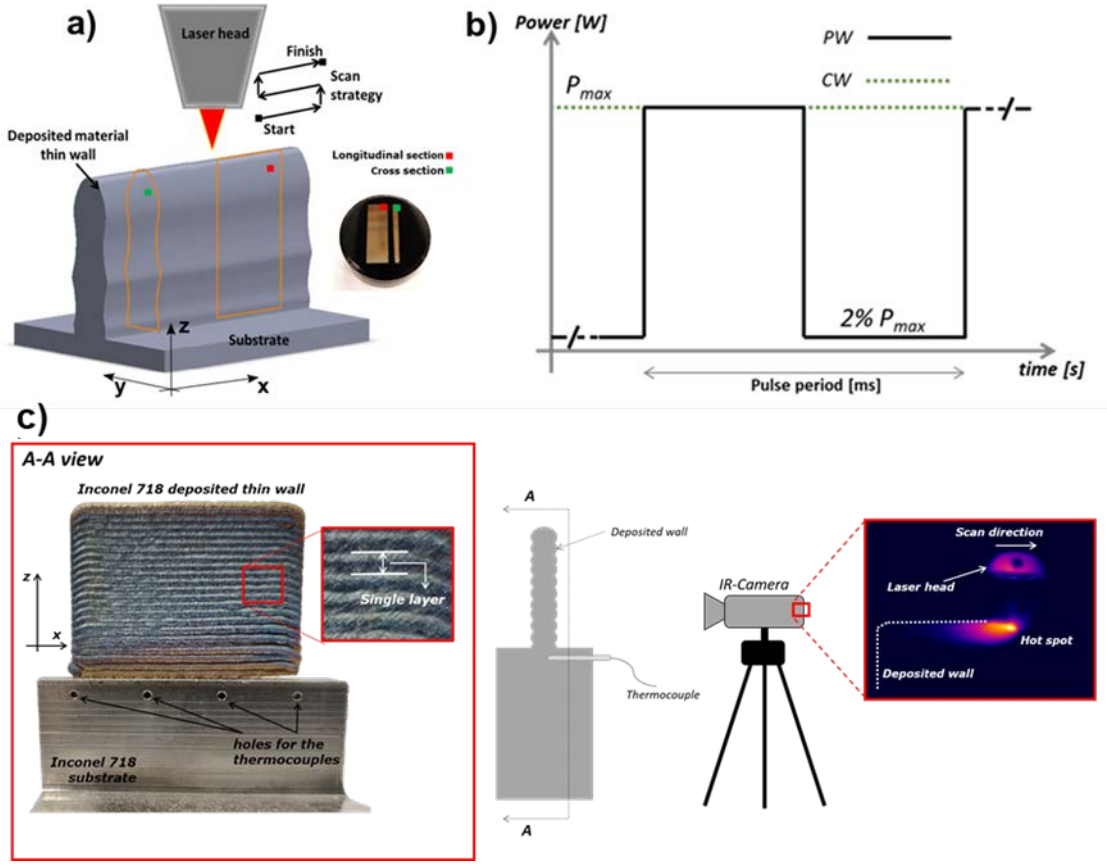

Figure 12.2. a) Schematic representation of the thin wall, the deposition strategy and the samples collected; b) pulsed wave and continuous wave graph; a schematic representation of the experimental set-up (c).

The strategy of the deposition was defined as continuous deposition (Fig. 2a), and the scan speed of the laser head at 275mm\min was kept constants for all the tests. As previously mentioned, the laser device was able to work in a pulsed wave regime (PW) (Fig. 2b), therefore, three frequencies of pulsed regime were defined and set equal to 10Hz, 100Hz and 1000Hz and

a further deposition with a continuous wave regime (CW) was performed for comparison. Moreover, the thermal field was also investigated by an infra-red camera, positioned in front of the substrate during the deposition, and three thermocouples (K-type) were located 1mm beneath the surface substrate (Fig. 2c). The temperature of the first deposited layers acquired by the thermocouples was compared with the thermal profile obtained by the infra-red camera. The obtained thin walls were collected and sectioned as showed in Fig. 2a for metallographic and hardness analyses. The surface quality in terms of surface roughness S_a of the side face of each thin wall, was evaluated by the Alicona Infinite Focus G5 plus. The cross and longitudinal section samples (cross and longitudinal section) were embedded in a phenolic resin, subsequently ground and polished, and electro-etched (8V for 10s) using H_3PO_4 electrolytic solution to reveal the microstructure a well as the segregations. Back Scattered Electron Microscopy (BSEM) and Energy Dispersive X-ray diffraction (EDX) analyses were both carried out to characterize the microstructure and the segregation. Furthermore, to evaluate the melt pool boundary, an Optical Microscope (OM) was also used to analyse the samples. The latter analysis was performed after the samples were chemically etched by the Kalling's n.2. The microhardness was measured using a micro indenter (Buehler Wilson VH1202), using a load of 500g with a dwell time of 10s and ten indentations were carried out in each region of the sample analysed, with a total of 30 indentations per sample. Finally, the average value for each region analysed was considered.

Results

Thermal Analysis of the Deposited Thin Walls

The thermal analysis aimed to evaluate the thermal profile during the deposition, and the temperature distribution on the entire deposited parts depending on the process parameters set, for example laser mode and frequencies. The thermal analysis results were reported in Fig. 3. This demonstrates in detail the temperature cycle on a single point positioned in the middle

region of the wall, and the comparisons among the CW and the different frequencies of the pulsed laser are also shown. Fig. 3b represents the portion of the graph where the heat source hits the node considered in the grid and defined on the software used to analyse the file acquired by the infrared camera.

It is possible to note that the fluctuation of the thermal field signals, due to the nature of the heat input, showed the same frequency (10Hz) of the heat source (laser) as also highlighted by Fig. 4. The temperature fluctuations at higher frequencies of the pulsed laser were difficult to capture by the camera due to the low frame per second acquisition rate of the camera. Fig. 3c shows the average temperature measured within the thermal peak. The higher fluctuation, due to the lower frequencies of the pulsed laser, is also highlighted by the standard deviation. The standard deviation becomes smaller when the frequency of the pulsed laser increases due to the higher heat input, and less heat dissipation. Moreover, increasing the frequency of the pulsed laser till the CW laser mode the temperatures increased from 1435°C (10Hz) to 1898°C (CW).

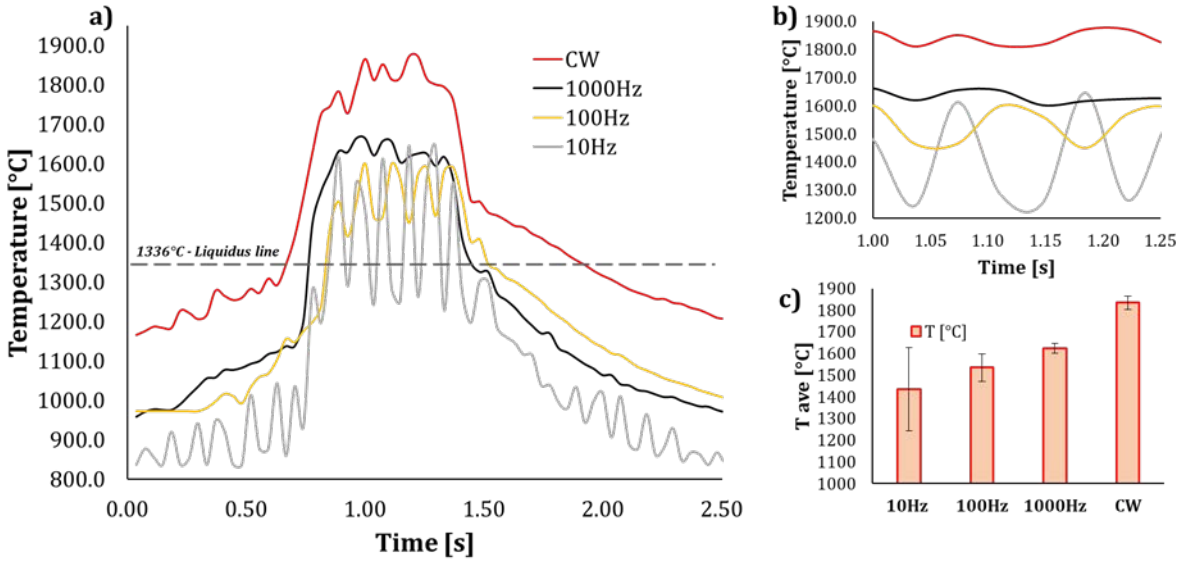

Figure. 12.3 a) single-point temperature profile within the middle region of the wall; b) temperature profile within the thermal peak zone; c) average temperature evaluated within each thermal peak region.

Fig. 4 shows the comparison between the temperature registered on the melt pool when CW and 10Hz PW laser are used. The temperature measured when the CW laser was used is almost constant and the average value was approximately equal to 1900°C. The slight oscillations were due to the random sparks caused by the partially melted powders expulsed by the melt pool because of the turbulence that developed. The black curve represents the pulsed laser (10Hz), and the dark orange curve represents the temperature profile measured considering the maximum thermal signal within the melt pool. The melt pool was subjected to a continuous heating, and cooling cycle due to the pulsed laser. When the laser went from ON to OFF, the temperature within the melt pool decreased from almost 1700°C to values lower than 1300°C. This result highlights that lower temperatures were achieved with the use of pulsed laser, and thus local thermal cycles within each layer happened during the deposition process. On the contrary, the CW laser mode induced the thermal cycles layer by layer as showed in Fig. 3a.

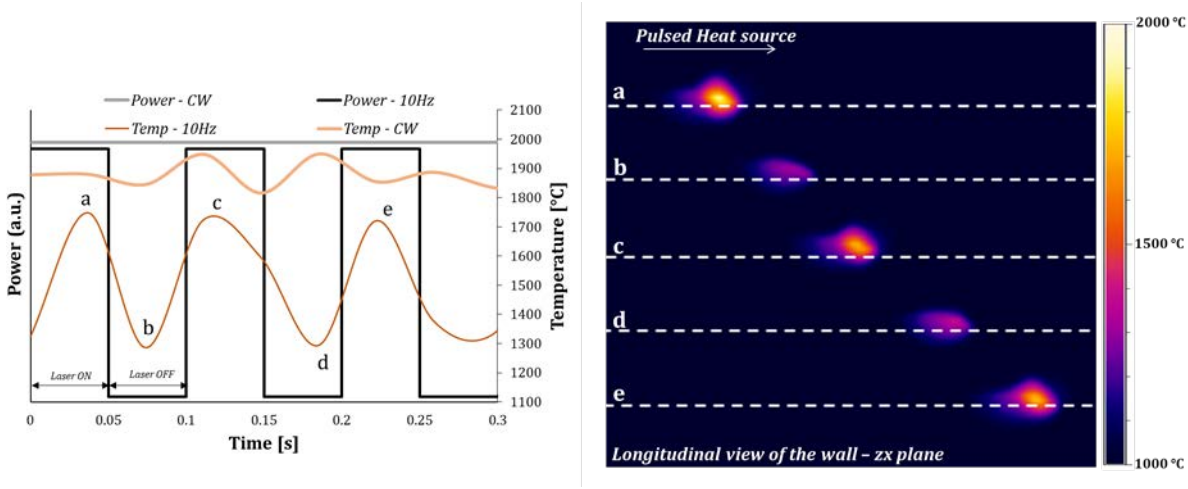

Figure. 12.4 Temperature profile related to the laser power mode and "heartbeat" effect evaluated by the infrared camera.

In Fig. 5 illustrates the temperatures acquired by the thermocouple during the entire deposition process. The CW allowed higher temperatures to be reached compared with the pulsed laser, and a decreasing of the temperature was observed while the frequency decreased from 1000Hz

to 10Hz due to the higher cooling rate was observed. A detailed analysis of the temperature profiles had been carried out (A box) to better evaluate the maximum peak temperatures measured during the deposition. Increasing the frequency of the PW laser until the CW laser regime led to an increase of the accumulated temperature, indeed the evaluated values are 232°C, 241°C, 258°C and 342°C for the 10Hz, 100Hz, 1000Hz and CW respectively.

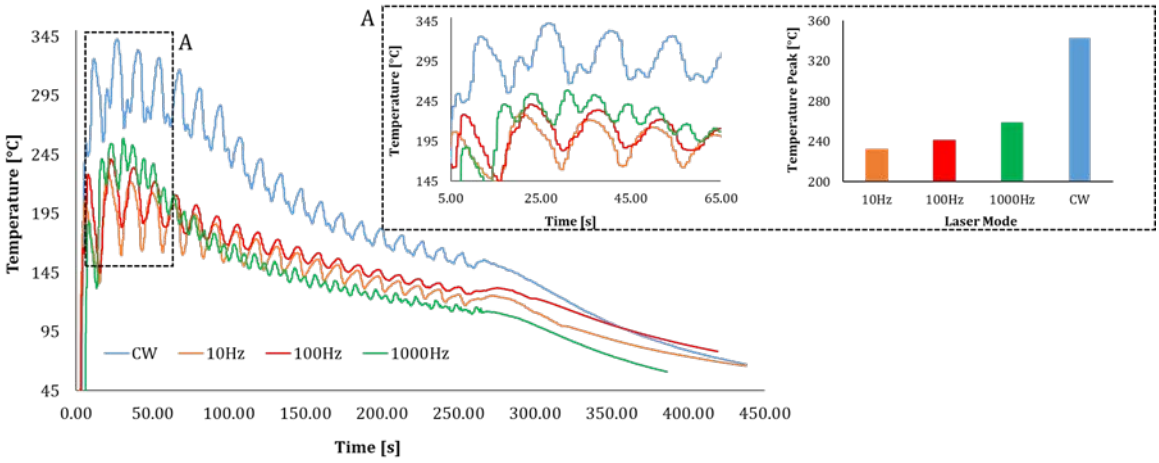

Figure.12.5. Temperature profiles acquired by thermocouple during the entire DLD process depending on the laser mode used (CW or pulsed).

Surface Quality and Microstructure Analysis

The side surface of each wall has been analysed by the SEM and the results are shown in Fig. 6. Each picture refers to the z-x plane and two main features are distinguished: the appearance of the different layers that characterize the walls, and the amount of the unmelted particles. In general, the number of unmelted particles was lower when the PW laser (Fig. 6a, 6b and 6c) was used instead of the CW (Fig. 6c).

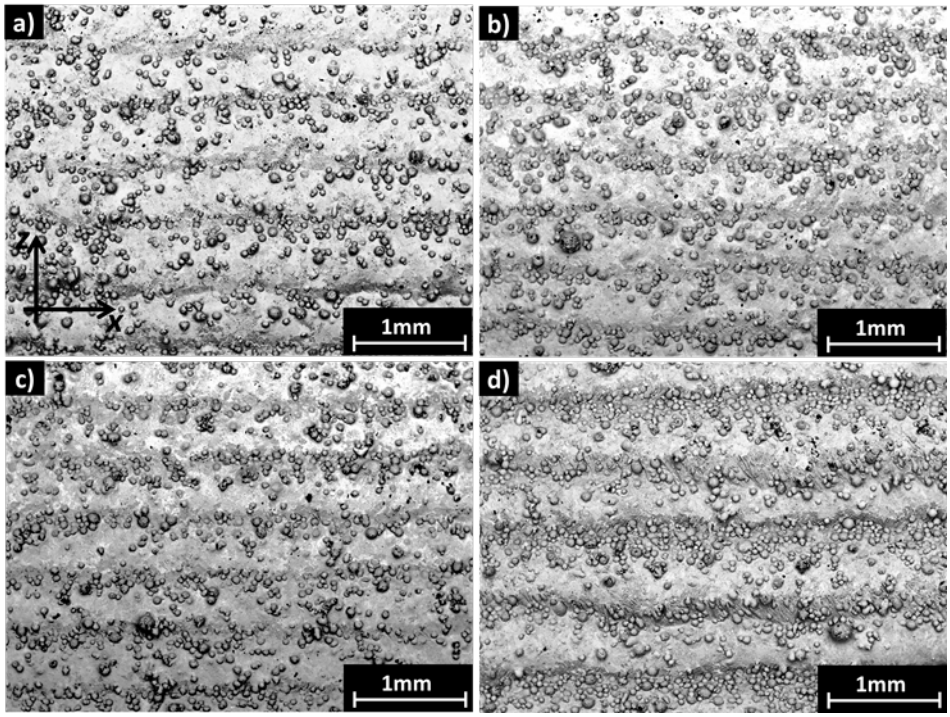

Figure.12.6. SEM of the z-x plane of the thin walls; a) 10Hz, b) 100Hz, c) 1000Hz and d) continuous wave.

The surface roughness (S_a) of the side surface of the produced samples has also been measured and the results are reported in Fig. 7.

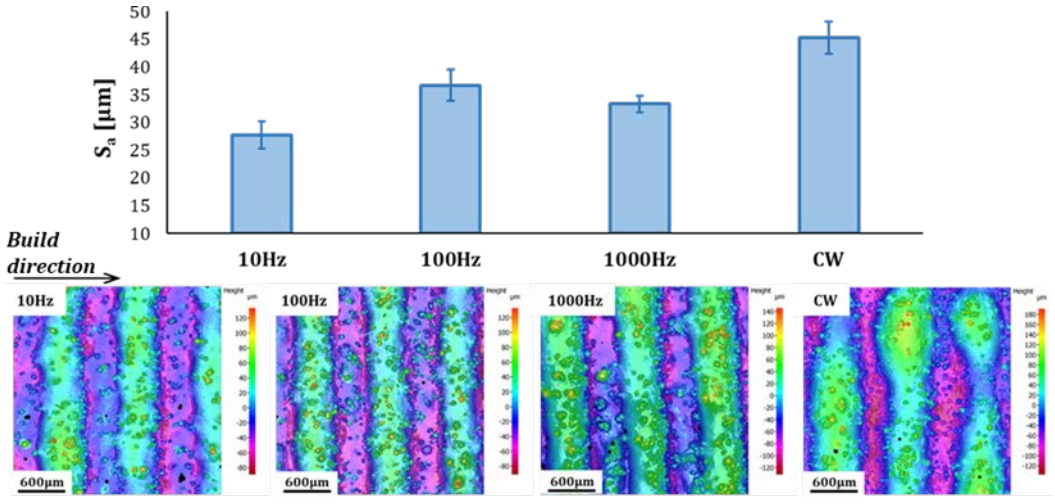

Figure.12.7. Surface roughness analysis carried out on the walls produced by PW and CW laser mode.

The surface conditions were affected by the frequency set during the deposition, indeed the pulsing laser perturbs the melt pool, as well as the powder flow that crosses the laser beam. The lower frequency (10Hz) led to better surface roughness of 27μm, while increasing the frequency to 1000Hz and the CW regime, the surface roughness increased up to 46μm.

Fig. 8 shows the microstructure observed by optical microscope on the cross and longitudinal section of the thin walls produced by PW and CW laser mode. In Fig. 8a, 8c, 8e and 8g the melt pool on the cross-section is highlighted by the dashed white lines, to highlight the changes at the various value of frequency. On the longitudinal sections (Fig. 8b, 8d, 8f and 8h) the deposited layer, the growth direction of the grains and the discrete melt pool bands are visible. It is possible to notice that the layer bands depicted by the horizontal dashed lines are approximately 0.5mm thick, especially when the PW laser is used, while the samples produced by CW laser mode showed thicker layer bands of approximately 0.57mm. The discrete melt pool bands are clearly evident when the 10Hz frequency was used, while higher frequencies involved more laser on-laser off cycles per unit time making difficult the formation of the bands. On the contrary, when the CW laser is adopted, the discrete band is not expected due to the constant presence of the heat source, and indeed it was not visible in the longitudinal section (Fig. 8b). Moreover, from Fig. 8 it is also possible to notice that few pores are randomly distributed as see along the cross-sectional and the longitudinal sections of the thin walls. The porosity analyses carried out by imaging analysis did not show any significant variation between the walls produced with different pulsed laser frequency and between the continuous and the pulsed laser mode. Therefore, the frequency of the laser did not significantly affect the porosity, keeping the porosity fraction at $< 0.95\%$.

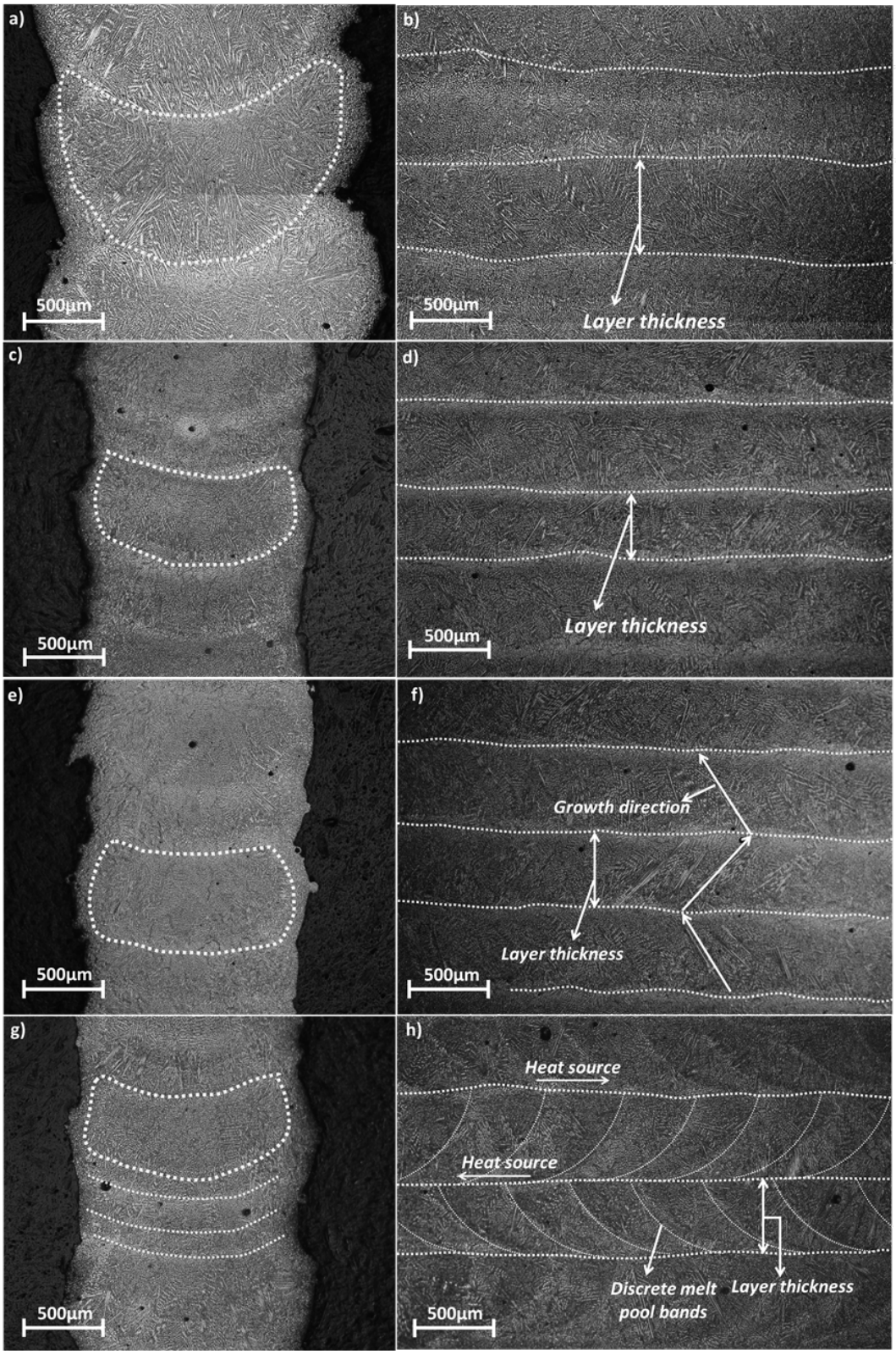

Figure.12.8. Cross-section of the thin walls a) CW, c) 1000Hz, e) 100Hz, g) 10Hz; longitudinal section of the thin walls b) CW, d) 1000Hz, f)100Hz and h) 10Hz.

The EBSD maps are reported in Fig. 9 and show the orientation of the crystals, as well as the shape of the grains on the cross and longitudinal section. The orientation of the grains suggests the deposition strategy adopted, continuous from left to right and vice versa since they grew following the heat source. Although this effect is mainly evident when the PW laser is at a high frequency (1000Hz) and CW laser are employed (Fig. 9a and 9b). The use of 100Hz showed a transition from random to zig-zag distribution, whereas the lowest frequency (10Hz) allowed a random distribution of the grains. Indeed, no preferential growth orientation was highlighted by the EBSD map (Fig. 9c).

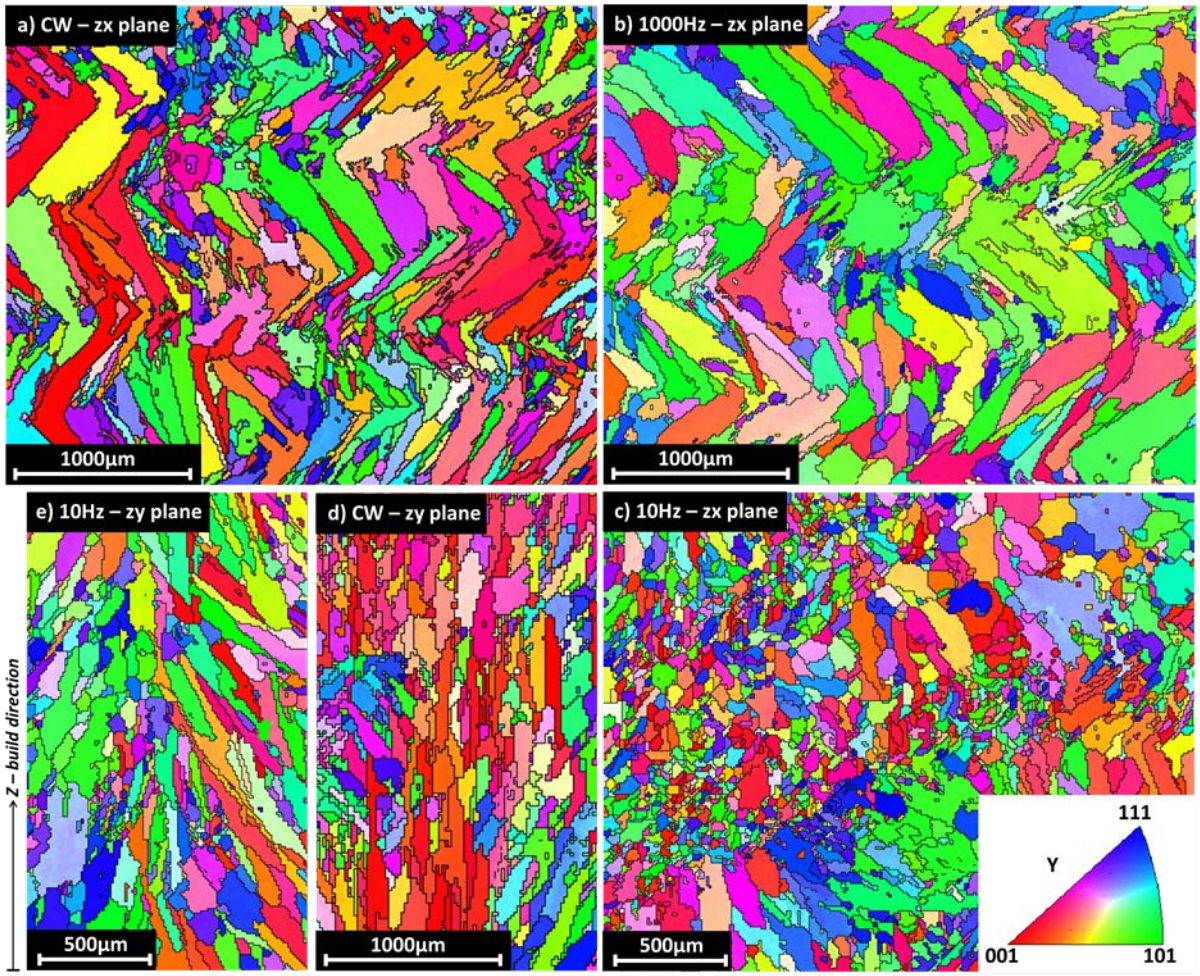

Figure.12.9. EBSD map of the longitudinal section zx plane ((a), (b) and (c)), cross section of the thin walls ((d) and (e)).

Moreover, the cross-section of the samples produced by CW laser showed grains mainly oriented to the <001> direction, while although more random distribution was obtained when the PW laser was used at 10Hz frequency (Fig. 9e and 9d).

The primary dendrite arm spacings (PDAS) have been measured on the cross-section of each sample produced, depending on the frequency of the PW laser, and compared with the one related to the sample produced by CW laser (Fig. 10). The 10 measurements per area were taken within three regions; top, middle, and bottom of each wall and for each region the average value was considered. Fig. 10 shows the variation of the microstructure among the “bottom”, “middle” and “top” regions of the thin walls cross-region (z-x section). The example of how the PDAS measurement was performed is also shown and the results of the average measurements collected within the three regions mentioned are also reported in the graph (Fig. 10). Although the results show similar trends, the most significant difference is in the middle of the wall, indeed the PDAS measurements are quite different depending on the laser mode used, and the frequency applied. Moreover, the 10Hz frequency produced walls where the PDAS showed a trend from the bottom till the top of the wall that was quite different from the other trends registered. It is important to highlight that there is a difference of approximately 1μm considering the PDAS between the middle region and the top/bottom, when CW laser and the PW (1000Hz, 100Hz) are used. On the contrary, the use of PW laser with a frequency of 10Hz did not significantly affect the microstructure size. (Fig. 10).

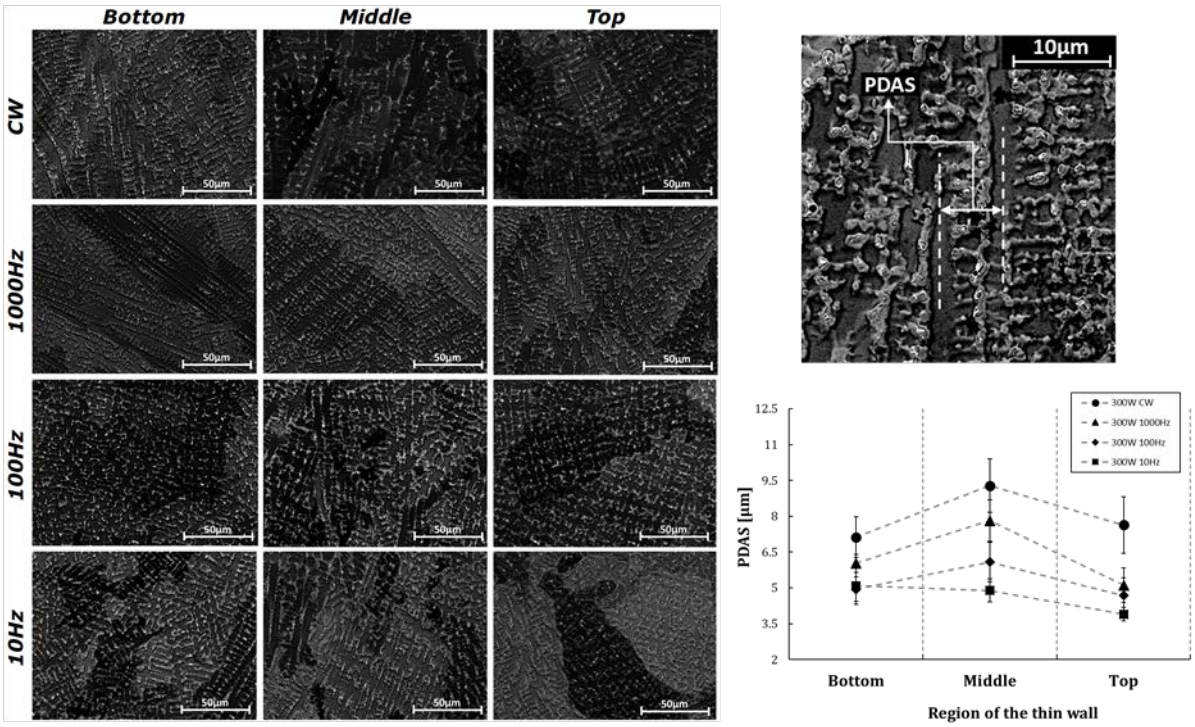

Figure.12.10. SEM of the cross-section of the thin walls depending on the frequencies and PDAS measurement.

Segregation Analysis

The EDS analysis was performed on the cross and longitudinal section of each wall to characterize the segregation regions highlighted by the BSEM analysis (Fig. 11). As expected, the white spots; material with higher atomic density, are mainly composed by Mo and Nb, chemical elements that mainly characterize the Laves phase in the Inconel 718 [8]. Indeed, the redistribution coefficient of the Nb and the Mo is lower than 1 and suggests that they easily segregate in the liquid region and remaining there during the solidification.

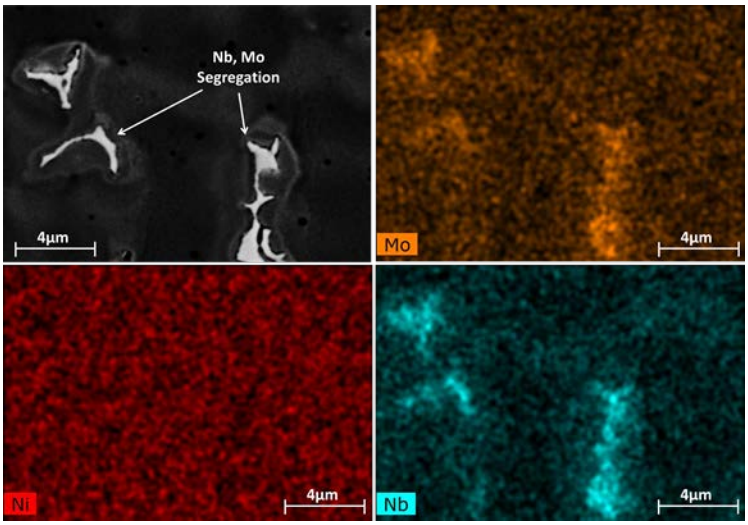

Figure.12.11. BSEM of the segregated region and the EDS analysis of the white spots.

To calculate the area of the segregated regions within the cross-section of each sample, several greyscale micrographs were converted in black and white two channels through the threshold level regulation (Fig. 12). In these new pictures (Fig. 12b) the segregated regions were in black, while the γ matrix was white, therefore, the percentage area could be easily calculated. An example of the adopted technique is reported in Fig. 12b, and the collected results were reported in a graph showed in Fig. 13.

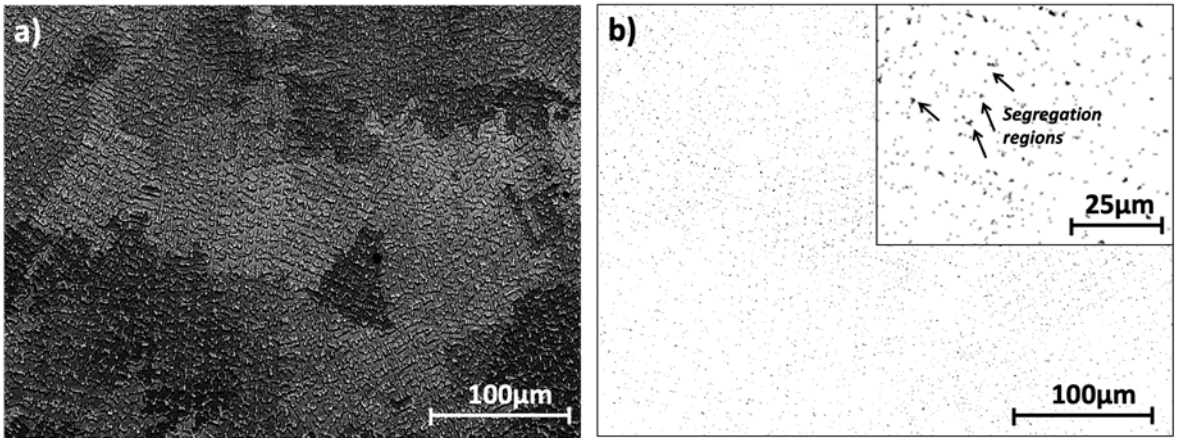

Figure.12.12. a) BSEM micrograph of the thin wall cross-section; b) threshold set on picture (a) to balance the black-white level and measure the %area of the segregated regions.

The %area of segregation did not show a significant difference between the bottom and the top of the thin walls when the PW laser with the frequency of 100Hz, 1000Hz or CW laser mode was used. Indeed, the trends were quite similar if compared each other. On the other hand,

decreasing the frequency to 10Hz permitted a reduction around the segregation, and keep the distribution almost similar from the bottom till the top of the thin walls (Fig. 13).

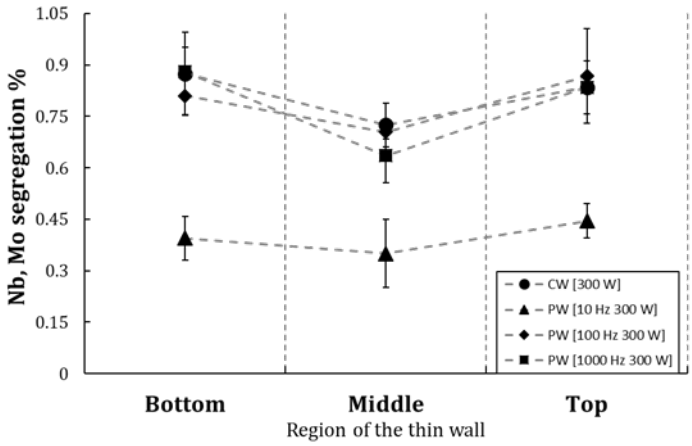

Figure.12.13. %Area of the segregated region measured in the bottom, middle and top region of the thin walls cross-sections.

Hardness Analysis

The microhardness on the cross-section of each wall was measured and the results reported in Fig. 14 and Fig. 15. The gradient map showed that the hardness values were different depending on the height of the deposited walls, and that frequency also played an important role. To quantify the average value of hardness for each wall, the region of interest considered has been divided into three parts starting from the bottom of 0mm to 6mm, and then from 6mm to 14mm and the last part from 14mm to 19mm of the height. The results are shown in Fig. 15.

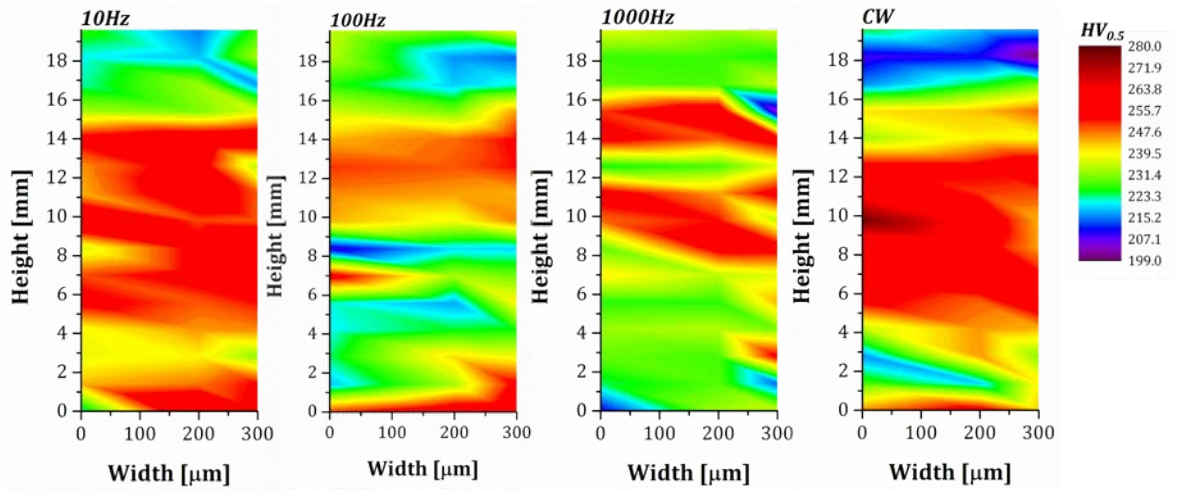

Figure.12.14. Hardness measurements of the cross-section of the thin walls (gradient map).

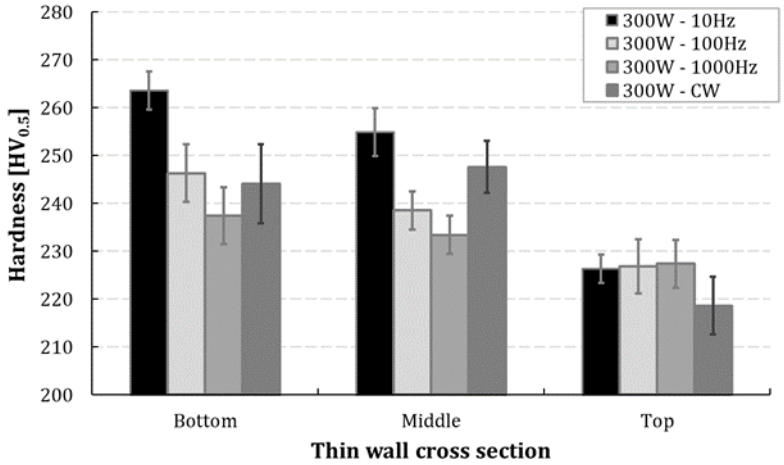

Figure.12.15. Hardness average values measured within the cross-section.

Regardless of the PW or CW laser mode used, the hardness trend among the samples analysed did not show any significant changes. In general, the hardness was higher on the bottom and the middle part of the deposited wall and continued to decrease in the top part.

Discussion

Effect of Pulsing Frequency on the Thermal Gradient

The laser mode used during the DLD showed a significant effect on the thermal field. This developed due to the interaction among the powder, heat source and substrate seen in the initial steps of the deposition. The transition of the frequency from 10Hz to 1000Hz of pulsed laser was used until the CW showed an increment of heat within the melt pool, and in general in the overall deposition process. The use of the pulsed laser showed a melt pool characterized by a "heart-beat" behaviour, and, therefore, the development of local thermal cycles (Fig. 3a, Fig. 4 and Fig. 16. A higher frequency (e.g., 1000Hz) led to a thermal field comparable with the CW, while the transition frequency was represented by 100Hz. An interesting local thermal cycle was represented by the 10Hz frequency that led to low heat accumulation, a higher cooling rate and, therefore, the melt pool was subjected by local solidification-melting cycles. Fig. 16 shows the comparison between the temperature measured when the CW and the 10Hz pulsed lasers were used during the DLD process. The temperatures are compared with the power signals set on the laser, and the cyclic temperature oscillations are exactly related to the power graph when the pulsed laser (10Hz) was set. Therefore, when a low frequency such as 10Hz is set with 300W of laser power, the material locally undergoes melting and solidification cycles, and this effect is subsequently occurring when the next layers are deposited. On the contrary, using higher frequencies such as 1000Hz or CW laser modes results in the local thermal cycles being neglected and underdeveloped. Consequently, the only thermal cycles induced on the material are due to the subsequent deposition of the next layers.

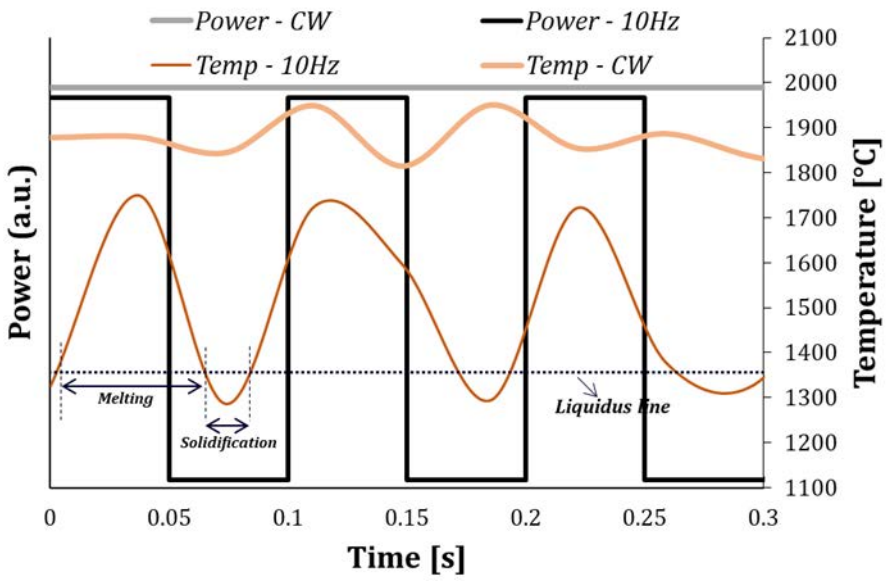

Figure.12.16. Comparison of the thermal profiles when pulsed and CW laser modes are used. The use of 10Hz frequency led to local thermal cycles with temperatures between the solidification and the melting region.

Focusing on the pulsed laser, it is possible to summarize that among the three frequencies investigated, the 10Hz reaches an effective cooling rate that leads the temperature to decrease within the solidification region. The cooling rate measured when 100Hz was used, allows the temperature to reach values slightly higher than the melting temperature during cooling when the laser is set on OFF. Therefore, 100Hz represents the transition frequency and a higher value of pulsed frequency which led to thermal field behaviour comparable to the one produced by the CW laser.

Moreover, the thermal field, ten seconds after the deposition process was completed, has also been analysed to qualitatively evaluate the amount of absorbed or dissipated heat. It is possible to claim that the use of a pulsed laser clearly helped reduce the accumulation of the heat in the deposited material, and this result is also evident from the beginning of the manufacturing process as shown by the thermocouples results (Fig. 5). Fig. 17 shows the distribution of the temperature on the z-x plane of the deposited walls ten seconds after the deposition process was completed. The wall produced by the CW laser showed a higher temperature compared

with the ones produced by the pulsed laser. The lower accumulation of heat has been reached by the lower frequency (10Hz) of the pulsed laser (Fig. 17d).

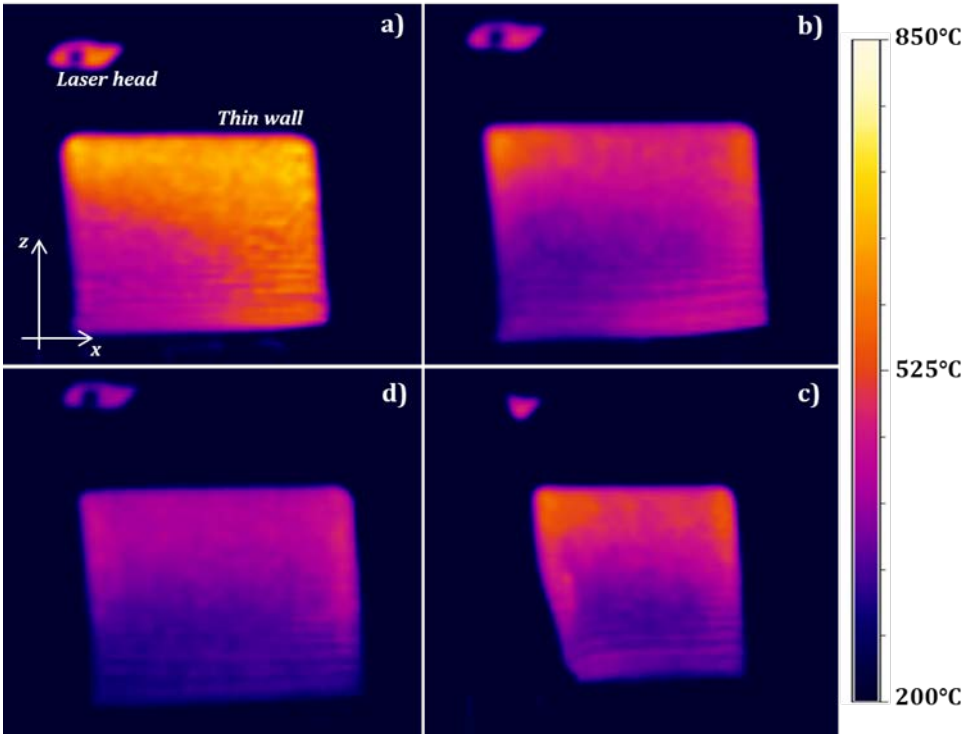

Figure.12.17. Temperature distribution on the z-x plane of the thin walls produced by DLD; a) CW laser; b) 1000Hz; c) 100Hz and d) 10Hz pulsed laser.

Effect of Pulsing Frequency on Surface Quality and Microstructure

Fig. 6 and Fig. 7 show the results of the analyses carried out on the longitudinal surface of the produced walls when different values of the pulsed laser were adopted during the deposition. Focusing on Fig. 6 between each deposited layer there was an accumulation of unmelted powder particles, and their accumulation was significant when the frequency was increased till the CW regime was reached. The surface roughness S_a was also quantified as showed in Fig. 7, and the trend obtained was qualitatively observed also by the SEM analysis. The lowest S_a value measured was 28μm, when the frequency of the pulsed laser was set equal to 10Hz and the S_a increased by 33%, 21% and 63% when the frequency was set equal to 100Hz, 1000Hz and CW respectively.

A similar trend that highlights lower surface roughness when the PW laser is used has been reported by Shah et al. 2010. These quantified results suggest that the increase of the frequency critically increases the surface roughness [26]. The reason for the surface roughness modification was mainly related to the surface disturbance induced by the Marangoni flow, and, therefore, to the mixing and melting of the powder particles within the melt pool. As suggested by Fuhrich et al. 2001, the fluid flow during welding defines the shape of the melt pool. Moreover, the liquid flow pattern is usually produced by the surface tension driven convection known as Marangoni effect [27]. Considering the chemistry of the alloy used in this work, the percentage in weight of S was declared to be equal to 0.015%, which was high enough to lead a positive thermocapillary gradient ($\frac{\partial \gamma}{\partial T}$) [28,29]. A positive thermocapillary gradient provokes a centripetal Marangoni convention, therefore, the positive temperature coefficient of the surface tension led to a significant penetration depth, and a high aspect ratio of the weld pool is usually expected. Fig. 18 schematically reported the cross-section of the walls with the relative melt pool shape when the CW and the 10Hz PW laser were used. In detail, the divergence region of the laser irradiates the melted material, and, therefore, the melt pool, while the powder is blown within this zone. Since the width of the melt pool when using the CW laser was slightly bigger than the laser beam, a cooler region represented by the section ABC was characterized by lower temperature. Indeed, most of the heat in this region was conducted by the melted material, and not directly by the laser effect. Moreover, due to the positive thermocapillary gradient, a higher surface tension was generated in the region at a higher temperature that corresponded to the centre of the melt pool. Therefore, the combination of the Marangoni flow that pushed part of the peripheral particles. Along with a lower temperature this promoted the accumulation of un-melted particles with consequent formation of a rough surface between the deposited layers as also reported in Fig. 6d.

The use of the pulsed laser during the laser metal deposition resulted in modified melt pool behaviour inducing a high surface disturbance. The high surface disturbance of the melt pool improved the mixing action of the powder within the melt pool, therefore, the powder melted more effectively. Fig. 18 also suggests that the region of the deposited material A'B'C', that was not directly irradiated by the laser beam, and therefore melted, was significantly smaller compared with the one that was formed when the CW laser was used. Consequently, the heat accumulated in this region due to higher conduction, and the particles melted more effectively. Moreover, due to the less energy per time unit generated by the pulsed laser, the temperature peaks were significantly lower, and this reduced the penetration depth leading to a less U-shaped melt pool and reduced waviness effect on the external surface (Fig. 6a).

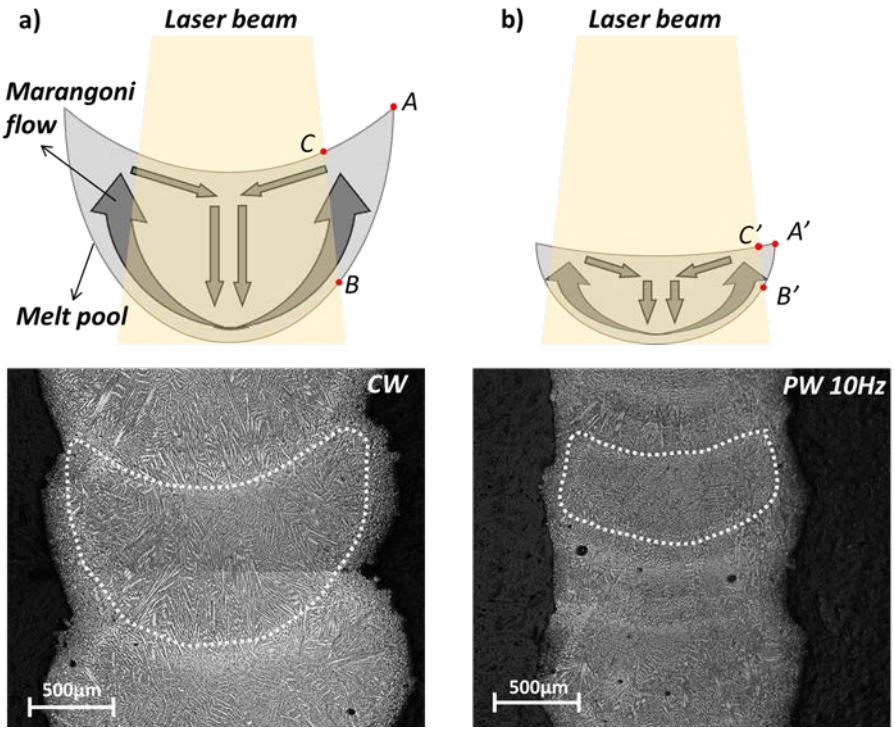

Figure.12.18. Marangoni flow within the cross-section of the thin walls when (a) CW and (b) 10Hz PW laser are used.

The different frequencies investigated, and the CW regime of the laser, showed a different effect on the microstructure as reported in Fig. 8, Fig. 9, and Fig. 10. In general, when the laser

mode was set as CW, the heat source and the related energy was kept constant during the deposition, therefore, the geometry of the melt pool was not expected to change. Observing the longitudinal section of the thin wall in Fig. 8b, the microstructure grew epitaxially, and the growing direction was dictated by the heat source movement layer by layer. Using the pulsed laser with 1000Hz and 100Hz, a similar development of the columnar dendrites was observed with the CW and is shown in Fig. 8d, Fig. 8f. Moreover, when the frequency was set equal to 100Hz, a slight appearance of the discrete melt pool boundaries was visible, although, they were not clearly distinguishable as showed by Fig. 8h. In detail, since the scan speed was 275mm/min (4.58mm/s), and the pulsing frequency was 10Hz (10 pulse/s) it is possible to observe that the discrete melt pool band distance, approximately 450μm corresponded to a single laser pulse. Indeed, considering 0.5s, five discrete melt pool bands with a total length of approximately 2.18 mm, should be expected due to the frequency and the scan speed set. In Fig. 8h the five distinguishable discrete melt pool band had a total length of approximately 2.24mm. Considering the orientation of the grains, the dendrites grew differently and were oriented to the centre of each discrete melt pool generated by the pulsed laser. Therefore, it is clear that the pulsed laser, and particularly lower frequency, were able to modify the growing orientation of the dendritic microstructure within the melt pool and layer by layer. The formation of discrete melt pool bands interrupted the formation of long dendrites, since every pulse generated a new melt pool with a new liquid-to-solid, and nucleation of new dendrites from the discrete band (Fig. 8h). The refinement of the microstructure when the pulsed laser was operated, was also clearly confirmed by the EBSD analysis shown in Fig. 9. The use of the CW, and pulsed laser mode (1000Hz) showed similar results in terms of microstructural growth mode and orientation. Indeed Fig. 9a and 9b illustrate a similar zigzag growing orientation due to the continuous movement of the heat source (laser) from the left to the right and vice-versa. The grains were elongated with a predominant dimension through the build

direction (z-direction). Although the predominant size of the grains was comparable with the layer thickness (Fig. 9a) when the laser mode was pulsed, the grains started to show a small refinement (Fig. 9b). This became more significant when the frequency was decreased to 10Hz as showed by Fig. 9c. Therefore, the frequency of the laser played an important role in microstructure refinement. Indeed, the lower frequency, with a more randomly distributed microstructure, with an aspect ratio of the grains very close to 1 enabled a thin part to be manufactured. This latter result was better highlighted by the EBSD carried out on the cross-section of the thin walls (Fig. 9d and Fig. 9e). The grains obtained due to the 10Hz pulsed laser were more randomly distributed, with no preferential growth direction, indeed in fact the grains were growing among the <001>, <111> and <101> directions. On the contrary, the grains obtained with the CW laser grew more vertically and showed a preferential growth orientation <001> (crystals in red). The use of low frequency of the pulsed laser completely changed the growth orientation of the grains that are usually driven by the heat source movement. Considering the thermal analysis, the higher cooling rate due to the pulsed laser allowed a reduction in heat accumulation, and, therefore, the grains did not have enough time to grow through the preferential orientation driven by the heat source. Indeed, lower frequency means bigger time step during which the laser is off, and this corresponds to longer solidification time for the melted material. A significant effect of the solidification time was observed on the sample produced with the lower frequency of the pulsed laser at 10Hz shown in Fig.16. As discussed in paragraph 3.1, higher frequencies than 10Hz showed a thermal field behaviour comparable to the one observed when CW laser was used, and this result explained the slight difference in the microstructure when 100Hz, 1000Hz and CW were used. The microstructural size has been quantified considering the PDAS as showed in Fig. 10. The effects of the heat accumulation and dissipation, and, therefore, the cooling rate, are evident on the size of the primary dendrites. Although the analysis considered the cross-section (z-y plane) of each

produced wall, the EBSD analyses highlighted the transition between coarse and fine microstructure on the longitudinal section (z-x plane) when the laser was pulsed with different frequencies. Significant differences in the PDAS started from the middle of the wall till the top, and the different thermal gradient (G) and solidification rate (R) were key factors in this. Chen et al. 2016 [30] investigated the dendritic microstructure behaviour and morphology when DLD was performed with Inconel 718. They used an analytical relation between the PDAS and the cooling rate as showed in Equation 1:

$$\lambda = 80\varepsilon^{-0.33}$$

where λ represents the PDAS and the ε represents the cooling rate ($G \cdot R$) measured in °C/s. Although, the Equation 1 was developed by Katayama and Matsunawa [31] for a laser welded stainless steels, it has been successfully used to estimate the DAS considering different class of materials [30,32]. Manipulating Equation 1 to get the ε value, the cooling rate, depending on the PDAS experimentally measured was reported in Fig. 19. Two different effects, depending on the laser mode used, can be observed by the obtained results. In general, an increase in the cooling rate was due to the decrease of the frequency, and it is also related to the region of the wall considered. The cooling rate obtained with the CW or pulsed laser (100Hz, 1000Hz) showed a similar trend, higher cooling rate in the bottom and top region of the wall. This suggested rapid cooling due to the presence of the substrate, and the air respectively that act as heat sinks. The middle region of the walls showed a lower value due to the accumulation of heat, and this result justify also the coarse microstructure observed within this region. On the contrary, when the 10Hz frequency was used, the cooling rate increased from the boot till the top of the wall suggesting an enhanced dissipation of the heat, and, therefore, finer microstructure as shown by Fig. 10. The cooling rate measured by the thermal field acquired by the infrared camera was compared with the one obtained by the PDAS measurements.

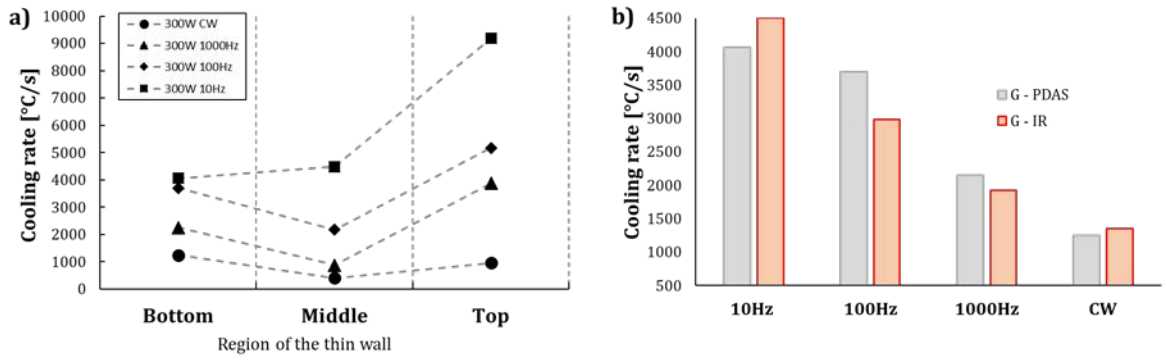

Figure.12.19: Cooling rate, a) evaluated by PDAS; b) comparison between the cooling rate evaluated by PDAS and IR camera considering the bottom region of the wall.

Effect of Pulsing Frequency on Segregation

During the welding procedures or the additive manufacturing process of the Inconel 718 alloy, a particular formation problem of Nb rich phases, known as the Laves phase, is generally experienced. The Laves phase is an intermetallic phase represented by Ni, Cr, $Fe_{2,}$ Nb, Mo, Ti and its formation is observed within the interdendritic region during the solidification process. This phase is undesirable due to its dual detrimental effects on the mechanical properties. since the Laves phase induces the brittle behaviour and it depletes the γ matrix of useful alloying elements (e.g., Nb and Ti) that forms the strengthening phases (γ' and γ'') after the heat treatments. Moreover, the brittle nature of the Laves phase usually represents a favourable site for cracks formation and propagation [33,34]. In this study, the use of CW and pulsed laser was effective in modifying the segregation morphology in terms of shape and its distribution within the γ matrix. Indeed, the pulsed laser allowed to achieve finer microstructure compared with the CW laser (Fig. 10), therefore, a different distribution of the segregation was also achieved. Moreover, the frequency also played an important role since the PDAS was smaller (10Hz pulsed laser frequency) suggesting finer microstructure. Indeed, the dendritic grains continuously nucleated and grew, but with limited size due to the fluctuation of the thermal

field induced by the pulsed heat source which avoided the development of long columnar grains. The finer microstructure led to the formation of segregation regions more homogenously distributed, while the long inter-connected chains of Laves phase were observed when a higher frequency (1000Hz) and CW laser mode were used. The effectiveness of the heat treatment to drastically reduce or eliminate the segregation regions is usually affected by the morphology of the Laves phase. The exceedingly small Nb-enriched regions with a homogenous distribution showed advantages when the heat treatments (Solution treatment) were performed. This is clearly reported in the literature due to the better diffusion of Nb within the γ matrix to form the strengthening phase γ'' [20]. The morphology changes from inter-connected long Laves phases chains, to very short and isolated segregated regions, was favoured by the pulsed laser due to the combination of cyclic temperatures variations within the melt pool, enhanced cooling rate and fluctuating thermal gradient. Indeed, the interrupted heat source drove the continuous formation of new dendrites nucleation, but with limited size due to the interrupted heat flow. Therefore, less Nb was segregated compared to the one observed on the samples produced by a higher frequency, or the CW and the segregated regions resulted finer (Fig. 20).

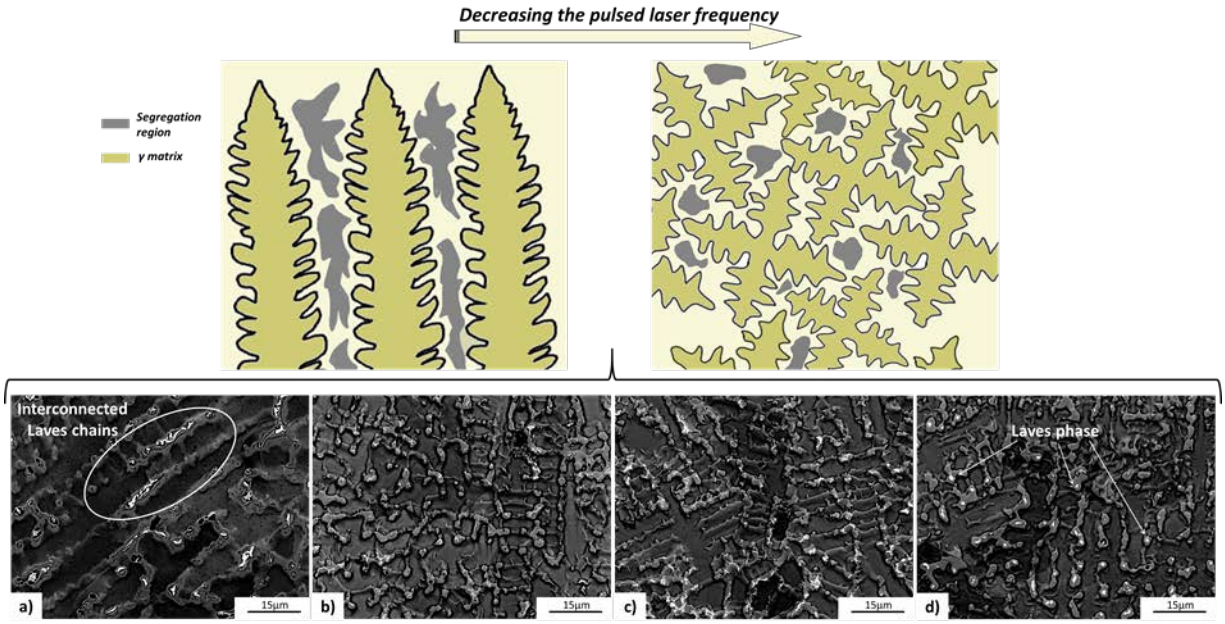

Figure. 12.20: Variation of the segregation region morphology depending on the pulsed laser frequency; a) CW, b) 1000Hz, c) 100Hz and d) 10Hz.

Effect of Pulsing Frequency on Mechanical Properties

The micro-hardness analysis carried out on the different samples highlighted some differences as shown in Fig. 14 and Fig. 15. The Inconel 718 is primarily strengthened by the γ'' formation (Ni_3Nb). However, during the DLD process, the rapid solidification does not allow the formation of the γ''-phase resulting in a low strength material. The low hardness values measured shown in Fig. 14 and Fig. 15 demonstrate the strengthening phase γ' was not developed but two main differences can be observed. Firstly, there is a clear difference in terms of hardness distribution when the PW and the CW laser are used to produce the samples. Indeed, as suggested in Fig. 14, the hardness distribution measured on the PW samples were generally high close to the substrate. This decreased gradually reaching the top of the wall, while the one measured on the sample produced by CW, showed a constant hardness distribution and a rapid drop only on the top part. The second difference is evident among the samples produced only by the pulsed laser. As observed, the frequency of the pulsed laser affected the microstructure, segregation distribution, and, therefore, the hardness. Higher

values of hardness were observed in the region of the material where a higher cooling rate, lower heat accumulation, and smaller PDAS were measured (lower frequency of the pulsed laser). Moreover, the sample produced by 10Hz pulsed laser showed almost the same value of hardness within the 14mm of the deposited material. This result highlights that the pulsed laser, and, the 10Hz frequency led to important material enhancements. Indeed, the higher and constant cooling rate within the 14mm of the deposited material (Fig. 19a), induced the nucleation and growth of smaller dendrites characterized by similar PDAS values (Fig. 10) and, therefore, higher hardness value. On the contrary, increasing the frequency to 100Hz and 1000Hz, the higher values of PDAS due to the higher heat accumulation and lower cooling rate, unavoidably induced a decrease of the hardness. Moreover, the changing in cooling rate from the bottom to the middle region of the wall, induced a variation in the microstructure size (PDAS), that led to an irregular hardness distribution as highlighted by the coloured map related to the 100Hz and 1000Hz in Fig. 14.

Conclusion

In this work, the effect of different pulsed wave laser frequencies, in comparison to continuous wave laser, on the surface roughness, microstructure, segregation and hardness was investigated during DLD. Infrared imaging was used to estimate the cooling rates induced by the laser mode and frequency. The surface quality and the roughness were evaluated by SEM and laser confocal microscopy. Micro-segregation was characterised using SEM and EDX analyses while the microstructure characteristics were analysed using EBSD. The hardness of the produced parts was assessed by micro-indentation carried out on the longitudinal section of the samples. The main conclusion can be summarised as follows:

1. The thermal field analysis highlights that the use of the pulsed laser allow to reduce the heat accumulated and therefore lower temperature are also involved in the deposition

process. Moreover, the use of low frequencies (in particular 10Hz) results in higher cooling rate and localized thermal cycles due to the variable heat source.

2. The surface quality of the produced parts improves when the pulsed laser is used, and better results are achievable with lower frequencies due to the melt pool shape modification. The pulsed laser allows to modify the melt pool shape due to the combination of Marangoni flow, reduce accumulated heat and better mix the particles, resulting in reduced waviness of the external surface (therefore, better surface quality).
3. The PDAS and the grains morphology as well as the orientation growth are affected by different kind of frequencies set when the pulsed laser is used. With the CW and high frequencies (e.g., 1000Hz) the microstructure develops showing a zigzag growing path drove by the heat source movement. The use of a low frequency (e.g., 10Hz) resulted in a more randomly oriented microstructure. Moreover, the microstructure experienced a transition from finer to coarser with an increase of the frequency to 1000 Hz, as well as through the use of the CW laser mode.
4. The fine microstructure induced by the pulsed wave laser avoids the formation of long interconnected Laves phase chains, resulting in a reduced amount of segregation.
5. The hardness is affected using the different laser modes (i.e., continuous wave or pulsed wave). The use of the pulsed wave enhances the hardness of the deposited material due to the combined effect of the reduced segregated phases and the finer microstructure. The latter can show a better response to the heat treatment (solution treatment and ageing) as highlighted by the literature.

In future research, the conventional heat treatments such as solution treatment and ageing as well as Hot Isostatic Pressing can be investigated to study their effects on parts produced by pulsed wave laser with different frequencies as well as the continuous wave laser.

Acknowledgments

The authors would like to acknowledge the European research project that founded this research. The project belongs to Horizon 2020 research and innovation programmed Novel ALL-IN-ONE machines, robots, and systems for affordable, worldwide and lifetime Distributed 3D hybrid manufacturing and repair operations (Project ID: 723795). AA would like to acknowledge the funding by the Royal Commission of Jubail and Yanbu (Kingdom of Saudi Arabia) for funding his PhD project.

CRediT authorship contribution statement

Stano Imbrogno: designed the study and performed the experimental tests and the analysis of the results. Writing – review and editing

Abdullah Alhuzaim: contributed the experimental tests

Moataz Attallah: supervision, support on experimental feasibility and infrastructure.

References

[1] C. Chen, H.C. Wu, M.F. Chiang, Laser cladding in repair of IN738 turbine blades, Int. Heat Treat. Surf. Eng. 2 (2008) 140–146. https://doi.org/10.1179/174951508X446484.

[2] A. Weisheit, A. Gasser, G. Backes, T. Jambor, N. Pirch, K. Wissenbach, Direct Laser Cladding , Current Status and Future Scope of Application, in: 2013: pp. 221–240. https://doi.org/10.1007/978-3-642-28359-8_5.

[3] D. Gu, D. Gu, Laser Additive Manufacturing (AM): Classification, Processing Philosophy, and Metallurgical Mechanisms, in: Laser Addit. Manuf. High-Performance Mater., Springer Berlin Heidelberg, 2015: pp. 15–71. https://doi.org/10.1007/978-3-662-46089-4_2.

[4] M.J. Donachie, S.J. Donachie, Superalloys a Technical Guide Second Edition Superalloys: A Technical Guide (#06128G) www.asminternational.org, 2002. www.asminternational.org (accessed June 8, 2020).

[5] F. Campbell, Manufacturing Technology for Aerospace Structural Materials, Elsevier Ltd, 2006. https://doi.org/10.1016/B978-1-85617-495-4.X5000-8.

[6] M. Durand-Charre, The microstructure of superalloys, Gordon and Breach Science Publishers, 1997.

[7] Y. Chen, Y. Guo, M. Xu, C. Ma, Q. Zhang, L. Wang, J. Yao, Z. Li, Study on the element segregation and Laves phase formation in the laser metal deposited IN718 superalloy by flat top laser and gaussian distribution laser, Mater. Sci. Eng. A. 754 (2019) 339–347. https://doi.org/10.1016/j.msea.2019.03.096.

[8] C. Radhakrishna, K. Prasad Rao, The formation and control of Laves phase in superalloy 718 welds, J. Mater. Sci. 32 (1997) 1977–1984. https://doi.org/10.1023/A:1018541915113.

[9] R.C. Reed, The Superalloys fundamentals and applications, Cambridge University Press, 2006. https://doi.org/10.1017/CBO9780511541285.

[10] Z. Li, J. Chen, S. Sui, C. Zhong, X. Lu, X. Lin, The microstructure evolution and tensile properties of Inconel 718 fabricated by high-deposition-rate laser directed energy deposition, Addit. Manuf. (2019) 100941. https://doi.org/10.1016/j.addma.2019.100941.

[11] S. Sui, J. Chen, E. Fan, H. Yang, X. Lin, W. Huang, The influence of Laves phases on the high-cycle fatigue behavior of laser additive manufactured Inconel 718, Mater. Sci. Eng. A. 695 (2017) 6–13. https://doi.org/10.1016/j.msea.2017.03.098.

[12] T. Antonsson, H. Fredriksson, The effect of cooling rate on the solidification of INCONEL 718, Metall. Mater. Trans. B Process Metall. Mater. Process. Sci. 36 (2005) 85–96. https://doi.org/10.1007/s11663-005-0009-0.

[13] Y.C. Zhang, Z.G. Li, P.L. Nie, Y.X. Wu, Effect of ultrarapid cooling on microstructure of laser cladding IN718 coating, Surf. Eng. 29 (2013) 414–418. https://doi.org/10.1179/1743294413Y.0000000142.

[14] H. Qi, M. Azer, A. Ritter, Studies of standard heat treatment effects on microstructure and mechanical properties of laser net shape manufactured INCONEL 718, Metall. Mater. Trans. A Phys. Metall. Mater. Sci. 40 (2009) 2410–2422. https://doi.org/10.1007/s11661-009-9949-3.

[15] M. Ma, Z. Wang, X. Zeng, Effect of energy input on microstructural evolution of direct laser fabricated IN718 alloy, Mater. Charact. 106 (2015) 420–427. https://doi.org/10.1016/j.matchar.2015.06.027.

[16] Y. Zhai, D.A. Lados, E.J. Brown, G.N. Vigilante, Understanding the microstructure and mechanical properties of Ti-6Al-4V and Inconel 718 alloys manufactured by Laser

Engineered Net Shaping, Addit. Manuf. 27 (2019) 334–344. https://doi.org/10.1016/j.addma.2019.02.017.
[17] D. Kong, C. Dong, X. Ni, L. Zhang, C. Man, J. Yao, Y. Ji, Y. Ying, K. Xiao, X. Cheng, X. Li, High-throughput fabrication of nickel-based alloys with different Nb contents via a dual-feed additive manufacturing system: Effect of Nb content on microstructural and mechanical properties, J. Alloys Compd. 785 (2019) 826–837. https://doi.org/10.1016/j.jallcom.2019.01.263.
[18] M. Gharbi, P. Peyre, C. Gorny, M. Carin, S. Morville, P. Le Masson, D. Carron, R. Fabbro, Influence of a pulsed laser regime on surface finish induced by the direct metal deposition process on a Ti64 alloy, J. Mater. Process. Technol. 214 (2014) 485–495. https://doi.org/10.1016/j.jmatprotec.2013.10.004.
[19] H. Xiao, S.M. Li, W.J. Xiao, Y.Q. Li, L.M. Cha, J. Mazumder, L.J. Song, Effects of laser modes on Nb segregation and Laves phase formation during laser additive manufacturing of nickel-based superalloy, Mater. Lett. 188 (2017) 260–262. https://doi.org/10.1016/j.matlet.2016.10.118.
[20] H. Xiao, S. Li, X. Han, J. Mazumder, L. Song, Laves phase control of Inconel 718 alloy using quasi-continuous-wave laser additive manufacturing, Mater. Des. 122 (2017) 330–339. https://doi.org/10.1016/j.matdes.2017.03.004.
[21] H. Xiao, P. Xie, M. Cheng, L. Song, Enhancing mechanical properties of quasi-continuous-wave laser additive manufactured Inconel 718 through controlling the niobium-rich precipitates, Addit. Manuf. 34 (2020) 101278. https://doi.org/10.1016/j.addma.2020.101278.
[22] G.D.J. Ram, A.V. Reddy, K.P. Rao, G.M. Reddy, Control of laves phase in inconel 718 GTA welds with current pulsing, Sci. Technol. Weld. Join. 9 (2004) 390–398. https://doi.org/10.1179/136217104225021788.
[23] X. Wang, D. Deng, H. Yi, H. Xu, S. Yang, H. Zhang, Influences of pulse laser parameters on properties of AISI316L stainless steel thin-walled part by laser material deposition, Opt. Laser Technol. 92 (2017) 5–14. https://doi.org/10.1016/j.optlastec.2016.12.021.
[24] S. Li, H. Xiao, K. Liu, W. Xiao, Y. Li, X. Han, J. Mazumder, L. Song, Melt-pool motion, temperature variation and dendritic morphology of Inconel 718 during pulsed- and continuous-wave laser additive manufacturing: A comparative study, Mater. Des. 119 (2017) 351–360. https://doi.org/10.1016/j.matdes.2017.01.065.
[25] G. Zhu, D. Li, A. Zhang, G. Pi, Y. Tang, The influence of standoff variations on the forming accuracy in laser direct metal deposition, Rapid Prototyp. J. 17 (2011) 98–106. https://doi.org/10.1108/13552541111113844.
[26] K. Shah, A.J. Pinkerton, A. Salman, L. Li, Effects of melt pool variables and process parameters in laser direct metal deposition of aerospace alloys, Mater. Manuf. Process. 25 (2010) 1372–1380. https://doi.org/10.1080/10426914.2010.480999.
[27] T. Fuhrich, P. Berger, H. Hügel, Marangoni effect in laser deep penetration welding of steel, J. Laser Appl. 13 (2001) 178–186. https://doi.org/10.2351/1.1404412.
[28] P.D. Lee, P.N. Quested, M. McLean, Modelling of Marangoni effects in electron beam melting, Philos. Trans. R. Soc. London. Ser. A Math. Phys. Eng. Sci. 356 (1998) 1027–1043. https://doi.org/10.1098/rsta.1998.0207.
[29] Y. Lee, S.S. Babu, D.F. Farson, Influence of Fluid Convection on Weld Pool Formation in Laser Cladding Solidification Microstructure Control in Electron Beam Additive Manufacturing View project, n.d. https://www.researchgate.net/publication/268278864 (accessed June 8, 2020).

[30] Y. Chen, F. Lu, K. Zhang, P. Nie, S.R. Elmi Hosseini, K. Feng, Z. Li, Dendritic microstructure and hot cracking of laser additive manufactured Inconel 718 under improved base cooling, J. Alloys Compd. 670 (2016) 312–321. https://doi.org/10.1016/j.jallcom.2016.01.250.
[31] S. Katayama, A. Matsunawa, Solidification microstructure of laser welded stainless steels, Journal of Laser Applications, (1984) 60. https://doi.org/10.2351/1.5057623.
[32] J.N. Dupont, C. V. Robino, A.R. Marder, M.R. Notis, Solidification of Nb-bearing superalloys: Part II. Pseudoternary solidification surfaces, Metall. Mater. Trans. A Phys. Metall. Mater. Sci. 29 (1998) 2797–2806. https://doi.org/10.1007/s11661-998-0320-x.
[33] S.G.K. Manikandan, D. Sivakumar, M. Kamaraj, Welding the inconel 718 superalloy: Reduction of micro-segregation and laves phases, Elsevier, 2019. https://doi.org/10.1016/C2018-0-01653-9.
[34] J.N. DuPont, J.C. Lippold, S.D. Kiser, Welding Metallurgy and Weldability of Nickel-Base Alloys, John Wiley & Sons, Inc., Hoboken, NJ, USA, 2009. https://doi.org/10.1002/9780470500262.